Electromagnetic Inspired Acoustic Metamaterials: Studying the Applications of Sound-Metastructures Interactions Based on Different Wave Phenomena

PAR

Seyyed Hussein SEYYED ESFAHLANI

EPFL

ÉCOLE POLYTECHNIQUE
FÉDÉRALE DE LAUSANNE

Suisse
2017

As you start to walk on the way,
the way appears.
— Rumi

To my family

Acknowledgements

Abstract

This thesis deals with electromagnetic inspired acoustic metamaterials, enabling sound-matter interactions in different wave scenarios that include propagation, guided-waves, radiation, refraction, reflection and transmission. To this end, a particular emphasis is placed on introducing novel applications for acoustic metamaterials operating on each one of the aforementioned wave scenarios.

A few years ago, metamaterials have been introduced as a new class of composite artificial materials, engineered to produce unusual effective material properties not readily available in nature. Electromagnetic metamaterials are probably the oldest class of metamaterials, being nowadays in the process of reaching maturity and being proposed for interesting commercial applications. On the other hand, as in most young but not yet mature emerging fields of science, acoustic metamaterials are still providing lots of fertile and unexplored ground for research and study.

Despite many inherent physical differences, the propagation of electromagnetic and acoustic waves are both governed by a similar mathematical model, the so-called Helmholtz wave equation. The main purpose of this work is to leverage this amazing similarity by translating recent advances in electromagnetic metamaterials into their corresponding, previously unseen, applications in acoustics.

The first contribution of this thesis is to adapt the classic electromagnetic transmission-line theory to allow the design of acoustic metamaterials. The proposed circuit-based theory finds a direct application in the design of composite right/left hand transmission-line metamaterials, which yield novel guided-wave applications for acoustic metamaterials. Then, the developed theory is leveraged to model and achieve optimal design of different acoustic metamaterial-based devices, such as leaky-wave antennas and reflector-type metasurfaces.

The second part of the thesis spins around acoustic leaky-wave antennas and their different functionalities, showing that they are able to act as acoustic dispersive prisms in the refraction mode and as acoustic single sensor direction finder in the radiation mode.

Studying reflection phenomena in sound-metasurface interactions constitutes the next part of this thesis, where a membrane-capped cavity is introduced performing as an ultra-thin unit-cell for reflective acoustic metasurfaces. This leads to exciting applications of the concept, like acoustic reflectarray antennas and acoustic metasurface skin-cloaks.

Finally, the last part of this thesis deals with transmission phenomena in acoustic metasurfaces and, especially, in orbital angular momentum metasurfaces. This concept results in the design of an innovative labyrinthine-type helicoidal unit-cell that is used for phase coding a surface

and transforming impinging acoustic wavefronts into transmitted helical wavefronts.

Résumé

Cette thèse introduit des métamatériaux acoustiques inspirés de concepts analogues dans le domaine de l'électromagnétisme, permettant de traiter des interactions entre le son et la matière dans le cadre de la propagation d'ondes, d'ondes-guidées, du rayonnement, de la réfraction, de la réflexion et de la transmission. Un soin particulier est apporté pour proposer de nouvelles applications à ces concepts de métamatériaux acoustiques mettant en pratique chacune des modalités mentionnées ci-dessus.

Voilà quelques années que le concept de métamatériau a été proposé pour décrire une nouvelle catégorie de matériaux artificiels composites, conçus de manière à présenter des propriétés physiques effectives inédites dans la nature. Les premiers métamatériaux étudiés dans le domaine de l'électromagnétisme ont atteint une maturité qui permet désormais d'envisager des applications commerciales. D'un autre côté, les concepts de métamatériaux acoustiques ne sont apparus que très récemment dans la littérature et n'ont pas atteint un degré de maturité suffisant, laissant un champ d'investigations encore inexploré mais néanmoins fertile.

En dépit de nombreuses différences physiques intrinsèques, les propagations des ondes électromagnétiques et acoustiques sont gouvernées par un même modèle mathématique, à savoir l'équation des ondes de Helmholtz. La motivation principale de ce travail est de tirer profit de ces étonnantes similarités en transposant les avancées récentes du domaine des métamatériaux électromagnétiques vers des applications analogues inédites en acoustique.

La première contribution de cette thèse consiste à adapter la théorie classique des lignes de transmission électromagnétiques pour envisager un design spécifique de métamatériau acoustique. L'approche proposée, sous la forme de circuits électriques analogues, trouve une application directe dans le dimensionnement d'un métamatériau acoustique basé sur une ligne de transmission composite « gauche/droite », donnant lieu à de nouvelles applications en ondes guidées. Le modèle développé sera ensuite adapté pour dimensionner différents appareils acoustiques, tels que des antennes à ondes de fuites ou des métasurfaces réflectrices.

La deuxième partie de la thèse tourne autour du concept d'antenne acoustique à ondes de fuite, illustrant ses différentes fonctionnalités et démontrant ses applications, tant comme prisme acoustique dispersif dans le mode réfraction, que comme détecteur directionnel à capteur acoustique unique dans le mode rayonnement.

L'étude des phénomènes de réflexion issues des interactions son-métasurface constitue la suite de la thèse, dans laquelle une petite cavité fermée par une fine membrane est utilisée comme élément unitaire ultra-mince d'une métasurface acoustique réflectrice. Ce design permet d'aboutir à des applications innovantes telles qu'une antenne reflectarray acoustique

et un voile d'invisibilité acoustique.

Enfin, la dernière partie de la thèse traite des phénomènes de transmission par des métasurfaces acoustiques, en s'intéressant à des métasurfaces à moment angulaire orbital. Cette propriété résulte du design d'éléments unitaires innovants basés sur de minuscules labyrinthes acoustiques dans un support cylindrique, utilisés pour coder la phase d'une onde transmise entre ses extrêmités, permettant de transformer des fronts d'ondes plan incidents en fronts tournant à la sortie.

Mots-clés:

Métamatériaux Acoustiques, Métamatériaux Electromagnétiques, Métamatériaux Composites Gauche/Droite, Métamatériaux Lignes de Transmission, Antenne Acoustique à Ondes de Fuite, Prisme Acoustique Dispersif, Recherche de Source Acoustique à l'aide d'un Seul Capteur, Metasurface Acoustique, Reflectarray Acoustique, Metasurface Acoustique à Moment Angulaire Orbital.

Zusammenfassung

Diese Dissertation untersucht elektromagnetisch-inspirierte akustische Metamaterialien für die Interaktion von Schall und Materie für verschiedene Wellenphänomene wie Ausbreitung, geführte Wellen, Strahlung, Brechung, Reflexion und Übertragung. Dabei wird besonderes Augenmerk auf die Einführung neuartiger Anwendungen von akustischen Metamaterialien gelegt.

Vor ein paar Jahren wurden Metamaterialien als eine neue Art von zusammengesetzten künstlichen Materialien präsentiert, die so konstruiert sind, daß sie ungewöhnliche effektive Materialeigenschaften aufweisen, die so in der Natur nicht zu finden sind. Akustische Metamaterialien gehören zu den neuesten Unterdisziplinen dieses Gebietes. Dagegen haben elektromagnetische Metamaterialien, als älterer Teilbereich, die Einführungsphase seit einiger Zeit überschritten und viele Vorschläge für kommerzielle Anwendungen existieren bereits. Umgekehrt, wie für jeden neuen Bereich der Wissenschaft, bieten akustische Metamaterialien noch viel Raum für Forschung und Studium.

Die Ausbreitung von elektromagnetischen und akustischen Wellen wird, trotz vieler inhärenter Unterschiede, durch die gleiche mathematische Beziehung, die sogenannte Helmholtz-Gleichung beschrieben. Der Hauptzweck dieser Arbeit ist es, diese Ähnlichkeit auszunutzen und Kenntnisse aus dem Bereich elektromagnetischer Metamaterialen auf neuartige Anwendungen in der Akustik zu übertragen.

Der erste Beitrag dieser Arbeit ist die Modellierung von Metastrukturen mit Hilfe der Leitungstheorie, um akustische Metamaterialien zu entwerfen. Die auf der Schaltungslehre basierende Theorie wird dann auf die Entwicklung von rechts- und linkshändigen Metamaterialen für Übertragungsleitungen angewendet. Im weiteren Verlauf werden damit akustische Metamaterialanwendungen entworfen und optimiert, wie z. B. Leckwellenantennen und reflektorartige Metaoberflächen.

Der zweite Teil dreht sich um akustische Leckwellenantennen und ihre verschiedenen Funktionalitäten: im Brechungsmodus als akustisches dispersives Prisma und im Strahlungsmodus als akustischer Einsensor-Richtungssucher.

Der nächste Teil beschäftigt sich mit der Wechselwirkung von Schall und Metaoberflächen. Ein mit einer Kappe versehener Hohlraumresonator wird als ultradünne reflektorartige akustische Metaoberfläche vorgestellt. Dieses Konzept wird anschließend im Rahmen von Reflektarrayantennen und Tarnung mit Hilfe von akustischen Metaoberflächen als Beispiele für Anwendungen von akustischen Metastrukturen auf dem Gebiet von Wellenreflexion präsentiert.

Der letzte Teil dieser Arbeit behandelt Übertragungsphänomene in Metaoberflächen. Dabei

wird eine akustische Orbital-Drehimpuls-Metaoberfläche präsentiert. In diesem Zusammenhang wird zunächst eine neue labyrinthartige spiralförmige Elementarzelle entwickelt und anschließend für die Phasencodierung einer Oberfläche verwendet, die eine auftreffende akustische Wellenfront in eine schraubenförmige Wellenfront umwandelt.

Stichwörter:

Akustische Metamaterialien, elektromagnetische Metamaterialien, rechts-/linkshändige Metamaterialien, Übertragungsleitungmetamaterialien, akustische Leckwellenantenne, akustischen dispersives Prisma, akustischer Einsensor-Richtungssucher, akustische Metaoberfläche, akustische Reflectarray, akustische Orbital-Drehimpuls-Metaoberfläche

Contents

Contents

Contents

List of Figures

List of Figures

List of Tables

Acronyms

CRLH	Composite Right/Left Hand
RH	Right Hand
LH	Left Hand
TL	Transmission-Line
LWA	Leaky-Wave Antenna
OAM	Orbital Angular Momentum
SLS	Selective Laser Sintering
1D/2D/3D	One/Two/Three Dimensional
FFT	Fast Fourier Transform
DUT	Device Under Test
SC	Spectral Centroid
FEM	Finite Element Method
PWR	Power
CIE	Commission Internationale de l'Eclairage
SSDF	Single Sensor Direction Finding(er)

1 Introduction

1.1 Metamaterials

Etymology
Metamaterial is a compound word composed of two terms 'Meta' and 'Material'. 'Meta' literary means 'beyond' then 'metamaterial' means 'beyond-material'.

Definition
Metamaterial is referred to composite artificial materials which are engineered to produce unusual effective material properties or exhibit exotic behaviors which are not readily available in nature. These anomalous behaviors are not due to their microscopic but effective material properties resulting from arrangement, geometrical shapes and dimensions of the engineered composite.

Classification
Metamaterials can be grouped using different criteria such as:

- Geometry: They can be 1,2 or 3 dimensional structures.

- Physics: Metamaterials can be studied in electromagnetic, acoustic, thermodynamic, mechanic, optic or other realms.

- Effective material properties: They can be categorized based on their negative, positive, extreme or near-zero effective material properties.

1.1.1 Electromagnetic metamaterials

The history of metamaterial may date back to the study of artificial materials for manipulating electromagnetic waves. Jagadish Chandra Bose in 1898 conducted experiments on substances with chiral properties and Karl Ferdinand Lindman studied wave interaction with metallic helices as artificial chiral media in 1914 [1]. However, it was Winston E. Kock who developed

materials that had similar characteristics to what we today call it metamaterials in the late 1940s [2]. In 1967, Victor Veselago theoretically described negative-index materials and proved that such hypothetical materials could transmit waves with phase velocity anti-parallel to the direction of Poynting vector which is contrary to wave propagation in conventional materials. His theoretical findings is considered as one of the pillars of the metamaterial field [3]. Although some studies were conducted on artificial materials, realizing media with effective material parameters, and photonic and phononic crystals in the 1970s until the 1990s, it was Pendry who brought metamaterials to limelight. Indeed he proposed a practical way to fully realize the Left-Handed (LH) metamaterial (as opposed to Right-Handed (RH) materials) which allows an electromagnetic wave to convey energy with group and phase velocities in opposite directions. He first proposed that metallic wires aligned along the direction of a wave could provide negative permittivity (dielectric function $\epsilon < 0$) [4, 5] and then, he demonstrated that a split ring (C shape) with its axis placed along the direction of wave propagation could exhibit negative permeability ($\mu < 0$) [6]. Consequently, based on Pendry's work, composite medium with simultaneously negative permeability and permittivity was reported [7]. In 2000 and 2001, Smith et al. published theoretical and practical studies on negative index materials which exhibit negative refraction [8, 9] and John Pendry proved that such a negative index material makes a perfect lens [10].

1.1.2 Acoustic metamaterials

Inspired by electromagnetic metamaterials, the term acoustic metamaterial is now broadly applied to engineered acoustic materials, usually composites, in which an internal structure is used to induce effective properties in the artificial material and these effective properties are substantially different from those found in its components [11, 12]. However, the term metamaterial is not very precisely defined and a good definition may be, a material with 'on-demand' effective properties, without the constraints imposed by what nature provides. For acoustic metamaterials, the goal is to create a structural building block that, when assembled into a larger sample, exhibits desired values of mass density and bulk modulus different from the material itself. Indeed, acoustic wave propagation is controlled by the mass density and the bulk modulus of a material and in conventional media, both of these parameters are positive and cannot be easily altered. However, if metamaterials are constructed using resonant sub-wavelength meta-atoms, then it is possible to obtain values of the effective acoustic material parameters that are not observed in nature. One of the most unusual regimes for acoustic metamaterials arises when the real parts of the effective mass density and bulk modulus are negative ($\rho < 0$, $K < 0$) in the same frequency range which would physically mean that the material moves to left when being pushed to the right and expands upon compression. It can be proved that such a material, with simultaneous negative mass density and bulk modulus, exhibits negative index of refraction for sound waves [11, 12].

Although materials with negative mass density and bulk modulus are the most investigated types of acoustic metamaterials, this field covers much broader types of engineered materials and its boundaries go beyond materials with negative indices. Indeed, as of today any en-

gineered material with extreme material behaviours, such as non linearity, inhomogeneity, anisotropy, tunability, etc. can be defined as metamaterials. Figure. 1.1a can give a global illustration of this definition, where two axes in the horizontal plane represent the mass density (ρ) and bulk modulus (K) as the two fundamental material properties in acoustics, whereas the vertical axis shows the degree of non linearity, anisotropy, inhomogeneity, as the acoustic behaviours of the material, denoted by Ω. Therefore, the white region in Fig. 1.1a shows the conventional materials readily available in nature, and all the other regions represent metamaterials. What is referred to as conventional materials here, are all materials having positive mass density and bulk modulus which exhibits low to moderate degrees of Ω. Decomposed into its three main planes, Fig. 1.1b represents the plane which only describes the fundamental material properties. In this figure, all the regions in light orange represent the acoustic metamaterials. It should be also noted that in the first quadrant the regions with near zero or extremely high values of mass density and bulk modulus are considered as acoustic metamaterials. In Fig. 1.1c the region in light green represents the acoustic materials with unusual values of bulk modulus and/or with an extreme degree of Ω which are categorized as acoustic metamaterials. For instance, a mechanically tunable array of Helmholtz resonators shunted to an acoustic waveguide which exhibits controllable negative bulk modulus is categorized as acoustic metamaterials of this group. Finally, light blue region in Fig. 1.1d illustrates the acoustic metamaterials with unusual values of mass density and/or with an extreme degree of Ω. The array of tunable membranes such as piezoelectric resonators in a series configuration inside an acoustic waveguide can present controllable negative mass density which is an example for acoustic metamaterials of this group. Here, the tunability of the piezoelectric resonators are represented by a point in Ω axis.

 In addition to the presented general definition on acoustic metamaterials, there is a constraint which sometimes predominates this global definition. This strict constraint dictates that only engineered materials with subwavelength unit-cells (smaller than $\lambda/10$) can be defined as metamaterials. Indeed, the most common approach to constructing acoustic metamaterials is based on the use of structures whose interaction with acoustic waves is dominated by the internal behaviour of a single unit-cell of a periodic structure, often referred to as a meta-atom. To make this internal meta-atom response dominant, its size generally needs to be much smaller (about ten times smaller) than the smallest acoustic wavelength that is being used. By contrast, in phononic (for sound) or photonic (for light) crystals, unusual wave behaviour is created via the mutual interaction (multiple scattering) of unit-cells whose dimensions are typically about half of the operating wavelength [11]. It has been recently shown how local and multiple scattering responses can be combined in a single structure which blurs the line between these different classes of artificial media [13]. The subwavelength constraint ensures that the metamaterial behaves as a real material in the sense that the material response is not affected by the shape or boundaries of the sample. This equivalence will not hold for periodic materials in the phononic crystal regime, in which long-range interactions and spatial dispersion dominate the response. Instead, when the material response is determined by the local meta-atom response, effective bulk-material properties can be defined and estimated from simulations or measurements of very small samples.
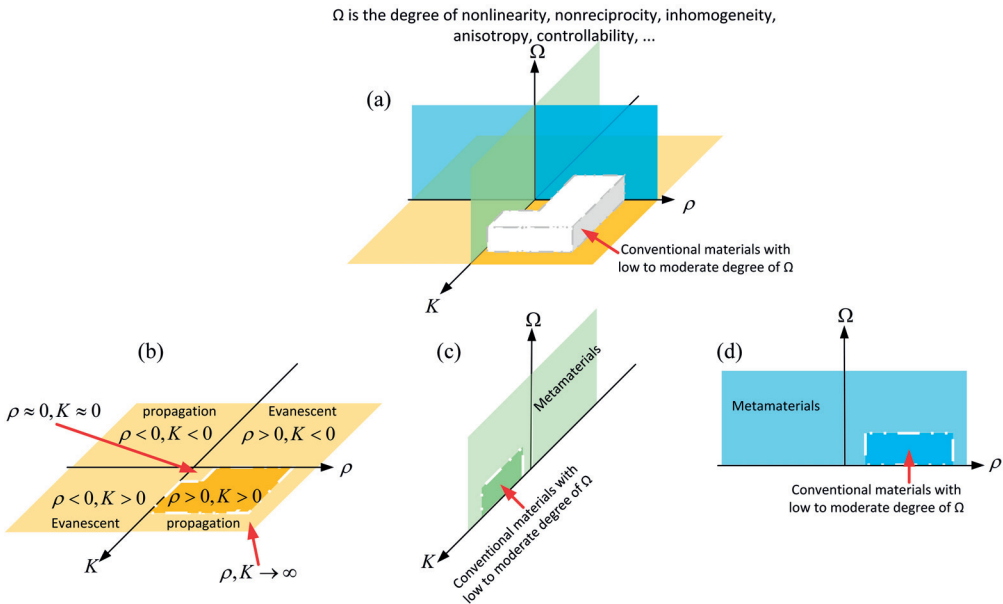
Figure 1.1: Definition of acoustic metamaterials used in this thesis. The region in white shows the conventional materials.

1.1.3 Literature review and state of the art

The literature review in acoustic metamaterials and generally in metamaterial is an elaborate task and needs a careful study of the literature from the past, because what is defined today as metamaterial is much more general than fifteen years ago and the boundaries are still moving. Here, the literature review has been performed based on the definition provided in Fig. 1.1a and it is presented in three time periods: before 2000 which mostly deals with periodic structures especially acoustic lenses, from 2000 to 2010 where the research was highly concentrated on classical concepts of metamaterials such as achieving materials with negative indices and finally after 2010 where the research was mostly directed towards the applications of acoustic metamaterials.

Figure. 1.2 shows the time-laps of the evolution of the acoustic metamaterials where some major research contributions which extended the boundaries of this field have been included and highlighted. This figure consists of four horizontal black lines, denoted as time lines, and each of them has been segmented into two or more sections and in a chronological order a specific year has been assigned to each section. A single illustration has been assigned to the corresponding section for the year of the publication/report. This time-laps explicitly shows, despite the fact that the emergence of acoustic metamaterials may date back to as early as 1949, the research in this field has only been accelerated and grown since 2010 and the presented work is also the results of the research performed in this time span. In the following section, the major advances presented in Fig. 1.2 are briefly explained in chronological order and this figure can be referred to as a guideline.
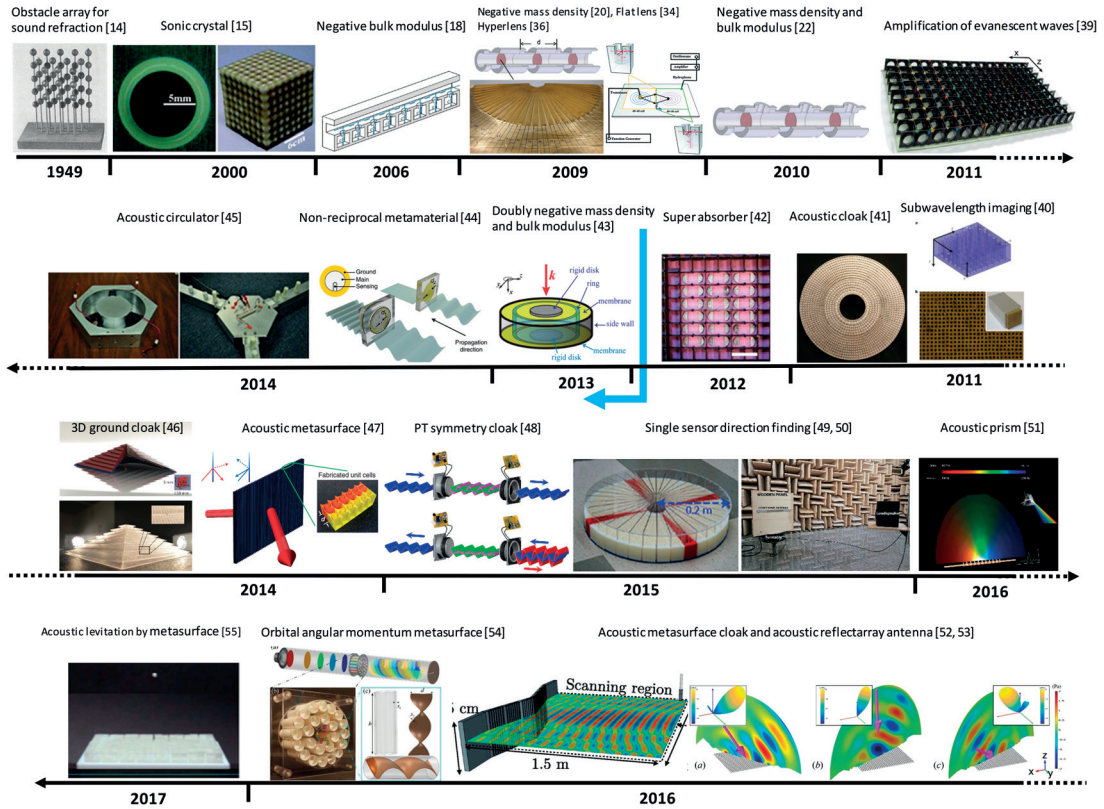
Figure 1.2: Time-laps of the evolution of acoustic metamaterials. Blue arrow depicts the time of the start of this thesis.

Before 2000:

The first trace of acoustic metamaterials may be found in the work of Winston E. Kock in 1949 [14]. He used the analogy between electromagnetics and acoustics to design apparatuses consisting of arrays of spherical obstacles, as shown in Fig. 1.2, which were small compared to the wavelength and were able to control the wavefronts of the transmitted wave. Although, phononic crystals (as periodic structures similar to metamaterials) became hot research topic in the 1990s, the size of their constituent unit-cells were comparable to the wavelength and this distinguished them from metamaterials.

Form 2000 to 2010:

In this period of time, researchers were still investigating acoustic negative index metamaterials, therefore the literature review is presented in two different sections: towards obtaining negative material properties and beyond negative index metamaterials.

Path towards negative index acoustic metamaterials.

Shown in the first time line of Fig. 1.2, in 2000, Liu proposed silicone-coated metallic spheres embedded in epoxy, called sonic crystals, to create locally resonant structures and achieved effective negative mass density [15]. This study can be considered as milestone for modern acoustic metamaterials. In 2004, Li conducted a numerical study on rubber spheres suspended in water and showed that monopolar and dipolar resonant modes can coexist and such a configutaion exhibits double negative refraction index [16] a similar study on localized resonances was also performed by Movchan [17] in the same year. Later in 2006, Fang used a waveguide shunted by a series of Helmholtz resonators, shown in Fig. 1.2, to exhibit effective negative bulk modulus [18]. In 2007, theoretical studies were reported on the method to retrieve effective acoustic material properties [19]. Finally, in 2009, Lee et al. published two experimental studies on negative mass [20] (top left of section 2009 in Fig. 1.2) and negative bulk modulus [21] which was followed by the third study from the same group in 2010 on demonstrating the acoustic double negativity using a waveguide shunted by a series of holes and decorated with clamped membranes between each two consecutive holes [22]. The breakthrough on achieving the double negative index material has been shown in section 2010 of Fig. 1.2.

Beyond double negative acoustic metamaterials.

Reviewing the history of acoustic metamaterials reveals that, unlike its electromagnetic counterpart, the experimental demonstration of double negativity in acoustic metamterials which was reported in 2010 [22], experienced a ten years lag from the first observation of localized resonances which was reported in 2000 [15]. However, between 2000 and 2010, acoustic metamaterials growed in theoretical and also experimental aspects and many interesting application proposals beyond negative index property were reported in this period of time. For example, in 2002, time reversal mirror was proposed to overcome the diffraction limit [23] or between 2006 and 2009, transformation acoustics was proposed and developed for acoustic cloaking [24, 25, 26, 27, 28, 29] and the idea of sound collimation and confinement were studied [30, 31]. Acoustic superlensing [32, 33] and first acoustic flat lens [34] (see the left subfigure of section 2009 in Fig. 1.2) as well as far-field image magnification by hyperlens were theoretically and experimentally proved [35, 36] (shown at bottom right of the section 2009 in Fig. 1.2). Moreover, extraordinary acoustic transmission through periodically perforated slab was reported [37, 38] in these years.

Form 2011 to 2017:

Before the start of this thesis (2011 and 2012).

After the first experimental report on negative index acoustic metamaterials, the main research direction was oriented towards experiment. In 2011 the experimental results on amplification of evanescent acoustic waves using metamaterial slab [39] and deep-subwavelength imaging in the order of $\lambda/50$ by a holey-structure [40] were reported (see section 2011 in the first time-line and right subfigure in the second timeline of Fig. 1.2, respectively). Moreover, shown in

the section 2011 of Fig. 1.2 over the second timeline, a study on broadband acoustic cloak for ultrasound waves was published the same year [41]. Although, the idea of using metamaterials as sound absorber, proposed in 2000, was the first application which has been forseen for these engineered structures [15], it was only after 2012 that the absorber like capability of acoustic metamaterials was highlighted by introducing a super absorber for low frequency sound using membrane based metamaterial [42] which has been shown in section 2012 of Fig. 1.2.

After the start of this thesis (2013-2017).
As shown in Fig. 1.2, achieving double negative material properties by different approach, using coupled membranes [43], was the breakthrough in 2013. In 2014 non-reciprocal acoustic metamaterial [44], acoustic circulator [45], acoustic 3D ground cloak [46] and acoustic metasurface [47] were proposed which have been depicted in the section 2014 of the Fig. 1.2 respectively. As shown in the chronological order in Fig. 1.2, the acoustic sensor cloak based on parity-time symmetry [48] using electrodynamic loudspeakers and single sensor sound source localization based on anisotropic engineered structure [49] and acoustic leaky-wave antenna [50] were the highlights of 2015. Finally, acoustic prism [51], acoustic reflectarry antenna, acoustic metasurface cloaking [52, 53] and acoustic orbital angular momentum metasurface [54] were proposed and experimentally validated in 2016 and recently, acoustic metasurface was leveraged for acoustic levitation [55] which is one of the ground breaking studies that may find commercial applications in near future. All these developments have been shown in the sections dedicated to 2016 and 2017 in Fig. 1.2 respectively.

As of today:

Having briefly reviewed the literature in acoustic metamaterials, it can be highlighted that acoustic metamaterials have considerably evolved during the past seventeen years. The field with a single objective of achieving a negative refractive index, has turned into a live and active domain which pushes the boundaries of classical acoustics towards novel functionalities. Such a claim is supported using Fig. 1.3 which depicts the lineage of acoustic metamaterials as of today.

In order to read the family tree of Fig. 1.3 the following notes can be considered: the tree is consists of one group as ancestors called Metamaterials and 4 main descendant groups denoted descendingly by: Properties/Behaviours, Concepts, Functionalities and Applications. Moreover, the arrows show the link between heritage lines in a descending trend from 'ancestor(s)' to 'descendant(s)' and a color has been assigned to each member of the tree which is inherited from its ancestors. Finally, dashed lines represent the different applications which have been investigated in this thesis.

The lineage of the three different categories of metamaterials have been depicted under Metamaterials, where it is clearly shown that the acoustic metamaterials have been directly inspired by electromagnetic counterparts and in turn, they have inspired the Elastic metamaterials. The first descendant of Metamaterials are fundamental metamaterial properties or behaviours

which define the term metamaterials and have been explained in the previous section and depicted in Fig. 1.1 as well. The second heritage line is devoted to the physical concepts that metamaterials make it possible due to the one or more of the exotic material properties or behaviours. For instance, in the realm of acoustics non-reciprocity can be achieved either by non-linearity/active materials or both. In the same manner, acoustic superlens can be achieved by single or double negative material properties. The third and fourth heritage line are dedicated for the applications derived from different concepts. As an example, the acoustic leaky-wave antenna is the descendent of Composite Right/Left Hand Transmission-Line (CRLH TL) metamaterials (Chapter 2) and it can be exploited as an acoustic prism or single sensor direction finder (Chapter 3). As an other example acoustic reflect array is only one type of acoustic metasurfaces and two different applications such as levitation or cloaking (Chapter 4) can be foreseen for it. In addition to providing a general overview on the applications of acoustic metamaterials and their origin, Fig. 1.3 gives a statistical overview on which material property or behaviour is more dominant form application point of view. Indeed, the green as a dominant color in this tree proves that Anisotropy, Inhomogeneity and Loss as material behaviours dominate the research directions in acoustic metamaterials. Moreover, this family tree shows that despite having lots of potentials, active or non-linear metamaterials have not grown as expected and they can become the subject of future researches.

Note:

In order to avoid any misunderstanding, three important notes should be considered about the family tree of Fig. 1.3. First, it is not claimed that this figure is exhaustive and covers all the acoustic metamaterials. Indeed, in order to decrease the complexity, only major or well-known applications which are probable to have commercial applications, have been listed in this tree. Second, the categorization of heritage lines are not very precise or strict. For instance, energy harvesting as a descendent of active metamaterials can be considered as a concept or functionality or an application. Here, it is categorized as concepts, in order to decrease the complexity of the figure in terms of crossing arrows. Finally, in this family tree, the term Functionality has been used in the meaning of particularity. In other words, it refers to applications which are too general and can be used in different scenarios. For example, transmitarray is only one of the particularities of the metasurfaces as a general concept and it can be used for different applications such as OAM wave generation, levitation, etc.
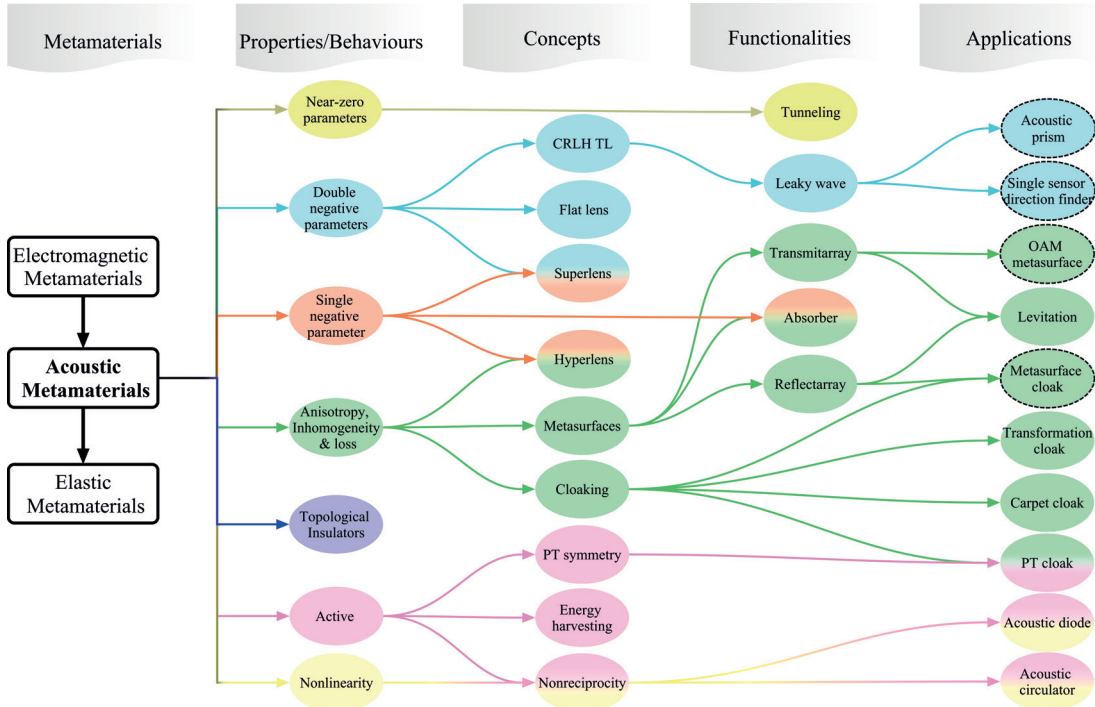
Figure 1.3: The tree of acoustic metamaterials.

1.2 Objectives

As shown in Fig. 1.2, at the time when this thesis began (December 2012), the field of acoustic metamaterials was spinning around some classical problems such as achieving negative index properties or flat lenses. However, at the same period of time, electromagnetic counterparts were pushing the boundaries towards novel functionalities. Comparing the applications in the family tree of Fig. 1.3 with the evolution time-laps of Fig. 1.2, it is concluded that most of the applications for acoustic metamaterials were proposed after 2013. Indeed, the time of the start of this thesis coincided with a general move toward the extension of the boundaries of acoustic metamaterials towards novel applications. Thus, following this trend, the goal of this thesis was to use the available theoretical, numerical and modelling tools to propose, optimize and realize novel devices with intriguing applications beyond some classical concepts like Snell's law. To achieve this goal some main questions were proposed to be answered, including:

- How does sound **propagation** in acoustic metamaterials is modeled with TL theory?

- What are the **guided-wave** properties of acoustic metamaterials?

- What is the advantage of using acoustic metamaterials to achieve acoustic **radiation** devices?

- How do acoustic metamaterials affect **refraction** wave phenomenon?

- How does wave react in terms of **reflection** and **transmission** when it impinges meta-structures with surface impedance inhomogeneity?

As it was highlighted in bold fonts, answers to these questions are all around investigating different wave phenomena in sound-matter interactions such as: propagation and guided-waves, radiation, refraction, reflection and transmission.

Figure 1.4 schematically describes the aforementioned questions where the different sound-
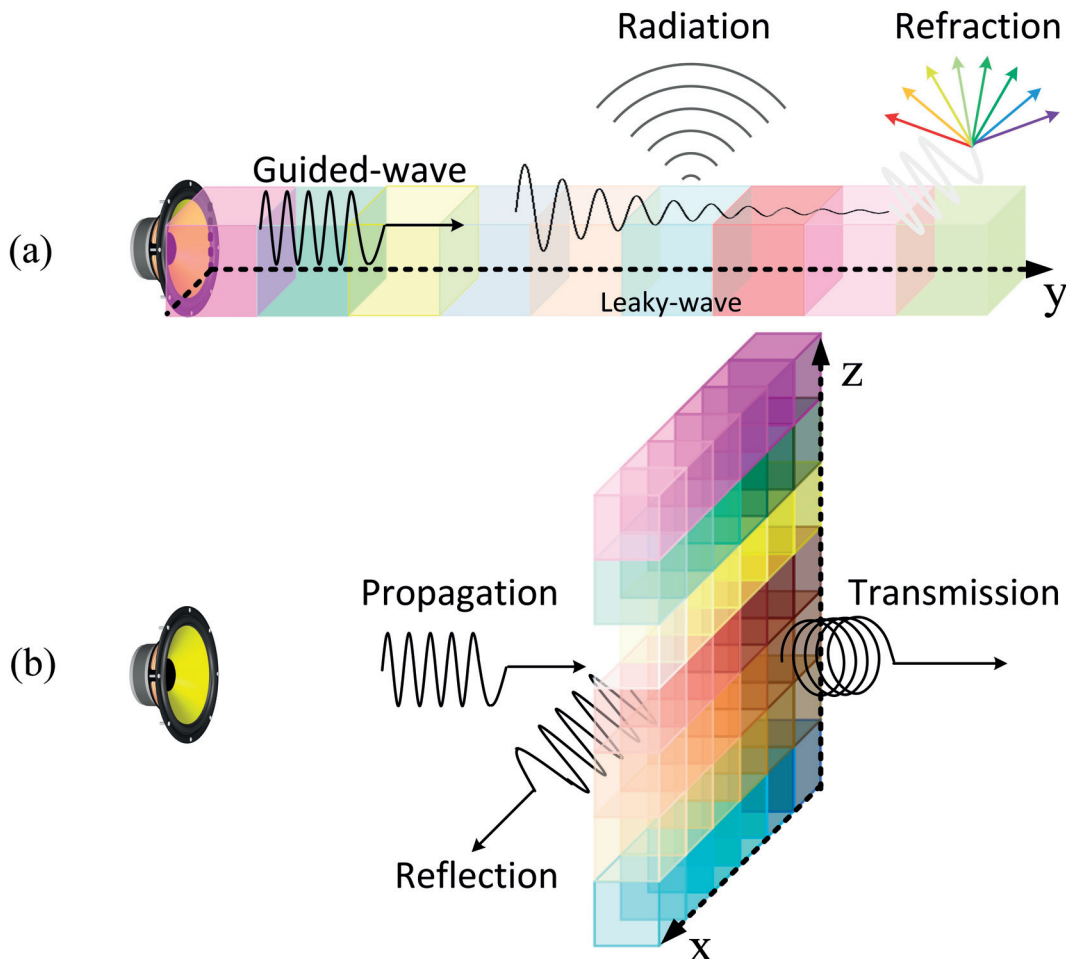
Figure 1.4: Different acoustic wave phenomena which will be covered in this thesis.

matter interaction scenarios in 1D and 2D meta-structures have been demonstrated. Here, the 1D structure is referred to meta-structure composed of meta-atoms only varying in one direction (y-axis as shown in Fig. 1.4a) while a 2D configuration is referred to variation of meta-atoms in two directions (here x and z directions as shown in Fig. 1.4b), where each coloured cube represents different meta-atoms of the meta-structures. Using, Fig. 1.4 a short explanations on each wave-matter interaction phenomena in acoustics realm are provided.
Propagation: As Feynman said in his Lectures on Physics: '... if an object is moved at one

place in the air, we observe that there is a disturbance which travels through the air. If we ask what kind of disturbance, we would say that we would expect that the motion of the object produces a change of pressure. Of course, if the object is moved gently, the air merely flows around it, but what we are concerned with is a rapid motion so that there is not sufficient time for such a flow. Then, with the motion, the air is compressed and change of pressure is produced which pushes on additional air. This air is in turn compressed, which leads again to an extra pressure, and a wave is propagated [56].' In other words, the propagation of sound is the result of oscillating system where the wave oscillations appear not only as time-oscillation at one place but also as spatial-oscillation at one time and its properties are studied between the source and the receiver as a consequence of the Newton's laws, and we shall not consider the interaction with the source and the receiver [56]. In this sense, the propagation of sound wave is limited to wave oscillations inside the meta-structure of Fig. 1.4a (e.g. studying the propagating behaviours of the leaky-waves or guided-waves inside the meta-structure) or between source and meta-structure as in Fig. 1.4b. In chapter 2 the TL theory is proposed to model the propagation of sound waves in conventional, negative index and CRLH materials.

Guided-wave: When the wave propagates in the free space it is almost impossible to control where the energy will go. Indeed, the fields are spread out and the pressure waves are not guided. According to Feynman: '... Now it is time to see what happens when oscillating fields are confined in one or more dimensions. We will discover the interesting new phenomenon when the fields are confined in only two dimensions and allowed to go free in the third dimension, they propagate. These are called guided-waves [56]'. Therefore, in the 1D meta-structure of Fig. 1.4a, the acoustic wave has been confined in two directions while it is being guided in the y direction. The guided-wave properties of CRLH TL metamaterials are studied in chapter 2.

Radiation: Acoustic radiation is the emission of sound energy in the form of disturbances in the material properties of the medium in which the wave spreads out or radiates. Thus, acoustic radiation is in the opposite point of the guide-wave phenomenon. For instance, Fig. 1.4a as a meta-structure can support guided-waves or leaky-waves (fast-wave) modes. While the former is confined in the meta-structure and propagates inside in y direction, the later can radiate to 3D space if the radiation conditions are fulfilled. In other words there should be some means for energy exchange between meta-structure and the free space. To study the radiation phenomenon in acoustic metamaterials, in chapter 3 the leaky-wave mode and the radiation behaviour of the CRLH TL metamaterials are presented.

Refraction: Refraction is the change in the direction of the wave propagation due to a change in its transmission medium. That is the necessary conditions to achieve refraction is, first, transmission medium where the wave propagates through and the second, a change in the transmission medium which results in the change of the direction of the propagating wave. For instance, the proposed meta-structure of Fig. 1.4a, is a transmission medium where the wave can propagate through and its composed of many different unit-cells which can exhibit dispersive behaviours, replicating the change in the transmitting medium. Moreover, it is open to 3D free space which ensures the change in the direction can be fulfilled. Hence, such a meta-structure can exhibit frequency dependent refraction index. One part of chapter 3 has

been dedicated to study the refraction phenomenon in acoustic metamaterials.

Reflection: Reflection is the change in direction of a sound wave at an interface between two different media so that the sound returns into the medium from which it originated. For instance, in Fig. 1.4b the acoustic wave impinges a meta-structure in the vertical direction and changes the direction in slant towards the medium it originated. In this figure, to demonstrate the anomalous reflection behaviour of the meta-structure, the Snell's law has been intentionally violated. Leveraging the exotic properties of acoustic metasurfaces to manipulate the reflected wavefront, the reflection phenomenon is investigated in chapter 4.

Transmission: Transmission is the passage of acoustic waves from the interface between two media. For example, in Fig. 1.4b a propagating wave impinges a meta-structure from the left side and it is transmitted to the right side where its plane wavefront has been transformed to helical wavefront, while passing through the meta-structure. Chapter 5 has been dedicated to study the interaction of sound with transmit type metasurfaces.

1.3 Organization of the thesis

This thesis consists of four main chapters on electromagnetic inspired acoustic metamaterials. Two chapters have been dedicated for the introduction and conclusion. Moreover, an Appendix has been placed at the end of the thesis which mostly covers mathematical derivations, fundamental definitions and equations to treat and model acoustic wave propagation in periodic or non periodic media. Figure. 1.5a shows the organization of the thesis, the title of each chapter and also interconnections between different chapters. The black dashed box represents the main chapters and the appendices are in red rectangular box. The arrows represent the connections between chapters, for instance the TL theory developed in chapter 2 has been used in the chapter 3 and 4 which is demonstrated by an arrow connecting chapter 2 to chapter 3 and 4. Figure. 1.5b summarizes different wave phenomena and connected them to the corresponding chapters. Moreover, it shows that the first four wave phenomena have been discussed in 1D meta-structures (as explained in 1D meta-structure, the unit-cells only vary in one direction), while the reflection and transmission have been studied in 2D meta-structures in chapter 4 and 5, respectively.

1.3.1 Chapter 2: Acoustic Transmission-Line Metamaterials

This chapter deals with the most fundamental concept namely wave propagation in sound-metastructure interaction. The target is to propose a scheme to design a double negative guided-wave structure for acoustic and investigate the wave propagation in such a structure using transmission-line model. For this purpose an acoustic Composite Right/Left Hand Transmission-Line (CRLH TL) metamaterial configuration is proposed which exhibits negative/zero/positive refractive index, and its effective material properties in dynamic regime (mass density and bulk modulus) is studied. Then, a transmission-line model to describe the exotic behaviours of the proposed 1D acoustic metamaterial is developed. Finally, using the

Appendix A
Acoustic
Waves

Appendix B
Transmission-
Line modeling

Appendix C
Plate

Appendix D
Network
Analysis

Appendix E
[S] and [T]
matrix
retrieval

Appendix F
Periodic
structures

(a)

Chapter1

Introduction

Chapter2

Acoustic Transmission-
Line Metamaterials

Chapter3

Acoustic Leaky-Wave
Antenna

Chapter4

Acoustic Metasurface as
Reflectarray antenna and
Carpet Cloak

Chapter5

Acoustic Orbital Angular
Momentum Metasurface

Chapter6

Conclusions and
Perspectives

(b)

Propagation | Guided-wave | Radiation | Refraction | Reflection | Transmission

Chapter 2 | Chapter 3 | Chapter 4 | Chapter 5

1D Metastructure | 2D Metastructure

Figure 1.5: Thesis organization.

simple, yet powerful TL method the Bloch parameters are derived which is used to study the propagation properties in the proposed 1D acoustic metamaterial as well as redesigning and optimizing the structure to suppress the band gap to achieve seamless transition from positive refractive index medium to negative index medium.

1.3.2 Chapter 3: Acoustic Leaky-Wave Antenna

Radiation and refraction in 1D TL metamaterials is studied in this chapter. By harnessing the dispersive nature of the 1D metamaterial and using the TL model developed in the previous chapter, along with a bit of inspiration from electromagnetics on the exploitation of the Leaky-Wave (LW) phenomenon, an artificial material is designed which performs acoustic prisming in full analogy to the optical dispersive prism. Then, using the acoustic prism example the refraction phenomenon is studied in acoustic metamaterials. In the next step the far-field radiation of the proposed 1D metamaterial is utilized to develop a Single Sensor Direction Finding (SSDF) device to localize the direction of the sound source without resorting to any complex signal processing which is achieved by using the one-to-one frequency-refraction relation of the acoustic leaky-wave radiation.

1.3.3 Chapter 4: Acoustic Metasurface as Reflectarray Antenna and Carpet Cloak

This chapter deals with on the reflection phenomenon from a 2D meta-structure where the anomalous property of the reflected wave from an acoustic metasurface is studied. First, the Snell's laws of reflection and refraction are revisited and tailored under the name of generalized Snell's law to adapt the anomalous reflected and transmitted wavefront behaviour of the metasurfaces. Then, an ultra-thin acoustic metasurface unit-cell based on membrane capped cavities is proposed and modelled using acoustic TL theory. Based on the developed generalized Snell's law and the designed membrane, an acoustic reflectarray is proposed to control the reflected wavefront. Finally, to demonstrate the functionality of this structure, it is applied as a carpet cloak to hide an obstacle from an impinging acoustic waves.

1.3.4 Chapter 5: Acoustic Orbital Angular Momentum Metasurface

This chapter investigates the transmission phenomenon through an acoustic meta-structure, where a transmit type acoustic metasurface aiming at transforming acoustic plane wavefronts to helical wavefronts is explored. Spin angular momentum waves, unlike electromagnetics, are not feasible in acoustics, due to the non polarized nature of acoustic waves. First, it is proven that Orbital Angular Momentum (OAM) waves can be generated if a special transmission phase distribution is fulfilled on the wavefront. Then, a new labyrinthine geometry based on helicoidal ruled surfaces is designed to represent the unit-cells. These unit-cells are used to generate helical wavefronts.

1.3.5 Chapter 6: Conclusions and Perspectives

This thesis is concluded with a short summary of the research performed during four years of PhD program and highlights the novelties presented through out this study. Moreover, some presumptive directions are proposed for the future researches in acoustic metamaterials.

1.4 Summary of the outcomes

1. Upgrading the TL model of acoustic CRLH TL and proposing a TL model to analyze acoustic leaky-wave antenna.

   - H. Esfahlani, S. Karkar and H. Lissek. "Optimization of an acoustic leaky-wave antenna based on acoustic metamaterial", Acoustics 2013, New Delhi, India, 2013

2. Designing a CRLH TL configuration to achieve a directive acoustic leaky-wave antenna and proposing its potential applications as acoustic dispersive prism and acoustic single sensor direction finder.

   - H. Esfahlani, S. Karkar and H. Lissek. "Acoustic Leaky-Wave Antenna", 8th International Congress on Advanced Electromagnetic Materials in Microwaves and Optics

- Metamaterials 2014, Copenhagen, Denmark, 2014.

3. Realization of the acoustic dispersive prism.

   - H. Esfahlani, S. Karkar, H. Lissek and J. R. Mosig "Acoustic dispersive prism", in Sci. Rep. 6, 18911, 2016.

   - H. Esfahlani, S. Karkar, H. Lissek and J. R. Mosig. "Electromagnetic Inspired Acoustic Leaky-wave Antenna", 10th European Conference on Antennas and Propagation (EuCAP), Davos, Switzerland, April, 10-15, 2016.

4. Realization of acoustic single sensor direction finder.

   - H. Esfahlani, S. Karkar, H. Lissek and J. R. Mosig "Exploiting the leaky-wave properties of transmission-line metamaterials for single-microphone direction finding", in The Journal of the Acoustical Society of America, vol. 139, num. 6, p. 3259-3266, 2016.

   - H. Lissek, H. Esfahlani, S. Karkar and J. R. Mosig. "Développement et validation d'une d'antenne acoustique à ondes de fuite", 13e Congrès Français d'Acoustique, Le Mans, 2016.

5. Designing an ultra-thin unit-cell for acoustic metasurfaces and proposing the idea of acoustic reflectarray antenna.

   - H. Esfahlani, S. Karkar and H. Lissek. "Acoustic Metasurface", META'15, the 6th International Conference on Metamaterials, Photonic Crystals and Plasmonics, City College of New York, New York City, NY, USA, 2015. **[Best Poster Award]**

6. Designing acoustic ultra-thin metasurface carpet cloak and acoustic reflectarray metasurface.

   - H. Esfahlani, S. Karkar, H. Lissek and J. R. Mosig "Acoustic carpet cloak based on ultra-thin metasurface", in Physical Review B, vol. 94, num. 1, p. 014302, 2016.

7. Design and fabrication of a helicoidal labyrinthine unit-cell for acoustic metasurfaces and proposing the OAM metasurface as its potential application.

   - H. Esfahlani, S. Karkar and H. Lissek. "On the design of unit-cells for acoustic metasurfaces", 9th International Congress on Advanced Electromagnetic Materials in Microwaves and Optics - Metamaterials 2015, Oxford, United Kingdom, 2015.

8. Realization of an OAM acoustic metasurface to transform an impinging plane wavefront to transmitted helical wavefront.

   - H. Esfahlani, H. Lissek, and J. R. Mosig "Generation of acoustic helical wavefronts using metasurfaces", in Physical Review B, vol. 95, num. 2, p. 024312, 2017.

2 Acoustic Transmission-Line Metamaterials

| Propagation | Guided-wave | Radiation | Refraction | Reflection | Transmission |

This chapter is a modified version of the materials published in Ref. [57] and orally presented in Ref. [58].

2.1 Introduction

Inspiration from electromagnetics:
In the realm of electromagnetics, there are two types of metamaterials: resonant type metamaterials which are consists of resonant inclusions, and non resonant type which are transmission-line (TL) based metamaterials. The resoant type metamaterials are inherently narrow band and lossy, however the TL based metamaterials show negative refractive index over larger bandwidth as well as lower loss. It has been shown that by loading a planar network of printed transmission-lines with series capacitors and shunt inductors in a dual (high-pass) configuration, a negative refractive index medium can be achieved [59]. Such a medium has been used, first, to provide an experimental validation that transmission-line metamaterials exhibit negative index in wide operating bandwidth, and second, to demonstrate the focusing ability predicted for Left-Handed (LH) metamaterials [60]. Moreover, as TL metamaterials provide anti parallel phase and group velocities in guided-wave configuration with confined energy within the structures, wide bandwidth and low loss, they can be used to study the propagating behaviour of electromagnetic waves in such media [61].

Efforts in acoustics:
Similar to electromagnetics, in acoustic there has been efforts to realize negative refractive index media. The first attempt was in 2000, by loading a host fluid medium with subwavelength elastic and/or fluid inclusions, for which effective parameter(s) such as the mass density and the bulk modulus take negative values in the designed frequency band [15], [16]. In the reso-

nant type negative index acoustic metamaterials, the particles forming the composite material should demonstrate monopolar and/or dipolar resonances which are led to a negative bulk modulus and/or a negative mass density, respectively. Hence, these types of metamaterials are inherently narrow band and lossy due to their resonant nature. Anomalous material properties over a much wider bandwidth and with lower losses can be achieved if it does not explicitly rely on resonance phenomenon. Hence, transmission-line type metamaterials have been developed to achieve negative material properties. For instance, a negative bulk modulus has been achieved with an acoustic waveguide loaded with array of subwavelength Helmholtz resonators [18], as well as Helmholtz-type resonators with slits [62] or side holes in a host waveguide [21]. In a similar way, an acoustic waveguide has been loaded with vibrating plates, exhibiting acoustic negative mass density [20]. Then, these two concepts have been combined to obtain double negative transmission-line metamaterials [22], [57] which can be modeled and analyzed with TL theory.

Propagation and guided-wave concepts in acoustic TL metamaterials:
Propagation of the wave and its behaviour is the most fundamental phenomenon to investigate in the wave-mater interaction. Additionally, form application point of view, the study of wave propagation in the guided-wave structures, where the wave remains confined within, is of utmost importance. Due to waveguiding property as well as having broad bandwidth and low loss, Composite Right/Left hand Transmission-Line (CRLH TL) metamaterials are the most appropriate configurations for this purpose. Since the TL theory is fully compatible with the design and modeling of CRLH TL metamaterials, the wave propagation study in such structures becomes even simpler. Moreover, the TL theory can be adapted to the Bloch theory (see Appendix F) as a fundamental tool to investigate periodic structures.
For the aforementioned mentioned reasons, this chapter is dedicated to the design, modeling and study of the sound wave propagation in acoustic CRLH TL metamaterial where the TL theory is used as a key feature in all steps. To this end, a 1D acoustic transmission-line (TL) metamaterial is designed to demonstrate the effect of negative/zero/positive refractive index medium on the propagation of acoustic waves and a TL model is proposed to analyse such a structure. The proposed structure is consists of an acoustic waveguide realizing series masses 'inductances' as well as parallel compliances 'capacitances' and periodically loaded with plates as series compliances 'capacitances' and transversally connected open channels as shunt masses 'inductances' (see Appendix B for analogy between electromagnetic and acoustic lumped circuit modules). Due to the non resonant nature of the proposed circuit based configuration, it can exhibit a negative refractive index, over a broader bandwidth compared to the resonant based devices. In this structure the transition between the negative and positive refractive index bands is very smooth (no band-gap), where, a zero index at the transition frequency is observed. Additionally, the TL model provides a powerful yet simple approach to understand, design, analyse and optimize the proposed structure in terms of Bloch dispersion and impedance.

2.1.1 Outline of the chapter

In this chapter, first the transmission-line models of the conventional and negative index materials are introduced. Then, these models are combined to get the circuit model of CRLH TL metamaterials. In the next step, the acoustic modules to realize each circuit component in the CRLH model is investigated and a design procedure to achieve a CRLH metamaterials without band-gap is presented. Finally, the CRLH TL model is realized using the acoustic modules and the numerical simulation results are presented to study the propagation behaviour of the wave in such a structure.

2.2 Transmission-Line Modeling

Transmission-line representation can be used to describe the propagation of waves in different systems. This section introduces the concept of TL-based acoustic metamaterials, where the conventions associated with TL formalism in a fluid is described and used to model a complex structure in acoustics.

In the presented acoustic circuit modeling, the time harmonic wave equation is considered as a base and the $e^{j\omega t}$ term is discarded, the voltage is replaced by acoustic pressure (p) and the current is substituted to the volume velocity (q) flowing through a surface (S). This representation has been explained in Appendix B by comparing mass-spring model to circuit model for the characterization of the plane wave propagation in an unbounded medium. It has also been explained that this model can be used for acoustic waveguides, where S is the waveguide cross-sectional area, that volume velocity flowing through.

By applying the circuit analogy, adopted from Kirchhoff's voltage and current laws to the
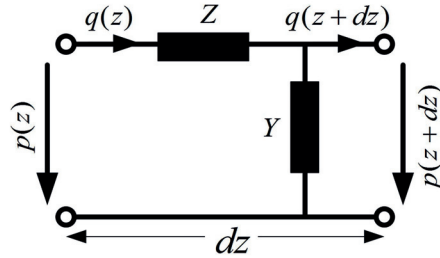
Figure 2.1: Incremental circuit model of an arbitrary medium.

incremental circuit model of Fig. 2.1, with Z as the acoustic impedance and Y as the acoustic admittance, the following relations are found

$$\frac{dp(z)}{dz} = -Zq(z), \tag{2.1a}$$

$$\frac{dq(z)}{dz} = -Yp(z). \tag{2.1b}$$

Plugging Eq. 2.1a into Eq. 2.1b, the system of Eq. 2.1 is simplified to,

$$\frac{d^2 p(z)}{dz^2} + YZp(z) = 0. \tag{2.2}$$

Equation 2.2 with a travelling wave type solution

$$p(z) = p^+ e^{-\sqrt{YZ}z} + p^- e^{\sqrt{YZ}z}, \tag{2.3}$$

is similar to the time harmonic Helmholtz equation if

$$\gamma^2 = YZ, \tag{2.4}$$

where γ is the complex propagation constant used in Helmholtz equation (For detailed study refer to Appendix A and B). Therefore, the circuit model of Fig. 2.1 can be used to model any medium where the wave propagation inside, is described by Helmholtz equation.
Using Eq. 2.3 and plugging it into Eq. 2.1a yields the volume velocity as:

$$q = \sqrt{\frac{Y}{Z}} \left(p^+ e^{-\sqrt{YZ}z} - p^- e^{\sqrt{YZ}z} \right), \tag{2.5}$$

which is used to calculate the characteristic impedance as

$$Z_c = \frac{p^+}{q^+} = \frac{p^-}{q^-} = \sqrt{\frac{Z}{Y}}. \tag{2.6}$$

After defining the propagation constant as the imaginary part of the complex propagation constant $\beta = \text{Im}[\gamma]$, the phase and group velocity of the propagating wave can be calculated by,

$$v_p = \frac{\omega}{\beta} = \frac{\omega}{\text{Im}\left[\sqrt{YZ}\right]}, \tag{2.7}$$

and

$$v_g = \left(\frac{\partial \omega}{\partial \beta} \right) = \left(\frac{\partial \omega}{\partial \text{Im}\left[\sqrt{YZ}\right]} \right), \tag{2.8}$$

respectively.

2.2.1 Conventional materials

By analogy with the definitions in Electromagnetics, the conventional materials can be called Right Hand (RH) materials [61]. For RH acoustic materials the phase velocity v_p and the group velocity v_g of the propagating acoustic wave have identical signs: $v_p v_g > 0$. By plugging $Z = j\omega m_a$, where m_a is an acoustic mass in [kg/m^4] and $Y = j\omega C_a$, where C_a is an acoustic compliance in [m^3/Pa], in the circuit model of Fig. 2.1 and using Eq. 2.7 and 2.8, the phase

and group velocity can be calculated as

$$v_p = \frac{\omega}{\beta} = \frac{1}{\sqrt{m_a C_a}} > 0, \tag{2.9}$$

and

$$v_g = \left(\frac{\partial \omega}{\partial \beta}\right) = \frac{1}{\sqrt{m_a C_a}} > 0, \tag{2.10}$$

where $\gamma = \sqrt{ZY} = j\omega\sqrt{m_a C_a}$ and $\beta = \sqrt{m_a C_a}$. Equation 2.9 and 2.10 satisfy the fundamental
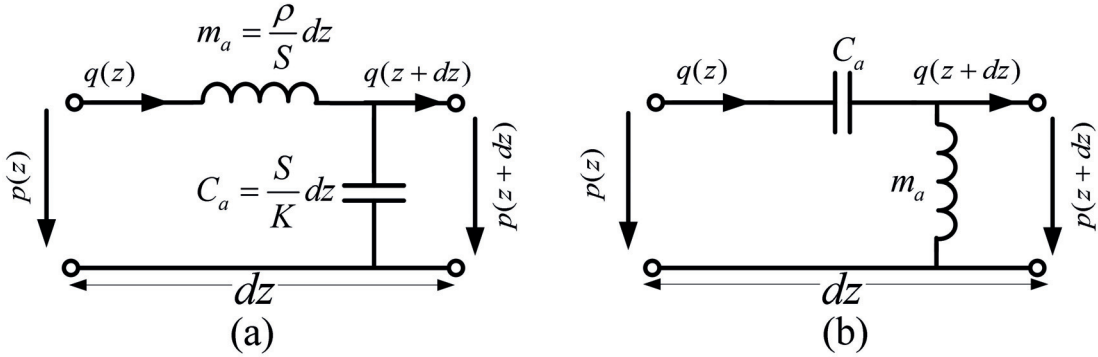
Figure 2.2: The circuit model for (a) a conventional medium and (b) a negative index medium.

relation ($v_p v_g > 0$) for RH medium. Thus, with the adopted convention, an incremental section (dz) of a conventional fluid can be described by the model of Fig. 2.2a. Assuming the linear disturbance of the medium at angular frequency (ω) and for a 1D model similar to TL structure, the conservation of momentum and mass can be written as (see Appendix A and B):

$$\frac{dp}{dz} = -j\omega\frac{\rho}{S}q, \tag{2.11a}$$

$$\frac{dq}{dz} = -j\omega\frac{S}{K}p. \tag{2.11b}$$

Comparing Eq. 2.11 to Eq. 2.1 reveals that: $Z = m_a = (\rho/S)dz$, and $Y = C_a = (S/K)dz$, where ρ and K are the mass density and bulk modulus of the medium, respectively. The characteristic impedance of the TL of Fig. 2.2a is given by $Z_{ac} = Z_c/S$ in [Ω_a=Pa s/m^3], where $Z_c = \sqrt{\rho K}$ is the characteristic acoustic impedance of the medium and calculated by Eq. 2.6. Following the same procedure, the sound wave velocity is found to be $c = \sqrt{K/\rho}$ and the wave vector is defined as $k = \omega/c$. For instance, for air as a conventional medium the fundamental parameters are $K = 137.4$ kPa, $\rho = 1.188$ kg/m^3, $c = 340$ m/s and $Z_c = 404$ Pa s/m.

2.2.2 Negative index materials

By adopting the definition of the negative index materials in Electromagnetics, acoustic negative index materials are considered as LH medium with antiparallel phase and group velocity ($v_p v_g < 0$). Following the same procedure as of previous section, it is proved that the circuit model of Fig. 2.2b with a dual topology of the conventional TL, where the series and parallel elements are interchanged, exhibits a negative refractive index with phase and group velocity having opposite signs over an infinite bandwidth. However, the transformed TL topology of Fig. 2.2b cannot be realized in a fully distributed manner and in order to be realized, it should be incorporated into conventional medium which is explained in the following section.

2.2.3 Composite right/left hand materials

To realize a negative index medium, the acoustic elements representing the circuit model of Fig. 2.2b should be periodically loaded into a host medium modeled with a conventional circuit topology of Fig. 2.2a. Hence, the resulting circuit model of the unit-cell is the one shown in Fig. 2.3. In such a circuit topology, the response is dominated by m_{ap} and C_{as} at low frequency and consequently exhibits LH behaviours and negative refractive index, whereas at higher frequency m_{as} and C_{ap} are dominant, which results in a RH behavior and positive refractive index. An interesting feature of this structure is that a smooth transition without stop band (band gap) between the LH and RH bands can be achieved under the balanced condition. The so called balanced condition happens when the resonance frequency of the series and parallel circuit elements are equal ($m_{as}C_{as} = m_{ap}C_{ap}$) [61].

Although the realization of the TL model of Fig. 2.3 seems to be straightforward at first, it follows some challenges. It is well known that series mass and parallel compliance are the inherent model of conventional medium such as acoustic waveguide. Moreover, shunt Helmholtz resonators comprise parallel masses. However, the realization of the series compliance requires something beyond regular elements, these elements are governed by Biharmonic equations which are discussed in the following sections.
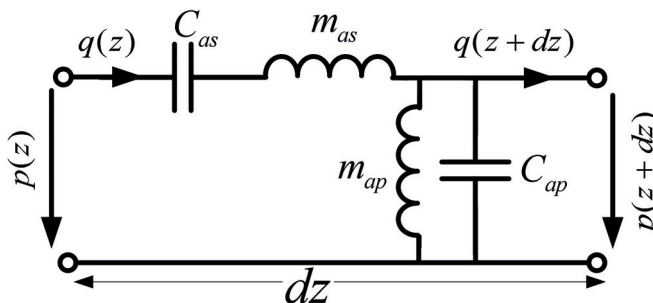
Figure 2.3: Incremental circuit model for a composite right/left hand metamaterials.

2.2.4 Generalization of the proposed circuit models

It must be pointed out that the circuits in Fig. 2.2 and Fig. 2.3 are lossless and hence correspond to lumped circuit model of any ideal structures discarding lossy materials. In TL circuit modeling, losses can be represented by equivalent resistances in the equivalent circuit and this does not restrict the generalization of the TL model. For instance, in the next chapter the radiation resistance as a source of power loss will be added to the circuit model to study the behaviour of the structure as an antenna. The same can be done for viscous losses but in order to simplify the modeling and design procedure this is not taken into account here, without discarding the generality of the following results.

2.3 Realization of The CRLH TL Metamaterial

The proposed configuration for the realization of the CRLH TL metamaterial is shown in Fig. 2.4. This configuration has a symmetry of revolution around z-axis and every unit-cell shown in the red box consists of:

- An acoustic waveguide with perfectly rigid walls is chosen as a host medium, where it is operated in its first mode (plane wave). As a conventional medium, the acoustic waveguide can be represented by the series masses and parallel compliances and it satisfies the RH elements in the CRLH metamaterial circuit model of Fig. 2.3.

- mechanical element consisting of clamped plate operating in their first vibrating mode is proposed for the implementation of the series compliance for which the restoring force provides the required compliance.
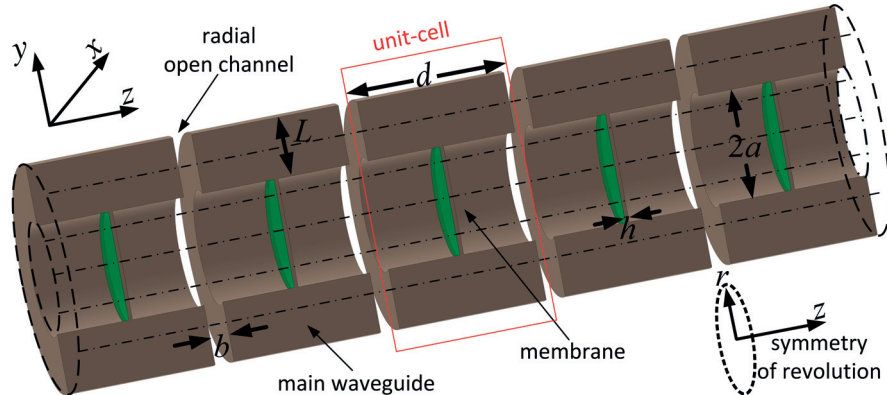
Figure 2.4: The proposed CRLH TL realized based on main acoustic waveguide incorporated with plates and transverse radial open channels. Here, the $yz-$plane cut view of the main channel has been shown for better visibility. This structure has the symmetry of revolution, therefore, the axisymmetrical finite element simulations can be used to decrease the time cost of numerical evaluation.

- Finally, shunt acoustic masses can be simply achieved with transversally connected radial open channels. As shown in Fig. 2.4, radial open channels integrated in the main waveguide is adopted as a solution. It should be note that as illustrated in red box in Fig. 2.4, in order to keep the symmetry, the unit-cell is defined by cutting the radial open channels, on each side of the main waveguide, in half.

Incorporating the clamped plates as well as radial stubs, which represent the LH elements, in the main waveguide as a RH medium, all the lumped circuit elements in the CRLH model of Fig. 2.3 are fulfilled. In the following section, a brief explanations on the analysis of the LH elements, namely clamped plate and radial stub, are provided.

2.3.1 Realization of the series acoustic compliance

As shown in Fig. 2.5a, the vibration of the circular plate, with clamped edges at its perimeter is considered where it has been incorporated into a host waveguide of same radius a. The vibrational behaviour of such a plate depends on its geometrical parameters such as thickness h and radius a as well as material properties such as mass density ρ_m, Young's modulus E and Poisson's ratio ν.

Theoretical modeling of the plate's impedance

Deformation of the plate:
A circular vibrating plate clamped at its edge, with cross sectional view as shown in Fig. 2.5a, can be modeled as a thin plate described by flexural waves equation as:

$$\nabla^4 \xi - k_m^4 \xi = \frac{\Delta p}{D}, \tag{2.12}$$

where $\xi(r)$ is the transverse displacement and satisfies the $k_m^2 = \omega \sqrt{\frac{\rho_m''}{D}}$, $\rho_m'' = \rho_m h$ and D designates its flexural rigidity, which is given by

$$D = \frac{Eh^3}{12(1 - \nu^2)}. \tag{2.13}$$

As shown in Fig. 2.5a, $\Delta p = p_1 - p_2$ represents the source term and it is defined as the net pressure applied on the plate, where p_1 and p_2 are the acoustic pressure on two sides of the plate. Bearing in mind that the system of clamped circular plate possesses a symmetry of revolution when treated under uniform pressure, then the general solution for Eq. 2.12 in polar coordinate, can be written as (see Appendix C):

$$\xi(r) = -\frac{\Delta p}{k_m^4 D} + A J_0(k_m r) + B I_0(k_m r), \tag{2.14}$$

where J_n and I_n are the regular and modified Bessel's functions of the first kind of order n, respectively. Using the boundary conditions for the case of clamped plate [$\xi(r = a) = 0, d\xi/dr|_{(r=a)} = 0$], A and B as unknown coefficients in Eq. 2.14 are obtained,

$$A = \frac{\Delta p}{k_m^4 D} \frac{I_1(k_m a)}{J_0(k_m a) I_1(k_m a) + J_1(k_m a) I_0(k_m a)} \tag{2.15}$$

$$B = \frac{\Delta p}{k_m^4 D} \frac{J_1(k_m a)}{J_0(k_m a) I_1(k_m a) + J_1(k_m a) I_0(k_m a)}. \tag{2.16}$$

Mechanical impedance of the plate:
The dynamic response of the plate can be described by its mechanical (acoustic) impedance and it is calculated as:

$$Z_m = \frac{\int \int_S \Delta p(r) dS}{j\omega \overline{\xi}}, \tag{2.17}$$

where $\overline{\xi} = 1/S \int \int_S \xi(r) dS$ is the mean transverse displacement over the plate surface. Considering the plate's vibration under uniform pressure distribution Eq. 2.17 is simplified as $Z_m = \frac{\Delta p S}{j\omega \overline{\xi}}$ and by using Eqs. 2.14, 2.15 and 2.16, the mechanical impedance Z_m reads:

$$Z_m = -j\omega m \frac{I_1(k_m a) J_0(k_m a) + J_1(k_m a) I_0(k_m a)}{I_1(k_m a) J_2(k_m a) - J_1(k_m a) I_2(k_m a)}, \tag{2.18}$$

where $m = \rho_m'' S = \rho_m S h$ represents the mass of the plate.

Acoustic impedance of the plate:
When a clamped plate inside a waveguide is actuated by an impinging pressure field, based on Newton's law, it starts to vibrate and exert an acceleration to the fluid inside the waveguide. In this scenario, the plate results in a discontinuity in the acoustic pressure field, however, the normal component of the acoustic velocity stays continuous on both sides of the plate. This velocity can be expressed in terms of plate's deformation after $v_\xi = j\omega \xi$ and the acoustic volume velocity q is given by

$$q = \int \int_S v_\xi(r) dS = \int \int_S j\omega \xi(r) dS = \overline{v}_\xi S = j\omega \overline{\xi} S. \tag{2.19}$$

As the behaviour of the plate is studied under uniform pressure field, then the acoustic impedance Z_{am} can be defined as

$$Z_{am} = \frac{\Delta p}{q} = \frac{j Z_m \omega \overline{\xi}}{j S^2 \omega \overline{\xi}} = \frac{Z_m}{S^2}, \tag{2.20}$$

where Z_m has been defined in Eq. 2.17 and expressed in Eq. 2.18. As explained before, a clamped plate results in pressure discontinuity over two sides of it while the volume velocity remains continuous. In analogy with electromagnetics, this is the definition of a series lumped circuit element. Thus, the equivalent acoustic circuit model of a plate in an acoustic waveguide is a series impedance Z_{am} as shown in Fig. 2.5b.

As detailed in Appendix C, the frequency of the first resonance for clamped plate is given by,
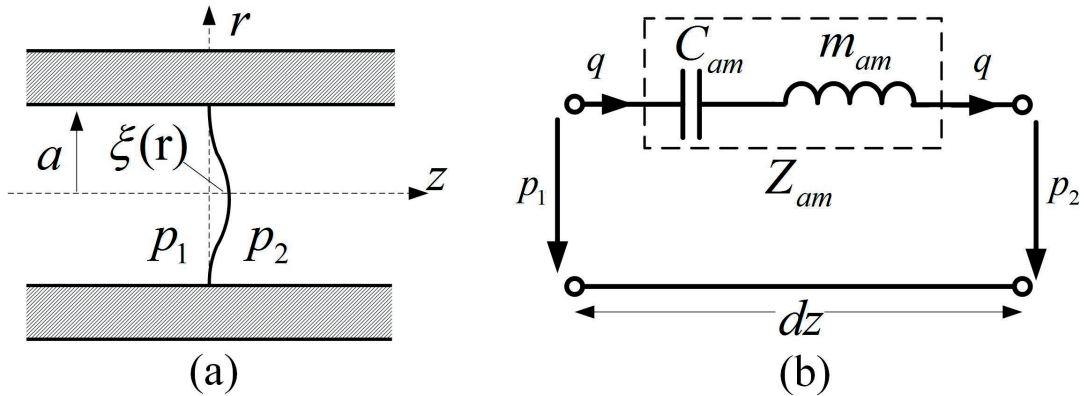
Figure 2.5: Elastic circular plate clamped at its edges to an acoustic waveguide. (a) Cut view. (b) Equivalent acoustic circuit.

$$f_r = 1.6259 \frac{1}{a^2} \sqrt{\frac{D}{\rho_m''}} = 0.4694 \frac{h}{a^2} \sqrt{\frac{E}{\rho_m (1 - \nu^2)}}, \tag{2.21}$$

At frequencies bellow or near first resonance the behaviour of the vibrating plate Z_{am} can be described by an acoustic mass m_{am} and a compliance C_{am} in series configuration as shown in Fig. 2.5b. To calculate these two elements, the resulting impedance $Z_{am}^* = j\omega m_{am} + \frac{1}{j\omega C_{am}}$ should fit the original impedance Z_{am} and its frequency derivative at the first resonance f_r. Thus, the values of m_{am} and C_{am} are calculated as [57]

$$m_{am} = 1.8830 \frac{\rho_m h}{\pi a^2} \tag{2.22}$$

and

$$C_{am} = \frac{\pi a^6}{196.51 D}. \tag{2.23}$$

Numerical validation of plate's impedance

Simulation procedure:

The presented theoretical modeling is numerically validated, using a clamped plate made of DuPont Kapton FPC ($E = 2.758$ GPa, $\nu=0.34$, and $\rho_m = 1420$ kg/m^3) having geometrical dimensions of $h = 125$ μm and $a = 9.06$ mm representing the thickness and the radius of the plate,

respectively. This plate-loaded waveguide has been simulated in Comsol Multiphysics with 2D axisymmetry geometry, using Acoustic-Solid Interaction physics module and under plane wave incidence. Then, by numerical evaluation of the pressure difference over two sides of the plate and dividing it by volume velocity the series impedance Z_{am} of Fig. 2.5b has be extracted.

Results:

Figure 2.6 shows the acoustic impedance of such a plate obtained from theory (Eqs. 2.18 and 2.20) and numerical simulation, where an excellent agreement is observed. Equation. 2.22 and 2.23 can be used to derive the mass density and compliance as follows: $m_{am} = 1296$ (kg/m^4) and $C_{am} = 17.42 \times 10^{-12}$ m^3/Pa for $f_r = 1059$ Hz. Figure 2.6 also shows that the plate impedance is dominated by a compliance below the resonance frequency f_r while it behaves as a series mass above the resonance frequency. Thus, the series compliance in the CRLH circuit model can be realized by a clamped plate operating below its first resonance frequency.
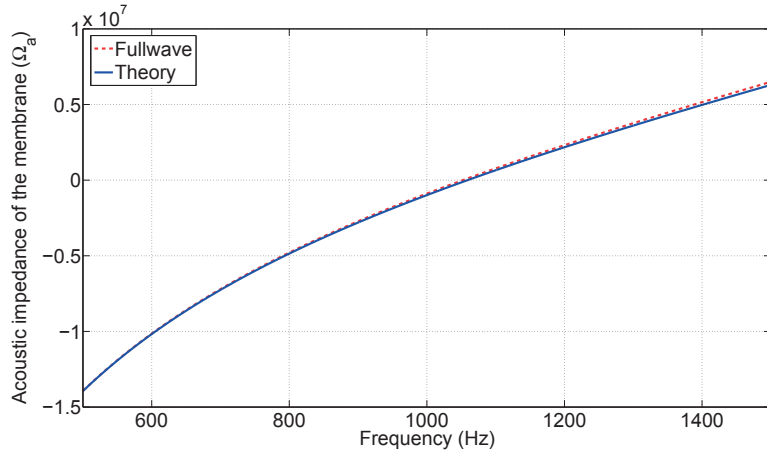
Figure 2.6: Imaginary part of the acoustic impedance for a clamped plate.

2.3.2 Realization of the shunt acoustic mass

It has been shown in Appendix B that short open tubes exhibit acoustic masses. If these short tubes are transversally connected to the main host waveguide, then they are called 'stubs' and can create a discontinuity in volume velocity as shown in Fig. 2.7. Thus, in analogy with electromagnetic TL theory, they can be modeled with shunt masses 'inductances'. Here, a radial stub, with a perfect symmetry of revolution, transversally connected to the main waveguide is considered. Geometrically, it consists of a radial channel of length L and width b where it is connected to a main acoustic waveguide of radius a, as shown in Fig. 2.7a. This stub is open at its both extremities to the main waveguide and the surrounding medium, thus it is subject to radiation. However, as b is considered to be very small, the stub can be approximated by $p = 0$, neglecting the radiation. Although this is a rough approximation, it

simplifies the circuit model without affecting the transmission-line behaviour of the structure.
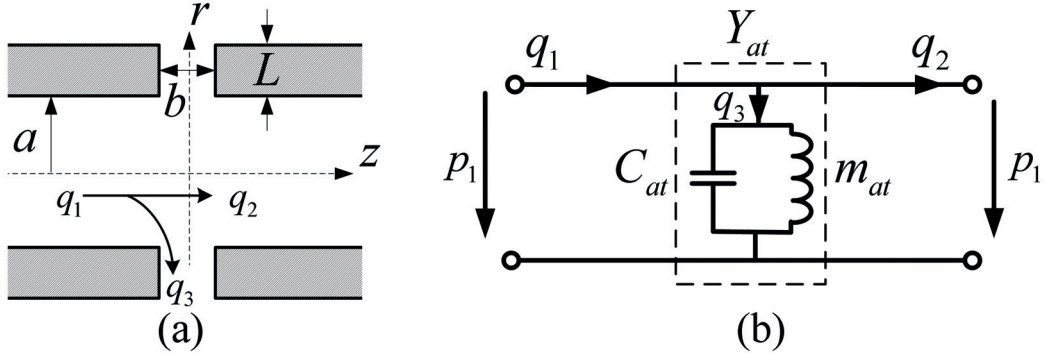
Figure 2.7: Cut view of the open radial stub (axisymmetry) connected to an acoustic circular waveguide (a) and its equivalent acoustic circuit (b).

Theoretical modeling of the radial stub

Introducing the radial stub to the waveguide results in deviating part of the volume velocity into the stub, however as b is small compared to wavelength the pressure keeps its continuity. Thus, the open channel connected to the main waveguide can be represented as an admittance Y_{at} in parallel in the equivalent circuit as shown in Fig. 2.7b. Here, Y_{at} is the input admittance of a radial channel in its fundamental mode. The TL theory can be also expanded for radial structures where the solutions are expressed in terms of Bessel functions instead of exponential functions ($e^{\pm jkz}$). Moreover, in these structures the propagation constant and characteristic impedance depend on the radial distance r [57]. Using the radial TL theory, the input acoustic impedance of a short circuited ($p = 0$) radial channel ($Z_{at} = 1/Y_{at}$), is given by [57, 63]

$$Z_{at} = jZ_{ac}(a)\mathrm{tn}[ka, k(a+L)], \tag{2.24}$$

Here, $\mathrm{tn}(x, y)$ is the small radial tangent function expressed by [57]

$$\mathrm{tn}(x, y) = \frac{J_0(x)N_0(y) - N_0(x)J_0(y)}{J_1(x)N_0(y) - N_1(x)J_0(y)}. \tag{2.25}$$

In the Eq. 2.25 J_n and N_n are the nth order Bessel's function of the first and second kind and $Z_{ac}(r)$ is the acoustic characteristic impedance of the radial TL at a given radial distance r, given by [57]

$$Z_{ac}(r) = \frac{Z_c}{2\pi r b}. \tag{2.26}$$

It is interesting to see that the Eq. 2.24 which is used to calculate the input acoustic impedance of the shorted radial channel is similar to that of a uniform TL $Z_{at} = jZ_{ac}\tan(kL)$, and only radial tangent (tn) has been replaced by tan.

At low frequency regime the impedance in Eq. 2.24 can be approximated by an acoustic mass as [57],

$$Z_{at} \approx j\omega m_{at0} \quad \text{with} \quad m_{at0} = \frac{\rho}{2\pi b}(1 + \frac{L}{a}). \tag{2.27}$$

This simple impedance model diverges from the impedance model of Eq. 2.24 as frequency increases, thus Eq. 2.27 is only accurate for very small stubs compared to the wavelength. As shown in Fig. 2.7b, by adding an acoustic compliance in parallel with the acoustic mass, this model can be improved to represent the radial channel in high frequency regime. To determine the value of C_{at} at a given frequency, the Eq. 2.24 and its frequency derivative should fit the impedance model of m_{at} and C_{at} at that frequency. It is good to remind that the mass and compliance of the clamped plate was also calculated following similar procedure (see Appendix B).

Termination effect in the radial stub

The presented radial stub has an open termination and it physically radiates into the surrounding medium. Thus, the load impedance assigned to open end of the tube is not exactly zero but Z_r which is called radiation impedance and consists of a real and imaginary part. As the radiation behaviour of the stub is not studied in this chapter, the real part can be neglected and this simplification does not have a significant effect in the circuit model. However, in the theoretical models the imaginary part of the Z_r is taken into account by increasing the length of the stub by ΔL. Numerical simulations can be used to determine the actual stub length L corresponding to the desired effective length $L_e = L + \Delta L$. It should be noted that, this approximation results in discrepancy between the dimensions used in the theoretical and numerical model. Indeed, for theoretical simulations, L_e is used as the length of the stub in order to take the termination effect into account, however, in fullwave simulations L is used as the actual length of the stub.

Numerical validation of the radial stub

Simulation procedure:
The stub-loaded waveguide has been numerically simulated in 2D axisymmetry geometry with Comsol Multiphysics using Pressure Acoustics physics module and under plane wave incidence, from which the shunt impedance $Z_{at}(= 1/Y_{at})$ of Fig. 2.7b can be derived by dividing the pressure to volume velocity over the input of the radial stub. In the numerical model, to adjust the effective length due to the open termination effect, the physical length of the stub has been decreased compared to the stub length used in the theoretical modeling.

This is done to approximately obtain the same acoustic mass in fullwave simulation and the theoretical model.

Results:

In order to validate the presented theoretical modeling of Eq. 2.24, a radial stub with $b = 1$ mm connected to an acoustic circular waveguide of radius $a = 9.06$ mm is considered. Figure 2.8 shows the input acoustic impedance of the aforementioned stub, where the theoretical relation of Eq. 2.24 for a stub of length $L = 48.95$ mm is compared to the fullwave simulation result for a stub with $L = 42.67$ mm. As explained before, the reason to compare two stubs with different lengths, is to the take the termination effect into account and Fig. 2.8 shows that the added length of $\Delta L = 48.95 - 42.67 = 6.25$ mm in the theoretical modeling has fully satisfied the termination effect, since good agreement between theoretical relation of Eq. 2.24 and numerical simulation is observed. The corresponding values for the elements of the approximate parallel resonant circuit of Fig. 2.7b can be also calculated by comparing it to the theoretical value of Eq. 2.24 and its derivative in a given frequency which results in: $m_{at} = 348.3$ (kg/m^4) and $C_{at} = 9.138 \times 10^{-12}$ m^3/Pa. It can be noted that using Eq. 2.27, the value of $m_{at0} = 351.1$ (kg/m^4) is calculated for the acoustic mass which is about 1% lower than $m_{at} = 348.3$ (kg/m^4). Figure 2.8 also confirms that the impedance of the radial stub shows almost pure acoustic mass behaviour which is due to the small width of the stub. However, in order to get a precise circuit modeling for wider stubs the shunt capacitance C_{at} should be taken into account.
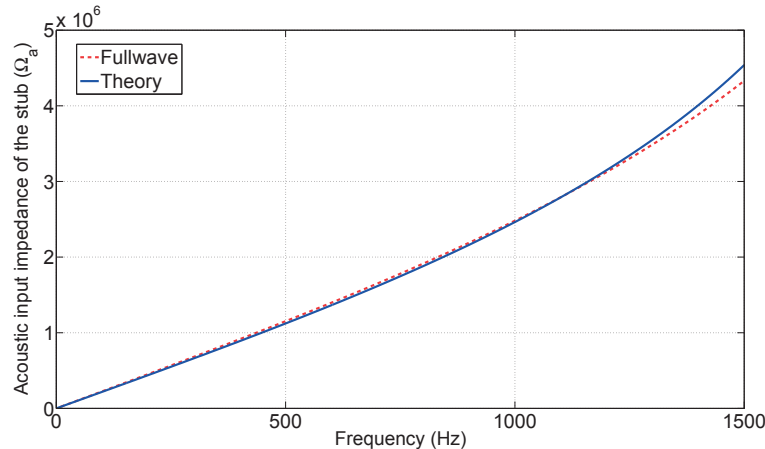
Figure 2.8: Imaginary part of input acoustic impedance of the considered radial stub. The theoretical impedance curve corresponds to Eq. 2.24 with $L = 48.95$ mm, the fullwave result corresponds to $L = 42.67$ mm.

2.4 Design of CRLH TL metamaterial

In this section the design procedure for CRLH TL metamaterial is presented. To this end: first the connection between proposed configuration of Fig. 2.4 and circuit topology of Fig. 2.3 is fully described. Then a tool for characterization of such periodic structures are introduced and finally based on previous step by using TL model the design procedure is explained.

2.4.1 CRLH TL unit-cell configuration vs. circuit topology

Using the proposed unit-cell configuration of Fig. 2.4 (in red box) and leveraging the symmetrical property of the unit-cell as well as the connection between ladder type and Π-type circuit topology (see Appendix D), the TL model of the CRLH unit-cell is obtained as in Fig. 2.9. Indeed, as radial channels, representing the shunt circuit elements, are placed on two extremities of the defined unit-cell, the Π-type circuit model is the most suitable circuit topology to describe the proposed unit-cell configuration. Where, the plate is represented by Z_{am}, the main waveguide on each side of the plate are modeled by two transmission-lines of length $(d-h)/2$ with characteristic impedance $Z_{ac} = Z_c/S$ and phase constant k and the two half-width radial stubs are represented by $Y_{at}/2$ on each side of the circuit model. The TL model of Fig. 2.9 can be simplified to lumped circuit model of Fig. 2.10 where, as shown in Fig. 2.2a, the TL section is replaced by the corresponding series acoustic mass and the shunt acoustic compliance, $m_{aTL} = (\rho/S)(d-h)$ and $C_{aTL} = (S/K)(d-h)$, respectively. Moreover, after replacing the Z_{am} and Y_{at} by their corresponding mass and compliance circuits, shown in Fig. 2.5b and 2.7b, the values of the series and parallel masses and compliances in circuit topology of Fig. 2.10 are found as:

$$\begin{cases} m_{as} = m_{am} + m_{aTL} \quad , \quad m_{ap} = m_{at} \\ C_{ap} = C_{at} + C_{aTL} \quad , \quad C_{as} = C_{am} \end{cases} \tag{2.28}$$

It should be noted that the circuit model of Fig. 2.10 is a good approximation for the TL model
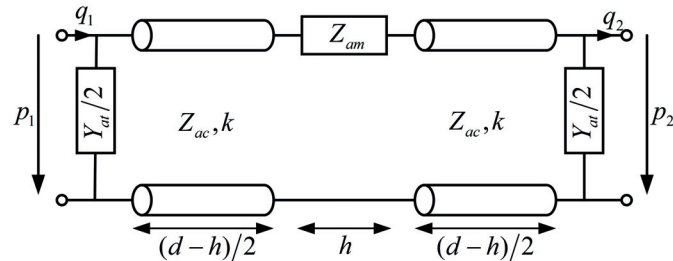
Figure 2.9: Equivalent acoustic TL model for the symmetrical Π-type unit-cell of CRLH TL structure.

of Fig. 2.9 if unit-cells are in subwavelength regime ($\sim \lambda/10$).
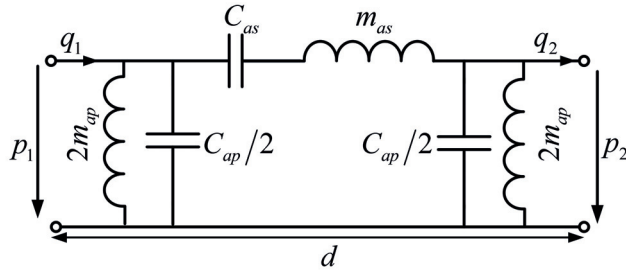
Figure 2.10: Lumped circuit model for the symmetrical Π-type unit-cell of the acoustic CRLH TL. This is the Π-type topology of the CRLH lumped element model shown in Fig. 2.3.

2.4.2 Characterization

Any uniform medium can be treated with an infinitely periodic model and maybe Newton was the first to use this in order to calculated the speed of sound in air. He modeled the air with an infinitely long spring-mass model and could get a rough approximation of the sound velocity [64]. After him such models extensively used and applied to describe periodic structures and today it is called Bloch theory. Usually periodic structures are characterized by their Bloch parameters, thus the performance of CRLH TL metamaterials as a subcategory of periodic structures can be determined by this theory, which is briefly explained thereafter.

A periodic structure supports eigenwaves called Bloch waves which are derived for a single unit-cell, however, in the subwavelength and infinite periodicity limit the Bloch waves are equal to the egienwaves derived for the same periodic structure without considering its periodicity. In other words, the Bloch waves are mathematically derived by analysing a single periodic unit-cell, however they represent the characteristics of the whole structure. For instance, in 1D case, the input and output pressure waves on the boundaries of a single unit-cell are related by $p_{n+1} = p_n e^{\pm \gamma_B z}$ where $\gamma_B = \alpha + j\beta$ is the Bloch propagation constant. Indeed, this is possible because all the unit-cells have the same effect on the propagation of the wave and this effect is expressed by $e^{\pm \gamma_B z}$ where γ_B can be considered as the periodic counterpart of γ attributed for regular medium. Therefore, γ_B should be a function of the different specifications of the unit-cell such as material properties and should describe the propagation behaviour of the wave for the completely periodic structure. In the similar way, by connecting the ratio of the pressure to the volume velocity on the boundaries of the unit-cell the Bloch impedance (Z_B) as a counterpart of characteristic impedance is calculated (see Appendix F for detailed explanation). Thus, a periodic structure can be described by its Bloch parameters γ_B and Z_B. Using network theory, the values of the γ_B and Z_B can be related to the transfer matrix [T] of the unit-cell in the periodic structure. For instance, for the proposed CRLH TL unit-cell which is reciprocal and symmetrical, the relations $\gamma_B = \text{arcosh}(T_{11})/d$ and $Z_B = \sqrt{T_{12}^2/(T_{11}^2 - 1)}$ are obtained where d is the length of the unit-cell. Moreover, the refractive index n is expressed using $n = \gamma_B/(jk)$.

2.4.3 Design

In order to design a CRLH TL metamaterial based on the proposed configuration of Fig. 2.4, the following constraints are enforced: (1) The transition frequency between RH and LH is set to be at f_0 = 1000 Hz. This frequency can be simply derived from lumped element circuit model of Fig. 2.3, which is expressed by [61]: $f_0 = \frac{1}{2\pi \sqrt[4]{m_{as}m_{ap}C_{as}C_{ap}}}$. (2) The length of the unit-cell should be very small compared to the wavelength, preferably $d < \lambda/10$. In this case, the transition frequency is chosen as a reference for λ. (3) In order to suppress the band gap in the transition frequency between LH and RH medium the balanced condition should be imposed where the resonance frequency of the equivalent series and parallel lumped circuit elements are equal. This condition can be mathematically expressed by [61]: $m_{as}C_{as} = m_{ap}C_{ap}$. (4) The Bloch impedance of the CRLH TL should be close to the characteristic impedance of the host medium. This criterion is imposed to ensure the possibility of good impedance matching from input waveguide to CRLH TL. The value of the Bloch impedance can be derived from circuit theory where at the transition frequency is simplified to [61]: $Z_B = \sqrt{m_{as}/C_{ap}} = \sqrt{m_{ap}/C_{as}}$. (5) Considering that the Bloch impedance of the CRLH TL does not highly depend on frequency, in order to achieve good power transmission, in a wide bandwidth, from input waveguide to CRLH TL metamaterial, the impedance of the input waveguide (Z_{ace}) is set to be equal to the Bloch impedance (Z_B).

The aforementioned constraints provide three main equations to calculate the four unknowns

Table 2.1: Values of the lumped elements associated with the proposed CRLH TL design (see Fig. 2.10 and Eq. 2.28).

Description	m_a (kg/m^4)	C_a (10^{-12} m^3/Pa)
Plate	m_{am} = 1296	C_{am} = 17.42
Radial stub	m_{at} = 348.3	C_{at} = 9.138
Host TL section	m_{aTL} = 156.1	C_{aTL} = 63.60
Series elements	m_{as} = 1452	C_{as} = 17.42
Shunt elements	m_{ap} = 348.3	C_{ap} = 72.73

Table 2.2: Gemetrical dimensions of the proposed CRLH TL design (see Fig. 2.4 and Fig. 2.13).

Description	Parameter	Value
Radius of the main waveguide (plate)	a	9.06 mm
Radius of the input waveguide	a_e	5.54 mm
Length of the radial stub	L	43.5 mm
Width of the radial stub	b	1 mm
Thickness of the plate	h	125 μm
Length of the unit-cell	d	34 mm

namely: m_{as}, C_{as}, m_{ap} and C_{ap}. The fourth equation can be chosen by imposing another constraint on γ_B or the bandwidth of the CRLH TL. For instance, the cut off frequency of the CRLH TL in LH and RH regions are given by:

$$f_{cL} = \frac{1}{2\pi\sqrt{m_{as}C_{ap}}} \left| 1 - \sqrt{1 + \sqrt{\frac{m_{as}C_{ap}}{m_{ap}C_{as}}}} \right| \tag{2.29a}$$

$$f_{cR} = \frac{1}{2\pi\sqrt{m_{as}C_{ap}}} \left(1 + \sqrt{1 + \sqrt{\frac{m_{as}C_{ap}}{m_{ap}C_{as}}}} \right) \tag{2.29b}$$

respectively [61], which can be used as the fourth constraint. Here, to simplify the design processes the fourth constraint is chosen to be some practical limitations imposed by nature. For instance the plate should be designed from available materials and here, Kapton with the thickness of 125 μm is used.

The imposed constraints are used to find the values of the circuit elements in Fig. 2.10 where the final results have been listed in Table 2.1. Then, by using the theoretical equations developed in the previous section to model waveguide, plate and radial stub, the geometrical dimensions and material properties of the proposed configuration of Fig. 2.13 are calculated which have been shown in Table 2.2. It is good to remind that in order to compensate the effect of some approximations, such as open termination of the radial stub, numerical fine tuning of the structure is performed by Comsol Multiphysics. In this case, considering a perfect shorted radial stub, the length L is analytically calculated to be 46.80 mm which is decreased to $L = 43.50$ mm after fine tuning process performed to achieve perfect balance condition in numerical simulations.

2.5 Simulation Results

The simulation results of the proposed CRLH TL is presented in three different sections: (1) Bloch parameters of the unit-cell is retrieved and the RH/LH behaviour of the structure is studied. (2) The scattering parameters are derived where the transmission property of the designed CRLH metamaterial as a guided-wave structure in investigated. (3) The radiation behaviour of the structure is briefly discussed while a detailed study is presented in the next chapter.

2.5.1 Bloch parameters

Numerical simulation of the CRLH unit-cell:
To retrieve the Bloch parameters ($\gamma_B = \alpha_B + j\gamma_B$, Z_B) for the proposed CRLH TL unit-cell, a 2D axisymmetrical geometry with Π-type configuration is numerically simulated under plane wave incidence. To this end the Acoustic-Solid interaction physics module of Comsol Multiphysics is used in frequency domain. Then, using the four-microphone measurement
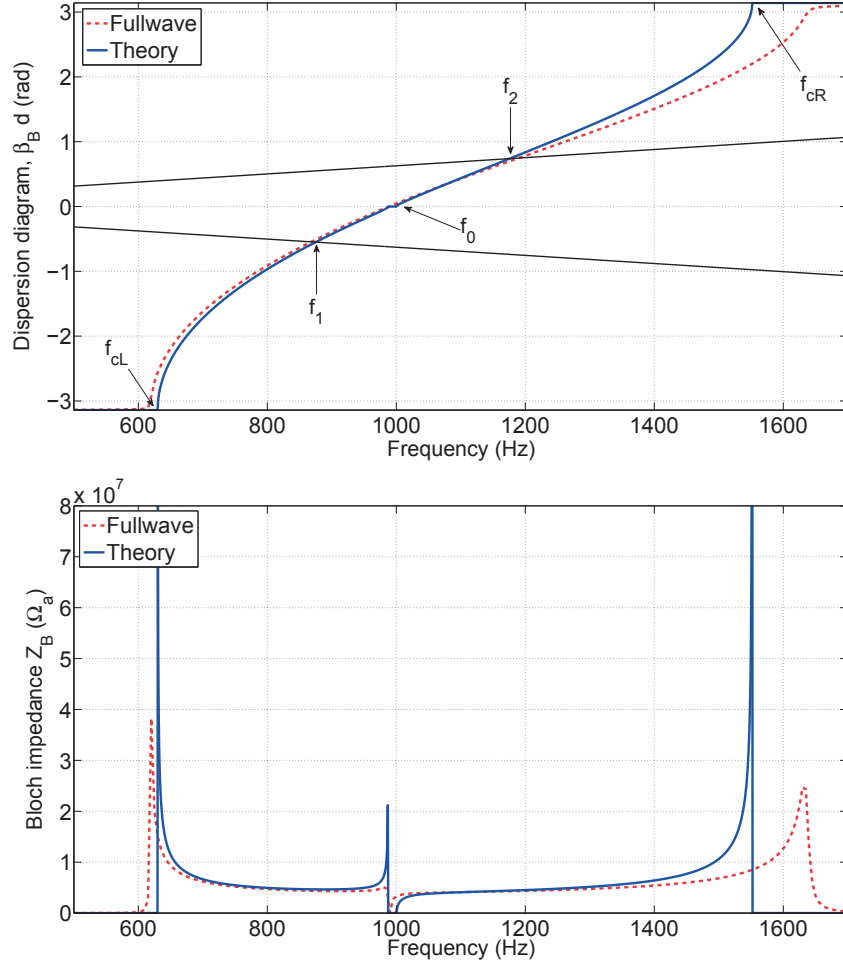
Figure 2.11: Bloch parameters, in red are the extracted results from numerical simulation by Comsol Multiphysics and in blue are the analytical results evaluated by circuit model. (top) The imaginary part of $\gamma_B d$, where f_{cL} and f_{cR} are LH and RH cut-off frequencies, respectively. f_0 is the transition frequency between the LH and RH bands, the region between f_1 and f_2 is called the fast-wave band. In analogy with electromagnetics, the sound lines (in black) correspond to the dispersion in air ($k = \pm\omega/c$). (bottom) is the real part of the Bloch impedance (Z_B).

method the reflection and transmission coefficients of the single CRLH unit-cell are evaluated (see Appendix E) and transformed to Bloch parameters (see Appendix F). Moreover, to get the analytical results the circuit model of Fig. 2.10 is used as a guideline, where the [T] matrix is calculated for this model (see Appendix D) and transformed to Bloch parameters using respective relations (see Appendix F) in Matlab. It should be noted that, as shown in Fig. 2.13 every unit-cell is composed of two half-width radial stubs and a plate which are all incorporated in the main waveguide.

Results:

It can be observed on the dispersion diagram of Fig. 2.11(top) that the acoustic CRLH TL metamaterial, is composed of five distinct frequency regions, namely: LH/RH guided regions where the wave propagates through the waveguide without any leakage $[f_{cL} - f_1]$ and $[f_2 - f_{cR}]$, LH/RH leaky-wave region $[f_1 - f_2]$ and the band-gap region between RH and LH region. By ensuring balanced condition the band-gap has disappeared in this cases and has turned into a single frequency transition from RH to LH region denoted by f_0 where the structure exhibits zero refractive index with non zero group velocity and infinite phase velocity. This structure demonstrates negative refractive index behaviour in a very broad bandwidth from $f_{cL} = 610$ Hz to $f_0 = 1000$ Hz, where the phase and group velocities are antiparallel ($v_p v_g < 0$). Between f_{cL} and f_1 the CRLH TL structure is in LH guided mode as the phase velocity inside the CRLH is smaller than outside medium and the wave is confined in the CRLH structure. However, between f_1 and f_0 the CRLH TL is in its LH fast wave regime that is: first, the phase velocity inside the structure is larger than outside and second the phase and group velocities are antiparallel. From $f_{cL} = 1000$ Hz to $f_0 = 1640$ Hz this structure exhibits a positive refractive index where in the $[f_0 - f_2]$ band it is in RH fast wave mode while in $[f_2 - f_{cR}]$ it is in RH guided wave regime. Figure 2.11(bottom) depicts the Bloch impedance of the CRLH TL unit-cell where a good agreement between numerical simulations and TL theory is observed. The Bloch impedance of the designed unit-cell is almost flat in all the guided-wave band $[f_{cL} - f_{cR}]$ which facilitates the broad input impedance matching of the structure. Here, the radius of the input acoustic waveguide for broadband matching is calculated to be $a_e = 5.54$ mm where the targeted Bloch impedance is $Z_B = 4.192\text{M}\Omega$ and the radius is calculated after $Z_B = Z_{ac} = Z_c / (\pi a_e^2)$.

2.5.2 Equivalent medium parameters

It is reminded that for an appropriate values of Z and Y, the TL model of Fig. 2.1 can describe any medium either RH or LH. Now, if the equivalent value of the mass density of the medium, denoted by ρ_{eq}, is assigned to Z and the equivalent value of the bulk modulus K_{eq} of the medium is assigned to Y, the following equalities are found:

$$\begin{cases} \rho_{eq} = \frac{Z}{j\omega} \frac{S}{d} \\ K_{eq}^{-1} = \frac{Y}{j\omega} \frac{1}{Sd}, \end{cases} \tag{2.30}$$

For the CRLH circuit model of Fig. 2.3, Z as a series and Y as a parallel circuit components are calculated by:

$$\begin{cases} Z = j\omega m_{as} + \frac{1}{j\omega C_{as}} \\ Y = j\omega C_{ap} + \frac{1}{j\omega m_{ap}}. \end{cases} \tag{2.31}$$

Using Eq. 2.30 and Eq. 2.31 the equivalent mass density and bulk modulus are found as

$$
\begin{cases}
\rho_{eq} = \dfrac{j\omega m_{as} + \frac{1}{j\omega C_{as}}}{j\omega} \dfrac{S}{d} \\[2ex]
K_{eq}^{-1} = \dfrac{j\omega C_{ap} + \frac{1}{j\omega m_{ap}}}{j\omega} \dfrac{1}{Sd}.
\end{cases}
\tag{2.32}
$$

Equation 2.32 expresses that any acoustic CRLH medium which is modeled by Fig. 2.3, is the equivalent of the hypothetical and homogenized medium with fundamental material properties ρ_{eq} and K_{eq}. Moreover, these expressions state that, in order to achieve negative mass density the series compliance is a prerequisite, while the parallel mass is the necessary element to achieve negative modulus. To better understand the equivalent medium parameters, the Eq. 2.32 is evaluated for the proposed CRLH configuration with the circuit elements listed in Table 2.1. To better visualize these quantities, the calculated equivalent mass density and bulk modulus in CRLH medium is normalized to mass density and bulk modulus in the air, where $\rho_{r,eq} = \rho_{eq}/\rho$ and $K_{r,eq}^{-1} = K_{eq}^{-1}/K^{-1}$ have been shown in Fig. 2.12. This figure shows that the CRLH medium exhibits negative values of bulk modulus and mass density over a broad bandwidth and both of the equivalent material properties become zero at the transition frequency f_0.

This should be noted that the equivalent medium parameters are only valid for subwavelength regime where the unit-cells of the metamaterials are small compared to the wavelength. For example in this case the wavelength of the sound wave tends to infinity at and near the transition frequency (f_0), thus the subwavelength rule is fully satisfied. However, the effective-medium theory loses its meaning as the size of the unit-cell becomes comparable to the wavelength of the sound.
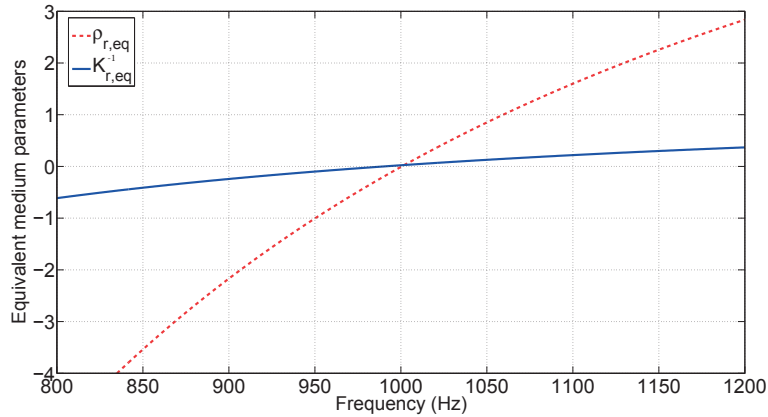
Figure 2.12: Normalized equivalent mass density and bulk modulus for the proposed CRLH TL configuration.

2.5.3 Scattering parameters

Numerical simulations of the 10 unit-cell CRLH TL:

Considering the 2D axisymmetrical geometry, the reflection and transmission coefficients of the proposed CRLH TL is numerically evaluated under plane wave incidence using Acoustic-Solid interaction module in Comsol Multiphysics. To this end a 10 unit-cell long CRLH structure is numerically simulated and four microphone measurement technique (see Appendix E) is used to characterized the reflection R and transmission coefficients T of the structure. Moreover, the analytical results of TL theory is assessed in Matlab by multiplying 10 [T] matrices, each representing single $\Pi-$type unit-cell, and the final result is transformed to [S] matrix ([T]^{10} $\rightarrow$[S]) in order to retrieve the reflection and transmission coefficients.

It should be noted that, as $\Pi-$type circuit topology is chosen for TL modelling, each unit-cell should be composed of two half-width ($b/2$) radial stubs at each side of the main waveguide and a clamped plate in the middle of each unit-cell (see Fig. 2.13). In circuit model this is equivalent to the admittance of $Y_{ap}/2$ to model the radial stubs, or equivalently an acoustic mass $2m_{ap}$ and an acoustic compliance $C_{ap}/2$ (see Fig. 2.10). Consequently, when stacking 10 unit-cells to get a longer CRLH TL, the final configuration should be terminated with two half stubs in its first and last unit-cells.

Results:
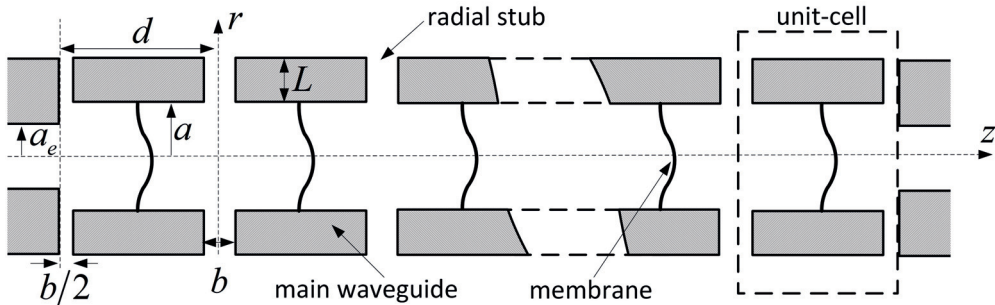
Figure 2.13: 2D schematic representation of the proposed CRLH TL metamaterial. This figure depicts an axisymmetric geometry with respect to z-axis.

Figure. 2.14(top) shows reflection and transmission coefficients obtained from numerical simulations and theoretical results of TL theory. It is observed that due to the good impedance matching in the input and output of the CRLH TL a very low reflection ($R < -10$ dB) is achieved in a broad frequency bandwidth of 700 Hz to 1450 Hz. Moreover, the reflection coefficient also confirms that the CRLH structure starts to guide the sound wave exactly after the left and right cut off frequencies in $f_{cL} = 610$ and Hz $f_{cR} = 1640$ Hz. Despite the good agreement between two methods to predict the reflection coefficient, the numerically evaluated transmission coefficient is lower than the theoretical value. This discrepancies is attributed to the radiation phenomenon and it will be discussed in the following section. Figure. 2.14(bottom) depicts the transmission phase in the CRLH TL where as expected the 0 phase is observed at the

transition frequency (1 kHz) which is attributed to the infinite phase velocity due to near zero material properties. In short, good agreement between the numerical simulations and TL theory also proves the accuracy of the TL theory in modeling complex CRLH TL structures.
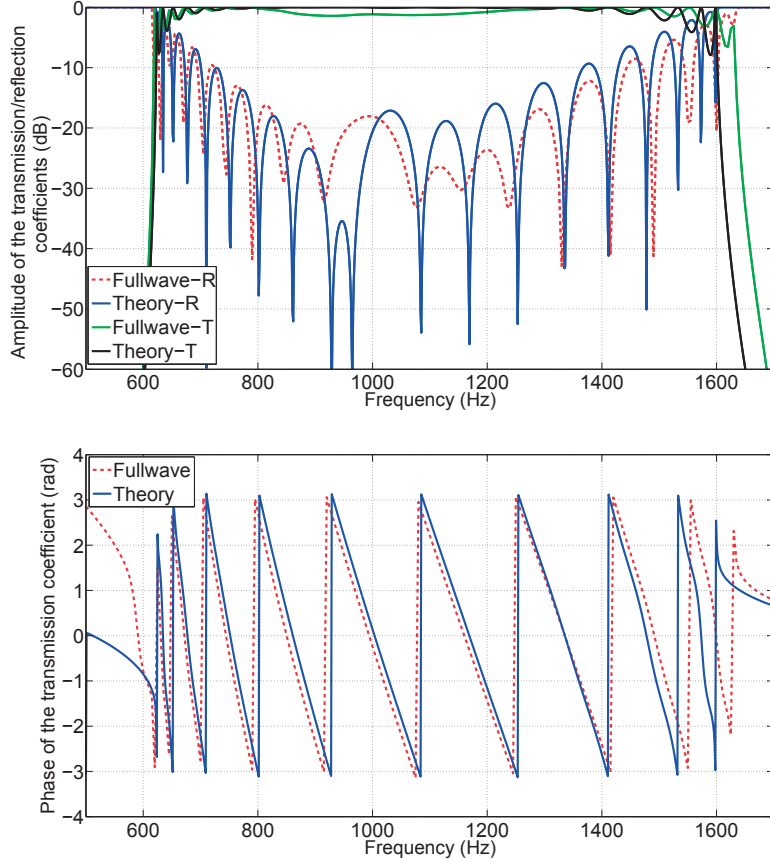
Figure 2.14: (top) Reflection (R) and transmission (T) coefficient for 10-cell-long CRLH TL. (bottom) The phase of T is shown derived by numerical simulation and theory where the phase is zero in the close proximity of f_0.

2.5.4 Radiation losses

For the proposed CRLH TL configuration all the sources of loss were neglected by using lossless acoustic components as well as considering the short circuited radial stub ($p = 0$). However, it is reminded that the imaginary part of the impedance due to the open stub has been compensated by increasing the length of the radial channel denoted by termination effect. In the numerical simulations the radial channels are not set to $p = 0$, but are left open to radiate into surrounding medium. Thus, contrary to TL modeling, in numerical simulations there is one source of energy loss due to the radiating stubs. In order to evaluate the amount of radiation loss in the presented CRLH TL configuration, the efficiency of the structure is numerically calculated using $\eta = |R|^2 + |T|^2$. Indeed, in the case of suppressed radiation the

amount of efficiency calculated by this formula is expected to be unity ($\eta = 1$). Figure 2.15 depicts the efficiency of the CRLH TL structure with 10 unit-cells where almost 25% of the power is lost by the radiation. As it is expected, the radiation happens where the structure is in its fast wave (leaky-wave) regime, between $f_1 = 875$ Hz and $f_2 = 1175$ Hz as shown in the dispersion diagram of Fig. 2.11a. Since, in the fast wave regime the phase velocity inside the CRLH structure is faster than the phase velocity outside (here air), the phase matching can be fulfilled and the wave can escape from CRLH to the air which is called leaky-wave radiation. In electromagnetic realm, the leaky-wave radiation from CRLH TL metamaterials has been studied where the peculiar properties of the CRLH TL to support RH $[f_1 - f_0]$, LH $[f_0 - f_2]$ and zero index (at f_0) have been leveraged for the realization of the leaky-wave antenna for frequency scanning the full space, from backfire at f_1 to endfire at f_2, including broadside direction which happens at f_0. Thus, the proposed CRLH TL with open radial channels can be considered as the analog of electromagnetic CRLH TL LW antenna.

It should be mentioned that, although the simplified circuit model proposed in this chapter
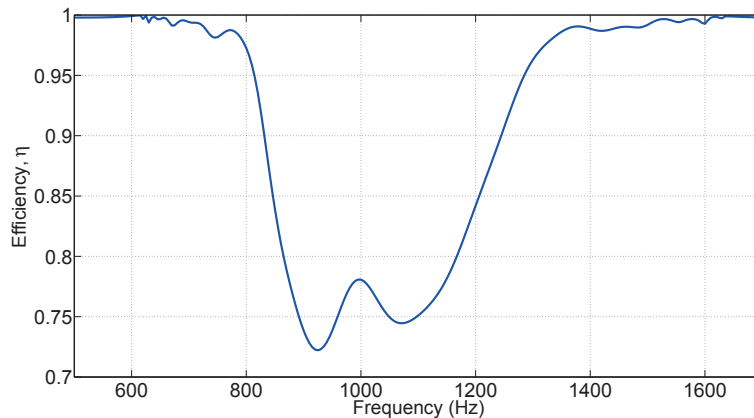
Figure 2.15: Numerically calculated efficiency of the proposed CRLH TL structure with 10 unit-cells.
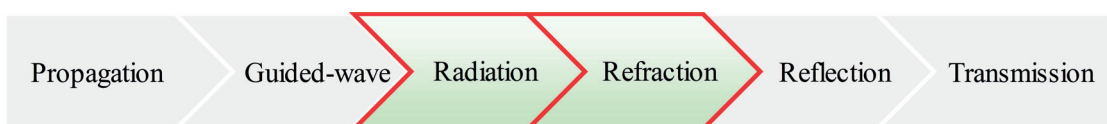
does not consider the radiation in CRLH structures, it can predict the fast wave region with very high accuracy. Indeed, the presented results show that for small amounts of losses per unit-cell the accuracy of the circuit model of CRLH TL is not affected.

2.6 Conclusion

In this chapter the propagation of acoustic waves in CRLH medium was investigated. First, the TL theory has been introduced to model conventional, negative index and CRLH medium. Then, it has been used to design an acoustic TL-based metamaterial with subwavelength unit-cells having lattice constant in the order of $\lambda/10$, exhibiting very broad operating bandwidth. The originality of the presented design was in using plates to realize the series compliances, while transverse radial open channels have been proposed to achieve the shunt acoustic masses. The proposed CRLH TL configuration has two interesting properties: First, due to the nonresonant behaviour, it exhibits a negative refractive index over a broad bandwidth (from 600 to 1000 Hz). Second, due to the enforced balanced condition, no band gap is observed between the positive and negative index frequency bands. This provides a smooth transition from LH medium to RH medium where in the transition frequency the zero refractive index and nonzero group velocity is achieved. Using Comsol Multiphysics the performance of the CRLH TL has been numerically validated and compared to the results obtained by TL theory where a good agreement between numerical and theoretical results for reflection and transmission coefficients as well as dispersion relation and Bloch impedance has been reported. In addition to the guided-wave behaviour of the CRLH TL structure which might find applications for phase compensation, the radiation properties of this structure can be studied which may result in interesting radiation applications. In this regard, by analogy with the CRLH TL based leaky-wave antennas (CRLH TL LWA) developed in Electromagnetics, the directive behaviour of the CRLH TL can be used to design acoustic sensors or sources with frequency scanning capability.

In short, this chapter was devoted to the main acoustic wave phenomena: sound wave propagation in guided-wave structures, which led to developing the TL theory to achieve CRLH acoustic metamaterials. In the following chapter, the investigation on the other types of sound-metastructure interaction is continued by covering the radiation and refraction phenomena where the acoustic CRLH TL, developed in this chapter, will be exploited to design an acoustic LWA to achieve novel functionalities such as acoustic dispersive prism and acoustic single sensor direction finder.

3 Acoustic Leaky-Wave Antenna

| Propagation | Guided-wave | Radiation | Refraction | Reflection | Transmission |

This chapter is a modified version of the materials published in Ref. [50, 51] and orally presented in Ref. [65], [66] and [67].

3.1   Introduction

Inspiration from electromagnetics:

In the previous chapter, in analogy with electromagnetic transmission-line metamaterials the concept of acoustic transmission-line metamaterials was investigated by illustrating the new properties achievable on guided-wave propagation. In this chapter, in analogy with electromagnetic the radiation characteristics of acoustic TL metamaterials are investigated. Indeed, when guided-wave type metamaterial is open to free space it radiates and can be used as an antenna for transmitting or receiving powers. This radiation from guided-wave structures happens when metamaterials support fast-wave mode, called leaky-wave mode. The advent of CRLH metamaterials as a guided-wave structure which support leaky-wave modes has revolutionized the electromagnetic Leaky-Wave Antennas (LWAs) [61]. Conventional LWA based on conventional materials only support RH propagation and consequently scans the broadside to endfire directions [68]. However, Composite Right/Left Hand Transmission-Line (CRLH TL) metamaterials support both RH and LH propagations, thus, they can do the full scanning from backfire to endfire including the broadside direction. The leaky-wave modes as well as the dispersive nature of the electromagnetic CRLH medium has been leveraged to propose leaky-wave antenna for direction finding radars [69] and spectral-spatial decomposition of microwaves in real-time basis [70], which is the equivalent of microwave dispersive prism. The aforementioned examples show that the combination of metamaterials along with classical devices like LWA has led to the emergence of diverse physical concepts and has opened doors to novel engineering applications.

Efforts in acoustics:

Recently, a metamaterial-based reversed rainbow prism whose refractive index is a decreasing function of frequency, has been presented in the microwave regime [71]. This has brought artificial dispersive prisms [72, 73] into the limelight where the metamaterial is used to deal with causality and passivity constraints. Surprisingly, while an active field of research in electromagnetics, there is no equivalent for dispersive prism in acoustic regime, mainly due to the weak acoustic dispersive nature of matter. Although some studies has been done on acoustic artificial dispersive media [74, 75] for acoustic rainbow trapping, it only covers guided-waves and not radiating ones. Another example where acoustic metamaterials can be inspired by the electromagnetic counterparts is metamaterial based radiating devices. In electromagnetics, metamaterial inspired radiating devices, like CRLH TL LWA have found applications in radars, but acoustic LWA is only a theoretical proposal [57] and an experimental validation [?] and not an optimized design with a direct application proposals.

Refraction and radiation phenomena in acoustic leaky-wave antenna:

Radiation and refraction phenomena are two important concepts in wave engineering. While the former (radiation) is usually studied directly as consequence of sound source (sources), the later is the result of change in the direction of propagation due to wave-matter interactions and usually studied for passive medium. However, if the indirect radiation from a secondary source is considered, then radiation and refraction (as well as reflection and transmission) can be studied for the same wave-metastructure configuration. For example a reflector antenna (having large radius of curvature with respect to operating wavelength), as a secondary source of sound, can be studied in terms of radiation or reflection. Likewise, a lens can be studied as a secondary radiator (antenna) or a transmitter. In the same manner, the output of the acoustic LWA in its near-field and far-field can be studied in refraction and radiation mode and two different functionalities can be exploited from such a device depending on the mode of operation. In this chapter a CRLH configuration similar to the structure of previous chapter which supports a fast-wave mode, called a leaky-wave, is studied as LWA. The main difference, compared to the configuration of the previous chapter is that, the radial axisymmetrical stubs are replaced by cylindrical stubs. This upgraded acoustic CRLH TL is used to exploit the LW phenomenon to obtain directive acoustic antenna with frequency scanning capability. Moreover, the dispersive prism functionality in the near-field radiating mode as well as Single Sensor Direction-Finding (SSDF) ability in its receiving mode in far-field are studied.

3.1.1   Outline of the chapter

This chapter starts with explaining the theory and operating mechanism of acoustic LWA and is followed by the presentation of mathematical formulations which describe LWA in terms of radiation efficiency and directivity. Then, a design platform based on acoustic modules to realize the LWA is introduced and a design methodology based on acoustic transmission-line models is presented. The chapter continues by introducing two applications for LWA

where, first, acoustic dispersive prism is explained and the theoretical, numerical and the measured results are presented and compared in the near-field region. Second, SSDF system as a novel concept of sound source localization, without resorting to beam-steering techniques based on multiple sensors, is introduced and validated through numerical simulations and experimental results. Concluding remarks summarize the outcomes of the chapter.

3.2 Leaky-Wave Antenna

The leaky-wave (LW) appellation, referring to the principle of power leakage along a waveguide, has been first developed in the 1940s [68] in the electromagnetic realm. Owing to the high directivity and frequency scanning capability of such an antenna, it became very attractive in electromagnetics. However, LWAs based on conventional RH materials exhibit only positive wavenumbers and, as a consequence, have the drawback of scanning only the one quadrant from broadside (0° or perpendicular to leaky waveguide) to endfire (90° or in the direction of leaky waveguide). However, as introduced in the previous chapter, with the introduction of CRLH TL metamaterials, which support both positive and negative wavenumbers, the backfire to endfire (-90°,90°) electromagnetic antenna has been made possible by design [61]. The same idea can be followed in acoustics to achieve an acoustic CRLH TL LWA which exhibits directive radiation beam and performs frequency scanning of the full half-space from backfire to endfire.

3.2.1 General description and properties

An acoustic LWA is a waveguiding structure that favours the sound power leakage through radiating openings as it propagates along its axis. Leaky-waves are usually employed in antenna applications, since the leakage phenomenon is generally associated with high directivity and therefore, their size is not constrained by the operating wavelength, but rather by the directivity specifications [76]. A simple leaky-wave structure can be represented by the schematic illustration of Fig. 3.1. In this figure a hypothetical leaky-wave structure of length L which is fed from right and blocked with anechoic termination in left, lies in the y-direction and radiates in yz-plane through openings of dimension w while d is the unit-cell length for periodic leaky-wave structure.

In the transmission mode (for which a source is emitting sound inside the waveguide), the sound pressure field leaking out of the waveguide, in free-field conditions, follows the form [61]:

$$p(y, z) = p_0 e^{-\gamma y} e^{-j k_z z}, \tag{3.1}$$

45
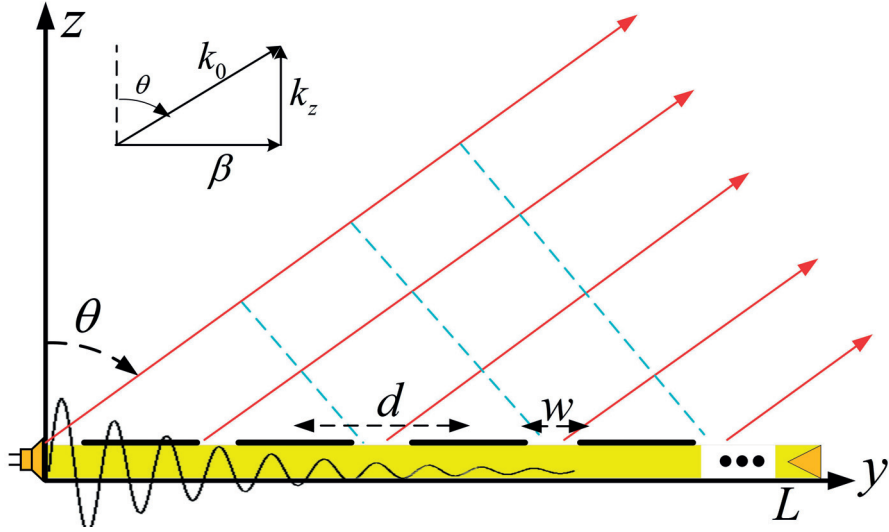
Figure 3.1: Schematic representation of a leaky-wave structure. A 1D waveguide of length L along the $y-$axis with openings of width w and a spatial spacing d. The solid and dashed lines above the structure represent the sound rays and wavefronts respectively.

where $\gamma = \alpha + j\beta$ is the complex propagation constant of the wave along the y direction, and k_z is the propagation constant perpendicular to this direction, related to β by (Fig. 3.1):

$$k_z \simeq \sqrt{k_0^2 - \beta^2}, \tag{3.2}$$

where $k_0 = \omega/c$ is the wavenumber, c being the sound velocity in the host medium, and ω the angular frequency of the wave. Equation 3.2 yields the following observations: if $\beta > k_0$ (the propagating wave inside the waveguide is slower than the sound velocity $v_p < c$), then k_z is imaginary and no sound is radiated outside the structure. Conversely, if $\beta < k_0$ ($v_p > c$, fast-wave), k_z is real and the wave leaks out. Thus, a slow wave, characterized by $\beta > k_0$, is a guided wave, whereas a fast-wave, characterized by $\beta < k_0$, is a leaky-wave. The region of the dispersion diagram where the condition $\beta < k_0$ is satisfied is called the radiation region, and any waveguiding structure presenting a dispersion curve $\omega(\beta)$ inside the radiation region is considered a leaky-wave structure [61]. Using Eq. 3.2, the propagation constant β is linked to the angle θ_0 of the main lobe by:

$$\theta_0 \simeq \sin^{-1}(\beta/k_0). \tag{3.3}$$

For a dispersive medium, the quantity β/k_0 depends on frequency and therefore the main beam angle can vary as a function of frequency, this property is called frequency scanning.

3.2.2 Radiation pattern

For a 1D hypothetical leaky-wave with continuous leakage along the structure (Fig. 3.1 with $w = d$), the radiated sound pressure towards the upper half space reads [77]:

$$p_{rad}(r,\theta) = \int_0^L p_0 e^{-\gamma y} \frac{e^{-jk_0 r}}{2\pi r} dy, \tag{3.4}$$

where r is the distance between the observation point and a position y along the LWA. In the far field, distance r can be approximated by $r \simeq r_0 - y\sin\theta$ (in the phase term $e^{-jk_0 r}$), and by $r \simeq r_0$ for the geometric attenuation $1/2\pi r$, where r_0 is the distance between the origin $(y, z = 0)$ and the observation point. After Eq. 3.4, the radiated sound pressure reads:

$$p_{rad}(r_0,\theta) = \frac{p_0}{\pi r_0} e^{-jk_0 r_0} e^{(-\gamma + jk_0\sin\theta)\frac{L}{2}} \frac{\sinh[(-\gamma + jk_0\sin\theta)\frac{L}{2}]}{-\gamma + jk_0\sin\theta}. \tag{3.5}$$

Using Eq. 3.5 the acoustic pressure radiated by an infinitely long leaky-wave structure ($L \to \infty$) the radiated power pattern is calculated as:

$$|p_{rad}(r_0,\theta)|^2 = \left(\frac{p_0}{2\pi r_0}\right)^2 \frac{1}{\alpha^2 + (\beta - k_0\sin\theta)^2}. \tag{3.6}$$

Let's now consider a periodic arrangement of open holes of width w situated between nd and $nd + w$ as in Fig. 3.1, where $n = 0,..,i$ is the index of the hole and d is the distance between two consecutive holes. The pressure radiated at an observation point (r_0,θ) is given by:

$$p_{rad}(r_0,\theta) = \sum_{n=0}^{N-1} \int_{nd}^{nd+w} p_0 e^{-\gamma y} \frac{e^{-jk_0 r}}{2\pi r} dy$$
$$= \frac{p_0}{\pi r_0} e^{-jk_0 r_0} e^{(-\gamma + jk_0\sin\theta)\frac{w}{2}} \frac{\sinh[(-\gamma + jk_0\sin\theta)\frac{w}{2}]}{-\gamma + jk_0\sin\theta} \sum_{n=0}^{N-1} e^{(-\gamma + jk_0\sin\theta)nd}, \tag{3.7}$$

where N is the number of radiating holes. Comparing Eq. 3.5 and Eq. 3.7, it appears that the arrangement of periodic holes behaves as an array of small radiating apertures. Moreover, the frequency at which the magnitude of the radiated pressure field of Eq. 3.5 and Eq. 3.7 is maximum for a given angle θ verifies Eq. 3.3, provided the length of the antenna or the number (N) of open holes is sufficiently large.

3.2.3 Radiation efficiency

The radiation efficiency of the leaky-wave structure is another important parameter for the design. It can be calculated by considering that the sound power sent at the input of a lossless leaky-wave structure is conserved in addition to the transmitted, reflected and radiated power ($\Psi_{in} = \Psi_{ref} + \Psi_{tran} + \Psi_{rad}$). Defining the radiation power efficiency of the LWA as the ratio of the radiated power to the input power, for a lossless structure with no reflection ($\Psi_{ref} = 0$)

the radiation efficiency is calculated as [76]:

$$\eta_{rad} = 1 - e^{-2\alpha L}, \tag{3.8}$$

where α is the real part of the complex propagation constant ($\gamma = \alpha + j\beta$) and accounts for the leaked power due to the radiation. The leakage factor (α) can be calculated by:

$$\Psi_2 = \Psi_1 e^{-2\alpha l_{12}}, \tag{3.9}$$

where Ψ_1 and Ψ_2 are the average power measured in two different cross sections of the leaky-wave that are separated by length l_{12}.

Using Eq. 3.8 and targeting a radiation efficiency of 90%, it yields:

$$\frac{L}{\lambda_0} \simeq \frac{0.18}{\alpha / k_0}. \tag{3.10}$$

Given a leakage factor (α), which depends on the design of the leaky-wave structure, Eq. 3.10 defines the necessary length to obtain a 90% radiation efficiency. Thus, the structure can be designed based on the framework introduced above to achieve a prescribed radiation efficiency.

3.2.4 Beamwidth

Using the radiation power pattern of Eq. 3.6 the half-power beamwidth $\Delta\theta = \theta_{\frac{1}{2}} - \theta_{-\frac{1}{2}}$ of the structure can be derived as follow:

$$|P_{rad}(\theta_{\pm\frac{1}{2}})|^2 = \frac{1}{2}|P_{rad}(\theta_0)|^2 \quad \longrightarrow \quad \left|\frac{1}{\alpha^2 + (\beta - k_0 \sin\theta_{\pm\frac{1}{2}})^2}\right| = \frac{1}{2}\left|\frac{1}{\alpha^2 + (\beta - k_0 \sin\theta_0)^2}\right|, \tag{3.11}$$

by plugging Eq. 3.3 on both sides of the Eq. 3.11, it is simplified to

$$(k_0 \sin\theta_0 - k_0 \sin\theta_{\pm\frac{1}{2}})^2 = \alpha^2 \quad \longrightarrow \quad \sin\theta_0 - \sin\theta_{\pm\frac{1}{2}} = \frac{\alpha}{k_0}. \tag{3.12}$$

Now, Eq. 3.12 can be written in a single equation as

$$\sin\theta_{+\frac{1}{2}} - \sin\theta_{-\frac{1}{2}} = 2\frac{\alpha}{k_0} \quad \longrightarrow \quad 2\sin\frac{\theta_{+\frac{1}{2}} - \theta_{-\frac{1}{2}}}{2}\cos\frac{\theta_{+\frac{1}{2}} + \theta_{-\frac{1}{2}}}{2} = 2\frac{\alpha}{k_0}. \tag{3.13}$$

Finally, the half-power beamwidth is calculated as

$$\sin\frac{\Delta\theta}{2} = \frac{\alpha}{k_0 \cos\theta_0}. \tag{3.14}$$

Using Eq. 3.2 and Eq. 3.3 and replacing the denominator of Eq. 3.14 by $k_0 \cos\theta_0 = \sqrt{k_0^2 - \beta^2}$ yields the relation between half-power beamwidth ($\propto$ 1/directivity) and frequency for LWA of

given length:

$$\sin\frac{\Delta\theta}{2} = \frac{\alpha}{\sqrt{k_0^2 - \beta^2}}. \tag{3.15}$$

For a structure with constant Leaky factor (α), the directivity depends on $\sqrt{k_0^2 - \beta^2}$ behaviour which tends to zero when $k_0^2 \approx \beta^2$ (the boundaries of the leaky region) and becomes maximum when $\beta \approx 0$. Then, starting from backward the directivity first increases with frequency, having the maximum directivity near broadside, and decreases in the forward direction. Moreover, substituting Eq. 3.10 in Eq. 3.14, the directivity of the acoustic leaky-wave antenna can be derived as a function of length L:

$$\sin\frac{\Delta\theta}{2} = \frac{0.18\lambda_0}{L\cos\theta_0}. \tag{3.16}$$

3.3 Application proposals

Reviewing the mathematical description of the LWA from the previous section reveals that leaky-wave concepts can be used to achieve an antenna having a frequency scanning directive radiation beam. Although, such a capability, on its own, can be of interest in acoustics, to prove LW as a useful acoustic concept, some direct device based application proposals should be presented. Here, based on the near-field radiating mode of the LWA, an acoustic dispersive prism is proposed as an application for acoustic LWA and its frequency dependent refractive index is studied for acoustic waves. Moreover, LWA operating in the far-field receiving mode results in a Single Sensor Direction-Finding (SSDF) device which can be considered as another application.

3.3.1 Challenges in developing acoustic dispersive prism

The optical dispersive prism relies on its dispersive nature (frequency dependant refractive index) and low reflectivity (good impedance match between the prism and the ambient medium). For instance, a shaped glass in air satisfies both conditions for visible light. In acoustics, negligible dispersion [74, 75] and weak impedance matching between the ambient medium and the matter prevents spectral separation and efficient energy transfer. Thus, due to the acoustical nature of materials, as well as design and fabrication difficulties, there is neither any natural acoustic counterpart of the optical prism, nor any artificial design reported so far exhibiting an equivalent acoustic behaviour. These are the two major problems that should be solved to design an acoustic dispersive prism.

3.3.2 Challenges in developing acoustic SSDF

The ability of the human's auditory system to focus selectively to one speaker in a multiple-speaker environment, has attracted the attention of researchers for many years [49]. In such a system the direction of the incoming sound should be estimated in order to locate the sound source and focus on it. Two types of multispeaker listening solutions are available in the literature, the first kind is based on audio features of the sound wave. For example, harmonic characteristics, temporal continuity, onset/offset of signal units can be used to overlapping audio signals into different sources [49]. The drawback of such an approach is that certain audio characteristics of the received signal have to be assumed and analyzed. The second kind relies on multisensor arrays to spatially filter sources. The major disadvantages of the second approach are the need for multiple sensors and system complexity. Recently, Xie et al. have brought the idea of single sensor sound localization into the focus of attention by introducing single-sensor cocktail party listener using acoustic metamaterials, capable of separating broadband signals produced by three separate sources [49]. Here, the challenge to obtain an alternative technique is that, the new device should be designed with a spatial based frequency filtering capability. Hence, depending on the direction of the incoming sound signal a specific component of the audio signal should be received by higher amplitude and the rest of the spectrum should be filtered out. Moreover, the required spatial based frequency filter should exhibit a one-to-one frequency-direction function to ensure that only one direction is assigned to every frequency component of the received signal.

3.3.3 Solution for challenges

To tackle the problem of low dispersion, CRLH TL metamaterials are proposed as a solution. Addressed in the previous chapter, the peculiar properties of metamaterials stem from their dispersion that can be harnessed and used in the design of dispersive prisms. The transmission-line metamaterial concept with positive/negative effective material properties (mass density and bulk modulus) can be a good candidate for acoustic dispersive prisms. As investigated in the previous chapter, acoustic TL metamaterials exhibit frequency-dependent refractive indices with positive/negative values which happen in the RH/LH regions, respectively [22, 57]. The RH behaviour is a consequence of the positive material properties which are intrinsic to natural materials. Additionally, the LH behaviour of the TL metamaterial stems from negative bulk modulus and negative mass density, which are realized with shunt ducts and clamped thin plates, respectively. Hence, having effective dispersive material properties, the acoustic TL metamaterials with positive/negative acoustic refractive indices can solve the problem of negligible dispersion.

To tackle the problem of low transmissivity, the leaky-wave mechanism is used which, as explained in the previous sections, overcomes the impedance mismatch between the CRLH TL and the ambient medium. As in electromagnetics, leaky-wave radiation is the process of acoustic power leakage along a waveguiding structure [65]. Matching the parallel components of the wavevector on the boundary between the leaky-wave structure and the external medium

leads to wave leakage along the waveguide. This phase matching condition happens when the phase velocity of the wave in the waveguide v_p is bigger than sound wave velocity in the ambient medium c. The frequency band where $v_p > c$ is referred to as fast-wave (leaky-wave) region [61]. The gradual energy leakage along a waveguide results in a directive beam radiated into the surrounding medium, with the beam direction depending on the frequency of operation.

The proposed solution based on CRLH TL LWA to solve the problems on the realization of the acoustic dispersive prism, also solves the problems identified to achieve SSDF. Indeed, the CRLH LWA is governed by Eq. 3.3 which is a mathematical representation for a single type of spatial based frequency filter. Moreover, this relation is a one-to-one function which ensures the uniqueness of the solution in estimating the direction of the incoming sound wave based on received frequency components.

By merging a leaky-wave with an acoustic CRLH TL, an appropriate platform for an acoustic prism as well as SSDF is achieved. However, the LH/RH leaky-wave regions should be designed to overlap the desired frequency spectrum, where the prism and SSDF are intended to operate. Moreover, the band-gap should be suppressed, owing to the balanced condition, to obtain the broadside functionality.

3.4 Realization of LWA

Figure 3.2 shows the configuration of the acoustic LWA, which is similar to the one proposed in the previous chapter except that the flanged cylindrical ducts are substituted for the axisymmetric radial open channels. This modification has been proposed firstly, to decrease the viscous loss due to the narrow sound path in axisymmetrical stubs and secondly, to prevent the monopolar behaviour of the axisymmetric structure, which is expected to present an omnidirectional radiation pattern. Indeed, the radiation pattern of such an axisymmetric leaky-wave antenna is 'doughnut'-shaped, with constant directivity around the symmetry axis of the structure. The proposed geometrical modification of the new LWA structure, with open channels facing only the positive z direction, is then intended to achieve directive pattern to sense (radiate) the sound waves only from (to) one half-space. Every unit-cell is composed of a waveguide and a thin plate clamped between two half ducts transversely connected to the waveguide. In order to comply with the unit-cell definition, the first and the last ducts (deep green) of the leaky-wave structure should be half cylindrical ducts, which are replaced by full cylindrical ducts of equivalent physical property but smaller diameters. The input and output cross sections of the waveguide are smaller to ensure the perfect impedance matching between the input and the leaky-wave structure. These alternations to the TL metamaterial configuration of previous chapter decrease the symmetry of the structure from axisymmetry to plane symmetry with respect to yz-plane as shown in Fig 3.2. It should be note that the transverse cylindrical channels still create back lob and in order to prevent this, LWA is flanged to an acoustically hard surface which will be discussed in the corresponding section.

3.4.1 Design platform and acoustic modules

An acoustic waveguide, which naturally conveys the RH behaviour is taken as the host medium. The acoustic mass and acoustic compliance of the waveguide are $m_{TL} = (\frac{\rho}{S} d)$ and $C_{TL} = (\frac{S}{K} d)$ where the ρ and K are mass density and bulk modulus of the inner medium, d is the length and S is the cross section of the waveguide. The 2D view of the proposed structure and circuit modelling of the elements are depicted for two adjacent unit-cells in Fig. 3.3. Neglecting viscous losses, the acoustic waveguide is modelled by a series mass and parallel compliance, represented by the green elements. The blue and purple elements, series compliances and parallel masses, which are responsible for the LH behaviour are implemented using thin plates and transverse ducts, respectively.

In the previous chapter the radiation property of the TL metamaterial due to the open radial
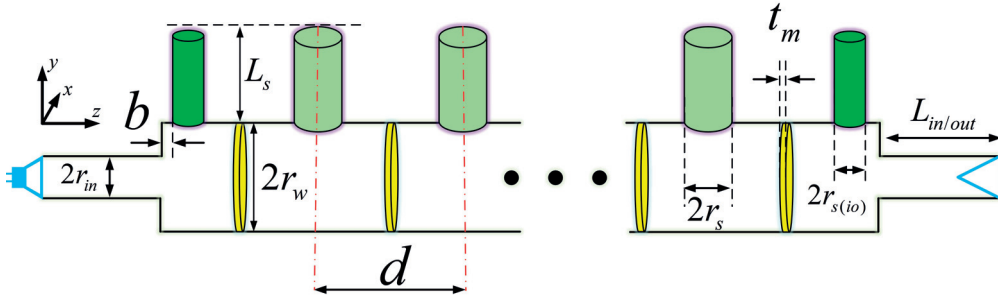
Figure 3.2: Schematic representation of the proposed acoustic leaky-wave antenna. The LWA has been presented in the transmitting mode as an acoustic dispersive prism. Vibrating thin plates (yellow) and open ducts (green) are assembled in an acoustic waveguide with circular cross section. The unit cell is located between the two dashed lines in red.
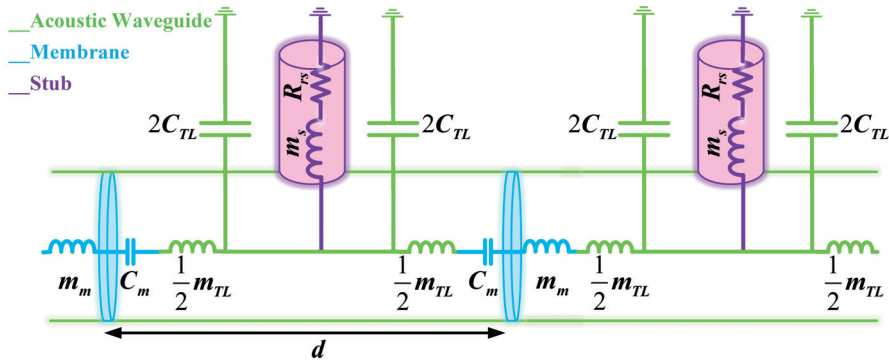
Figure 3.3: 2D configuration as well as lumped element circuit representation of two adjacent unit-cells of the acoustic leaky-wave antenna. The host waveguide and corresponding lumped elements are in green, thin plates and equivalent circuit modules are in blue, ducts and corresponding elements are in purple.

ducts was neglected. It is taken into account in this chapter by adding a radiation resistance to the CRLH TL model as in Fig. 3.4. The series mass (inductance) and parallel compliance
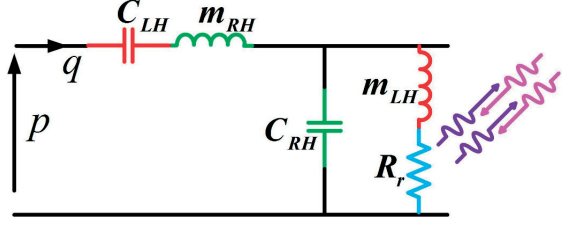
Figure 3.4: TL model of an acoustic leaky-wave structure supporting RH/LH propagation. Acoustic pressure p and volume velocity q are the acoustic analog of voltage and current, respectively.

(capacitance) support the RH propagation while the series compliance and parallel mass support the LH propagation. These four elements provide the basic circuit model for a CRLH TL metamaterial, as studied in the previous chapter, and the radiation resistance represents the leaky-wave nature of the structure and it is added to the circuit model in this chapter. Comparing Fig. 3.3 and 3.4 reveals that the acoustic mass of the thin plate (m_m) and the waveguide (m_{TL}) contribute to m_{RH}, whereas the compliance of the thin plate (C_m) and waveguide (C_{TL}) satisfy C_{LH} and C_{RH}, respectively. Finally, m_{LH} and R_r are accomplished by the open duct (m_s, R_{rs}).

The input acoustic impedance of a transverse cylindrical duct of length L_s terminated by an acoustic load Z_L is:

$$Z_I = \frac{Z_L + j Z_0 \tan(kL_s)}{1 + j \frac{Z_L}{Z_0} \tan(kL_s)}, \tag{3.17}$$

where k is the wave vector. The acoustic characteristic impedance of the medium is defined as $Z_0 = \frac{\rho c}{S}$, where ρ and c are the mass density and sound wave velocity of the medium.

For a duct radiating in a surrounding medium, the acoustic load in the transverse duct termination is: $Z_L = R_L + j X_L$, so Z_I will consist of real and imaginary parts given by Eq. 3.18 and 3.19. By properly choosing k, L_s and $S = \pi r_s^2$ (cross section of the transverse duct), the parallel mass and radiation resistance values can be tuned. Represented with blue resistor in Figure 3.4, the total resistance of the stub which contributes to the radiation is given by (see Appendix B)

$$R_{rs} = \Re(Z_I) = \frac{R_L \tan^2(kL_s) + R_L}{\frac{R_L^2 \tan^2(kL_s)}{Z_0^2} + \left(1 - \frac{X_L \tan(kL_s)}{Z_0}\right)^2} \tag{3.18}$$

and the mass representing the open duct is calculated as

$$m_s = \Im(Z_I) = \frac{-\frac{X_L^2}{Z_0} \tan(kL_s) - \frac{R_L^2}{Z_0} \tan(kL_s) + Z_0 \tan(kL_s) - X_L \tan^2(kL_s) + X_L}{\frac{R_L^2 \tan^2(kL_s)}{Z_0^2} + \left(1 - \frac{X_L \tan(kL_s)}{Z_0}\right)^2}. \tag{3.19}$$

The value of R_L and X_L for a flanged cylindrical open stub of radius r_s is given by

$$Z_L = Z_0 [\frac{1}{2}(kr_s)^2 + j\frac{8}{3\pi}kr_s]. \tag{3.20}$$

The series compliance can be implemented with a thin plate, clamped on its edges. The vibrating thin plate physically behaves as a compliance (capacitance) and mass (inductance), at below and above first resonant frequency, respectively. The behaviour of the thin plate depends on its radius r_w, thickness t_m, Young modulus E, Poisson's ratio v and mass density ρ_m. For a clamped circular thin plate with radius a the acoustic impedance is (see Appendix C):

$$Z_m = j\omega m_m + \frac{1}{j\omega C_m} = -j\omega M \frac{I_1(k_m r_w) J_0(k_m r_w) + J_1(k_m r_w) I_0(k_m r_w)}{I_1(k_m r_w) J_2(k_m r_w) - J_1(k_m a) I_2(k_m r_w)} \tag{3.21}$$

where k_m is the wave number in the thin plate and it is given by $k_m^2 = \omega\sqrt{\frac{\rho_m t_m}{D}}$ and D is the flexural rigidity of the thin plate that is defined by $D = \frac{E t_m^3}{12(1-v^2)}$ and $M = \frac{\rho_m t_m}{S}$. If the proposed unit-cell is periodically arranged and the homogeneity condition $d < \frac{\lambda}{10}$ is satisfied, a CRLH TL LWA is achieved.

3.4.2 Design principle

The acoustic LWA is modelled with five main circuit elements: L_{RH}, L_{LH}, C_{LH}, C_{RH} and R_r, where subscripts LH and RH represent left hand and right hand elements respectively as in Fig. 3.4. The aforementioned elements are linked to physical dimensions and material properties r_w, r_s, d, L_s, t_m, ρ_m, E_m and v_m (Fig. 3.2). The last four parameters (the thickness and material properties of the thin plate) are fixed and restricted by the available materials in the market. The only free parameter in hand to define the impedance of the plate is r_w which will be fixed with three other geometrical parameters (d, L_s and r_s) in the design process.
In CRLH TL LWA structure the transition frequency ω_0 where the transmission line character changes from LH to RH is controlled by

$$\omega_0 = \frac{1}{\sqrt[4]{L_{RH} C_{RH} C_{LH} L_{LH}}}. \tag{3.22}$$

As the band gap appears due to unbalanced resonances between series and shunt elements deteriorates the LWA radiation in the broadside direction, the balanced condition should be satisfied to suppress the stop band, which is expressed by:

$$\frac{L_{RH}}{C_{RH}} = \frac{L_{LH}}{C_{LH}}. \tag{3.23}$$

Equations 3.22 and 3.23 are the two necessary but not sufficient relations to design acoustic TL metamaterials with no band gap. Two more equations are needed to define four main circuit elements of the CRLH in Fig. 3.4 and one more to define the value of leaky-wave radiation (R_r).

Thus, the matching between input port and the CRLH TL to decrease the reflected power, the bandwidth of leaky-wave (fast wave region bandwidth), and the radiation rate (leakage rate) are usually the most important factors which allow designing acoustic leaky-wave structure. Using the circuit model of Fig. 3.4 and applying Floquet periodic boundary conditions the values of $\beta_B(f)$, $\alpha_B(f)$ and Z_B, which set the bandwidth, the radiation rate and the reflection coefficient of leaky-wave respectively, are found as a function of the circuit elements [61] (see Appendix F),

$$\beta_B(f) = \Im\left[\frac{1}{d}\cosh^{-1}\left(\frac{T_{11}+T_{22}}{2}\right)\right] \tag{3.24}$$

$$\alpha_B(f) = \Re\left[\frac{1}{d}\cosh^{-1}\left(\frac{T_{11}+T_{22}}{2}\right)\right] \tag{3.25}$$

$$Z_{B_\pm} = \frac{-2T_{12}}{(T_{11}-T_{22})\mp\sqrt{(T_{11}+T_{22})^2-4}} = \frac{(T_{11}-T_{22})\pm\sqrt{(T_{11}+T_{22})^2-4}}{2T_{21}} \tag{3.26}$$

where $(T_{11}, T_{12}, T_{21}, T_{22})$ are the elements of the transmission matrix $[T]$ that, in the case of Π-circuit model of Fig. 3.3, is given by (see Appendix D)

$$[T] = \begin{pmatrix} T_{11} & T_{12} \\ T_{21} & T_{22} \end{pmatrix}_\Pi = \begin{pmatrix} 1+\frac{Y^p Z^s}{2} & Z^s \\ \frac{Y^p}{4}(1+Y^p Z^s) & 1+\frac{Y^p Z^s}{2} \end{pmatrix} \tag{3.27}$$

and Z^s and Y^p are the total series impedance and parallel admittance of a unit-cell, respectively. Equations 3.17 - 3.27 can be used to set the design and the optimization procedure to find the values of circuit elements in Fig. 3.3 and finally, Eq. 3.17 - 3.21 are used to design the real prototype of Fig. 3.2.

3.4.3 Geometrical configuration

As explained in previous sections, the behaviour of the LWA as a dispersive structure depends on its dispersion relation ($\beta - f$ curve) and consequently, it is conditioned by the material properties and geometrical dimensions of the structure. Hence, based on the design procedure introduced for CRLH TL in the previous chapter and adapted to LWA structure in the last section, an acoustic LWA composed of 10 unit-cells and with an approximate length of $2\lambda \simeq$ 40cm (including the input and output extremities) is designed. Figure 3.5 illustrates a 2D schematic representation of the LW structure and the designed geometrical dimensions and material properties have been listed in Table 3.1 and Table 3.2, respectively.
The same geometrical configuration will be used in the rest of this chapter to demonstrate acoustic prism and acoustic SSDF functionality of LWA. The only difference between the two

applications is the operating mode of (source, or receiver). Moreover, it should be stressed here that, a minor alternation on the plate clamping has been applied in the SSDF experiments compared to acoustic prism, which will be discussed in the respective section.

Table 3.1: Dimensions of the designed structure.

Dimension	Symbol	Value (mm)
Unit-cell length	d	32.00
Duct radius	r_w	9.06
Terminating ducts radius	$r_{\text{in/out}}$	5.54
Terminating ducts length	$L_{\text{in/out}}$	125
Stub radius	r_s	4.00
Terminating stubs radius	$r_{s(\text{io})}$	2.90
Stub length	L_s	12.50
First stub position	b	1.10
Plate thickness	t_m	0.125

Table 3.2: Material properties of the designed structure.

Physical quantity	Symbol	Value	Unit
Mass density of air	ρ	1.188	kg/m^3
Bulk modulus of air	K	137.4	kPa
Celerity of sound in the air	c	340	m/s
Plate Young's modulus	E	2.758	GPa
Poisson ratio	ν	0.34	(-)
Plate mass density	ρ_m	1420	kg/m^3

3.5   Acoustic Dispersive Prism

The proposed acoustic dispersive prism structure, shown in Fig. 3.2, is composed of a fluid-filled rigid waveguide with uniformly spaced, transverse open channels (ducts/stubs) and vibrating thin plates being located between each pair of consecutive ducts, parallel to the cross section of the waveguide. Due to the passive nature of these subwavelength unit-cells, it can be considered a passive, highly dispersive material which exhibits prisming behaviour. To utilize this material, it is assumed that a sound source generates sound from the left input of the structure while the output on the right is terminated by an anechoic condition whilst the sound wave radiates from the transversal stubs. In the rest of this section, the full wave simulation results of the LWA structure, Fig. 3.2 with geometrical dimensions listed in Table
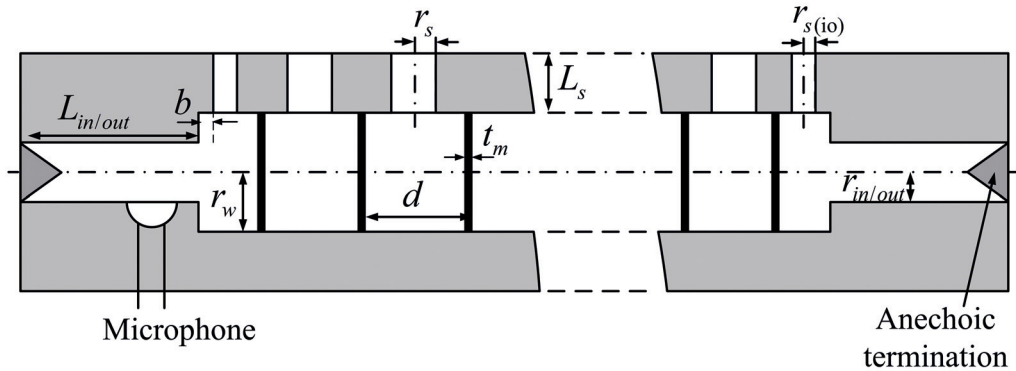
Figure 3.5: 2D schematic representation of acoustic leaky-wave antenna. The structure has been presented in the receiving mode as a single microphone direction finder. A microphone has been inserted at the left termination of the waveguide, and absorbing material (mineral wool) has filled the two terminations.

3.1 and Table 3.2 is presented. The full wave numerical simulations have been carried out using Comsol Multiphysics and the theoretical ones have been developed based on TL theory in Matlab which are compared to experimental data for fabricated prototype assessed in an anechoic chamber.

3.5.1 Numerical results

Method

Numerical simulation of the LWA unit-cell by Comsol:
To retrieve the dispersion relation the full wave simulation is performed using Acoustic-Solid Interaction module of Comsol in frequency domain. To this end one unit-cell of LWA composed of a main duct, clamped plate and transversal duct is placed in the standing wave tube as a Device Under Test (DUT), where (T_{11}, T_{12}, T_{21}, T_{22}) parameters of the unit cell is derived using [T] matrix retrieval method based on four microphone measurement setup [78] and Eq. 3.24 is used to find the dispersion relation ($f - \beta$).

Numerical simulation of the LW full structure by Comsol:
In order to decrease the numerical cost, the Acoustic-Shell Interaction physics module in frequency domain is used for simulations of the full structure. The open end of the stubs are flanged to an acoustic hard surface and the full structure is simulated in a spherical simulation domain bounded by Perfectly Matched Layer (PML) to realize non-reflecting boundaries. First, the leaky-wave input and output at the left and right sides are set to radiation boundary condition to ensure reflectionless conditions, moreover, the incident acoustic pressure is applied to only one port (left port as input). Then, the scattering matrix [S] of the full structure is numerically calculated using a 4-microphones measurement procedure [78], by numeri-

cally measuring the pressure field in 2 distinct points near the input and output of the LW structure (see Appendix E). Moreover, the near-field and far-field radiation pressure field can be evaluated in transmitting mode.

Evaluation of the analytical results based on TL theory using Matlab:
The TL model of the structure is numerically evaluated based on circuit model of Fig. 3.3 in Matlab. The Π-circuit model of the unit cell is developed, and the [T] matrix of one unit-cell is evaluated. Then the dispersion diagram as well as other characteristic parameters of the unit cell are computed using Eq. 3.24 - 3.27. Cascading 10 unit cells with $[T]_{\text{unit-cell}}$, the total transmission matrix of the full structure is calculated ($[T]_{\text{total}}=[T]_{\text{unit-cell}}^{10}$) and it is converted to scattering matrix ($[T]_{\text{total}} \rightarrow [S]_{\text{total}}$) to obtain the reflection and transmission coefficients of the structure.

Results
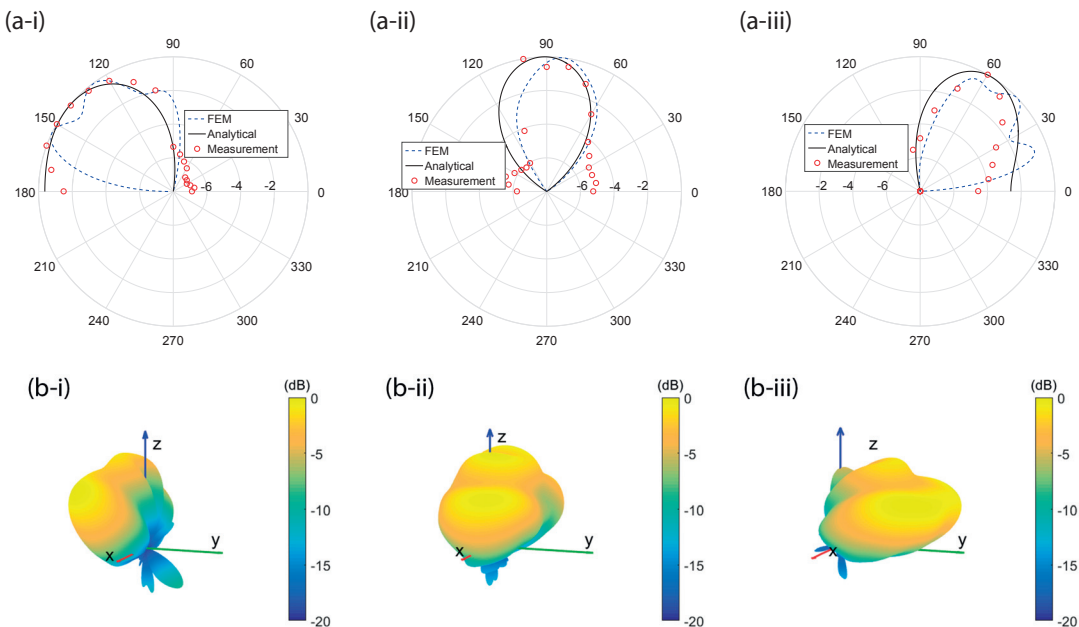
Figure 3.6: (a) The polar representation of the far-field radiation pattern of the structure in the yz-plane for 3 distinct frequencies: (a-i) 900 Hz, (a-ii) 1000 Hz and (a-iii) 1100 Hz. Each radiation pattern has been normalized to its maximum and then levelled to 8 dB. b) Maximum-normalized 3D far-field radiation patterns of the structure, extracted from Comsol simulations, provide information about the directivity of the structure as an acoustic antenna: (b-i) 900 Hz, (b-ii) 1000 Hz and (b-iii) 1100 Hz.

Figure 3.6 depicts the far-field radiation pattern of the structure, $20\log|\frac{p}{p_{max}}|$ where p is the far-field radiated pressure, obtained by full wave numerical simulation for the acoustic prism

along the y−direction and fed from the left $(-y)$, in 3 different frequencies: (a,b-i) At 900 Hz, the structure operates in the LH region, which corresponds to negative values of refractive index and radiates in the backward direction. (a,b-ii) At 1000 Hz, when $f - \beta$ curve crosses $\beta = 0$, the structure have near-zero effective mass and bulk modulus and consequently zero refractive index, which results in broadside radiation. (a,b-iii) At 1100 Hz, which lies in the RH region and corresponds to a positive refractive index and the structure radiates in the forward direction. Figure. 3.6a gives a polar representation in the yz-plane, which compares the radiation patterns derived using FEM, theoretical model of Eq. 3.7 (the value of γ is retrieved using TL method) and experimental data. These figures confirm that all three methods qualitatively agree, although small discrepancies between FEM and analytical method is noticeable. Indeed, the theoretical relation of Eq. 3.7 is based on 1D model, whereas the FEM considers a 3D geometry which might result in disagreement between actual distribution of pressure field inside the waveguide as in FEM and in the analytical model of Eq. 3.1, and consequently, discrepancies in the far-field radiation pattern. Figure. 3.6b represents the 3D radiation pattern of the structure. It shows that, by increasing the frequency of the sound source, the radiation pattern actually scans the upper hemisphere from backward to forward. The amplitude of the radiated sound pressure is maximal at a given angle, monotonically varying with frequency, according to Eq. 3.3. Moreover, despite having short length (2λ), the LWA exhibits a directive radiation pattern and it can be improved by increasing the length of the leaky-wave structure which has been mathematically proved by Eq. 3.16.

Figure 3.7 shows the reflection and transmission coefficients of the acoustic dispersive
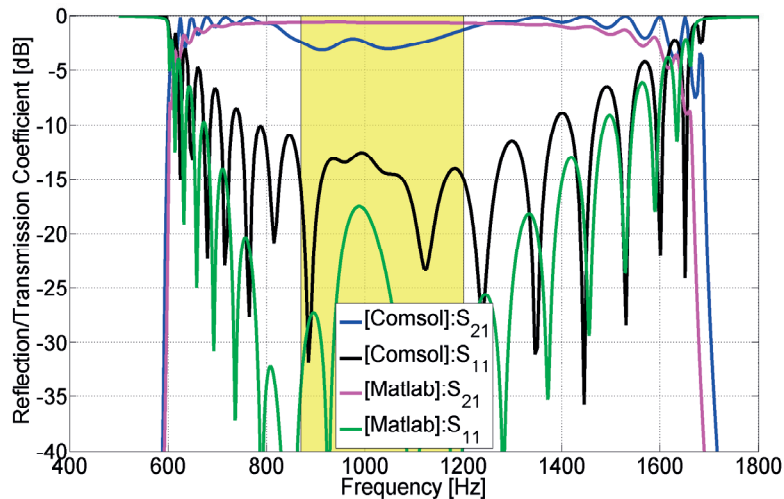
Figure 3.7: The reflection and transmission coefficient of the LWA structure with 10 unit-cells derived using four microphone measurement method by Comsol and TL theory by Matlab.

prism in the frequency range of 800 Hz - 1300 Hz, obtained using TL modeling as well as numerical simulation. The reflection coefficient of the structure is below -10 dB in the frequency band of interest, that is to say less than 10% of power is reflected back to the source. This value can be compared to a glass/air interface, where about 4% of the incident power

is reflected back. However, due to the short and finite length of the structure with 10 unit-cell, which is merely 1λ (at $f_0 = 1$kHZ) without taking the input and output extremities into account, only a few percentage of the input power is radiated. The radiation efficiency of the structure can be increased by increasing the number of unit-cells. For a lossless structure, the distribution of power and radiation efficiency are formulated by $P_{\text{Radiation}} = P_{\text{Input}} - P_{\text{Reflection}} - P_{\text{Transmission}}$ and $\eta = \frac{P_{\text{Radiation}}}{P_{\text{Input}}}$ respectively. Thus, the lower $P_{\text{Reflection}}$ and $P_{\text{Transmission}}$, the higher the efficiency (η).

While a low reflection is ensured by impedance matching at the waveguide input, the radiated
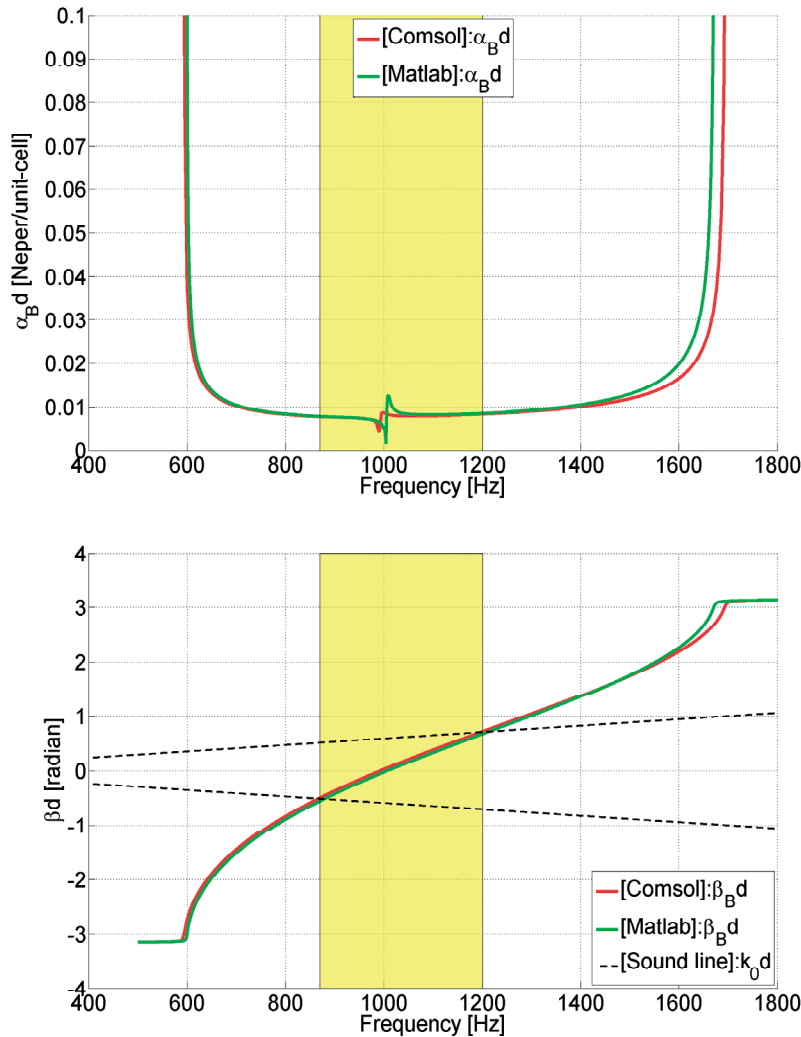
Figure 3.8: Bloch parameters for one unit-cell of the LWA (top) αd represents the leakage rate for one unit-cell. (bottom) Dispersion diagram of one unit-cell. The fast wave region where the wave leaks out of CRLH TL has been highlight.

power to the ambient medium depends on the amount of leaked energy. Consequently, radiation power depends on the length of the structure as well as the leakage rate (α_B) shown

in Fig. 3.8 (top). As the leakage happens through the ducts, increasing the number of the unit-cells will result in a higher radiation efficiency and for the later, the higher the value of αd, the greater the leaked power. However, very high values of α are not appropriate due to the loss of power in the first few unit-cells. Very small values of α are not appropriate either due to the need for longer structure to achieve reasonable radiation efficiencies and a compromise between two should be devised.

In the previous chapter, it was explained that the dispersion diagram $(f - \beta)$ of the CRLH unit-cell is composed of five distinct regions may be identified, namely the LH guided and the LH leaky regions, the band-gap, the RH leaky and the RH guided regions. As the LWA operates in both LH/RH leaky regions, the structure should be designed so as to discard the band gap region by ensuring balanced condition between RH and LH resonances. Moreover, suppressing the band gap enables the structure to radiate at broadside and to achieve near zero refractive index. Figure 3.8 (bottom) shows the dispersion diagram of the proposed structure for the balanced case (without band-gap) with a continuous transition between LH and RH region. The fast-wave region, where the phase velocity of the wave in the LWA is higher than the speed of sound in the ambient medium and leakage occurs (highlighted), is between the values of frequencies (f) for which $\beta_B d$ and $\pm k_0 d$ are crossing. This is situated between 800 Hz and 1300 Hz, which corresponds to wavelength range of 26 cm - 42.5 cm. In the fast wave region, the energy leaks out due to the phase matching at the interface between the LWA and the ambient medium. Hence, extracting $\beta(f)$ in the fast wave region from the dispersion diagram of Fig. 3.8 (bottom), and plugging it into Eq. 3.3, reveals the direction of radiation as a function of the frequency.

Figure 3.9 depicts the data processed from full wave simulation and TL modelling (the
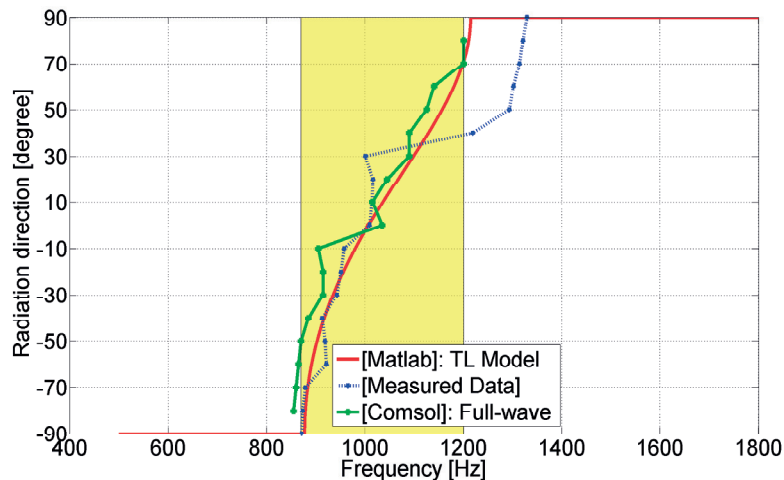
Figure 3.9: Numerical simulation, analytical TL model and experimental results of the radiation direction versus frequency for acoustic LWA.

expected trend) as well as measurements for radiation direction versus frequency. It is seen that the radiation direction, which only happens in the highlighted region, is a one-to-one

function of frequency. That is each frequency in the spectrum only radiates to specific direction which is one of the required criteria to achieve dispersive prism. The numerical results of Comsol and analytical results of TL theory are in qualitative agreement and both follow the same trend. Small discrepancies are observed near the transition frequency from RH to LH (1000 Hz). This can be due to the inaccuracies in TL modelling to fully take the plate vibration and radiation effect into account, as well as meshing problems in numerical simulations and using approximate model of Acoustic-Shell Interaction module instead of Acoustic-Solid Interaction physics module in Comsol.

3.5.2 Experimental validation

Method

The structure is fabricated by stacking 10 unit-cells, which are assembled using four screws located at the corners as shown in Fig. 3.10. The fabricated prototype is composed of 9 identical unit-cells of length 32 mm and two half unit-cells in the extremities (input/output). For impedance matching purpose, the radius of the input/output is different than the other unit-cells. Moreover, they are designed to be longer to ensure single mode excitation. Every unit-cell (green frame in Fig. 3.10) is assembled to the adjacent unit cell with a thin plate clamped in between using 4 screws. Two of the screws are used for alignment propose and the other pair for adjusting the clamping of each thin plate to the two adjacent unit-cells. Unit-cells are machined out of aluminium blocks. DuPont™ Kapton FPC is used for the thin plate. To ensure the clamping criteria of the thin plate, the resonant frequency of the last assembled thin plate is checked at each assembling stage. For this, step-by-step assembly process of the structure is simulated in Comsol and the velocity of the thin plate is normalized to a reference signal (input pressure). At each step n of the tuning process, the frequency response function v_n/p_{in} is measured, where v_n and p_{in} are the nth thin plate velocity and front pressure. Then, the achieved resonance frequency is compared to the one specified by Comsol simulations. According to this measurement, the tension of the thin plate is tuned using the four screws until the desired resonance frequency is achieved for each thin plate.

 Note:
The purpose of this section is to experimentally demonstrate the acoustic prism capability of the LWA and therefore the structure should be measured in the transmitting mode. That is, a sound source should be inserted in one extremity of the LWA and the resulting near-field or far-field sound pattern should be measured by a microphone in front of the LWA. However, due to the small radius of the LWA input, which makes the sound feeding and consequently measurement process cumbersome task, the structure has been measured in the receiving mode and by reciprocity, the measured data has been converted to transmitting mode radiation pattern of the LWA. For the white noise produced by a loudspeaker the spectrum of the received signal will depend on the direction from which the signal is received. Hence, by recording the received sound spectrum versus the direction of arrival from endfire to backfire
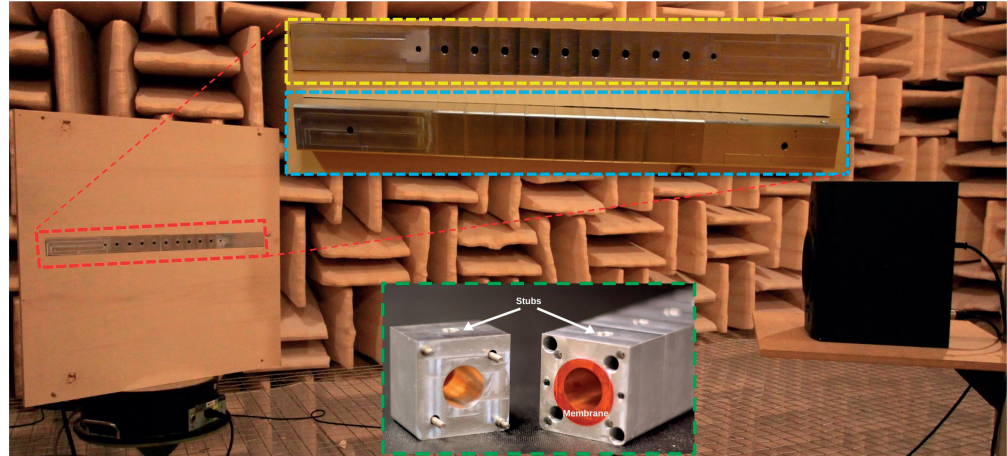
Figure 3.10: Fabricated prototype mounted on a wooden panel and experimental set-up in anechoic chamber.

and then, tabulating the amount of the received power in a single frequency with respect to the direction from which the received power spectrum has been measured, the far-field radiation pattern for that specific frequency is achieved.

Figure 3.10 shows the experimental set-up to measure the performance of the proposed structure. The full structure (red frame in Fig. 3.10) is mounted on a wooden panel which is fixed to the turntable and an acoustic source (loudspeaker) is placed in front of the wooden panel. Flanging the LWA to an acoustically hard surface, yields two effects. First, the flanged hard surface suppress the back lobes, thus preventing the structure from radiating (receiving) to (from) the back side. Second, it increases the radiated power towards the upper half-space. All the measurement process is done in an acoustic anechoic chamber. The received signal is measured by a microphone which is inserted transversely in an additional hole drilled in the backside of the structure near the input, while the two extremities of the waveguide are filled with a layer of mineral wool to achieve anechoic conditions. A detailed view of the front and back side are shown in yellow and blue dashed frame, respectively. White noise signal is used as source signal and the received power is measured every 10 degrees by rotating the turntable. A second microphone is installed on top of the flanged plate to measure the ambient noise, and for normalization purpose.

Results

Figure. 3.6a gives a polar representation in the yz-plane, which compares the numerically derived radiation patterns versus the experimental data derived by reciprocity, in the receiving mode. Although small discrepancies between numerical and measured results is seen, the qualitative agreement confirms that the fabricated prototype performs the frequency scanning of the radiation pattern. Indeed, it shows that, by increasing the frequency of the sound source from 900 Hz to 1100 Hz, the radiation pattern actually scans the upper hemisphere from backward to forward. To further validate the frequency scanning capability of LWA,

the measured direction of radiation versus frequency has been depicted in Fig. 3.9. AS it is expected, the LWA performance qualitatively follows Eq. 3.3, which is a one-to-one function, although some small divergences at higher frequencies are observed, the frequency-direction trend follow the same pattern.

The mentioned discrepancies, either in radiation pattern or frequency-direction curve are due to the band-gap resulting from the prototype fabrication. The band-gap is the consequence of an unbalanced RH/LH transition, mainly due to the misalignment of the vibrating thin plates resonances. Due to the very high sensitivity of the resonance frequency of the thin plate to the applied stress, the tuning process is difficult and small errors during the assembly of 10 thin plates in series can result in a misalignment of series and parallel resonances, thus creating an undesired band-gap. In addition to the imperfections in fabrications, some sources of error can be also attributed to the measurement process. This includes: misaligned between loudspeaker and the LWA or ambiguity in determining the broadside or 0° direction as a reference direction, uncertainty on the radiation pattern of the loud speaker as a reference source such as titled radiation pattern, possible inaccuracies on the precision of the angular rotation of the turn table or the problems regarding mounting the LWA on a wooden panel and turn table are some in the problems that can be listed. Moreover, the theoretical and numerical results are based on, respectively, a 1D and 3D model in the most perfect condition such as adding PML to avoid any reflections from extremities and perfect sound hard boundary, however in the proposed measurement setup the wool is used as an anechoic termination of the extremities, the wooden panel and aluminium blocks represent the hard surface and the measurement process is done in an anechoic chamber where neither of them are fully perfect conditions.

3.5.3 Discussion

Fulfilled prerequisites to achieve acoustic dispersive prism:
The proposed structure is based on the acoustic TL metamaterial concept with subwavelength unit cells and it can be treated as homogenized material. It is modelled with series mass and parallel compliance supporting the right hand propagation as well as series compliance and parallel mass supporting left hand propagation (Fig. 3.4). Thus, this subwavelength structure exhibits acoustic bandpass filter characteristics allowing the acoustic wave to pass in the working frequency band while filtering the off-spectrum frequency components. Furthermore, because of its dispersive nature, different phase velocities, and consequently distinct refractive indices, are associated with Fourier components of the input signal. Besides, the open, transverse ducts make the structure behave as a leaky-wave antenna which are modelled as parallel acoustic radiation resistances, shunting the TL metamaterial to the static pressure. Although the radiation resistance does not affect the TL metamaterial's function, it physically provides an appropriate condition for leaking acoustic waves towards the direction of radiation, depending on the frequency of the input. Thus, the leaky-wave mechanism favours a radiation direction that depends on the refractive index assigned by the TL metamaterial to each frequency component of the input wave.

Functionality of the acoustic dispersive prism:

Figure 3.11 presents the visualization of the acoustic dispersive prism refraction expressed by the CIE (Commission internationale de l'éclairage) frequency shifted standard observer color matching functions. The acoustic pressure wave in the frequency range of 800 Hz - 1300 Hz, enters the structure on the left side while the output of the proposed acoustic device is expected to mimic the rainbow pattern within the frequency range of the input signal. As the wave travels along the structure, it leaks out through the side openings, radiating towards frequency-mapped directions which are dictated by Eq. 3.3. In the frequency range of 800 Hz - 1000 Hz the structure has a LH behaviour and the output wave radiates in the backward direction (left quadrant). However, between 1000 Hz and 1300 Hz the behaviour becomes RH and the output wave radiates in the forward direction (right quadrant). Indeed, its the dispersive nature of the TL metamaterial along with the directive radiation character of the leaky-wave antenna which allows such a simple structure to fulfil the main prerequisites (high dispersion and transmissivity) to achieve an acoustic dispersive prism.

Features of the acoustic dispersive prism:

The proposed acoustic dispersive prism is smaller than 2λ at $f_0 = 1$kHz. In terms of compactness, it is comparable to small water droplets of diameter 0.01 mm (15λ), which are natural optical prisms. While these small droplets produce rainbows with overlapping colors and poor contrast in optics, the proposed acoustic prism may be designed to achieve a better resolution. Although the proposed acoustic dispersive prism directionally splits the sound wave according to its respective frequency components, a detailed study reveals other interesting features. The highly dispersive nature of the structure unveils a superprism-like behaviour, which leads to an extremely large angular dispersion. For light waves, a superprism sends optical beams with different wavelengths to considerably different angles (in space) and has been used to demonstrate wavelength demultiplexing. Having unit cells smaller than $\lambda/10$, the proposed structure acts as an acoustic superprism and works in the subwavelength regime, unlike its optical counterpart which is usually composed of photonic crystals with larger unit cells. Moreover, the superprism phenomenon is achieved in the audible frequency range (low frequencies), while the electromagnetic counterparts operate in optical frequency bands (high frequencies). In addition to the near-field ability which is led to acoustic prism, the far-field functionality of the structure also uncovers a directive acoustic antenna with frequency-dependent radiation directions which is the intrinsic behaviour of leaky-wave structures and as explained before this property is exploited as single sensor sound source direction finder (SSDF) which will be discussed in details in the following section.

3.6 Single Microphone Direction Finding

Since the Eq. 3.3 is a bijective function within the $[\frac{-\pi}{2}, \frac{\pi}{2}]$ range, there is only one direction angle that can be mapped to a specific frequency component. Then, the structure can be also
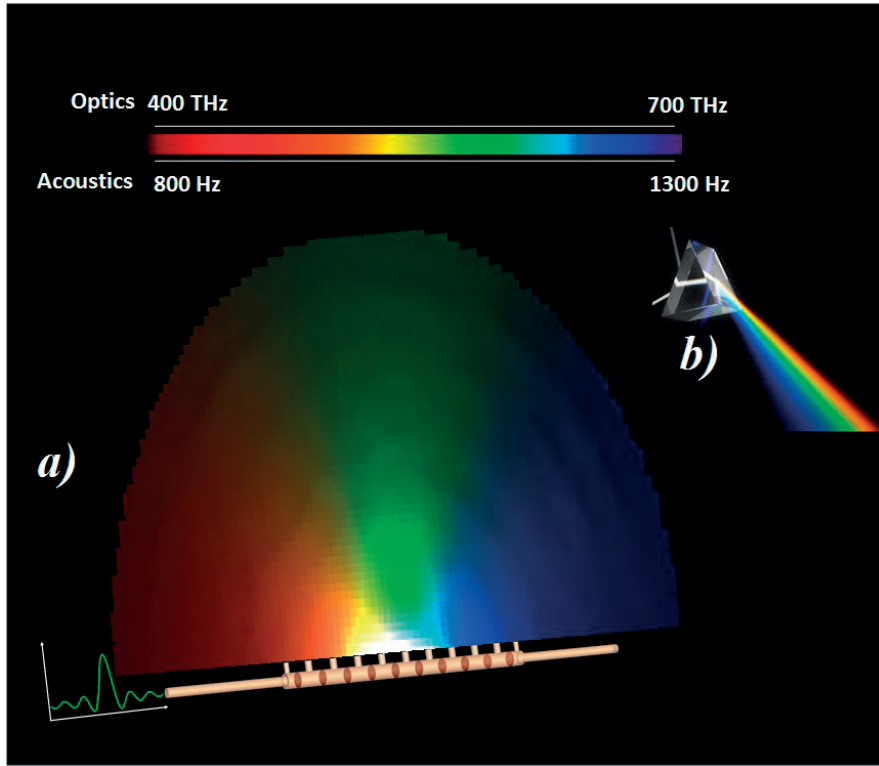
Figure 3.11: (a) Acoustic dispersive prism vs. (b) Optical dispersive prism. Sound wave in the frequency range of 800 Hz - 1300 Hz enters the dispersive prism from the left input and the acoustic rainbow pattern is produced as an output where the different colors represent the Fourier components of the input signal. The figure corresponds to the post processed simulation data extracted from Cosmol Multiphysics and visualized based on CIE curves.

used in reverse as a direction finder device. Indeed, if a broadband noise source is located at a given direction θ, radiating towards the structure, there would be a single frequency which is received with higher amplitude with respect to other components of the signal. By inserting a microphone at one termination of the waveguide, this single frequency with higher amplitude can be measured and mapped to the direction of arrival according to Eq. 3.3. This procedure to find the direction of incoming sound using only one microphone is new to acoustics and can be very practical. Moreover, the direction finding capability can be expanded to any arbitrary signal if prior knowledge of the transmitted signal is given or a second microphone is used for normalization.

Reminding the geometrical configuration

Based on the design procedure explained in the previous section the structure of Fig. 3.5 with 10 unit cells and an approximate length of 2λ is designed, where in practice a microphone is wall-mounted close to one termination and the two terminations presenting anechoic conditions are filled with a layer of mineral wool. As discussed before, the input and output

cross sections of the waveguide are designed smaller than the main duct to ensure perfect impedance matching with the leaky-wave structure. Moreover, the LWA presents a periodic structure, except for the first and last stubs. Indeed, in order to comply with the unit-cell definition, the first and the last transverse ducts should be geometrically half of the other stubs. Nevertheless, in order to improve impedance matching, the first and last stubs' dimensions have been modified, leading to the final dimensions presented in Table 3.1 (the material properties are also given in Table 3.2). Although, the proposed configuration for SSDF is the same as the structure used for acoustic prism, a different technique is used for better clamping of the plates. This alternation, which led in a significant improvement in the measured results, will be discussed in the respective section dedicated for experimental validation of SSDF.

3.6.1 Numerical results

Method

As the configuration of the SSDF and the geometry of the unit-cell which will be discussed in this section are similar to the acoustic prism, therefore, to avoid repetitions, only necessary explanations are briefly provided.

Numerical simulation of the LW full structure by Comsol:
The finite-element simulation (FEM) of the structure is carried out using Comol Multiphysics where the Acoustic-Shell Interaction physics module in frequency domain is used for simulating the full structure. The open end of the stubs are flanged to an acoustic hard surface and the full structure, as well as the acoustic domain represented by a half-sphere are bounded by a Perfectly Matched Layer (PML) to realize non-reflecting boundaries. Contrary to the acoustic prism functionality where the LWA is fed from one of its extremities and the radiated wave is the output of the model, here an acoustic background pressure field as an external incoming sound is applied to the spherical simulation area bounded with (PML) and the sound pressure, computed at the extremity (given position near the input) of the leaky-wave waveguide, is the output of the model. For instance, the background pressure field is applied to the simulation domain every 10 degrees and the spectrum of the received signal is recorded and assessed in the extremity of the LWA waveguide.

Evaluation of the analytical results based on TL theory using Matlab:
The evaluation of the analytical TL model is performed by Matlab where the method is similar to section 3.5.1 and the value of γ is processed from the TL model.
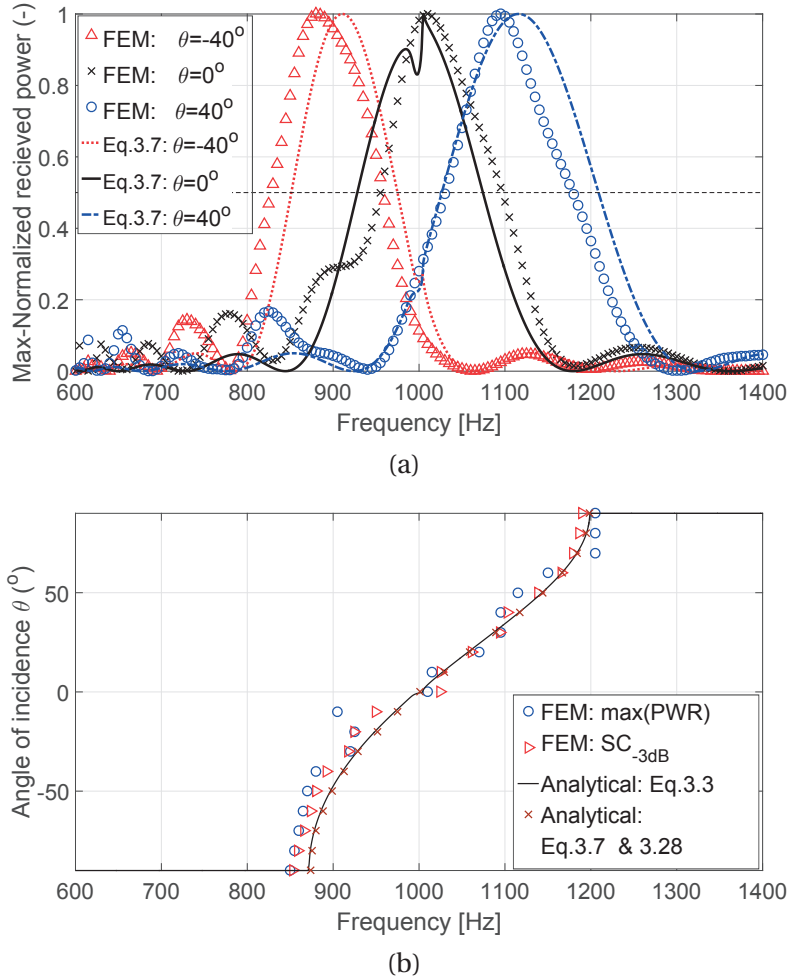
Figure 3.12: (a) Received power spectra sensed by the microphone in the LWA for the different plane wave incident angles (θ). Results of FEM are compared to Eq. 3.7. (b) Frequency-direction curve is presented, every 10°, for FEM and analytical method. Two different strategies are used to derive these data: frequency of the maximum received power amplitude (max(PWR)) versus incident angle and SC_{-3dB} of the received power versus incident angle.

Results

When LWA is used in the receiving mode, as presented in Fig. 3.5, a plane wave sound field with varying directions θ in the $yz-$plane is considered as the input of the model, and the sound power spectrum sensed at the microphone position is the output of the model for each angular direction θ. The normalized sound power spectra are derived from the FEM output data and illustrated in Fig. 3.12a for 3 different angles of incidence. These results are also compared to the ones processed with the theoretical model of Eq. 3.7. Based on reciprocity Eq. 3.7 holds for both transmitting and receiving modes with $w = 2r_{\text{stub}}$, $d = d_{\text{unit-cell}}$, and the value of γ retrieved using the TL method. As discussed before, the small discrepancies can be justified by the differences between the 1D configuration used in the analytical formulations

and the actual 3D configuration of the FEM. Moreover, the value of γ retrieved with the TL modeling might also result in small inaccuracies, which may be another source of errors. It can be seen that, for each incident angle, the power spectra sensed at the microphone position presents a lobe with maximal amplitude at a given frequency and this frequency varies with the angle θ according to Eq. 3.3. Based on the received power spectra of the LWA, the curves of Fig. 3.12b are derived and depict the dependence of frequency of the maximum amplitude of the received power (denoted max(PWR) in the following) with respect to incident angle for FEM and theoretical data. This confirms the functionality of LWA as a single microphone sound source localizer.

It should be noted that the received power spectra present, at angular directions near broadside, a double-bump (see the curve corresponding to the 0° direction in Fig. 3.12a). This phenomenon is due to the occurrence of a band-gap which is the consequence of unbalanced series and parallel resonances in the TL metamaterial design. Indeed, the geometrical dimensions and material properties have been chosen so as to be feasible in practice with readily available materials, which makes the unbalanced condition unavoidable. To overcome the potential ambiguity in the direction estimation, resulting from the secondary lobes observed on the power spectra, a new method for processing the power spectra is proposed. As the antenna behaves as a selective bandpass filter, the spectral centroid ($SC_{\text{-3dB}}$) of the received power can be substituted for the estimation of the frequency at which the maximum power is received. For each angular position, the frequency boundaries ($f_{\text{-3dB,min}}$, $f_{\text{-3dB,max}}$) are first determined as the frequencies for which half of the maximum power is received at the sensing position. Then the 3dB spectral centroid is computed as:

$$SC_{-3dB} = \frac{\Sigma_{f=f_{\text{-3dB, min}}}^{f_{\text{-3dB,max}}} f P(f)}{\Sigma_{f=f_{\text{-3dB, min}}}^{f_{\text{-3dB,max}}} P(f)}. \tag{3.28}$$

This technique may be very useful in presence of noisy experimental data. Therefore, it is validated by comparing the direction vs frequency functions obtained with the FEM and analytical models as illustrated in Fig. 3.12b.

The presented numerical and analytical results confirm that the designed structure is capable of steering towards the direction of the incoming sound signal using only a single microphone. In the following section, these result will serve as a reference and compared with the frequency-direction mapping achieved with an experimental prototype.

3.6.2 Experimental validation

Method

Prototype fabrication and assembly:
An experimental prototype following the design presented in Fig. 3.5 is fabricated by stacking 10 unit-cells made of aluminium, as illustrated on Fig. 3.13a. Contrary to assembly of acoustic prism, here to assemble the full structure, each plate (DuPont Kapton FPC) is glued on a 3D

(a)

(b)

$D_1 = 18.12mm$

$D_2 = 28.5mm$

$a = 41mm$

$h_1 = 500\mu m$

$h_2 = 250\mu m$

(c)
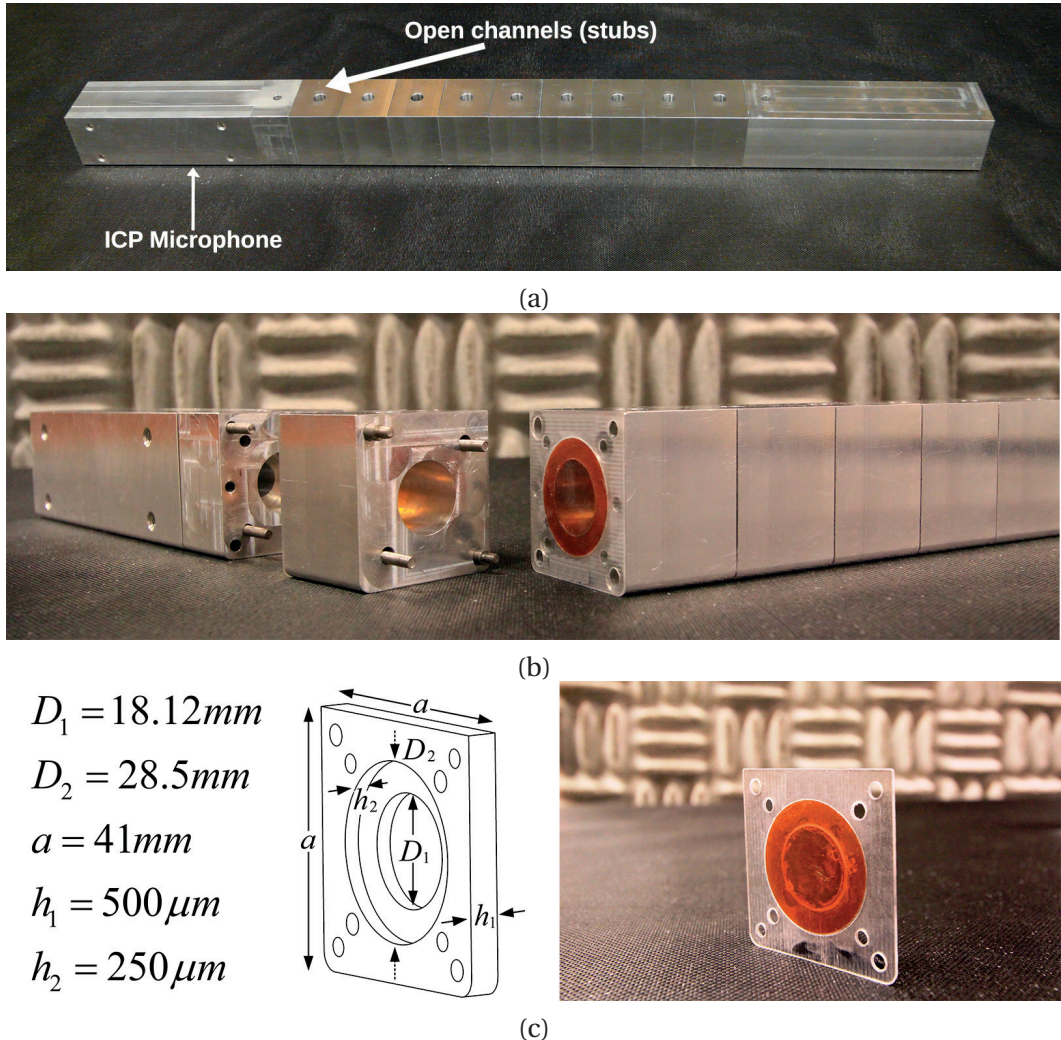
Figure 3.13: (a) Picture of the fabricated prototype: the holes on the top side correspond to the open channels (stubs), the ICP microphone used as the LWA single sensor being flush-mounted at one termination, on the opposite side (not visible here). (b) Picture of a disassembled LWA prototype, presenting a plate glued to a support which is sandwiched between two unit cells. (c) Picture of the plate support as well as its schematic representation and geometrical dimensions.

printed support, and squeezed between two adjacent unit-cells using four screws as in Fig. 3.13b. The 3D printed support in Fig. 3.13c is designed to decouple the stress applied on the plate by the adjacent unit-cells. Instead, uniform gluing of the plate over the support ensures uniform stress over the circumference of each plate, and almost uniform clamping condition can be achieved for all plates. This method is more practical and straightforward compared to the one relying on individual alignment of resonant frequency of each plate proposed in the previous section. To complete the assembly of the prototype, the two extremities of the fabricated structure are filled with layers of mineral wool to simulate anechoic boundary con-

(a)

(b)
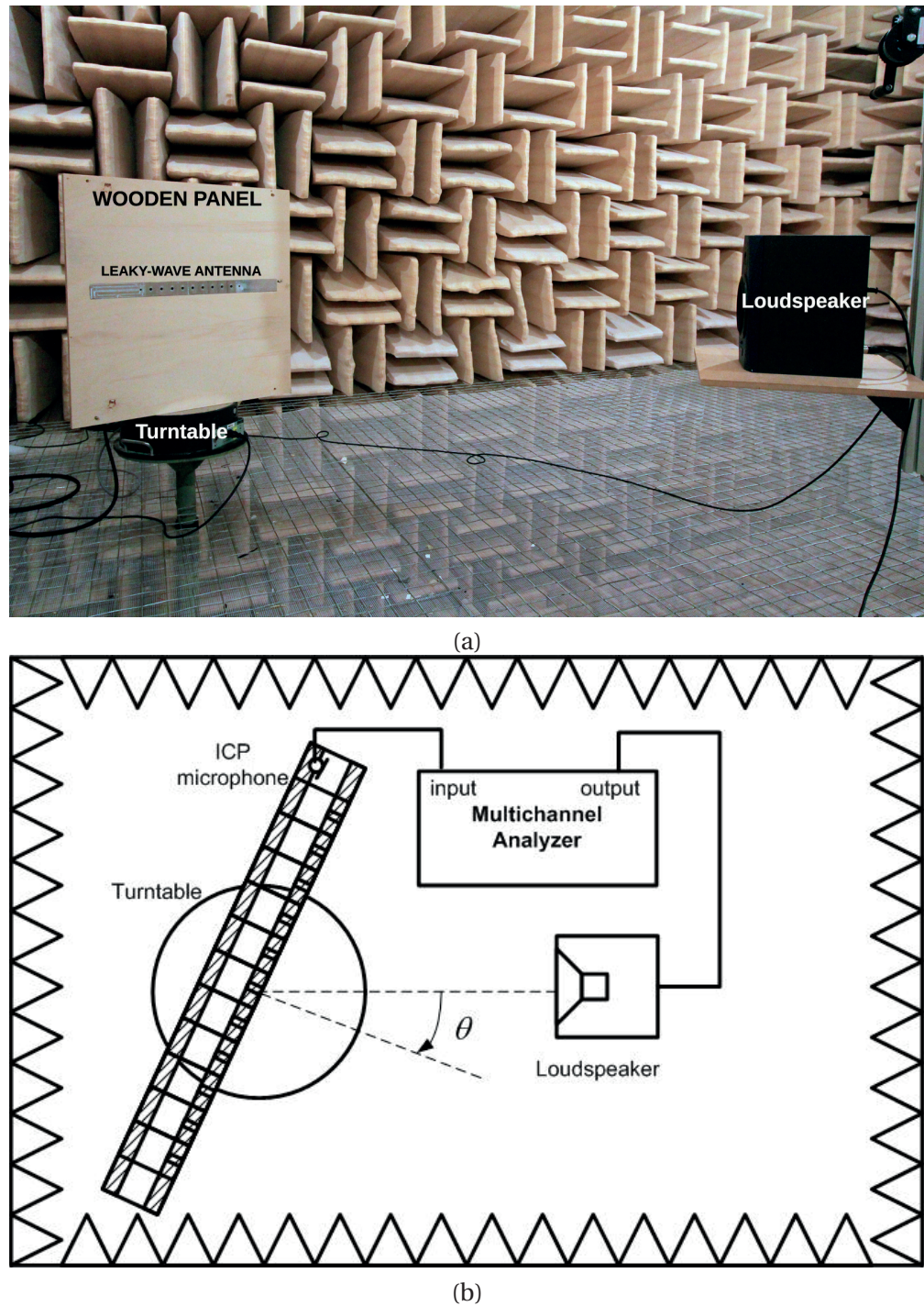
Figure 3.14: (a) Measurement setup in the anechoic chamber: the leaky-wave antenna is wall-mounted to a wooden panel, suppressing the back lobe and acting as a support, the whole being fixed on a turntable in front of a loudspeaker used as a sound source. (b) Schematic description of the experimental setup.

ditions, and a PCB Piezotronics 130D20 ICP microphone is flush-mounted at one termination of the structure, and used as the single sensor of the LWA. Finally, it is flanged to a wooden panel of dimensions 50 cm × 50 cm, which mimics the hard boundary conditions considered in the FEM model, while suppressing the back lobes.

Measurement setup:

To measure the performance of the fabricated prototype as a single-microphone direction finding, the LWA mounted on a panel is installed on a turntable (Bruel & Kjaer Type 5960, remote-controlled through a controller Type 5949) in an anechoic chamber, and a loudspeaker (sound source) is installed at 4 m from the center of the leaky-wave, as illustrated in Fig. 3.14. The sound generation and the microphone signal acquisition are operated with a Bruel & Kjaer Type 3160 Pulse multichannel analyzer. The FFT analysis is set on 3200 points within the [600 Hz-1400 Hz] frequency range, thus a frequency resolution of 0.25 Hz, and the signal generator delivers a sweep sine signal within the specified frequency range to the loudspeaker.

Results

For each angular position of the turntable, the power spectrum $P(f)$ of the received signal is processed. Figure 3.15a presents the normalized power spectra measured for different orientations of the turntable. As explained before, the main lobe observed on the power spectrum measurement presents a central frequency, that can then be mapped to the orientation of the turntable. It is noticeable that, for each orientation, the antenna presents a relatively narrow beam width, except around 0° where two lobes are visible. This can be explained by a misalignment of the elements of the LWA (plates and stubs), resulting in the occurrence of a band-gap around the transition frequency and emergence of second lobe in the received power spectra.

With a view to assessing the SSDF functionality of the LWA, the spectral centroid and max(PWR) are derived from the power amplitude received by the ICP microphone for each orientation θ of the turntable, and compared to the theoretical value obtained from Eq. 3.3. Figure 3.15b presents the frequency-direction curve of the LWA which confirms the good agreement between theoretical and measured data. Moreover, in order to overcome the ambiguity resulting from the emergence of a second lobe near the broadside direction, the SC_{-3dB} is derived from experimental data using Eq. 3.28 and is plotted against the angular position of the turntable. As expected, the SC_{-3dB} derived from the measured data shows smoother variations compared to the max(PWR), and is in closer agreement with the theoretical curve.

3.6.3   Discussion

The results of Fig. 3.12b and Fig. 3.15b show that the theoretical, FEM and experimental data, present monotonically-increasing directions θ as a function of frequency f, which can then

(a)

(b)
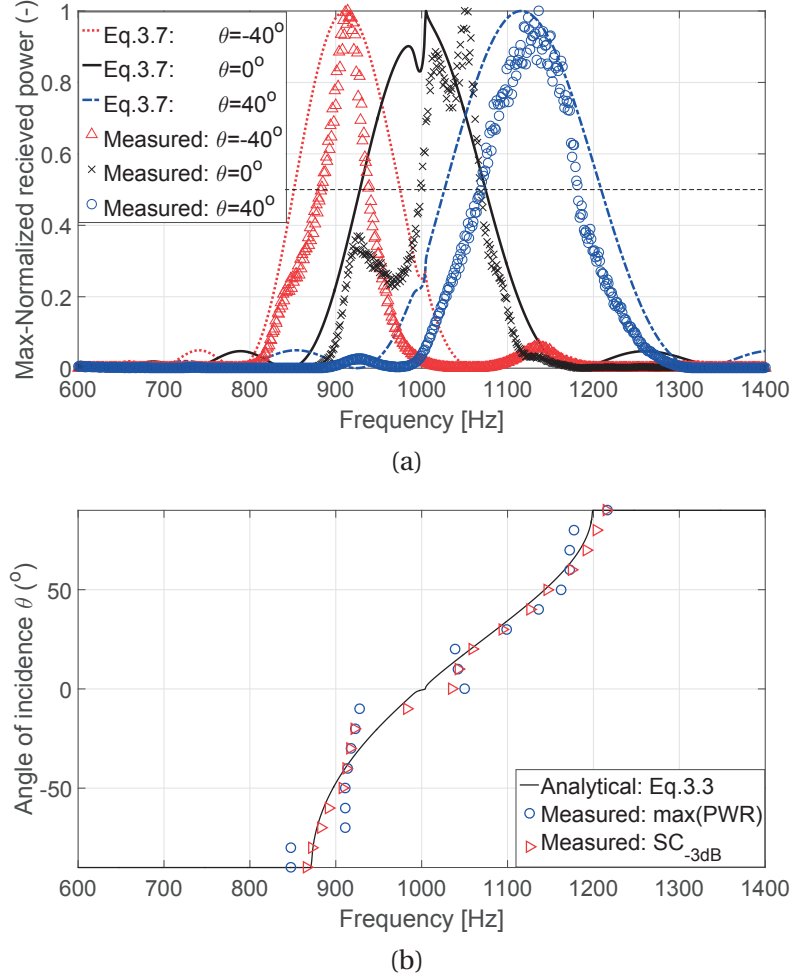
Figure 3.15: (a) Measured power spectra sensed by the microphone in the LWA for different angular positions of the turntable θ. (The experimental data are shown every 5 samples). Experimental results are compared to theoretical values of Eq. 3.7. (b) Frequency-direction curve of measured data is presented every 10° derived by two different methods: frequency of the maximum received power amplitude versus incident angle and received power SC_{-3dB} versus incident angle. The analytical expected curve is also presented for comparison.

be used for single-microphone direction finding applications. Furthermore, the frequency-direction mapping obtained with experimental and simulation data follows the theoretical trend, which also validates the theoretical formulas. The small discrepancies observed between measured data and the theoretical trend can be explained by two reasons: the first reason might be the differences in the fabricated prototype compared to the optimal design parameters considered in the theoretical formulation, especially the difficulty to ensure perfectly uniform clamped boundary conditions on the plates in the experimental prototype. The second reason might be the differences between the simulation and experimental conditions. Indeed, the imperfect anechoic conditions in the waveguide extremities, as well as the likely

imperfect frequency response of the loudspeaker may significantly differ from the simulation condition. Due to the listed problems and occurrence of second lobe near the broadside (particularly visible in the measured results in Fig. 3.15a, a statistical method of spectral centroid of the data is used to get smoother frequency-direction curves. It should also be emphasized that the presented results have been confirmed with several measurements, after mounting/dismantling of the prototypes, highlighting the robustness of the LWA structure and simplicity of the implementation when plate glued 3D printed frames are used.

3.7 Conclusion

Exploiting the anomalous guided-wave capability of the CRLH TL, studied in the previous chapter, the acoustic CRLH TL LWA was presented in this chapter and its radiation and refraction properties were investigated by introducing two functionality of CRLH TL LWA as acoustic dispersive prism and acoustic single sensor direction finder. The proposed CRLH TL LWA consists of a periodic structure composed of vibrating plates along a waveguide, and side open channels allowing sound leakage along the structure. Each unit-cell is modelled as series mass and parallel compliance (supporting the right-hand or positive index propagation), combined with series compliance and parallel mass (supporting left-hand or negative index propagation). Thus, it behaves as an acoustic bandpass filter. To consider the open end of the transverse ducts, radiation resistances are added in series to the acoustic masses which represent acoustic impedance of the stub. Such an upgrade in the circuit-model make the structure behave as a leaky-wave antenna, allowing the radiation of an acoustic wave to the ambient medium. For the sake of simplicity, the coupling between consecutive stubs is neglected, assuming they are distant enough.

In the transmitting mode and near-field region, the proposed structure shows the prisming behaviour due to its dispersive and radiative nature. Moreover, because of the highly frequency dependent refractive index, the proposed structure can be considered as superprism, where the close frequency components of the sound wave are refracted to large angles in space and apart from each other. In the receiving mode and far-field region, such a device can be used as a single sensor direction finder (SSDF), without resorting to multiple-sensors and beam-steering techniques. It can be seen as an interesting alternative to the state-of-the-art techniques for sound source localization, and may find direct applications to sonar.

Using three different concepts, namely CRLH medium, TL theory and LWA, from electromagnets to propose interesting yet functional devices like acoustic prism and SSDF for sound, leads the inventive mind towards molding the electromagnetic and acoustic LWA to single platform to achieve double functionality. Indeed, both acoustic and electromagnetic LWAs are based on similar physics and they can share the same waveguiding structure as a host medium. This suggests that a conventional (RH) electromagnetic LW radiating in the forward direction can turn into an acoustic LWA with not so much effort. Therefore, the presented results in this chapter may encourage future developments, with a view to merge acoustic/-electromagnetic LWA within the same structure, and proposing a new generation of mixed radar-sonar concepts based on LWA.

In short, this chapter was devoted to two main acoustic wave phenomena: radiation and refraction, which resulted in a new type of acoustic radiator called acoustic LWA. The investigation on the other types of sound-metastructure interaction is continued in the next chapter by covering the reflection in metamaterials and its potential applications.

4 Acoustic Metasurface as Reflectarray Antenna and Carpet Cloak

| Propagation | Guided-wave | Radiation | Refraction | Reflection | Transmission |

This chapter is a modified version of the materials published in Ref. [52] and orally presented in Ref. [79].

4.1 Introduction

Inspiration from electromagnetics:
Metasurfaces, first proposed in the electromagnetic realm, are artificially engineered surfaces composed of subwavelength unit-cells which manipulate the reflected and (or) transmitted wavefronts in a preferred, predefined and unconventional way. The peculiar macroscopic behavior of metasurfaces in response to incident waves led to revisit the laws of reflection and refraction and the generalized Snell's law was proposed to deal with such surfaces [80]. In the realm of electromagnetics, in addition to the wavefront manipulation [81], the functionality of these surfaces has been extended to wave absorption engineering [82], polarization tailoring [83], frequency filtering [84] and metasurface carpet cloaking [85, 86].

Efforts in acoustics:
Recently, the concept of acoustic metasurface has been proposed to manipulate the reflected or transmitted wavefronts of the impinging acoustic wave [87] and other functionalities of such as acoustic matching [88], unidirectional transmission [89, 90], lensing [91], absorbers [42, 92] and cloaking [93, 94] have been proposed.
Shaping wavefronts using acoustic metasurface requires to control the phase of the reflected wave. In several studies on acoustic metasurfaces [95]-[96] the phase control has been achieved using a unit-cell presenting a space coiling structure [97]. Space coiling is a technique where the phase control is done by the accumulation of the phase along the sound path in a labyrinthine-type structure [47]. Thus, the acoustic wave travels an effective acoustic

path to ensure a certain phase lag/lead (compared to predefined reference phase) to the price of relatively bulky unit-cells [98, 99]. Another technique is to use various materials with different refractive indices but similar acoustic impedances [100]. Recently, Helmholtz resonators [101]-[53], membranes [102] and pentamode metamaterials [103] based unit-cells have been proposed as acoustic metasurface unit-cells to control the phase of the acoustic wave. However, most of these studies on metasurface unit-cell designs still suffer from being bulky, having limited bandwidth, high loss, non-uniform reflected wave amplitude and do not present the aptitude for reconfigurability.

Reflection phenomenon in reflectarray metasurface and metasurface carpet cloak:
The two previous chapters were dedicated to the propagation of sound wave in guided-wave structures as well as radiation and refraction phenomena in acoustic metamaterials. In the same way, the sound-metamaterial interaction peculiarities can be studied to manipulate the reflected waves with a view to achieving intriguing yet useful functionalities. To start, it is good to remind that according to the impedance-governed generalized Snell's law of reflection [104], reflector-type metasurfaces are used to manipulate the reflected wavefronts at will and the acoustic impedance of the surface is the controlling factor to engineer the reflection phase, and consequently reflection wavefront. Thus, following a surface impedance design strategy, a unit-cell can be designed, aiming at saving space and providing much thinner geometries than the ones reported so far. To achieve the desired thin acoustic metasurface, lumped element acoustic modules representing acoustic impedances should be proposed with an easily tunable mass/compliance (inductive/capacitive) behavior. Since, the unit-cell is designed following the impedance based approach, designing the total surface acoustic impedance of the metasurface for required applications will be easy and straightforward too. Such a flat surface with inhomogeneous acoustic surface impedance may be used to replace a curved reflector as a secondary antenna or be used for deflecting or concentrating sound. Moreover, the functionalities of acoustic metasurfaces can be extended to acoustic carpet cloaking, exactly like in the electromagnetic counterpart. Since, the detection of an obstacle is achieved by analysing the reflected acoustic waves, by engineering the reflected wavefront the illusion of cloaked obstacle can be achieved. Unlike the bulky transformation type cloaks the proposed surface impedance based strategy is sufficient to design skin-like carpet cloaks and create the illusion of bare ground when an object is covered by such a reflector-type metasurface.

4.1.1 Outline of the chapter

In this chapter the Snell's law is first revisited for inhomogeneous surfaces and the Generalized Snell's law is derived to deal with reflections from structures with surface impedance inhomogeneity. Then, membrane capped cavity is introduced as an ultra-thin uni-cell for surface impedance engineering. Using the proposed unit-cell configuration an acoustic reflectarray metasurface, in analogy with electromagnetic reflectarray antenna is designed. Finally, the proposed reflector type metasurface is leveraged to introduce acoustic metasurface clocking.

4.2 Reflector-type Acoustic Metasurface

Acoustic reflectarray metasurfaces, aiming at manipulating the reflected wavefronts, do not obey the Snell's law at macroscopic level. To mathematically describe these surfaces, the Snell's law should be revisited. In optics this modification has been done using Fermat's principle under the name of Generalized Laws of reflection and refraction [80], while in acoustic it was treated using Green's function under the name of Impedance-governed generalized Snell's law [87]. Here different procedure based on the Fermat's principle is used to derive the generalized Snell's law for acoustic reflector-type metasurfaces.

4.2.1 Fermat's principle

Let's suppose that, a monochromatic acoustic plane wave impinges a lossless, inhomogeneous surface with subwavelength reflection phase discontinuity. According to Fermat's principle,
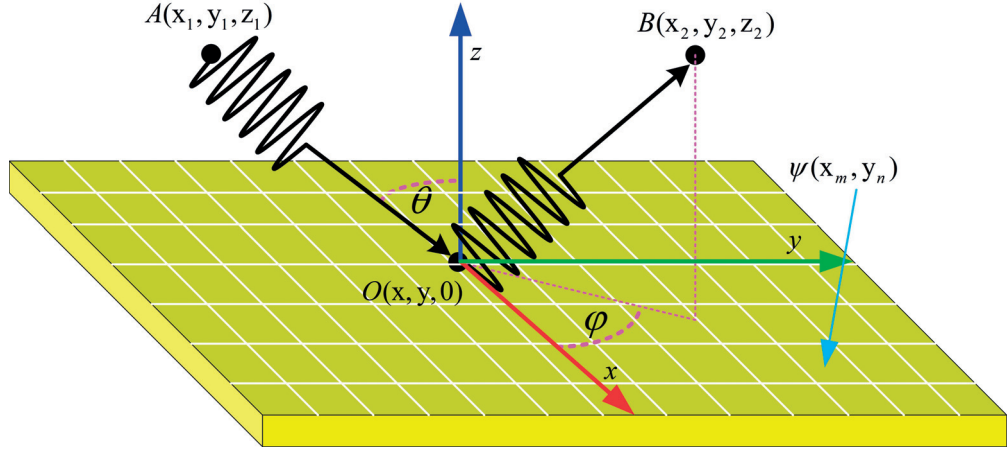
Figure 4.1: Acoustic wave impinges a surface with non-zero phase gradient.

the path travelled between two points A and B by a sound wave is the path that can be traversed in the least time. The mathematical interpretation of the Fermat's principle with the notations illustrated in Fig. 4.1 is

$$\tau_{\text{total}} = \frac{\psi(x, y)}{\omega_0} + \frac{OA + OB}{c},$$ (4.1)

where A is the source location, O the intersection between the ray and the surface, and B observation point. Speed of sound is represented by c, τ is the time and $\psi(x, y)$ is the surface phase function (phase of the reflection coefficient). Using Fig. 4.1, the Eq. 4.1 is formulated in Cartesian coordinate as

$$\tau_{\text{total}} = \frac{1}{c} \left(\frac{\psi(x, y)}{k} + \sqrt{(x - x_1)^2 + (y - y_1)^2 + z_1^2} + \sqrt{(x - x_2)^2 + (y - y_2)^2 + z_2^2} \right).$$ (4.2)

The Fermat's principle dictates that the effective length of the path followed by the wave between two fixed points, A and B should be extremum. This can be mathematically interpreted as finding the critical points of the Eq. 4.2 based on $\frac{\partial \tau_{total}}{\partial x} = 0$ and $\frac{\partial \tau_{total}}{\partial y} = 0$. Therefore, the critical point for the Eq. 4.2 is calculated as

$$\frac{\partial \tau_{total}}{\partial x} = 0 \rightarrow \frac{1}{k} \frac{\partial \psi(x, y)}{\partial x} + \frac{x - x_1}{\sqrt{(x - x_1)^2 + (y - y_1)^2 + z_1^2}} + \frac{x - x_2}{\sqrt{(x - x_2)^2 + (y - y_2)^2 + z_2^2}} = 0 \quad (4.3a)$$

$$\frac{\partial \tau_{total}}{\partial y} = 0 \rightarrow \frac{1}{k} \frac{\partial \psi(x, y)}{\partial y} + \frac{y - y_1}{\sqrt{(x - x_1)^2 + (y - y_1)^2 + z_1^2}} + \frac{y - y_2}{\sqrt{(x - x_2)^2 + (y - y_2)^2 + z_2^2}} = 0. \quad (4.3b)$$

Simplifying the system of Eq. 4.3 and rewriting it in spherical coordinate, the Fermat's principle is summarized as generalized Snell's law for acoustic waves:

$$-\frac{1}{k} \frac{\partial \psi(x, y)}{\partial x} = \sin\theta_r \cos\phi_r + \sin\theta_i \cos\phi_i \quad (4.4a)$$

$$-\frac{1}{k} \frac{\partial \psi(x, y)}{\partial y} = \sin\theta_r \sin\phi_r + \sin\theta_i \sin\phi_i, \quad (4.4b)$$

where ϕ is the azimuth angle with respect to x-axis, θ is the elevation angle with respect to z-axis, k is the wave number and the subscript i and r are indicating incident and reflected wave, respectively. Equation. 4.4 reveals that the gradient of the phase over the surface determines the direction of the reflected wave.

4.2.2 Acoustic surface impedance and generalized Snell's law

If the surface of Fig. 4.1 is discretized into subwavelength rectangles of $d_x \times d_y$ in xy-plane, denoted as unit-cells, then, Eq. 4.4 can be written as,

$$\frac{\psi(x_m, y) - \psi(x_{m-1}, y)}{x_m - x_{m-1}} = -k(\sin\theta_r \cos\phi_r + \sin\theta_i \cos\phi_i) \quad (4.5a)$$

$$\frac{\psi(x, y_n) - \psi(x, y_{n-1})}{y_n - y_{n-1}} = -k(\sin\theta_r \sin\phi_r + \sin\theta_i \sin\phi_i), \quad (4.5b)$$

where m and n are integers and represent the indices of the discretized surface along x and y, respectively. Considering the fact that gradient of the phase over the surface determines the direction of reflected wave and not the value of the phase, then the phase of the first element can be fixed to zero and the recursive Eq. 4.5 is formulated as,

$$\psi(x_m, y) = -kd_x m(\sin\theta_r \cos\phi_r + \sin\theta_i \cos\phi_i) \quad (4.6a)$$

$$\psi(x, y_n) = -kd_y n(\sin\theta_r \sin\phi_r + \sin\theta_i \sin\phi_i). \quad (4.6b)$$

Eventually, the system of Eq. 4.6 can be reformed and presented as a single equation which describes the discretized phase function over the surface for predefined incident and reflected wave angles,

$$\psi(x_m, y_n) = -kd_x m(\sin\theta_r \cos\phi_r + \sin\theta_i \cos\phi_i) - kd_y n(\sin\theta_r \sin\phi_r + \sin\theta_i \sin\phi_i). \quad (4.7)$$

The Eq. 4.7 dictates that to achieve a predefined reflection angle (θ_r, ϕ_r) for a preset incident sound wave in the direction of (θ_i, ϕ_i), the phase of the surface reflection coefficient should be engineered according to ψ.

Since the reflection coefficient of the surface is governed by its acoustic impedance, the phase function of the metasurface can be attributed to the acoustic impedance of the surface. Thus, by properly choosing the acoustic impedance of each unit-cell on the surface, a metasurface with anomalous reflection behavior can be designed. In order to realize a non-zero phase gradient surface to fully control the reflected wave, a unit-cell configuration which can produce full phase range $(0-2\pi)$ reflection coefficient is proposed in the next section where its acoustic impedance is easily tuned by slight change in the geometry.

4.3 Metasurface Unit-Cell

To design a unit-cell which covers the full phase range for reflected waves, an acoustic configuration with both mass/compliance behavior (inductive/capacitive nature) is required. The most straightforward acoustic module with inductive/capacitive reactive part is a Helmholtz resonator, where the cavity presents compliance behavior and the narrow neck represents the mass [101]-[53]. However, Helmholtz resonators are relativity bulky modules and their acoustic behavior highly depends on their dimensions, hence they are not geometrically versatile to cover a flat surface. Moreover, Helmholtz resonators are not potentially suitable for active unit-cell design or to be made tunable and reconfigurable.

4.3.1 Analytical modeling

The proposed metasurface unit-cell is composed of a cubic cavity with acoustically hard walls and a vibrating membrane which is clamped at its edges to the cavity, in which the damping will be first neglected (the effects of damping will be further discussed in the next section). The cavity with subwavelength dimensions can be modeled as acoustic compliance (capacitance):

$$C_b = \frac{V_b}{\rho_{\text{air}} c_{\text{air}}^2}, \quad (4.8)$$

where V_b is the volume of the cavity and $(\rho_{\text{air}}, c_{\text{air}})$ are the mass density and sound velocity of the air, respectively. As discussed in chapter 2 and chapter 3, the membrane contributes to both mass/compliance (inductive/capacitive) behavior depending on its geometrical dimensions, material properties and operating frequency. Clamped rectangular membrane vibrating in its

first mode can be modeled with lumped element circuit model of Fig. 4.2a and the values of m_{ae} and C_{ae} as equivalent acoustic mass and compliance are given by

$$C_{ae} = \frac{1}{(ab)^2} \left(\frac{a^3(1 - v^2)}{\pi^4 E t_m^3 b[1 + \frac{2}{3}(1 - v)(\frac{a}{b})^2 + (\frac{a}{b})^4]} \right) \tag{4.9a}$$

$$m_{ae} = \frac{1}{(ab)^2} \frac{9}{4} \rho_m t_m ab, \tag{4.9b}$$

where (a, b, t_m) are the length, the width, the thickness and (ρ_m, E, v) are the mass density, the bulk modulus and the Poisson ratio of the membrane, respectively (See appendix C for detailed explanations).

Using the transmission line model of Fig. 4.2a, the total acoustic impedance of the proposed
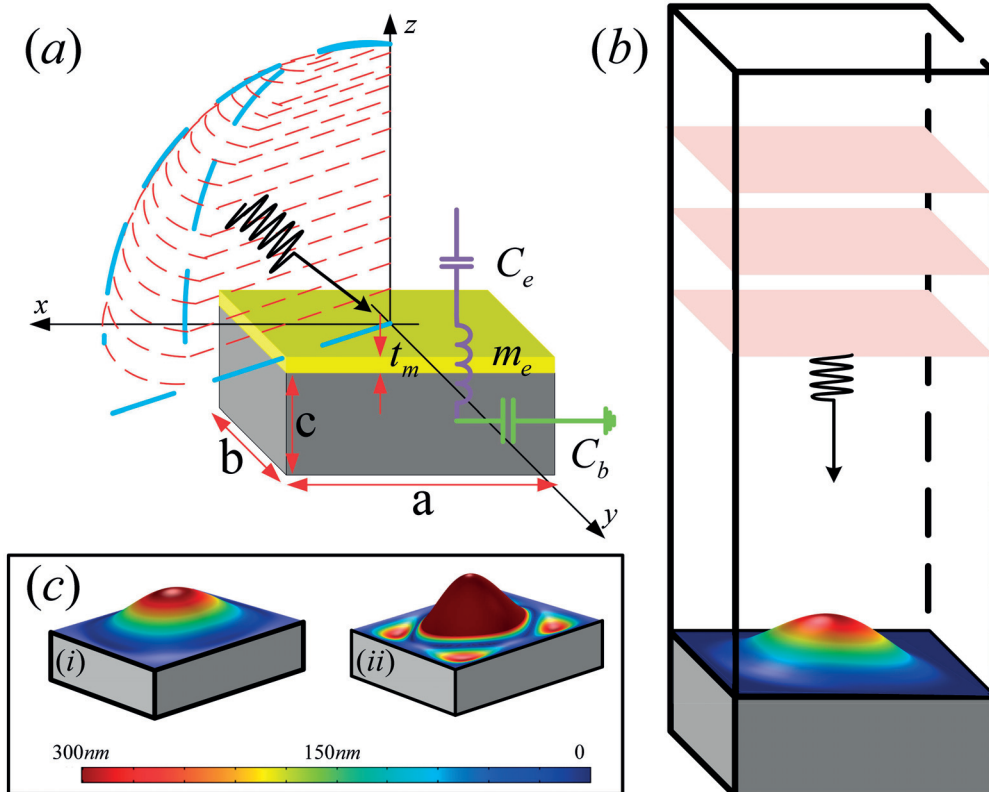
Figure 4.2: (a) Acoustic metasurface unit-cell and corresponding transmission-line model. The unit-cell is composed of a cavity (grey) with acoustically hard walls which is capped with a clamped membrane (yellow). Reflection phase study zone is shown in red dashed lines. (b) To retrieve the phase profile of the unit-cell, it is placed in a waveguide simulator. (c) Eigenmodes of the unit-cell for a high and a low thickness membranes (i) $t_m = 266 \, \mu m$ (ii) $t_m = 86 \, \mu m$.

unit-cell Z_{at} is calculated by

$$Z_{at} = j\omega m_{ae} + \frac{1}{j\omega C_{ae}} + \frac{1}{j\omega C_b}. \tag{4.10}$$

This analytical model of the unit-cell acoustic impedance is illustrated on Fig. 4.3 and compared to a numerical model achieved with a finite-element software (Comsol Multiphysics), further described in the following. Figure 4.2 shows that the analytical model of Z_{at} qualitatively follows the numerical results for thick membranes. However, the model tends to diverge from numerical results for unit-cells with thinner membranes. This is due to the excitation of higher order modes for unit-cells with thin membranes. The unit-cell membrane vibrates in its first mode (Fig. 4.2c-i) for the thickness $>\sim120$ μm as shown in eigenfrequency study in the inset of Fig. 4.3 and this is in consistent with the first mode excitation assumption to derive Eq. 4.9. However, the assumption is violated for thin membranes ($<\sim120$ μm) as shown in Fig. 4.2c-ii. Moreover, the dependency of the unit-cell impedance to the incident angle is neglected in the analytical model of Z_{at}. Considering the angular dependency of the total impedance, the reflection coefficient of the unit-cell is found to be:

$$\Gamma(\theta_i, \phi_i) = \frac{Z_{at}(\theta_i, \phi_i) - Z_c}{Z_{at}(\theta_i, \phi_i) + Z_c}, \tag{4.11}$$

where Z_c is the characteristic impedance of the medium and $Z_{at}(\theta_i, \phi_i)$ direction dependent total mechanical impedance of the unit-cell.

A close study of Eq. 4.8-4.11 reveals that the phase of the reflection coefficient is a function
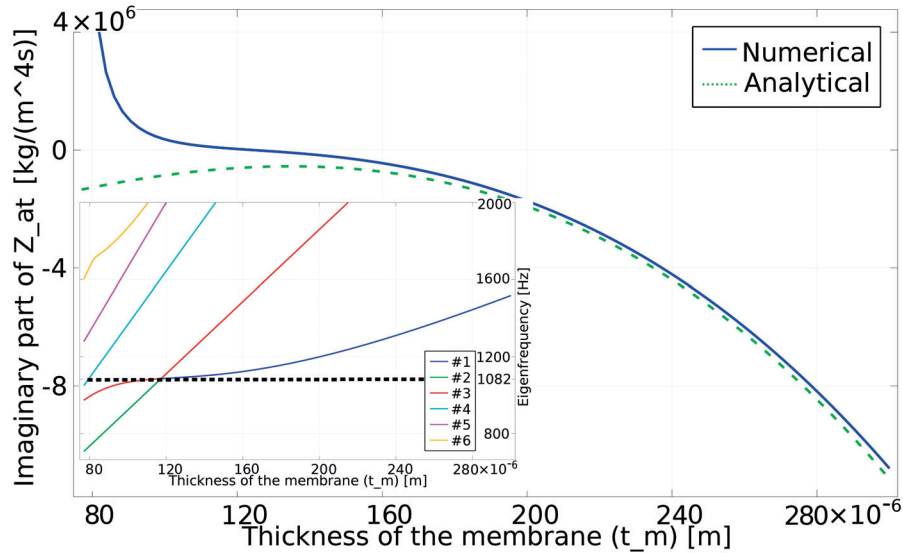
Figure 4.3: Imaginary part of the acoustic impedance of the unit-cell at $f = 1082$ Hz: numerical vs analytical method. (Inset) First six eigensolutions of the unit-cell versus thickness of the membrane. The unit-cell dimensions are 23 mm×23 mm×10 mm capped by Kapton membrane.

of geometrical dimensions and material properties of the unit-cell, operating frequency and direction of wave incidence. Moreover, encapsulated in Eq. 4.9, the inductive/capacitive nature of the membrane highly depends on the thickness of the membrane (t_m). Thus, the phase of the reflection coefficient can sweep the full phase range by varying the thickness of

the membrane in the range of few hundreds of micrometer. Using the proposed configuration, the designed unit-cells of almost similar geometrical dimensions but different impedances, can cover surface of any shape, like LEGO$^{\text{TM}}$ pieces. Moreover, by replacing the passive membranes with active ones, tunable unit-cells can be designed.

Although, the presented analytical modeling provides a qualitative description of the membrane capped unit-cell, as discussed it is only valid for pure first mode vibration of the membrane in the normal incident condition. To retrieve the accurate reflection coefficient behavior of the unit-cell taking the higher order modes and incident direction into account a fullwave simulation of the structure should be performed.

4.3.2 Numerical simulation

A finite element commercial software (Comsol Multiphysics) is used for the numerical simulations of the unit-cell. Acoustic-Shell Interaction physics module is used to extract the phase of the reflection coefficient. The unit-cell cavity is set to sound hard boundary and the membrane is assumed to be clamped at four edges to the cavity. The simulation geometry is completed by placing the unit-cell in a test waveguide (Fig. 4.2b). In order to consider effects of adjacent unit-cells (mutual coupling) for the case of slant incident waves, the boundaries of the waveguide simulator are set to Floquet boundary condition while radiation boundary condition is assigned to the upper extremity of the waveguide. The dependence of the unit-cell impedance $Z_{at}(\theta_i, \phi_i)$ to the direction of incident wave is also accounted by sweeping it in both azimuth and elevation plane. For a square cavity ($a = b$) there are four symmetry lines (Fig. 4.2a) and reflection phase study zone is reduced to ($0 < \phi < \frac{\pi}{4}$, $0 < \theta < \frac{\pi}{2}$). The reflection coefficient is retrieved using two-microphone measurement method [78].

The unit-cell dimensions are designed to be 23 mm×23 mm×10 mm capped by Kapton membrane with following material properties: $E = 2.758$ GPa, $\nu = 0.34$ and $\rho_m = 1420$ kg/m^3. The membrane is considered lossless for the time being, the effects of losses being assessed in the next section. Operating frequency is set to $f = 1082$ Hz and air with $c_{\text{air}} = 340$ m/s and $\rho_{\text{air}} = 1.188$ kg/m^3 is chosen as a background medium. In the proposed unit-cell the thickness variation of 70 μm to 300 μm results in phase profile which covers full reflection phase range. Since, the mentioned thickness range is negligible compared to the total height of the unit-cell (10 mm), designed unit-cells will be geometrically identical but with different reflection phase and consequently a thin and flat metasurface can be achieved. The phase profile of the proposed unit-cell versus membrane thickness is depicted in Fig. 4.4 for ($\phi = 45^o, 0^o$ and $0 < \theta < \frac{\pi}{2}$) incident angles. The close study of the unit-cell geometry and phase profile for full study zone reveals that the dependence of the phase profile to azimuth angle ϕ and elevation angle θ is relatively small. This means, bearing some tolerances the phase profile of the normal incidence can be used for the metasurface design. However, in order to achieve accurate results the phase profile of the prescribed incident direction should be retrieved.
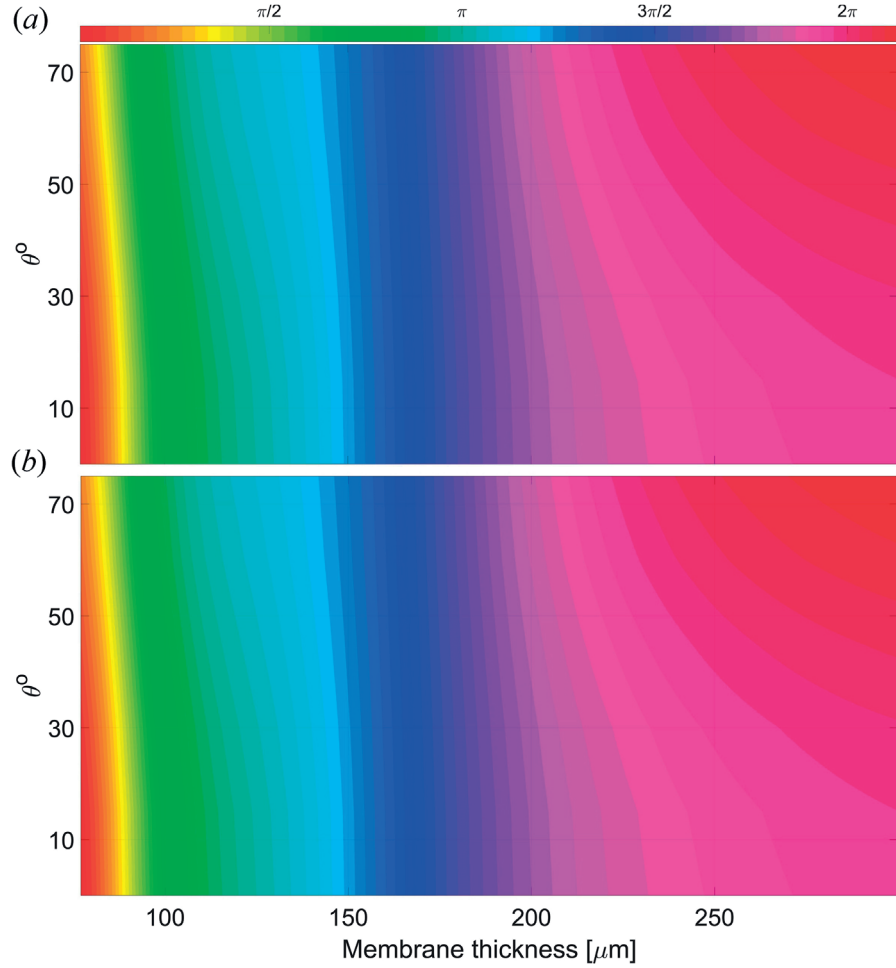
Figure 4.4: Phase profiles of the proposed unit-cell (phase of $\Gamma(\theta_i, \phi_i)$) versus membrane thickness for acoustic pressure wave with incident azimuth angle of (a) $\phi = 0^o$ and (b) $\phi = 45^o$ and elevation angle of $0^o < \theta < 75^o$.

4.4 Reflectarray Metasurface

In this section, to validate the functionality of the proposed unit-cell configuration, a 30×30 unit-cell reflectarray metasurface aiming at deflecting the incident acoustic wave in an anomalous way and operating at $f = 1082$ Hz is designed. Using such a unit-cell in metasurface design, the bulky acoustic elements are replaced by the subwavelength and ultra-thin ones.

4.4.1 Design

To design a reflectarray metasurface the incident (θ_i, ϕ_i) and the desired reflection (θ_r, ϕ_r) angles, operating frequency and the metasurface array factors d_x and d_y (in this case a and b) should be defined. Plugging these variables into Eq. 4.7 yields the surface phase function

allowing the manipulation of the reflected sound wavefront to the predefined direction. This surface phase function defines the required phase gradient which should be assigned to individual unit-cell with (m, n) index located in (md_x, nd_y) and the thickness of the membranes (t_m) for the metasurface unit-cells are set based on the required surface phase function and using the phase profile of the unit-cell for the specified direction of incidence (θ_i, ϕ_i).

4.4.2   Numerical simulation

Acoustic reflectarray metasurfaces are designed in three different scenarios to deflect incident sound wave (θ_i, ϕ_i) to (θ_r, ϕ_r) direction and it is simulated using Comsol Multiphysics. Acoustic-Shell Interaction physics module is used to simulated the structure where a spherical perfectly matched layer (PML) is applied around the metasurface to truncate the simulation domain and simulate an unbounded medium. The thickness of the membranes are set to the designed values and the background pressure field is applied to the simulation domain representing incident acoustic field. The near-field and far-field radiation pattern of the acoustic reflectarray metasurface are depicted in Fig. 4.5 for three distinct and predefined incident and reflected angles. Close study of the metasurface far-field radiation pattern reveals that the designed metasurfaces for predefined reflection directions of (a) $(\theta_r = 45^o, \phi_r = 120^o)$, (b) $(\theta_r = 31^o, \phi_r = 212^o)$, (c) $(\theta_r = 31^o, \phi_r = 30^o)$ deflect the sound waves to $(\theta_r = 44^o, \phi_r = 116^o)$, $(\theta_r = 30^o, \phi_r = 210^o)$ and $(\theta_r = 34^o, \phi_r = 26^o)$, respectively. The small discrepancy of maximum 4° between defined goals and designed values confirms the validity of both presented design procedure and unit-cell design. It is clear that the proposed unit-cell and designed metasurface is capable of handling the incoming waves with different incident angles in elevation and azimuth plane and deflecting the sound wave to predefined direction in elevation and azimuth plane. Moreover, investigating the far-field radiation pattern of the metasurface inset of Fig. 4.5 reveals that this structure has directive radiation which can be an alternative for acoustic reflectors. The presented acoustic metasurface is in the order of $(\sim \lambda/30)$ which is much smaller than conventional labyrinthine type structures, usually in the order of $(\sim \lambda/3 - \sim \lambda/2)$. This highlights the advantage of using membrane-based, rather than labyrinthine-type, unit-cells, with a view to designing ultra-thin metasurfaces. Such designs encourages the use of metasurfaces for acoustic noise reduction/cancellation, acoustic wave concentration for biomedical applications or acoustic levitation proposes. In the next section the proposed reflectarray metasurface is leveraged to design an acoustic carpet cloak.

4.5   Metasurface Carpet Cloak

When an acoustic wave impinges a flat surface the distribution of scattered (locally reflected) pressure field follows the Snell's law. However, applying a slight modification to the surface, such as placing an object on it, the scattered field is perturbed. A target can be detected by studying the mentioned perturbed scattered field which is the principle of radars/sonars. To hide an object from an acoustic field, the scattered field distribution should be manipulated
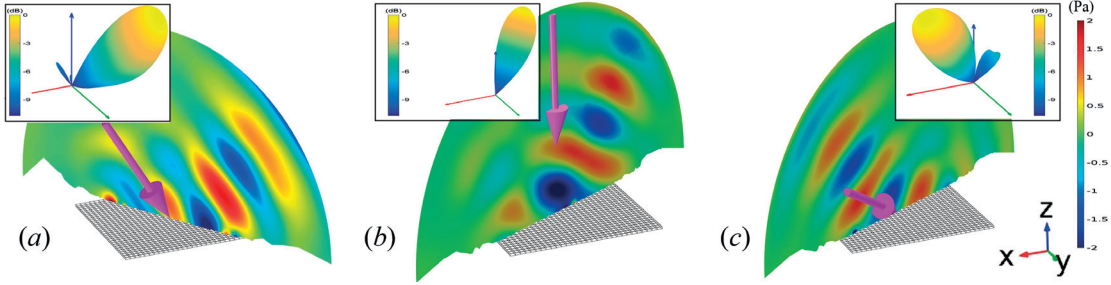
Figure 4.5: The near-field scattered pressure (main) and the far-field radiation pattern (inset) for the acoustic reflectarray metasurface at $f = 1082$ Hz for three different incident and reflection angles. (a) $(\theta_i = 30^o, \phi_i = 0^o) \rightarrow (\theta_r = 45^o, \phi_r = 120^o)$, (b) $(\theta_i = 0^o, \phi_i = 0^o) \rightarrow (\theta_r = 30^o, \phi_r = 210^o)$, (c) $(\theta_i = 60^o, \phi_i = 45^o) \rightarrow (\theta_r = 30^o, \phi_r = 30^o)$. Direction of incident acoustic wave is shown by arrow.

in a way that the pressure field perturbation due to the object is cancelled, mimicking (illusion of) wave scattering from bare ground.

4.5.1 Analytical description

Reflectarray metasurface can be used as an acoustic carpet cloak to manipulate the scattered field from a scatterer, placed over the ground, and create the illusion of bare ground reflection. Let's suppose an acoustic scatterer is placed over an acoustically hard flat surface (bare ground). The proposed configuration is a triangular bump in $xz-$plane which is invariant in $y-$direction (Fig. 4.6). If an acoustic plane wave (p_i, k_i), with the incident angle of θ impinges the scatterer (Fig. 4.6) with the slant angle δ from the ground, the reflected field locally follows the Snell's law ($\gamma_i = \gamma_r$). However, covering the scatterer with metasurface cloak, the incident field is reflected following $(\gamma_r^L = \gamma_i^L + 2\delta)$ and $(\gamma_r^R = \gamma_i^R - 2\delta)$, in the left and the right side of the scatterer, respectively. The modification of the reflected wave angle by 2δ is to compensate the effect of scatterer on the reflected wavefronts. The aforementioned modification to fulfil the required relations between incident and the reflection angles to achieve cloaking on the left and right side of the configuration of Fig. 4.6, can be also written as $(\gamma_i^L = \theta - \delta, \gamma_r^L = \theta + \delta)$ and $(\gamma_i^R = \theta + \delta, \gamma_r^R = \theta - \delta)$. Here, the L and R represent the left and right side of the scatterer as superscripts and i is the incident and r indicates the reflection direction as subscripts. Neglecting the diffractions from the edges, the perturbation in the scattered field due to the triangular bump is related to the local height of each point over the scatterer and this can be compensated using reflectarray metasurface. Considering the illustration of the 2D carpet cloak depicted in Fig. 4.6 and applying the generalized Snell's law of reflection as in Eq. 4.7, the required general phase function to manipulated the reflected wavefront from this surface is calculated as

$$\psi(x_m) = -kd_x m(\sin\gamma_r \cos 0 + \sin\gamma_i \cos 180), \tag{4.12}$$

where the m is the index of unit-cells over the scatterer and increases in the left to right direction. Plugging the necessary relations for incident and reflection angles to achieve cloaking into Eq. 4.12 (i.e. $\gamma_i^L = \theta - \delta$ and $\gamma_r^L = \theta + \delta$), the required surface phase function for the left face of the bump (ψ^L) can be calculated as,

$$\psi^L(x_m) = -kd_x m(\sin\theta\cos\delta + \cos\theta\sin\delta - \sin\theta\cos\delta + \cos\theta\sin\delta). \tag{4.13}$$

The Eq. 4.13 can be simplified to

$$\psi^L(x_m) = -2kd_x m\cos\theta\sin\delta = -2kh_m^L\cos\theta \tag{4.14}$$

where h_m^L is the local height of the unit-cell m on the left side of the scatterer. It should be stressed here that the Eq. 4.14 gives the distribution of the phase on the left side of the triangular bump and not the exact value of the phase. Indeed, the metasurface cloak should be studied in the context of the background medium. That is, to achieve carpet cloaking functionality, the reflection phase of the bump should be continuous on the edges where the two sides of the triangular scatterer intersect the background. Here, the sound hard boundary condition has been chosen as the background medium which exhibits the reflection coefficient of $\Gamma = +1$. Thus, choosing zero as the reference for the phase can satisfy the phase continuity from the background to the metasurface. As Eq. 4.14 has been derived by the generalized Snell's law of Eq. 4.7, where zero has been set as the reference phase, then the Eq. 4.14 should satisfy the phase continuity and no phase de-embedding is required. For instance, for the first unit-cell on the left side of the scatterer, Eq. 4.14 dictates $\psi^L(x_1) = 0$ as $h_1^L \simeq 0$, which proves that phase continuity from background to metasurface cloak has been automatically satisfied. The next important point is the phase continuity in the intersection of the left and the right side of the triangular cloak. Indeed, due to the symmetry of the triangular configuration with respect to z-axis, applying the same phase distribution as of the left side to the right surface of the bump, two aforementioned phase continuity criteria are satisfied and the carpet cloaking capability is achieved. Briefly, the designed metasurface should provide the phase lag to compensate the height of the bump on each point and this can be expressed in a single relation which holds for both sides of the triangular metasurface cloak as

$$\psi(x_m) = -2kh_m\cos(\theta), \tag{4.15}$$

where, h_m is the local height of the unit-cell over the scatterer, with respect to background, both in right and left side. Note that this relation is different from the electromagnetic metasurface carpet cloak over PEC (Perfect Electric Conductor) ground, where $\Gamma = -1$ and due to the phase continuity constraints on the edges the phase gradient of the metasurface carpet cloak follows $\psi(x_m) = \pi - 2kh_m\cos(\theta)$.
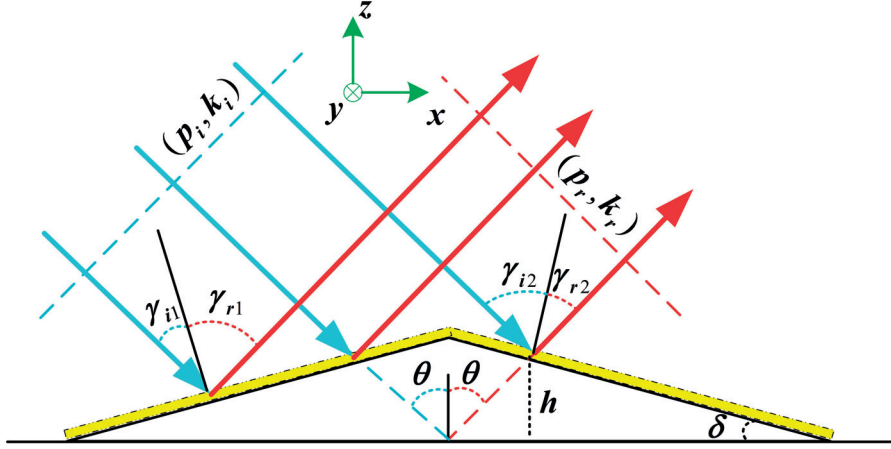
Figure 4.6: A triangular bump as an acoustic scatterer (black line) cloaked with a thin acoustic metasurface (yellow).

4.5.2 Numerical simulation

To verify the behavior of the acoustic metasurface cloak, the geometry of Fig. 4.6 is numerically investigated for the cases of bare ground, bare scatterer and cloaked scatterer exposed to the normal and slant impinging acoustic waves. The total pressure field of the isosceles triangular cloaked/uncloaked bump is studied for acoustic incident wave using Acoustic-Shell Interaction module. To achieve such a design, one stack of metasurface unit-cell covers a triangular bump, truncated by two parallel periodic boundary conditions in $xz-$plane which ensures the set-up is invariant in the $y-$direction. The back-plane of the simulation domain representing the ground as well as lower surface of the metasurface representing the cavities are set to acoustic hard boundary condition, the upper plane of the metasurface is composed of membranes with different thickness which are defined by Eq. 4.15. Finally, simulation domain is truncated by a PML semicylinder to ensure free space radiation condition.

The absolute acoustic pressure field is presented in Fig. 4.7(a-ii) for a triangular scatterer with the slant angle of $\delta = 30^o$ which is illuminated by a normal incident acoustic plane wave. Then, this scatterer is covered with a metasurface composed of 30 membrane based unit-cells and the absolute acoustic pressure field is presented in Fig. 4.7(a-iii) which is similar to the distribution of absolute pressure field over a bare ground depicted in Fig. 4.7(a-i). For the second scenario, the slant angle of the scatterer is chosen to be $\delta = 15^o$ and it is covered with 30 unit-cells metasurface cloak and the incident angle is set to $\theta = 45^o$. The absolute pressure field is compared in three different cases of scatterer with/without cloak and bare ground. Comparing the absolute pressure field over scatterer Fig. 4.7(b,ii) and over bare ground in Fig. 4.7(b,i) reveals that the field scattered from the uncloaked bump perturbs the absolute field and creates a shadow region. However, covering the scatterer with a thin metasurface cloak as in Fig. 4.7(b,iii) actually creates the illusion of the bare ground situation, showing that cloaking is also effective for slant incident angles.
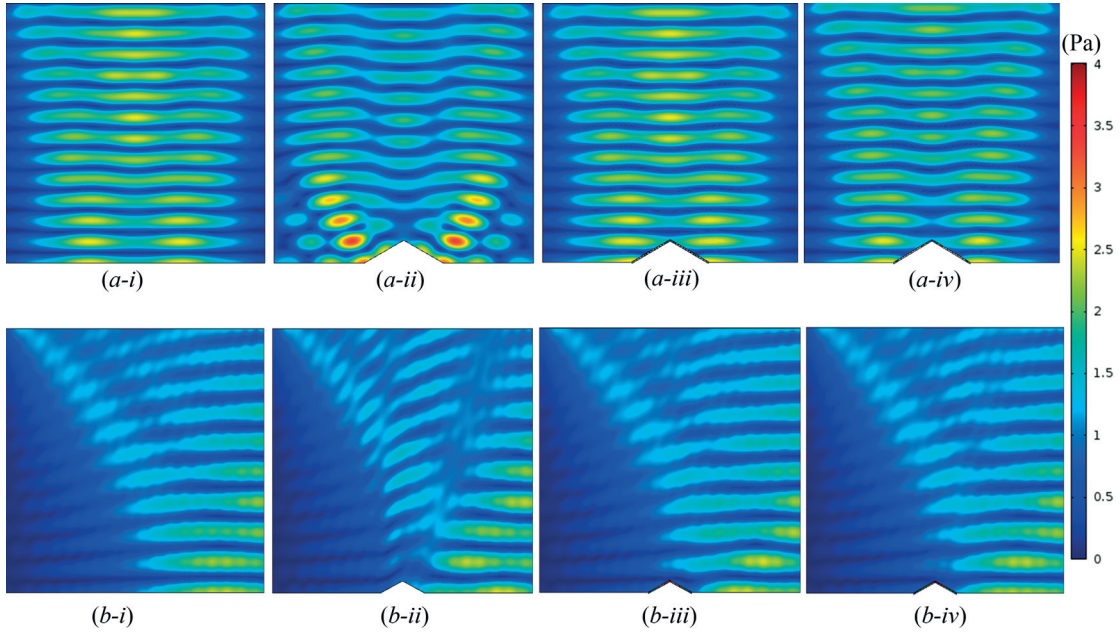
Figure 4.7: Absolute acoustic pressure field at $f = 1082$ Hz for (a) vertical incident and a bump with slant angle of $\delta = 30^o$ (b) 45° incident angle and a bump with slant angle of $\delta = 15^o$, (i) Acoustic hard surface, (ii) Bare bump, (iii) Cloaked bump neglecting damping. (iv) Cloaked bump including the damping ($\eta_s = 0.1$).

Last, in order to consider the effects of viscoelastic losses, an isotropic structural loss factor ($\eta_s = 0.1$) is taken into account in the simulation. It should be noted that the value of structural damping does not only depend on the material properties but also on the boundary conditions and the setup configuration, and it is usually determined from measurements. However, realistic values of η_s lie within the range $0.01 < \eta_s < 0.1$ for the type of elastic membranes used in the simulations [105]. Considering the upper limit of η_s as a worst case, and performing the same set of simulations as in the preceding, Fig. 4.7(a,b-iv) show that structural losses does not affect much the functionality of the carpet cloak, even with a rather high value of damping.

Comparing Fig.4.7(a,b-iii) and Fig.4.7(a,b-iv) shows that the effect of damping factor is more dominant in the near field and it decreases as we go farther from the cloak. Then, the carpet cloak keeps its functionality even with introducing a high level of losses. The effect of losses has also been studied for electromagnetic metasurface carpet cloak [106, 107, 86] and it was shown that, even for very large values of $\tan \delta$ (substrate loss), the cloaking metasurface is able to recover the far-field pattern. This is consistent with the results achieved on the acoustic metasurface carpet cloak proposed here, the pressure amplitudes in the far-field presenting the same color range on Fig. 4.7 (a,b-iii) and Fig. 4.7 (a,b-iv). A close look at the wavefronts on top of Fig. 4.7(a) shows that the maximum pressure amplitude is 2.4 Pa (yellow color range) for the undamped case (Fig. 4.7(a-iii)), where it is 2.15 Pa (a bit greener) for the damped case (Fig. 4.7(a-iv). The level difference is then lower than 1 dB, which is considered negligible.

This result confirms that, with such membrane-based unit-cells, the losses can be neglected without affecting the performance of the metasurface. Moreover, the choice of membrane-based metasurfaces does not only allow the design of ultra-thin carpet cloaks, but it also overcomes the damping issues that are inherent to labyrinthine-type unit-cells.

4.6 Conclusion

Following the investigations on different wave phenomena, in this chapter the interaction of sound wave with 2D metastructures was investigated in reflection regime. First, a mathematical tool for wavefront engineering, namely the generalized Snell's law for reflecting acoustic wave, was derived using the Fermat principle and the wavefronts of the reflected wave was related to the phase gradient of the surface. Then, the relation between non-zero phase gradient and inhomogeneous acoustic surface impedance was discussed and finally after designing impedance based ultra-thin unit-cells, novel acoustic functionalities for the designed acoustic metasurfaces were investigated.

Surface impedance governed phase manipulation of the reflected wave led to a new design of ultra-thin unit-cells based on membrane capped cavities where the TL theory, developed in the second chapter, was leveraged to model and characterize the proposed unit-cells. Unlike other metasurface unit-cells found in the literature, the phase manipulation of which relies on the effective acoustic path, the surface impedance is responsible for the reflected wave phase lag/lead in the proposed structure and this results in ultra-thin unit-cells. Due to the high sensitivity of the unit-cell impedance to the membrane thickness, unit-cells with similar geometries and dimensions but distinct impedances can be designed. This type of unit-cell is very versatile and can be used in many different designs and will be compatible with the fast growing 3D prototyping technology when the resolution of 3D printers reach the micrometer scale.

The proposed ultra-thin unit-cell was also used to design an acoustic reflectarray metasurface in the audio frequency regime. This very thin metasurface ($\sim \lambda/30$) is capable of manipulating reflected acoustic waves in a prescribed direction. This may find applications in noise engineering and biomedical imaging as well as acoustic levitation. Furthermore, acoustic reflectarray metasurfaces may be used as an alternative to acoustic shaped reflector antennas. Moreover, the skin-like acoustic metasurface carpet cloak, which works based on manipulating the reflected wavefront, was suggested, formulated and numerically validated. The proposed ultra-thin membrane capped cavity unit-cells were used to engineer the carpet cloak where the acoustic surface impedance of the cloak was leveraged to manipulate the scattered wave field for hiding a target to the acoustic waves. Since the metasurface carpet cloak is easy to design and the design parameters are practically realizable, it should become a good alternative to transformation based cloaks, which usually confront feasibility challenges. Moreover, this type of cloak is very versatile and can be turned into active and tunable configurations if the passive membranes are replaced by semi-active or active electroacoustic transducers.

Until now, the main concepts in sound-matter interaction including propagation, guided-waves, radiation, refraction and reflection have been studied, in the following chapter the sound-metastructure interaction in transmission scenario is presented and a novel functionality of acoustic metasurfaces for manipulating the transmitted sound is unveiled.

5 Acoustic Orbital Angular Momentum Metasurface

| Propagation | Guided-wave | Radiation | Refraction | Reflection | Transmission |

This chapter is a modified version of the materials published in Ref. [54] and orally presented in Ref. [108].

5.1 Introduction

Inspiration from electromagnetics:
The discovery that waves can carry angular momentum may date back to Poynting and his claim on angular momentum of the circularly polarized light [109] which was later validated experimentally [110]. While the angular momentum due to the circular polarization is linked to the photon spin, there is another type of angular momentum due to the spatial distribution of electromagnetic waves which is called orbital angular momentum (OAM) [111]. In 1992, Allen et al. studied the mechanical torque resulted by electromagnetic orbital angular momentum waves [112], which has led to extensive theoretical and experimental studies on optical trapping, tweezers, spanners, etc [113].

Efforts in acoustics:
Although acoustic waves are not naturally polarized to produce spin angular momentum, they still can carry orbital angular momentum. The wave field singularity or a dislocation in the wavefront as a key feature of wave vortices was first studied in 1979 for acoustic waves [114]. Twenty years later, Hefner et al. produced the first ultrasonic beam with helical phase and screw dislocation [115]. Moreover, it was shown using the concept of pseudomomentum that acoustical vortices have the same properties as their optical counterparts. Thus, for a pressure wavefront with a phase dependence of the from $e^{jl\phi}$ (ϕ and l being the azimuthal angle and the topological charge respectively), the torque is proportional to the absorbed power and to l/ω ratio, where ω is the angular frequency [116]. Thereafter, different studies have been

conducted on the theoretical and practical aspects of acoustic angular momentum and screw type dislocations [117, 118]. Moreover, the transfer of acoustic angular momentum to matter has been empirically validated [119, 120].

Several methods have been proposed to create acoustic helicoidal waves, carrying angular momentum. Hefner et al. used an active PVDF with a tangential helical surface supported by a twisted ring to create the first sonic helicoidal beam [115]. Later, Ealo et al. improved this configuration using ferroelectrics [121]. However, a vertical dislocation of 1λ is required in the twisted ring (transducer diaphragm) and this technique is only suitable for ultrasounds. Hefner et al. proposed then an alternative technique, based on a circular array of phase shifted transducers [122]. This method has been adopted since then in most of the studies to create acoustical vortices, requiring many transducers which are individually controlled [123]. Gspan et al. used optoacoustic for the generation of ultrasonic screw dislocations [124]. They used a pulsed laser beam to illuminate an absorbing spiral phase plate which ultimately produces ultrasonic pulses with helical phase. Besides being complicated, this is a low efficiency procedure which needs high power short laser pulses. Wang et al. proposed the use of spiral shape structure to get acoustic vortices in ultrasonic frequencies [125] and recently, Naify et al. used leaky wave antenna to create helical waves, although this method leads to very compact structures, it can create nonuniform wavefront due to the difference in the amount of leaked power between input and output [126].

Transmission phenomenon and OAM metasurface:
A close study of the aforementioned techniques reveals that to generate acoustic vortices the wavefront of the acoustic waves should be engineered to produce the phase dependence of the form $e^{jl\phi}$. Hence, a new technique can be thought, on the basis of sound-metastructures interaction, where the wavefront of the impinging planewave is transformed to transmitted helical wave. Explained in the previous chapter, acoustic metasurface can be used to manipulate the wavefront of the reflected wave, however another scenario can be devised where the metasurface is in the transmit mode. Such a metastructure is in the category of artificially engineered surfaces which are called transmit type metasurfaces. These surfaces are composed of unit-cells which manipulate the transmitted wavefronts by adding a phase lag/lead to the impinging waves [51]. Jiang et al. [127] and Ye et al. [128] used acoustic Helmholtz resonators as unit-cells to get acoustic OAM and could design an OAM metasurface with the thickness of $\lambda/2$ (where λ is the wavelength of the frequency of operation). In this method a single source and a passive transmit type metasurface is introduced to generate acoustic vortices. Such a metasurface can be composed of any transmit type unit-cells which controls the phase shift of the transmitted wave. These unit-cells are arranged in a discretized configuration to passively transform an incident plane wavefront into the desired transmitted helical wavefront. This method presents the advantage of overcoming the restrictions on using many acoustic sources, and it can be easily 3D-printed. Therefore, such a straightforward principle can be adopted for easy production of acoustic angular momentum with minimum complexity and using a single source.

5.1.1   Outline of the chapter

In this chapter, paraxial Helmholtz equation which support OAM waves is presented, then a new unit-cell configuration based on space coiling technique [96, 129] is introduced. This labyrinthine type unit-cell allows an efficient use of space [108] which decreases the thickness of the acoustic transmit type unit-cells down to $\lambda/3$. Moreover, it can be analytically defined which facilitates the design and optimization procedure. Next, the proposed unit-cell is used for the phase coding of a digitized surface, which converts acoustic plane wavefronts to acoustic helical wavefronts. Finally, the measurement results of the structure, fabricated through 3D-printing, validates the theoretical proposal.

5.2   Paraxial Helmholtz Equation

A wave is considered to be paraxial when its wavefront normals are paraxial rays. In order to construct a paraxial wave, it is better to start with a plane wave pe^{-jkz} and consider it as a carrier wave, then modulate its complex envelope p with a slowly varying function of position as $p(x,y,z)$. Hence, the complex amplitude of the modulated wave becomes

$$P(x,y,z) = p(x,y,z)e^{-jkz}. \tag{5.1}$$

The variation of the envelope $p(x,y,z)$ and its derivative with position z must be slow within the distance of a wavelength $\lambda = 2\pi/k$ so that the wave approximatly maintain its plane wave nature [130]. For the paraxial wave of Eq. 5.1 to satisfy the Helmholtz equation, the complex envelope $p(x,y,z)$ must satisfy the following equation

$$\nabla_T^2 p - j2k\frac{\partial p}{\partial z} = 0, \tag{5.2}$$

where $\nabla_T^2 = \partial^2/\partial x^2 + \partial^2/\partial y^2$ is the transverse Laplacian operator. Equation 5.2 is the slowly varying envelope approximation of Helmholtz equation and it is called paraxial Helmholtz equation [130].

A complete set of solutions to paraxial Helmholtz equation can be obtained in cylindrical coordinates (ρ, ϕ, z), where any other solution for paraxial equation can be written as a superposition of these solutions and it is called Laguerre-Gaussian solution. The complex amplitude of the Laguerre-Gaussian solution is expressed by

$$p(r,\phi,z) = G(r,z)A_{n,l}(r,z)\Psi_n(z)\Phi_l(\phi) \tag{5.3}$$

In Eq. 5.3, $G(r,z)$ is the Gaussian envelope of the beam, $A_{n,l}$ is the amplitude structure near the dark core, $\Psi_n(z)$ is the Gouy phase and $\Phi_l(\phi)$ is the phase structure of the beam, which are defined as

$$G(r,z) = \frac{D}{(1+z^2/z_R^2)^{1/2}}e^{\left(\frac{r^2}{w^2(z)}\right)}e^{\left(-j\frac{kr^2 z}{2(z^2+z_R^2)}\right)}, \tag{5.4}$$

$$A_{n,l}(r,z) = \left(\frac{r\sqrt{2}}{w(z)}\right)^{|l|} L_{(n-|l|)/2}^{|l|}\left(\frac{2r^2}{w^2(z)}\right), \tag{5.5}$$

$$\Psi_n(z) = e^{-j(n+1)\psi(z)}, \tag{5.6}$$

$$\Phi_l(\phi) = e^{jl\phi}, \tag{5.7}$$

where D is a constant for the normalization, $z_R = kw_0^2/2$ is the Rayleigh distance (w_0 being the width of the beam at $z = 0$ and k the wave number), $w(z) = w_0[1+(z/z_R)^2]^{1/2}$ describes the evolution of the size of the Gaussian beam while propagating, $L_{(n-|l|)/2}^{|l|}$ denotes the generalized Laguerre polynomials with $n = |l|, |l|+2,...$ the radial index, $\psi = \tan^{-1} z/z_R$ and l the topological charge [117].

A detailed study of the Laguerre-Gaussian solution reveals that the intensity of the beam is a function of r and z, so that it is circularly symmetric. For $l \neq 0$, the beam has zero intensity at the center $r = 0$ and an annular intensity pattern. The phase has the same dependence on r and z as the Gaussian beam, but has an additional term proportional to azimuthal angle ϕ, and also Gouy phase is added by the factor $(n+1)$. Because of the linear dependence of the phase on ϕ (for $l \neq 0$) the wavefront rotates helically as the wave travels in the z direction. Beams with such spiral phase are of interest since they carry angular momentum that can impart torque to the system they imping [130]. Equation 5.7 is the phase dependence that was discussed in the previous section to introduce the helical wavefront and it will be used in the rest of this chapter as the main feature of acoustic waves which carry orbital angular momentum.

5.3   Metasurface Unit-Cell

Contrary to the previous chapter where the unit-cell designed to control the reflected wave, in this chapter the unit-cell should be designed to transmit the impinging wave. Hence, the amplitude of the transmission coefficient should be uniform and its phase should cover the full phase range $(0-2\pi)$. The most straightforward acoustic module with such characteristics is a labyrinthine type unit-cell. In labyrinthine unit-cells the actual length of the wave path not the thickness of the unit-cell defines the phase lag/lead of the transmitted wave with respect to input wave. The behavior of labyrinthine unit-cells highly depends on their shapes and physical dimensions, hence, the choice of the unit-cell geometry, as well as its optimized design can increase the performance and decrease the size of the final metasurface realized by such unit-cells.

5.3.1 Geometrical configuration

To achieve a labyrinthine unit-cell, a helicoid geometry is defined so as to use space most efficiently. The helicoid is a ruled surface that is described by a straight line rotating at a given angular rate around a fixed axis. When a cylindrical tube intersects a helicoid, the resulting geometry is a space coiled structure which connects the two ends of the cylindrical tube through two helical acoustic paths, longer than the physical length of the tube.

As depicted in Fig. 5.1, each transversal cross-section of the proposed geometry is composed
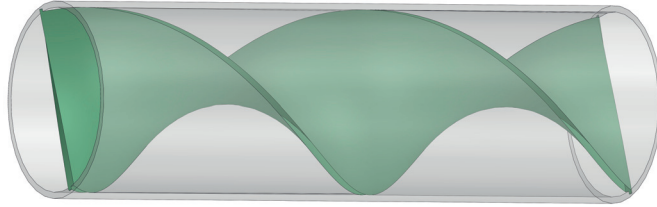
Figure 5.1: Helicoid unit-cell: helicoid is shown in green and the intersecting tube in transparent gray.

of two fluid-filled half-disks, separated by the helicoid. This means that, unlike the previous spatially modulated space coiled structures reported so far, the whole cross section of the tube is used to transmit sound waves through the structure. These unit-cells allow designing phase-coded metasurface with transmission phase profile of $(0 - 2\pi)$ and near unitary amplitude. It is obvious that the phase of the transmitted wave depends on the effective length of the twisted ducts. Thus, the transmission phase can be engineered by modifying the number of helicoid turns along the tube. However, the presence of the helicoidal wall at the entrance of the duct results in a discontinuity between the outer and inner medium, which leads to an impedance mismatch. Moreover, such impedance mismatch may be further increased by the densification of the labyrinthine path and increasing the number of turns. To mitigate this issue as shown in Fig. 5.2, the twisting profile of the helicoid is modulated along the length of the structure using piecewise functions, allowing optimizing the transmission coefficient in terms of phase and amplitude.

5.3.2 Design

The mathematical relation, $\vec{r}(\rho, t) = <x, y, z> = < \rho \cos(2\pi \int_0^t f(\tau) d\tau), \rho \sin(2\pi \int_0^t f(\tau) d\tau), b\, t >$ describes the helicoid, where ρ is the radius of helicoid, b is the constant rate of gradual displacement along $z-$axis, and for $b = 1$, t defines the height of the unit-cell. The spatial modulation function of the helicoid is $f(\tau) = f_c + f_\Delta x_m(t)$, where f_c is the average spatial frequency of twists, f_Δ is the deviation from f_c and $x_m(t)$ is a piecewise function allowing
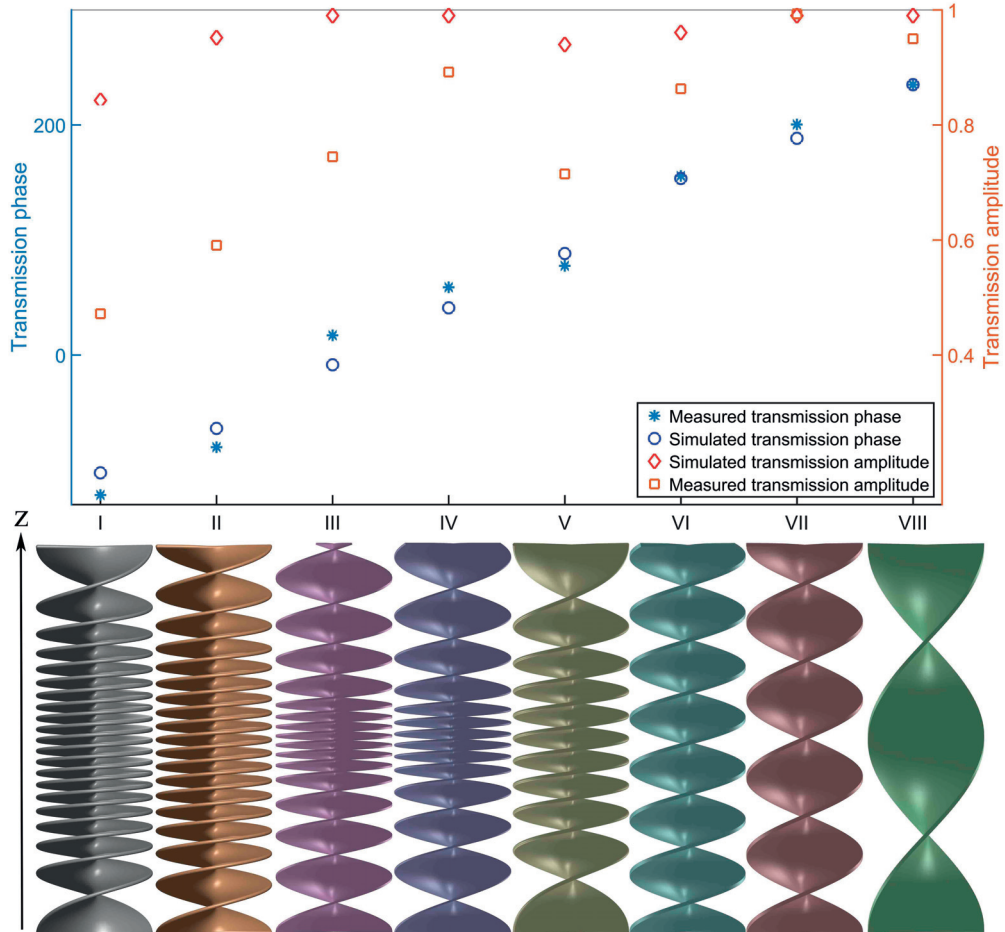
Figure 5.2: Top: Sound transmission coefficient phase (blue) [in degree] and amplitude (red); Bottom: geometries of the 8 simulated configurations. Left: densely twisted (modulated) helicoids. Right: coarsely twisted helicoids.

changing the spatial variations. Hence, the helicoid can be described in detail in the form of:

$$\begin{cases} x = \rho \cos(2\pi \int_0^t f(\tau)d\tau) = \rho \cos(2\pi \int_0^t [f_c + f_\Delta x_m(t)]d\tau) = \rho \cos(2\pi f_c t + 2\pi f_\Delta \int_0^t x_m(t)d\tau) & 0 < t < h \\ y = \rho \sin(2\pi \int_0^t f(\tau)d\tau) = \rho \sin(2\pi \int_0^t [f_c + f_\Delta x_m(t)]d\tau) = \rho \sin(2\pi f_c t + 2\pi f_\Delta \int_0^t x_m(t)d\tau) & -\frac{d}{2} < \rho < \frac{d}{2} \\ z = bt & b = 1. \end{cases}$$

$$(5.8)$$

Therefore, f_c controls the phase of the transmission coefficient, whereas f_Δ and x_m have an influence on the amplitude of the transmission coefficient, acting on the impedance matching. Using Eq. 5.8 the helicoidal unit-cells can be geometrically defined in any numerical software and optimized to achieve unitary transmission coefficient which covers full phase. Table. 5.2 summarizes the physical dimensions as well as mathematical descriptions of the designed helicoidal unit-cells, shown in Fig. 5.2, which cover the $(0-2\pi)$ transmission phase for acoustic

waves.

Table 5.1: Geometrical dimensions and mathematical definitions of the helcoidal unit-cells.

Unit-cell	d[mm]	h[mm]	N	$f_c = \frac{N}{h}$	$f_m = \frac{1}{h}$	k	$f_\Delta = k(f_c - f_m)$	$x_m(t)$
I	30	100	10	0.1	0.01	0.9	0.081	$\cos(2\pi f_m t)$
II	30	100	9	0.09	0.01	0.7	0.056	$\cos(2\pi f_m t)$
III	30	100	7.8	0.078	0.01	1	0.068	$u(x) = \begin{cases} \cos(2\pi \frac{2f_m}{3} t) & 0 < t < \frac{3h}{8} \\ \cos(2\pi 2 f_m t + \pi) & \frac{3h}{8} < t < \frac{5h}{8} \\ \cos(2\pi \frac{2f_m}{3} t + \frac{2\pi}{3}) & \frac{5h}{8} < t < h \end{cases}$
IV	30	100	6.6	0.066	0.01	1	0.056	$c(t)$
V	30	100	5	0.05	0.01	0.9	0.036	$\cos(2\pi f_m t)$
VI	30	100	3.6	0.036	0.01	0.1	0.0026	$\cos(2\pi f_m t)$
VII	30	100	2.5	0.025	0.01	0	0	$\cos(2\pi f_m t)$
VIII	30	100	1	0.01	0.01	0	0	$\cos(2\pi f_m t)$

5.3.3 Numerical simulations and measurement results

Figure. 5.2 (bottom) represents eight spatially modulated helicoids. The geometrical modulations of these twisted surfaces, hosted inside cylindrical tubes, are described by piecewise functions $f(\tau)$ (defined in the Table. 5.2), which have been optimized to provide a smooth transition between the sound pressure at the input (p_i) and at the output (p_t), focusing on improving the impedance matching and on ensuring near unity transmission coefficient as required for such metasurface unit-cells.

Simulation procedure:
The numerical assessment of the proposed helicoidal unit-cell has been performed in Comsol Multiphysics using Pressure Acoustic physics module in frequency domain. The helicoidal unit-cell has been placed in a long waveguide, representing standing wave tube and its transmission phase and amplitude have been evaluated under plane wave incidence using four microphones measurement method (see Appendix E). Neglecting any source of losses, sound hard boundary condition has been assigned to the waveguide and unit-cell walls, moreover, both extremities of the standing wave tube has been set to plane wave radiation, representing anechoic termination for plane wave. Due to the complexity of the geometrical configuration of the structure, for some unit-cells SolidWorks has been linked to Comsol to facilitate the geometrical rendering. Moreover, in order to decrease the simulation time, all the unit-cells have been numerically evaluated for a single frequency ($f = 1060$ HZ).

Measurement set up:
After optimized design of heliocoidal unit-cells in Comsol Multiphysics to cover full phase and uniform transmission coefficients, the unit-cell prototypes of Fig. 5.2 have been 3D-printed using Selective Laser Sintering (SLS). Then, the sound transmission coefficient p_t/p_i of each unit-cell has been measured in a test tube by 4-microphone method. Four microphone measurement is performed by a set up composed of two cylindrical waveguides separated by a device under test. This set up is fed by an acoustic source in one extremity of the waveguide

and it is blocked by anechoic termination in the other end. Finally, the sound pressure is measured in four distinct locations, two on each side of the DUT. Figure 5.3 shows a four microphone set up to measure the scattering parameters of the helicoidal unit-cell. This method has been explained in more details in the Appendix E and shown in Fig. E.1. Finally, the resulting numerical and measured sound transmission coefficient amplitudes and phases are reported in Fig. 5.2 (top) for the operating frequency of 1060 Hz.

Discussion:

As can be seen in Fig. 5.2 (top), the measured sound transmission coefficients phases of the
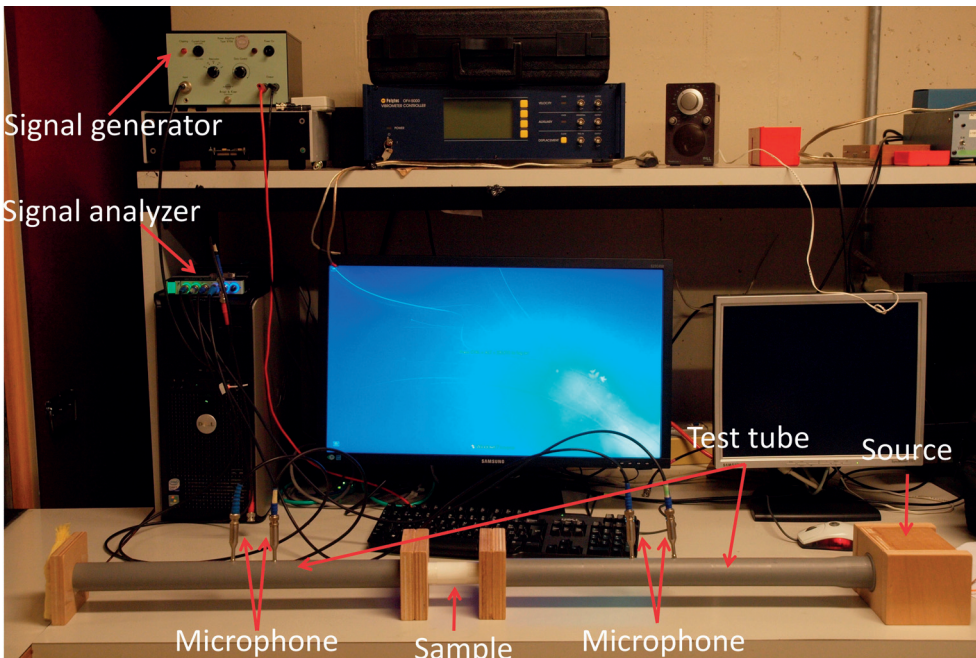
Figure 5.3: Four microphone measurement setup.

fabricated prototypes agree well with the numerical results for all unit-cells, spanning the $(0-2\pi)$ range with $\pi/4$ phase steps, whereas the transmission coefficients present almost near-unity amplitudes only for the coarser unit-cells (IV to VIII). For unit-cells I-III, the measured amplitudes decrease as the number of helicoidal turns increases, and discrepancies between simulation and measurement results increase. The observed differences which is affecting the denser unit-cells, are due to several design simplification that are listed in the following:

- In the numerical simulation, the helicoidal and cylindrical walls have been considered smooth surfaces with zero thickness presenting hard boundary conditions. Therefore, the only acoustic pressure field has been accounted for in the Comsol simulations, hence the internal walls of the structure are set to hard boundary conditions, yielding the wall vibration has been intentionally discarded. This simplifications are justified by the difficulty to render the actual wall thickness in the geometrical rendering of

Comsol and not paying the price of prohibitive computational costs, relative to meshing and numerical processing. However, due to the 3D-printing technology employed for building the prototypes, the actually fabricated helicoidal and cylindrical walls present unpredictable porosity and are not smooth, with random surface states varying around average thickness of 0.5mm and 1mm respectively (considering the fabrication precision, each prototype present varying thicknesses around the average). Such construction tolerances result in increasing the frictions within channels, and also in making the walls vibrate under the incident sound field, thus transferring part of the incident acoustic energy into mechanical energy, present in measurement but neglected in simulations. This affect the transmission performance and result in a significant amount of the sound intensity reflected back toward the input of the channel. Intuitively, these sound intensity reflections are likely to be dominant in the denser unit-cells and almost vanish for coarser labyrinthine paths.

- Moreover, in 3D-printed prototypes using SLS, the remaining building powder that inevitably remains in the labyrinthine paths after construction, can be cleaned for coarse unit-cells using compressed air, whereas it is difficult, if not impossible for denser twisted shapes. Consequently not cleaned properly in denser unit-cells, the remaining powder can block the channels, affecting the sound transmission performance and increasing sound power reflection and absorption for the denser unit-cells.

- The thermoviscous losses have been neglected, for the sake of reducing the computational cost. However, the thickness of the helicoidal walls are of the same order of magnitude as the width of the narrow acoustic paths, especially for the denser unit-cells and they affect the transmission characteristics. In addition to the thermoviscous losses resulting from the ultra-thin labyrinthine pathways, disregarded porosity of the prototypes walls, as well as dissipation associated with the remaining excess powder of the fabrication process is another neglected loss factor contributing to decreasing the transmission coefficient which increases for denser unit-cells due to the longer and narrower paths.

To verify the aforementioned sources of discrepancies between simulation and measurement results in Fig. 5.2, the value of the lost power ($\alpha = 1 - |R|^2 - |T|^2$), as well as reflected ($|R|^2$) and transmitted ($|T|^2$) power coefficients have been measured for the 8 helicoidal unit-cells and the results are presented in Fig. 5.4. As expected the percentages of the reflected and lost power depend on the number of helicoidal turns and increase as unit-cells density increases. While the designed unit-cells have been optimized for best impedance matching, as explained, the occurrence of unpredictable losses and reflections in the fabricated prototypes yields the observable discrepancies between the measurements and simulations of sound power transmission coefficient amplitudes. These discrepancies are relatively small for coarse unit-cells with few number of turns, for which the values of sound power reflection coefficients and losses are much lower than the transmitted one, and increase for denser unit-cells and highlighted by the higher values of reflections and losses.

The most straightforward way to minimize the influence of the aforementioned problems
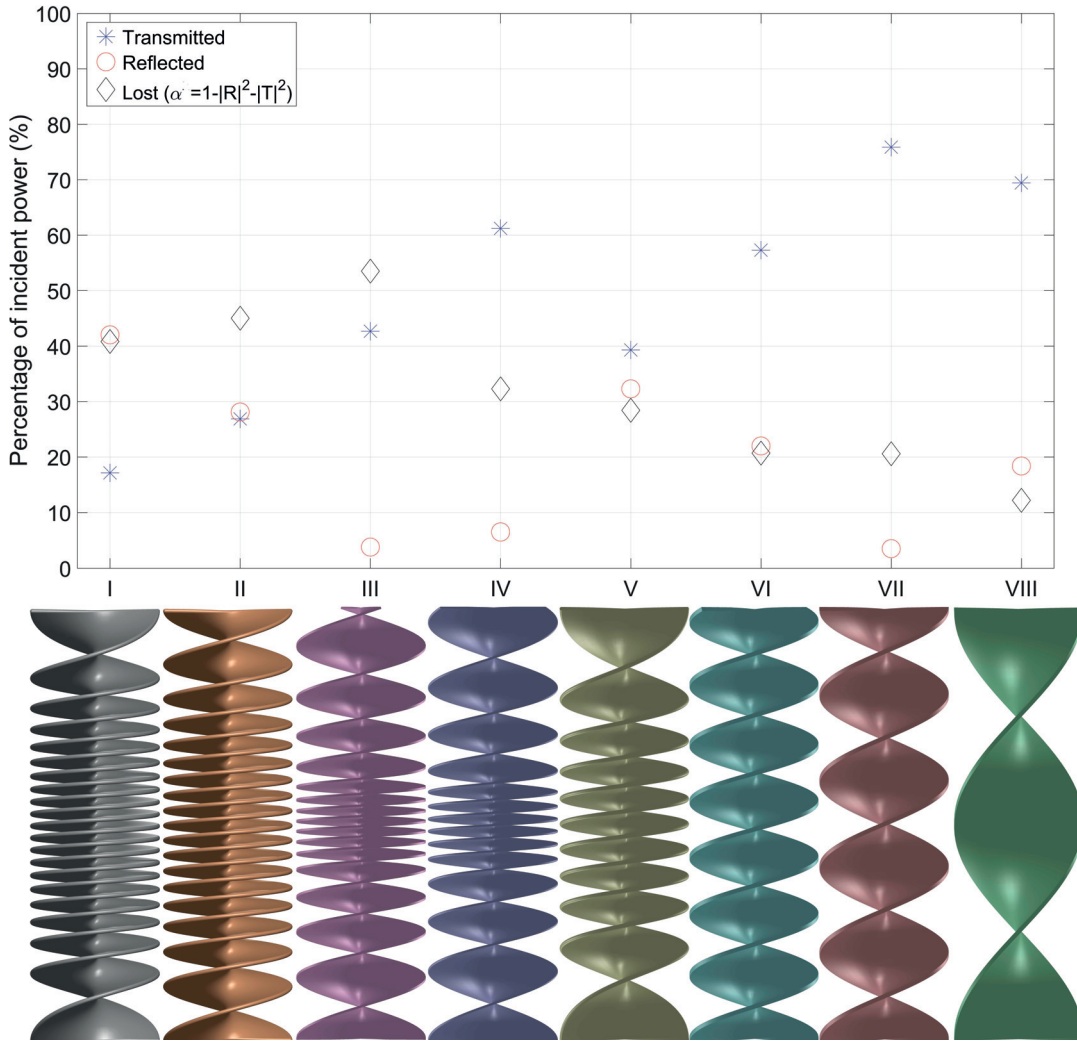
Figure 5.4: Measured transmitted, reflected and lost power in the helicoidal unit-cells.

consists in increasing the global length of each unit-cell (h) which results in reducing fabrication problems and errors due to the lower density of helicoidal turns, and consequently lower value of absorption and reflection. However, this solution presents the critical shortcoming of increasing the global thickness of the structure, which contradicts the metasurface denomination. Another option consists in choosing an alternative piecewise function $f(\tau)$ for the modulation of helicoid to decrease both the sound power reflection and lost power coefficients. There is also another solution that is, rather than focusing on achieving unitary sound power transmission coefficient on all unit-cells, which is finally not required to obtain a doughnut shaped beam with helical phase front, a uniform transmission coefficient among unit-cells can be targeted. This can be done by partially blocking the output of each unit-cell, to the price of a degradation of the overall transmission performance. Then, the proposed design still preserves the thickness criterion of acoustic metasurfaces, transforming an incident plane

wave into a helicoidal wave, to the price of a relative deterioration of the efficiency in terms of power transmission.

5.4 OAM metasurface

To convert a plane wavefront from one upstream propagating medium into a helicoidal wavefront carrying orbital angular momentum in a downstream medium, a specific interface with surface-dependant transmission phase should be designed. Such a surface should be coded in such a way that, first the wave uniformly passes through it and at same time the transmitted wave experience a spatially predefined phase lag to mimic wavefront with phase dependence of $e^{jl\phi}$ type.

5.4.1 Geometrical configuration

A metasurface with a circular arrangement of unit-cells is proposed, the transmission phase of which are set according to the design presented in the preceding section. To achieve the acoustic vortices with a topological charge of integer value l, the proposed circular configuration should cover the phase range of $(0 - 2\pi l)$ that is, the unit-cells in the transmission phase range $(0 - 2\pi)$ should intermittently cover the circular arrangement of the metasurface for l times. To achieve OAM metasurface, for circular surface which is segmented into M equal sectors, each sector being composed of m equal and equidistant unit-cells with circular cross-sections, each of the $(M \times m)$ sections should be individually phase-coded using the designed labyrinthine type unit-cells. In the proposed configuration, M controls the resolution of the generated helical wave, as well as its topological charge, and m controls the amount of power which passes through each sector.

Figure. 5.5 depicts the acoustic OAM metasurface designed with helicoidal unit-cells to convert plane wavefronts into acoustic helical waves with the topological charge of $l = 1$. The surface is divided into $M = 8$ circular sectors, each representing transmit coefficients with the phase shift of $\pi/4$ with respect to its adjacent sectors and each sector is filled by $m = 3$ similar unit-cells as designed in Fig. 5.2. While the presented example in this study targets $l = 1$, the metasurface can be designed to achieve higher values of the topological charge l provided that the proposed unit-cells in M sectors encompass the phase $(0 - 2\pi l)$ for every circular row.

5.4.2 Experimental setup

Figure. 5.6a illustrates the schematic representation of the experimental set up composed of two waveguides separated by the proposed metasurface prototype and the detailed dimensions are listed in Table 3.1. The metasurface consists of an array of $M \times m$ regularly spaced labyrinthine unit-cells ($h = 100$mm), squeezed by two square plates. The plates have dimensions 240mm×240mm×8mm and are made out of acrylic glass, with circular holes of diameters $d = 30$mm. The holes are drilled equidistantly in two concentric circular rows
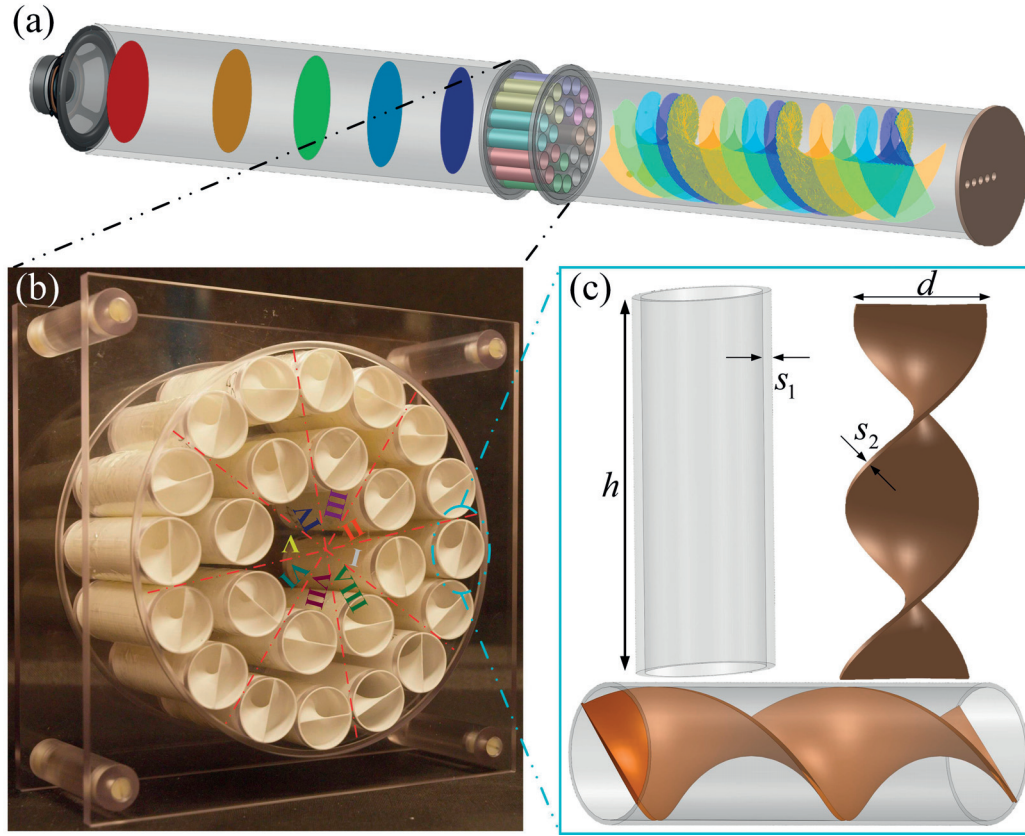
Figure 5.5: (a) Measurement setup for the assessment of the metasurface, with an illustration of the resulting acoustic wave structure in the upstream and the downstream. (b) 3D printed metasurface prototype composed of 8 circular sectors (dashed red lines) decorated with 3 unit-cells in each sector. Numbers from I to VIII correspond to helicoidal unit-cells designed in Fig. 5.2. (c) Helicoidal unit-cells with global dimensions: $d = 30$mm, $h = 100$mm, $S_1 = 1$mm, $S_2 = 0.5$mm and different levels of space coiling.

containing 8 and 16 holes, as depicted in Fig. 5.6b. The diameter of the holes holding the unit-cells is chosen to be 0.8mm bigger than $d = 30$mm (unit-cell diameter) in order to fit the helicoidal unit-cells in the support holes. Each of the 8 sectors of the metasurface is filled with 3 identical samples of one of the 8 different unit-cells shown in Fig. 5.5c and designed in the previous section. The metasurface is placed between two cylindrical tubes of inner diameter 194mm and length 800mm. An electrodynamic loudspeaker is located at the termination of one duct (upstream), and the other termination is closed by an acrylic glass plate, holding a row of 5 PCB 130D20 1/4 inches measurement microphones. The microphone support is free to rotate around the waveguide axis, in order to scan the whole cross-section, thanks to a circular groove adapted to the periphery of the duct. Finally, the perimeter of the tube is graded, and the acoustic wavefront is measured by spinning the measuring plate from 0° to 360°. The measured sound pressure is then processed with a Bruel & Kjaer Type 3160 Pulse multichannel analyzer. Although the closed termination presented by the microphone plate
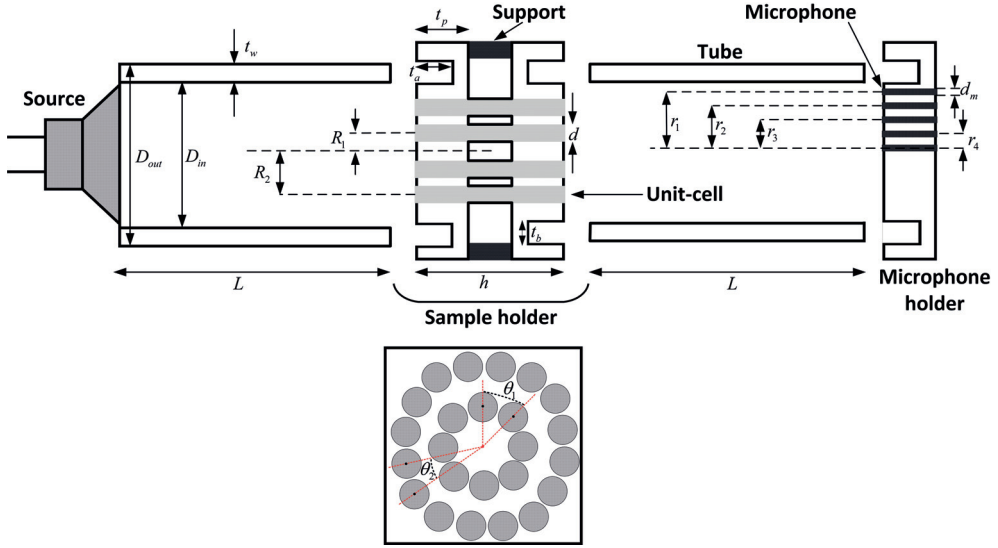
Figure 5.6: Schematic representation of the acoustic OAM measurement setup.

Table 5.2: OAM measurement setup dimensions.

Symbol	Value (mm)	Symbol	Value (mm)
D_{out}	200	h	100
D_{in}	194	θ_1	45°
t_w	3	θ_2	22.5^o
t_b	3.5	R_1	45
t_a	4	R_2	81.50
t_p	8	r_1	88
d	30	r_2	66
d_m	7	r_3	44
L	800	r_4	22

to the acoustic field yields standing waves, the acoustical vortices are still preserved and can be measured over the transversal plane. Figure 5.7 shows the experimental set up used to measure the helical out put wave front of the OAM metasurface.

5.4.3 Numerical simulations and measurement results

Simulation procedure:
The numerical assessment of the proposed prototype is done with commercial finite element analysis software Comsol Multiphysics, following a geometry similar to the one presented on Fig. 5.5a, with the substitution of an anechoic condition for the microphone holder. All boundaries in the simulation set up are set to sound hard boundary condition except the input and output of the test tube which are defined as pressure sound source and absorbing
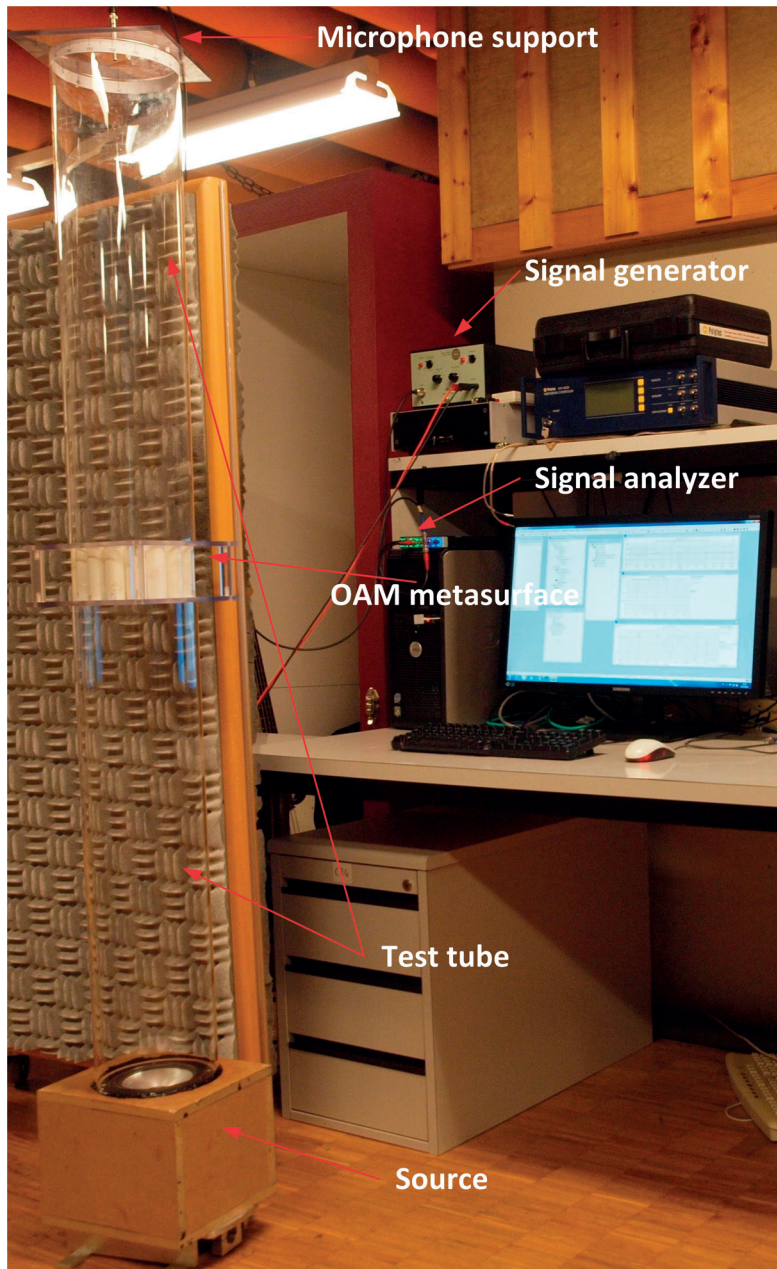
Figure 5.7: Acoustic OAM measurement setup.

boundary condition, respectively. Finally, the Pressure Acoustic physics module is used in the frequency domain to simulate the structure.

Discussion:

Figure. 5.8 illustrates the sound pressure amplitude (a) and phase (b) over the microphone holder surface, both with measurements (i) and numerical simulation (ii). The phase of the sound pressure is covering the full phase of $(0 - 2\pi)$ over the cross-section as it is expected
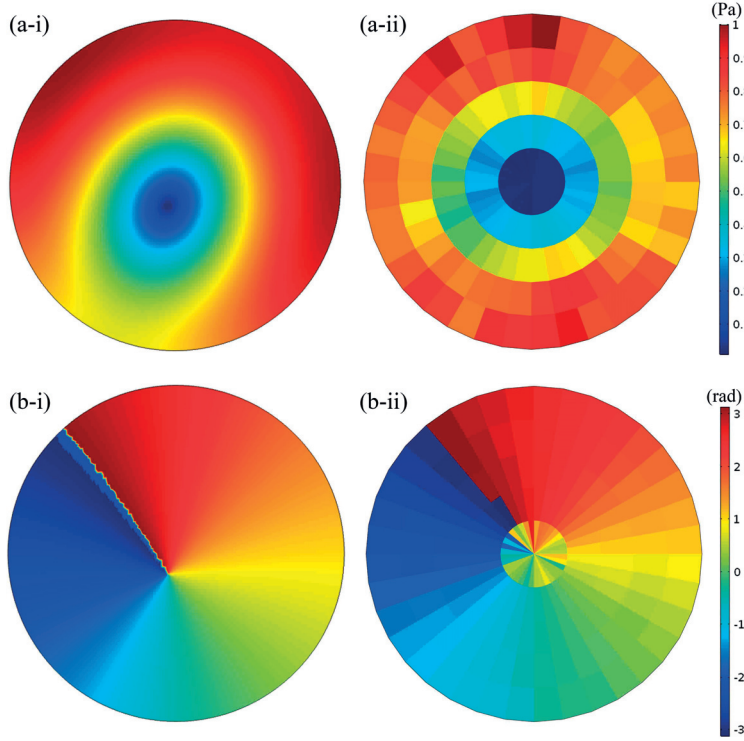
Figure 5.8: Simulated and measured acoustic field distribution in the transversal plane, at frequency $f = 1060$ Hz. (a) Amplitude and (b) Phase for (i) Simulation and (ii) Measurement.

for acoustic vortices, despite a singularity point (where all pressure phase are concentrated) slightly off center. This may be explained by the lack of uniformity of the transmission amplitudes observed within the different unit-cells depicted in Fig. 5.2. In Fig. 5.8b the singularity point can be also visualized on the pressure amplitude distribution over the measured surface as the region where sound pressure amplitude drops to zero. A close study of the measured pressure amplitude distribution reveals that, opposite to the simulated results, the pressure dip is symmetrical and centered. This is due to the coarse spatial resolution of the measurement set up. Moreover, a phase ambiguity arises near the center [114]. The point with the lowest pressure amplitude also coincides with the point of phase singularity, in agreement with the theoretical descriptions of acoustic vortices. In these acoustic vortices, the amplitude distribution is expected to be symmetrically doughnut-shaped. However, the simulated and measured data disagree in particular for the points further away from the center where lobes of higher amplitude do appear. This is also explained by the non-uniform amplitudes of the unit-cells and the discrepancies between the theoretically designed and practically implemented unit-cells. The spatially shifted singularity point, as well as the asymmetry of the amplitude distribution in the wavefront, can be corrected by better aligning the transmission amplitudes. To correct the deviation of the metasurface output amplitude from the simulated OAM beam for a metasurface with a given area, the amount of transmitted power can be balanced and made uniform by adjusting the density of unit-cells per sector (number per sector).

5.5 Conclusion

Following the study of reflection type acoustic metasurfaces presented in the previous chapter, in this chapter the interaction of sound wave with a transmit type acoustic metasurface was investigated to control the wavefront of the transmitted wave. Indeed, to control the wavefront of the acoustic wave which is transmitted through a metastructure, the phase and amplitude of the acoustic wave are the two parameters in hand which are specified by the phase and amplitude of the transmission coefficient assigned to the metastructure or its constituent meta-atoms denoted by unit-cells. Hence, by discretizing the metastructures to subwavelength unit-cells and engineering the transmission coefficient of each unit-cell, the required engineered transmitted wavefront is achieved. Accordingly, a new method to produce acoustic vortices based on acoustic metasurfaces was introduced which converts acoustic plane waves (generated from a single sound source) to helical waves. The proposed strategy relies on phase coding a surface using labyrinthine unit-cells with a view to engineering the transmission phase through each unit-cell. Moreover, a mathematical framework was presented which enables fast design and optimization and facilitates geometrical rendering, meshing and numerical simulation. Spatial frequency modulation was used to improve the impedance matching to achieve uniform transmission. Additionally, the physical length of the proposed unit-cell has been reduced to less than $\lambda/3$, which is especially important for low frequency sounds. Finally, 3D prototyping technology has been employed for easy fabrication of such a complex structure and the fabricated prototype was measured to demonstrate functionality of acoustic transmit type metasurface to transform impinging acoustic plane wave to acoustic helical wave. Using fast prototyping technique to fabricate the metasurface, makes the proposed method a simple yet practical and economical way to generate helical waves which can be used to demonstrate sound wave rotation. The easy production of acoustic vortices should open new horizons in many areas, like transfer of acoustic angular momentum to matter, acoustic trapping, tweezers, spanners and underwater alignment applications.

By covering the transmission phenomenon in acoustic metasurfaces in this chapter, all the main wave-matter interaction scenarios were studied through out this thesis. In the following chapter this thesis concluded by summarizing and highlighting the main achievements of this work on different wave phenomena presented in this chapter and three previous ones.

6 Conclusions and Perspectives

6.1 Summary of the results

This thesis had studied different wave phenomena, like propagation, guided-waves, radiation, refraction, reflection and transmission, which arise when sound waves interact with the metastructures defined in this thesis as acoustic metamaterials. Each one of the aforementioned wave phenomena have been investigated in the frame of different scenarios, all including acoustic metamaterials. This has led to innovative designs and to create novel functionalities of paramount relevance from engineering and application points of view. After an introductory chapter, including a brief survey on the history of metamaterials and a short bibliographic study in acoustic metamaterials, the main results achieved in this research have been reported in the next four chapters, and are summarized here again:

- *Lumped circuit modelling and transmission-line based description of acoustic CRLH metamaterials (Chapter 2).*
  Specific versions of transmission-line (TL) and lumped circuit theory were proposed as simple yet powerful models to analyse acoustic metamaterials. Then, an acoustic CRLH metamaterial was designed using TL theory, which allowed the study of its guided-wave behaviour.

- *Upgrading the transmission-line model of CRLH metamaterials to describe and design acoustic leaky-wave antennas (Chapter 3).*
  In analogy with the well-known optical dispersive prism, an acoustic dispersive prism was proposed to physically decompose an input broadband sound signal into its Fourier components. To achieve such a structure two significant barriers were overcome: firstly, the negligible dispersion of the usual materials' response to acoustic waves in the audio frequency regime and, secondly, the bad impedance matching between the ambient medium and the matter. These barriers are responsible of preventing, respectively, adequate spectral separation and efficient energy transfer. These problems were tackled by leveraging the dispersive nature of acoustic metamaterials and the radiation charac-

teristics of acoustic leaky-wave antennas.

- *Design, analytical modelling and fabrication of acoustic single sensor sound source localizer (Chapter 3).*
  Using the one-to-one frequency-direction function of our leaky wave antenna, it can be deduced that in the radiation (or fast-wave) region of the antenna every direction of arrival can be assigned to each frequency. Therefore, if the antenna is used in the receiving mode, the direction of the incoming sound wave can be mapped into the spectrum of the received power and the location of the sound source can be located by the received power (amplitude of the signal). Hence localizing a source using only one microphone and without resorting to the phase information of the received signal is now possible.

- *Design and lumped circuit modelling of acoustic ultra-thin metasurface as reflectarray antenna (Chapter 4).*
  A membrane-capped cavity design was proposed as an ultra-thin unit-cell to achieve an engineered metasurface with prescribed impedance. This allows a complete manipulation of the reflected wavefront. The ultra-thin feature of this unit-cell is the result of exploiting the frequency dependent mass/modulus type response of the membrane, where the phase lag/lead is controlled by changing the membrane thickness. Due to the very high sensitivity of the impedance of the membrane to its thickness, the full reflection phase span of $[0-2\pi]$ is feasible by only changing the thickness of the membrane in the order of 200 μm. Finally, this unit-cell with the thickness of only $\lambda/30$ was used to design the acoustic counterpart of an electromagnetic reflectarray antenna. The novelty and main impact of this study for the acoustic community resides in the substantial thinness of the achieved device, which fulfils the acoustic metasurface criterion requiring subwavelength thickness.

- *Design and numerical assessment of ultra-thin acoustic carpet cloak (Chapter 4).*
  When an acoustic wave impinges an obstacle placed over an acoustically hard surface, the resulting shape of the back scattered field may differ substantially from the original back scattered field due to the bare ground. An acoustic metasurface is proposed to manipulate the back scattered wave, creating the illusion of reflection from a bare ground. This was achieved using the proposed ultra-thin unit-cell based on membrane capped cavity. The resulting subwavelength acoustic carpet cloak is comparable in terms of thinness to optical skin cloaks, and represent a valid and improved alternative to transformation-based acoustic cloaks.

- *Design and fabrication of acoustic helicoidal labyrinthine unit-cell and generation of acoustic helical wavefront (Chapter 5).*

New acoustic helical unit-cells were proposed, designed and fabricated, based on the unique property of helicoidal surfaces to modulate the space and create a means to add any required phase to the transmitted wave. The novelty of this geometry resides not only in the space saving provided by its ($\lambda/3$) thickness but also in its potential for being spatially modulated for impedance matching purposes without changing the sound path cross section. These helicoidal unit-cells were used to design an acoustic orbital angular momentum metasurface where the surface is phase-coded into 8 distinct $\pi/4$ spaced phased unit-cells. It was numerically and empirically demonstrated that the resulting metasurface can transform an acoustic plane wave-front into a helical wave-front. Acoustic orbital angular momentum metasurfaces can be used for alignment purposes and also to transfer angular momentum from a fluid to matter. Moreover, it can be exploited to control the angular rotation of levitating particles.

6.2 Perspectives

As stated from the beginning of this thesis, this work is on electromagnetic inspired acoustic metamaterials and therefore we were focused on the possible applications of acoustic metamaterials which have been borrowed from electromagnetics. Moreover, being inside a newly emerging field, we have been able only to touch the rich diversity of acoustic metamaterials and to provide hints towards their promising applications, but undoubtedly, much more amount of time and resources will be needed to end into actual real-life applications. Moreover, the multidisciplinary nature of this field requires the collaboration of researchers from different fields to ensure its productivity and success. Here, we propose some additional research directions which are believed to lead to result in substantially improved acoustic metamaterials.

6.2.1 Three dimensional printing and additive manufacturing

In the recent years, the use of 3D printing as a nascent technology was really noticeable in all metamaterial communities. Especially, and as witnessed by literature, a rising trend toward using fast prototyping is clearly observed in the acoustic metamaterial community. For example, in this thesis the construction of several complex prototypes would have been very difficult if not impossible if additive manufacturing hadn't been used. The connection between metamaterials and the 3D printing can be compared to the connection between photolithography and printed circuit technology, which revolutionized the electronic devices. The near future will probably witness very powerful additive manufacturing techniques, that can produce not only very precise and high resolution details of a prototype, but can also have the potential for tailoring its material properties by using and mixing different raw materials. Therefore a visionary path for future research can be the full application of 3D printing to the design of acoustic metamaterials, in order to investigate its potentials and shortcomings to fulfil the needs that conventional materials cannot provide.

6.2.2 Nonlinear, active, inhomogeneous and anisotropic elements

Usually the unit-cells as meta-atoms of metamaterials are made of linear, passive, homogeneous and isotropic materials. Although, there is no restriction or convention on the material specifications of the unit-cells, such a choice is made to simplify the design procedure. Consequently, the designed metamaterials carry the ingrained drawbacks of their unit-cells. For example, passive acoustic metamaterials are limited by their operating short bandwidth, and it is not possible to tune their material properties or operating frequency band. To achieve more degrees of freedom on the design and also to better control the acoustic metamaterials the use of active elements seems to be an unavoidable fact. Any electrically, electromagnetically or mechanically controllable acoustic elements may be used for this purpose. Acoustic smart walls, inspired by acoustic metasurfaces, to selectively manipulated the impinging wave can be foreseen as a potential application in this scope. Following the same path, highly nonlinear unit-cells may be leveraged to achieve acoustic nonreciprocal devices or inhomogeneous and anisotropic unit-cells can be used in acoustic metasurfaces to achieve direction based functionalities.

6.2.3 Multidisciplinary research

Due to their peculiar responses and interesting potential applications, metamaterials have attracted attention from researchers working in many different scientific areas. By the same token, they should push these scientists from different areas dealing with wave phenomena to come together and brainstorm in joint conferences or by means of published literature. Nowadays, the acoustic circulator, the acoustic prism or the acoustic diode are no longer abstract concepts but real devices. And if in optics cloaking is hoped to hide an object or to create optical illusions, elastic cloaking could be an effective way to protect buildings from earthquakes. Step by step, metamaterials bridge the gap between different classical fields of physics and also get closer to quantum mechanics. Why not to leverage the multidisciplinary features of metamaterials towards multi-functional space-saving devices? In this regard, a circulator, diode, cloak or a prism is a device which works for either electromagnetic, acoustic or other types of waves.

6.2.4 Beyond metamaterials

In the course of research in the field of metamaterials some questions strike the mind and frequently no answers are readily found. It is believed that these questions could potentially originate new fields of research. For instance: What is the acoustic counterpart of lasers? What can replace an electromagnetic vector network analyser to simplify acoustic measurement? What about doing mathematical and/or logical operations with acoustic waves? What would be the advantages or disadvantages?

A Acoustic waves

Acoustic waves are the pressure fluctuations in a compressible fluid. The restoring forces responsible for propagating acoustic waves are the pressure changes that happen when the fluid is compressed or expanded. Back and forth movement of a fluid particles make the adjacent sections to be compressed or rarefied. The particle is an infinitesimal volume of the fluid that is large enough to contain millions of molecules and consequently be thought of a continuous medium, but also small enough that all acoustic variables are uniform throughout [131]. Although the molecules of a fluid are in motion, any small volume can be treated as an unchanging unit because those molecules leaving the volume are replaced by an equal amount. In the case of audible pressure field of moderate intensity, the fluid can be considered as lossless and the change in the density of the medium will be small compared with its equilibrium value.

A.1 Pedagogical approach

As Feynman explains in his lectures on physics [56] (Chapter 47), the physics of the sound waves involves three features :

I. *The gas moves and changes the density.*

If the position of a portion of unperturbed air is denoted by x and the small displacement of that portion due to the sound wave is shown by $\xi(x, t)$, then the new position of that perturbed portion will be $x + \xi(x, t)$. Following the same procedure for the unperturbed nearby portion $x + \Delta x$ leads to $x + \Delta x + \xi(x + \Delta x, t)$ as a new position of the perturbed nearby portion which has been schematically shown in Fig. A.1 (inspired by [56]). For plane wave sound which propagates in x-direction, the amount of air, per unit area, in undisturbed case will be $\rho_0 \Delta x$, where ρ_0 represents the density of the air. After sound passes and disturb the air, this aforementioned amount of air is squeezed between $x + \xi(x, t)$ and $x + \Delta x + \xi(x + \Delta x, t)$. Now the density of the perturbed air ρ is calculated as

$$\rho_0 \Delta x = \rho [x + \Delta x + \xi(x + \Delta x, t) - x - \xi(x, t)]. \tag{A.1}$$

As Δx is small, the Eq.A.1 can be reformulated as

$$\rho_0 \Delta x = \rho \left[\frac{\partial \xi}{\partial x} \Delta x + \Delta x \right]. \tag{A.2}$$

If the pressure and density of the air in the undisturbed and disturbed cases are denoted by (P_0, P) and (ρ_0, ρ), then

$$P = P_0 + P_e \tag{A.3a}$$

$$\rho = \rho_0 + \rho_e, \tag{A.3b}$$

where P_e and ρ_e are excess pressure and density and always very small compared to P_0 and ρ_0. Then Eq. A.2 is simplified to

$$\rho_e = -\rho_0 \frac{\partial \xi}{\partial x} - \rho_e \frac{\partial \xi}{\partial x}. \tag{A.4}$$

As $\rho_e \frac{\partial \xi}{\partial x}$ is small compared with $\rho_0 \frac{\partial \xi}{\partial x}$. Thus, the following relation is found:

$$\rho_e = -\rho_0 \frac{\partial \xi}{\partial x}. \tag{A.5}$$

II. *The change in density corresponds to a change in pressure.*
The pressure of any material is described as a function of its density ($P = f(\rho)$). As ρ_e is very small compared to ρ_0, by using Eq. A.3 and expanding it by tailor series, for first order approximation the relation of pressure and density for perturbed case is found as

$$P_0 + P_e = f(\rho_0 + \rho_e) = f(\rho_0) + \rho_e f'(\rho_0). \tag{A.6}$$

Here, $P_0 = f(\rho_0)$ and $f'(\rho_0)$ is the derivative of $f(\rho)$ at $\rho = \rho_0$. Thus, the relation of excess pressure P_e is calculated as

$$P_e = \kappa \rho_e, \tag{A.7a}$$

$$\kappa = f'(\rho_0) = \left(\frac{dP}{d\rho} \right)_0. \tag{A.7b}$$

III. *Pressure inequalities generate gas motion.*
As explained before the mass of a thin unperturbed slab of air of length Δx with unit area perpendicular to x is $\rho_0 \Delta x$. If this slab of air experience an acceleration of $\frac{\partial^2 \xi}{\partial t^2}$ so the net force on this slab will be equal to $\rho_0 \Delta x \frac{\partial^2 \xi}{\partial t^2}$. On the other hand, there are two forces that are applied to the slab of air at x and $x + \Delta x$ in the $+x$ and $-x$-directions respectively. Hence, the net force applied on the air slab is found as,

$$P(x, t) - P(x + \Delta x, t) = -\frac{\partial P}{\partial x} \Delta x = -\frac{\partial P_e}{\partial x} \Delta x. \tag{A.8}$$

and the equation of motion which is produced by the pressure is,

$$\rho_0 \frac{\partial^2 \xi}{\partial t^2} = -\frac{\partial P_e}{\partial x} \tag{A.9}$$

Using Eq. A.5, A.7 and A.9 the acoustic wave propagation equation which describes the behaviour of sound in matter is derived as

$$\frac{\partial^2 \xi}{\partial x^2} - \frac{1}{c_s^2} \frac{\partial^2 \xi}{\partial t^2} = 0, \tag{A.10}$$

where $c_s^2 = \kappa$. As any plane wave which moves with a constant velocity v has the form $f(x \pm vt)$ and it can be the solution of Eq. A.10 if $v = c_s$. It means the velocity of sound wave is denoted by c_s which is connected to the property of the medium after $c_s = \sqrt{\kappa} = \sqrt{\left(\frac{dP}{d\rho}\right)_0}$.
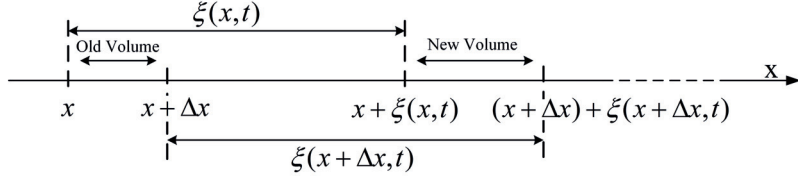
Figure A.1: An infinitesimal volume of a fluid in perturbed and unperturbed state.

A.2   General approach

A.2.1   The conservation of mass

The conservation of mass express that the mass can not be created nor destroyed. Let's suppose a fixed volume V of a fluid confined by a surface S. Conservation of mass dictates that the time rate of change of the mass inside a volume should be equal to the mass per unit time entering or leaving that same volume [132]. The net mass per unit time leaving a small area ΔS of the surface S is

$$\rho(x, t)\mathbf{v}(x, t) \cdot \mathbf{n}(x)\Delta S, \tag{A.11}$$

where ρ is the mass density of the fluid, $\mathbf{v}(x, t)$ is the vectorial fluid velocity at point x over the surface S and $\mathbf{n}(x)$ is the outward unit normal vector at point x. Thus, the net mass leaving the volume V per unit time is the integral of Eq. A.11 over surface S, and the conservation of mass is found as,

$$\frac{d}{dt} \int\int\int_V \rho(x, t) dV = -\int\int_S \rho(x, t)\mathbf{v}(x, t) \cdot \mathbf{n}(x) dS, \tag{A.12}$$

Using the Gauss' theorem ($\iint_S A \cdot \mathbf{n} dS = \iiint_V \nabla \cdot A dV$) the Eq. A.12 is simplified to

$$\int\int\int_V \left[\frac{\partial \rho}{\partial t} + \nabla \cdot (\rho \mathbf{v}) \right] dV = 0 \tag{A.13}$$

and finally

$$\frac{\partial \rho}{\partial t} + \nabla \cdot (\rho \mathbf{v}) = 0. \tag{A.14}$$

A.2.2 Euler's equation of motion for a fluid

Let's suppose a moving volume $V^*(t)$ in Fig. A.2 where each point on the surface $S^*(t)$ of this volume is moving with a fluid velocity $\mathbf{v}$ [132]. For constant mass of this volume the mass times the acceleration is equal to the time rate of change of momentum

$$\frac{d}{dt}\int\int\int_{V^*} \rho \mathbf{v} dV = \int\int_{S^*} f_S dS + \int\int\int_{V^*} f_B dV \tag{A.15}$$

Here, f_S represents surface force per unit area by the surrounding environment and includes the momentum transferred by the molecular motion on the surface S^* and also intermolecular force exerted on the molecules inside the volume by molecules outside it. f_B is the body force per unit volume (e.g. due to the gravity). As the gravity has negligible impact on the motion of particles only f_S is taken into account. As f_S is the force applied per unit area and $\mathbf{n}$ is the outward normal vector to the surface S^*, then by neglecting viscosity

$$f_S = -\mathbf{n} p \tag{A.16}$$

where p is the pressure. Using the gradient theorem ($\iint_S b\mathbf{n} dS = \iiint_V \nabla b dV$) and Eq. A.16, Eq. A.15 is reformulated as

$$\frac{d}{dt}\int\int\int_{V^*} \rho \mathbf{v} dV = -\iiint_{V^*} \nabla p dV. \tag{A.17}$$

Volume V^* which is the accumulation of many small fluid particles that the fluid velocity within each of them is everywhere the same as the velocity of their center of mass. Since the mass of each fluid particle is constant then the time rate of change of momentum of a particle of the moving volume is $\rho \Delta V^* d\mathbf{v}(\mathbf{R}(t), t)/dt$, where $\mathbf{R}(t)$ is the position of the particle at time t. Then

$$\frac{d\mathbf{v}(\mathbf{R}(t), t)}{dt} = \frac{\partial \mathbf{v}}{\partial t} + \frac{\partial \mathbf{v}}{\partial x}\frac{\partial x}{\partial t} + \frac{\partial \mathbf{v}}{\partial y}\frac{\partial y}{\partial t} + \frac{\partial \mathbf{v}}{\partial z}\frac{\partial z}{\partial t} = \frac{\partial \mathbf{v}}{\partial t} + (\mathbf{v} \cdot \nabla)\mathbf{v} = \frac{D\mathbf{v}}{Dt}. \tag{A.18}$$

Using Eq. A.17 and A.18 gives

$$\iiint_{V^*} \left(\rho \frac{D\mathbf{v}}{Dt} + \nabla p \right) dV = 0 \tag{A.19}$$

Thus, it is concluded that

$$\rho \frac{D\mathbf{v}}{Dt} + \nabla p = 0 \tag{A.20}$$
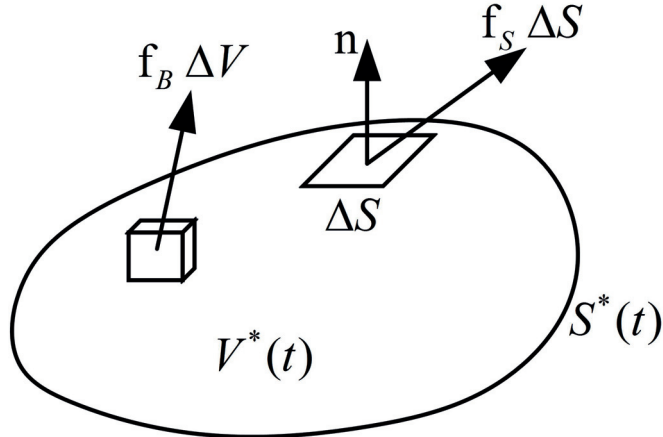
Figure A.2: Moving volume of fluid particles, each point on the surface moves with velocity $\mathbf{v}(\mathbf{x_S}(t), t)$

A.2.3 Pressure-Density relation

As also explained before, the relation between pressure and density can be written as $p = f(\rho)$ which was explained in section A.1. This relation can be also studied from thermodynamic point of view. Newton assumed acoustic wave propagation is done in isothermal condition which lead to the calculation of sound wave velocity 16% below the measured value. Later, Laplace assumed it to happen under adiabatic process which lead to exact value. In fact acoustic processes are nearly isentropic (adiabatic and reversible) and the thermal conductivity of the fluid and the temperature gradient are small enough that no appreciable thermal energy transfer between adjacent fluid particles [131]. For the perfect gas it is described by

$$\frac{p}{p_0} = \left(\frac{\rho}{\rho_0}\right)^\gamma \tag{A.21}$$

where $\gamma = l_p/l_v$ and l_p and l_v are the constant specific heat coefficients at constant pressure and volume respectively. However, for fluids other than perfect gas the relation should be determined experimentally and this process can be described by Taylor's expansion

$$p = p_0 + \left(\frac{dp}{d\rho}\right)_{\rho_0} (\rho - \rho_0) + \frac{1}{2}\left(\frac{d^2p}{d\rho^2}\right)_{\rho_0} (\rho - \rho_0)^2 + \dots \tag{A.22}$$

117

If the fluctuations are small then the second term needs to be taken into account and

$$p - p_0 \approx \beta \frac{(\rho - \rho_0)}{\rho_0} \tag{A.23}$$

where $\beta = \rho_0 (dp/d\rho)_{\rho_0}$ is the adiabatic bulk modulus.

A.3   Linear acoustics wave equation

Acoustic waves can be considered as small amplitude perturbations in the medium where $(p_0, \rho_0, \mathbf{v}_0)$ are the pressure, density and velocity of the unperturbed medium. Hence, the pressure and the density of the medium in the presence of the acoustic waves reads

$$p = p_0 + p_e \tag{A.24a}$$
$$\rho = \rho_0 + \rho_e, \tag{A.24b}$$

where p_e and ρ_e are the excess pressure and density due to the acoustic wave disturbance. Using Eq. A.24 and plugging it into Eq. A.14, A.20 and A.23 the linear form of these equations are calculated as [132]

$$\frac{\partial \rho_e}{\partial t} + \rho_0 \nabla \cdot (\mathbf{v_e}) = 0 \tag{A.25}$$

$$\rho_0 \frac{\partial \mathbf{v_e}}{\partial t} = -\nabla p_e \tag{A.26}$$

$$p_e \approx (\frac{dp}{d\rho})_{\rho_0} \rho_e = c^2 \rho_e \tag{A.27}$$

Using the linear form of equations of mass conservation, Euler's equation and pressure-density relation the acoustic wave equation is derived as

$$\nabla^2 p - \frac{1}{c^2} \frac{\partial^2 p}{\partial t^2} = 0. \tag{A.28}$$

B Transmission-line modelling

In electromagnetic a transmission-line is a structure designed to carry electromagnetic waves in a confined medium, these waves should be high in frequency that their wave nature taken into account and waveguides are the most well known devices used guided-wave applications. As the theory of electromagnetic and acoustic wave propagations are very similar mathematically (Helmholtz equation), techniques from transmission-line theory can be used to model acoustic structures and this is called acoustic transmission-line theory. Note that, for low frequencies that the wavelength is comparable to the acoustic or electromagnetic elements, for the sake of simplicity, the lumped circuit model is used instead of TL model. It is obvious that voltage as a cross parameter in the circuit theory is similar to pressure in acoustics and current as a through parameter can be represented by volume velocity. Based on these two assumptions the acoustic impedance can be defined as

$$z = \frac{p}{q}. \tag{B.1}$$

Note that the particle velocity is usually used in acoustic formulations as in Eq. A.26 and it is converted to volume velocity ($q = Sv$) to calculate the acoustic impedance. Here, S is the cross sectional area of the medium where the acoustic impedance is calculated and v is the particle velocity.

B.1 Telegrapher's equation in Electromagnetics vs. Spring-mass model in Acoustics

The telegrapher's equations are coupled linear differential equations between voltage and current that describe the voltage and current on an electrical transmission-line. For instance, two lossless parallel conductors can be considered as a transmission-line which is composed of an infinite series of two-port elementary components. These two port networks consist of series inductors $jLdx$ and parallel capacitors Cdx as in Fig. B.1. Considering the time harmonic regime and getting ride of $e^{j\omega t}$, the Kirchhoff's circuit law for such a infinitesimal

elementary circuit configuration reads [133]:
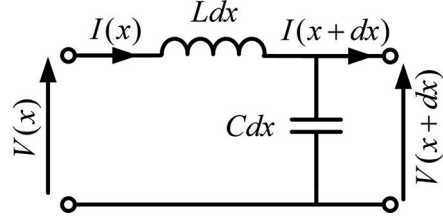
Figure B.1: Schematic representation of the infinitesimal section of the transmission line.

$$\frac{\partial V}{\partial x} = -j\omega L I \tag{B.2a}$$

$$\frac{\partial I}{\partial x} = -j\omega C V \tag{B.2b}$$

and combining these two equations leads to time harmonic wave like equation

$$\omega^2 V + \frac{1}{LC}\frac{\partial^2 V}{\partial x^2} = 0 \tag{B.3a}$$

$$\omega^2 I + \frac{1}{LC}\frac{\partial^2 I}{\partial x^2} = 0. \tag{B.3b}$$

Now lets came back to acoustics, using Eq. A.25-A.27 in the time harmonic regime the relation of acoustic pressure (p) and particle velocity (v) can be written as

$$\nabla p = -j\omega\rho v \tag{B.4a}$$

$$\nabla \cdot v = -\frac{j\omega}{K}p, \tag{B.4b}$$

where $K = \rho_0 c^2$ is the bulk modulus of the fluid. The system of Eq. B.4 in 1D form is simplified to

$$\frac{\partial p}{\partial x} = -j\omega\rho v \tag{B.5a}$$

$$\frac{\partial v}{\partial x} = -j\omega\frac{1}{K}p \tag{B.5b}$$

Assuming p (pressure) is the analogue of V (voltage) and v (velocity) is the analogue to I (current), by analogy between Eq. B.2 and Eq. B.5 the acoustic equivalent of electromagnetic components can be deduced and summarized as: if $P \sim V$ and $v \sim I$ then $\rho \sim L$ and $1/K \sim C$. In mechanical engineering, a spring-mass system is a straightforward approach to deal with complex problems. Figure B.2 depicts such a model for lossless acoustic wave propagation in a fluid, this model can be described as a periodic sequence of spring-mass which was first proposed by Newton [64]. The length l is introduced to define the distance between the masses and k and m represent spring constant and mass, respectively. Then, for the system at rest, the position of the nth mass is expressed by $x_n = nl$ and the dynamic behaviour of the nth

mass becomes [134]:

$$m\frac{\partial^2 \xi_n}{\partial t^2} - k[(\xi_{n+1} - \xi_n) + (\xi_n - \xi_{n-1})] = 0,$$

(B.6)

where ξ_n is the displacement of nth mass from its equilibrium state. If l is considered as an infinitesimal segment of the fluid then E. B.6 is written as

$$\frac{\partial^2 \xi}{\partial t^2} - \frac{k}{m}\frac{\partial^2 \xi}{\partial x^2} = 0.$$

(B.7)

Finally, comparing the Eq. B.3 and B.7 it is concluded that telegrapher's circuit model and
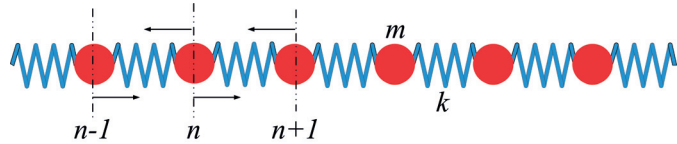
Figure B.2: Schematic representation of spring-mass system for acoustic wave propagation in a fluid.

spring-mass model results in the same wave equation if, $L \sim m$ and $C \sim \frac{1}{k}$, respectively. Such a circuit model is called the lossless TL model of the acoustic wave propagation in the air or in a tube and it is equivalent to the aforementioned mechanical model of periodic sequence of spring-mass system.

B.2   Acoustic lumped circuit model

Lumped circuit models use circuit elements which are too small compared to the wavelength and this leads to negligible error in the propagation time/phase. However, if the wavelength is comparable to lumped elements, the general TL theory should be used.

B.2.1   Acoustic impedance of a pipe terminated with an arbitrary impedance

Lets assume that in a tube depicted in Fig. B.3, with cross-sectional area S and length l which is terminated at $x = l$ with an arbitrary acoustic impedance Z_L, the fluid is driven by a piston at $x = 0$ with angular frequency ω. The wave inside the tube is written in the form of:

$$p = ae^{j[\omega t + \gamma(l-x)]} + be^{j[\omega t - \gamma(l-x)]},$$

(B.8)

and using Eq. A.26, the volume velocity is calculated as,

$$q = \frac{S}{\rho_0 c}[ae^{j[\omega t + \gamma(l-x)]} - be^{j[\omega t - \gamma(l-x)]}]$$

(B.9)

121

and the acoustic impedance at $x = 0$ and L reads:

$$Z(x = l, t) = \frac{p(x = l, t)}{q(x = l, t)} = \frac{\rho_0 c}{S} \frac{a + b}{a - b} = Z_L \tag{B.10}$$

$$Z(x = 0, t) = \frac{p(x = 0, t)}{q(x = 0, t)} = \frac{\rho_0 c}{S} \frac{ae^{j\gamma l} + be^{-j\gamma l}}{ae^{j\gamma l} - be^{-j\gamma l}} \tag{B.11}$$

respectively. By eliminating a and b from Eq. B.11 using B.10 the relation for input impedance of a tube with an arbitrary termination is found [131]

$$Z_0 = Z_c \frac{Z_L + jZ_c \tan \gamma l}{Z_c + jZ_L \tan \gamma l}, \tag{B.12}$$

where $\gamma = \frac{\omega}{c}$ is the wave vector and $Z_c = \frac{\rho_0 c}{S}$ is the acoustic characteristic impedance.
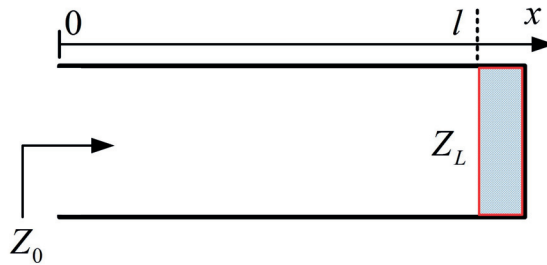
Figure B.3: Schematic representation of a tube terminated with an acoustic impedance Z_L.

B.2.2   Acoustic lumped circuit model of a short length open pipe

For a very short pipe ($l < \lambda/20$) with an open end ($Z_L = 0$) the Eq. B.12 will be [135]

$$Z_0 = jZ_c \tan \gamma l \approx jZ_c \gamma l = j\omega \frac{\rho_0 l}{S}. \tag{B.13}$$

Equation B.13 reveals that a short tube with an open end can be considered as a mass (inductance) of $\frac{\rho_0 l}{S}$.

B.2.3   Acoustic lumped circuit model of a short length pipe with hard termination

For a very short pipe ($l < \lambda/20$) with a hard termination ($Z_L \longrightarrow \infty$) the Eq. B.12 will be [135]

$$Z_0 = jZ_c \cot \gamma l \approx -j \frac{Z_c}{\gamma l} = -j \frac{1}{\omega \left(\frac{Sl}{\rho_0 c_0^2} \right)}. \tag{B.14}$$

Equation B.14 reveals that a short tube with hard termination can be considered as a compli-
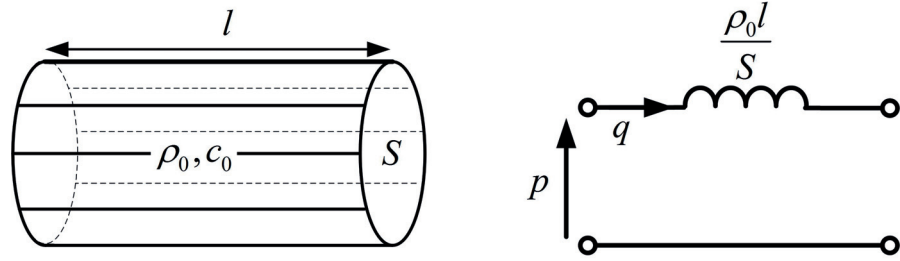
Figure B.4: Schematic representation of a short open tube and its equivalent acoustic lumped circuit model.
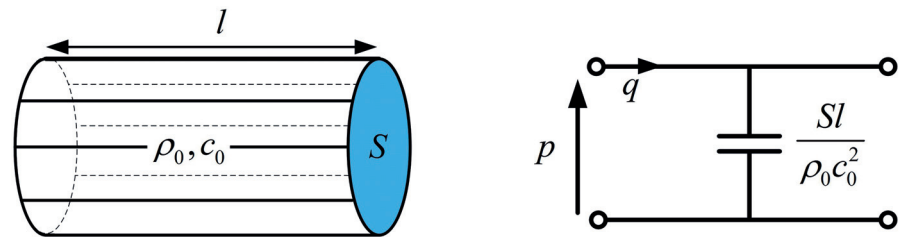
Figure B.5: Schematic representation of a shorted tube with hard termination (in blue) and its equivalent acoustic lumped circuit model.

ance (capacitance) of $\frac{Sl}{\rho_0 c_0^2}$ where compliance is the inverse of the stiffness (elastic modulus, spring constant).

B.2.4   Acoustic lumped circuit model of a long pipe

Acoustic waveguide is a long pipe with hard wall, which confines the acoustic wave inside. As plane wave can propagate inside the acoustic wave guide and the first mode in the acoustic waveguide is $(0,0)$ mode the circuit model of acoustic wave propagation in the air can be adopted for the first mode of acoustic waveguide. That is, the acoustic waveguide can be modelled as a series mass (inductance) and parallel compliance (capacitance). The values of mass and compliance are calculated for infinitesimal sections of a tube using Eq. B.13 and B.14.
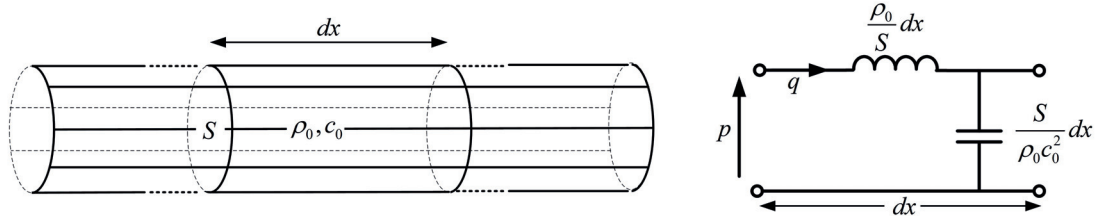
Figure B.6: Schematic representation of a long tube as an acoustic waveguide and equivalent acoustic lumped circuit model for an infinitesimal section.

B.2.5   Acoustic impedance of an open tube

If the pipe is open in its extremities, $Z_L \neq 0$, and the open end will radiate sound into surrounding medium. The purpose of this section is to derive the expression of $Z_L = Z_r$, called the radiation impedance of the open end tube. To this end, a flanged circular pipe is assumed, where the wavelength is large compared to transverse dimensions of the pipe. Therefore, the opening resembles a baffled piston in the low frequency limit. Considering all these assumptions, the problem is simplified to calculate the radiation of a baffled circular piston of radius a and normal complex velocity $v_0 = V_0 e^{j\omega t}$. By considering that dp is the incremental pressure that the motion of dS produces at other element of area dS' of the piston, the total pressure p at dS' can be obtained by integrating Eq. B.15 over the surface of the piston [131],

$$p = j\rho c \frac{V_0}{\lambda} \int \frac{1}{r} e^{j(\omega t - kr)} dS \tag{B.15}$$

where r is the distance between the source and the point that the pressure is being calculated. Note that, in order to calculate the pressure over the piston itself, r is the distance between dS and dS'. Thus, the total force f_s on the piston from the pressure is the integral of p over dS'. There two notes which simplify the calculation of radiation impedance: first, the integration over dS to get p and then over dS' to get f_s includes both force on dS' resulting from the motion of dS and vice versa. Second, based on acoustic reciprocity, these two forces must be the same. Hence, the result of the double integration is twice of the value that is obtained when the limits of integration were chosen to include the force between each pair of elements only once [131]. As shown in Fig. B.7 (inspired by [131]), if σ be the radial distance from the center of the piston to dS', then the maximum distance from dS' to any point within the circle is $2\sigma \cos\theta$. Hence, the entire area within the circle will be covered if the integration limits be from 0 to $2\sigma \cos\theta$ and then integrate θ from $-\pi/2$ to $\pi/2$ [131].

If the integration of dS' is extended over the entire surface of the piston by setting $dS' = \sigma d\sigma d\psi$ and integrating ψ from 0 to 2π and then σ from 0 to a. After multiplying this by two the desired expression is found as [131],

$$f_s = \int p \, dS' = 2j\rho c \frac{V_0}{\lambda} e^{j\omega t} \int_0^a \int_0^{2\pi} \int_{-\pi/2}^{\pi/2} \int_0^{2\sigma \cos\theta} \sigma e^{-jkr} dr \, d\theta \, d\psi \, d\sigma \tag{B.16}$$

Using Eq. B.16, the radiation mechanical impedance $Z_{mr} = \frac{f_s}{v_0}$ is found as:

$$Z_r = \rho c S \left[R_1(2ka) + j X_1(2ka) \right] \tag{B.17}$$

$$R_1(x) = 1 - \frac{2J_1(x)}{x} = \frac{x^2}{2 \times 4} - \frac{x^4}{2 \times 4^2 \times 6} + \frac{x^6}{2 \times 4^2 \times 6^2 \times 8} - \dots \tag{B.18}$$

$$X_1(x) = 1 - \frac{2H_1(x)}{x} = \frac{4}{\pi}\left(\frac{x}{3} - \frac{x^3}{3^2 \times 5} + \frac{x^5}{3^2 \times 5^2 \times 7} - \ldots\right). \tag{B.19}$$

In the low frequency limit the radiation impedance can be approximated by first terms of the power expansions. So the Z_{mr} will be [131],

$$Z_{mr} = \rho c S \left[\frac{1}{2}(ka)^2 + j\frac{8}{3\pi}ka\right]. \tag{B.20}$$

For an unflanged open pipe the experiments indicate that radiation impedance is approxi-
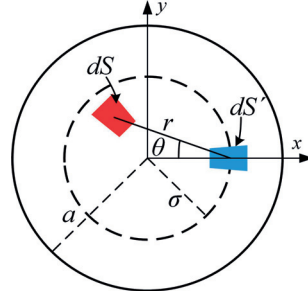
Figure B.7: Surface elements dS and dS' used in obtaining the reaction force on a radiating plane circular piston

mately [131],

$$Z_{mr} = \rho c S \left[\frac{1}{4}(ka)^2 + j0.6ka\right]. \tag{B.21}$$

As the formulas for the impedance of the open stub when the radiation impedance is taken into account become very complicated, these relations can be simplified with changing the actual length of the stub with effective length of the stub which is written as [131],

$$L_{\text{effective}} = L_{\text{actual}} + 0.848a \text{ (flanged)} \tag{B.22}$$

$$L_{\text{effective}} = L_{\text{actual}} + 0.6a \text{ (unflanged)} \tag{B.23}$$

C Dynamics of plate vibrations

C.1 Vibration equation

To deal with lossless vibrations of the clamped, isotropic, homogeneous plate the biaharmonic equation,

$$\nabla^4 \xi + \frac{k^4}{\omega^2} \frac{\partial^2 \xi}{\partial t^2} = \frac{\Delta p}{D} \tag{C.1}$$

with the following boundary conditions:

$$\begin{cases} \xi \,|_{r=a} = 0 \\ \frac{d\xi}{dr}\Big|_{r=a} = 0 \end{cases} \tag{C.2}$$

or:

$$\begin{cases} \xi \,|_{x=0,a} = 0 \qquad \xi \,|_{y=0,b} = 0 \\ \frac{d\xi}{dx}\Big|_{x=0,a} = 0 \quad \frac{d\xi}{dy}\Big|_{y=0,b} = 0, \end{cases} \tag{C.3}$$

should be solved for circular plate of radius a or rectangular plate of $a \times b$ respectively [136]. In this equation ξ represents the displacement of the plate, D is the flexural rigidity and defined as $D = \frac{Eh^3}{12(1-v^2)}$, Δp is the net pressure exerted on the plate and k is the propagation constant, defined as $k^2 = \omega \sqrt{\frac{\rho_m h}{D}}$, where ω is the angular frequency. (E, v, ρ_m, h) are the Young's modulus, the poisson's ratio, the mass density and the thickness of the plate respectively. If the applied pressure is considered as harmonic pressure with constant amplitude then the exerted pressure can be written as $\Delta p(t) = \Delta P e^{j\omega t}$ and by plugging it into Eq. C.1 the vibration equation in harmonic domain is derived as,

$$\nabla^4 \xi - k^4 \xi = \frac{\Delta P}{D}. \tag{C.4}$$

C.2 Energy equations

C.2.1 Kinetic energy

In general the kinetic energy of an object is defined as [137],

$$
\begin{cases}
K_t = \int \frac{1}{2} dm \dot{\xi}(t)^2 \\
K_\omega = \int \frac{\omega^2}{2} dm \xi(\omega)^2,
\end{cases}
\tag{C.5}
$$

in time and spectral domain receptively. For the case of clamped vibrating plate $dm = \rho_m dV$, where dV is the elementary volume of integration and $\dot{\xi}(t)$ is the velocity and ω is the angular frequency of the plate. If the point like (lumped) vibration is assumed then the kinetic energy with equivalent quantities can be defined as

$$
\begin{cases}
K_t = \frac{1}{2} m_{eq} \dot{\xi}_{eq}(t)^2 \\
K_\omega = \frac{\omega^2}{2} m_{eq} \xi_{eq}(\omega)^2,
\end{cases}
\tag{C.6}
$$

where m_{eq} is the equivalent mass of the vibrating plate and $\dot{\xi}_{eq}(t)$ and $\xi_{eq}(\omega)$ are the equivalent velocity (time domain) and the equivalent deformation (spectral domain) of the vibrating plate respectively. These quantities are defined as the weighted sum of the velocity or the deformation over the surface,

$$
\begin{cases}
\dot{\xi}_{eq} = \frac{1}{S} \int \dot{\xi} dS \\
\xi_{eq} = \frac{1}{S} \int \xi dS.
\end{cases}
\tag{C.7}
$$

C.2.2 Potential energy

The potential energy of the vibrating plate in both polar and rectangular coordinates are defined as [137]:

$$
U = \frac{1}{2} \int \int D \left\{ \left(\frac{\partial^2 \xi}{\partial r^2} + \frac{1}{r} \frac{\partial \xi}{\partial r} + \frac{1}{r^2} \frac{\partial^2 \xi}{\partial \phi^2} \right)^2 - 2(1-\nu) \left(\frac{\partial^2 \xi}{\partial r^2} \left(\frac{1}{r} \frac{\partial \xi}{\partial r} + \frac{1}{r^2} \frac{\partial^2 \xi}{\partial \phi^2} \right) - \left(\frac{\partial}{\partial r} \left(\frac{1}{r} \frac{\partial \xi}{\partial \phi} \right) \right)^2 \right) \right\} r \, dr \, d\phi
\tag{C.8}
$$

$$
U = \frac{1}{2} \int \int D \left\{ \left(\frac{\partial^2 \xi}{\partial x^2} \right)^2 + \left(\frac{\partial^2 \xi}{\partial y^2} \right)^2 + 2\nu \left(\frac{\partial^2 \xi}{\partial x^2} \right) \left(\frac{\partial^2 \xi}{\partial y^2} \right) + 2(1-\nu) \left(\frac{\partial^2 \xi}{\partial x \partial y} \right)^2 \right\} dx \, dy
\tag{C.9}
$$

If the point like (lumped) vibration is assumed then the potential energy with equivalent quantities can be defined as

$$U = \frac{1}{2} \frac{\xi_{eq}^2}{C_{eq}},$$

(C.10)

where ξ_{eq} is the equivalent deformation and it is defined as Eq. C.7 where C_{eq} is the equivalent compliance of the vibrating plate.

C.3 Impedance of a circular plate with clamped edges

C.3.1 Closed form method

Free vibration

The general solution for the Eq. C.4 in the polar coordinate system for free vibration ($\Delta P = 0$) is [77, 138]

$$\left(\nabla^2 \xi - k^2 \xi\right)\left(\nabla^2 \xi + k^2 \xi\right) = 0,$$

(C.11)

by proposing a solution in the form of

$$\xi(r, \phi) = R(r)P(\phi),$$

(C.12)

and plugging it into Eq. C.11, the free vibration equation of plate will be:

$$\left(\frac{1}{R}\frac{d^2 R}{dr^2} + \frac{1}{rR}\frac{dR}{dr} + \frac{1}{r^2 P}\frac{d^2 P}{d\phi^2} + k^2\right)\left(\frac{1}{R}\frac{d^2 R}{dr^2} + \frac{1}{rR}\frac{dR}{dr} + \frac{1}{r^2 P}\frac{d^2 P}{d\phi^2} - k^2\right) = 0.$$

(C.13)

Equation C.13 can be simplified as,

$$\frac{r^2}{R}\frac{d^2 R}{dr^2} + \frac{r}{R}\frac{dR}{dr} \pm r^2 k^2 = \frac{-1}{P}\frac{d^2 P}{d\phi^2},$$

(C.14)

where, the left side of this equation depends on r (not ϕ), while the right side depends only on ϕ. Thus, each side must be equal to a constant k_ϕ^2 which results in two independent equations for ϕ and r as:

$$\frac{d^2 P}{d\phi^2} + k_\phi^2 P = 0,$$

(C.15)

$$\frac{r^2}{R}\frac{d^2 R}{dr^2} + \frac{r}{R}\frac{dR}{dr} + \left(\pm r^2 k^2 - k_\phi^2\right) = 0.$$

(C.16)

The general solution for the equation (C.15) is

$$P(\phi) = A'' \cos(k_\phi \phi) + B'' \sin(k_\phi \phi). \tag{C.17}$$

Since the solution to ξ must be periodic in ϕ (that is, $\xi(r,\phi) = \xi(r,\phi \pm 2l\pi)$, k_ϕ must be an integer n. If $k_\phi = n$ then the general solution for the Eq. C.16 is

$$R(r) = AJ_n(kr) + A'N_n(kr) + BI_n(kr) + B'K_n(kr) \tag{C.18}$$

where J_n is the Bessel's function of the first kind of order n, N_n is the Neumann's function (Bessel function of the second kind) of the order n and I_n and K_n are the corresponding modified (hyperbolic) Bessel functions. Because of the finite solution for $r = 0$ the constants A' and B' should be zero (N_n and K_n are infinite for $r = 0$). Thus, possible solution for the free oscillation of a plate is

$$\xi(r,\phi) = [AJ_n(kr) + BI_n(kr)][A'' \cos(n\phi) + B'' \sin(n\phi)] \tag{C.19}$$

Applying the boundary conditions of Eq. C.2 corresponding to a circular plate of radius a, clamped at its edges, reveals

$$B = -A\frac{J_n(ka)}{I_n(ka)}, \tag{C.20}$$

$$A\left(I_n(ka)\frac{dJ_n(kr)}{dr} - J_n(ka)\frac{dI_n(kr)}{dr}\right) = 0 \qquad \text{at } (r = a). \tag{C.21}$$

Solutions of Eq. C.21 determines the natural frequencies of different modes. There are two types of solutions for this equation trivial and non trivial. For the trivial case of $A = 0$ no vibration happens however for the non trivial case new set of solutions arise which shall be denoted by k_{nm} where nm is the mth solution of the nth order Eq. C.21. Only for these special k_{nm} solutions, the Eq. C.19 satisfies the vibration equation for clamped plate and the corresponding boundary conditions and consequently the mentioned k_{nm} determines the only allowed frequencies for the free vibration of clamped plate ($k_{nm}^2 = \omega_{nm}\sqrt{\frac{\rho_m h}{D}}$). These frequencies may be denoted as the natural frequencies of the free vibrating plate where m and n represent the circular and radial nodes of different vibrating modes of clamped circular plate, respectively. The excited modes of freely vibrating circular plate clamped at its edges are shown in Fig. C.1 and the solutions of Eq. C.21 which fix the natural frequency of the vibrating fundamental modes accompanies each mode [77].

Forced vibration

For the case of forced oscillation the external exerted pressure should be taken into account which results in non zero trivial solutions for the boundary conditions. For the Eq. C.4 with

spatially uniform harmonic pressure source, another term should be added to the general solution of Eq. C.19, as in

$$\xi(r, \phi) = [A_n J_n(kr) + B_n I_n(kr)][A_n'' \cos(n\phi) + B_n'' \sin(n\phi)] - \frac{\Delta p}{k^4 D}. \tag{C.22}$$

Applying the boundary conditions of Eq. C.2, the following system of equations is derived.

$$\begin{cases} [A_n J_n(ka) + B_n I_n(ka)][A_n'' \cos(n\phi) + B_n'' \sin(n\phi)] = \frac{\Delta p}{k^4 D} \\ \left\{ A_n[-k J_{n+1}(ka) + \frac{n}{a} J_n(ka)] + B_n[k I_{n+1}(ka) + \frac{n}{a} I_n(ka)] \right\} \\ \qquad \cdot \left\{ A_n'' \cos(n\phi) + B_n'' \sin(n\phi) \right\} = 0. \end{cases} \tag{C.23}$$

For the vibration of clamped plate under spatially uniform harmonic pressure, the system of Eq. C.23 should hold for any ϕ. Thus, n should be zero, then Eq. C.23 is simplified to:

$$\begin{cases} A_0 J_0(ka) + B_0 I_0(ka) = \frac{\Delta p}{k^4 D} \\ -A_0 k J_1(ka) + B_0 k I_1(ka) = 0 \end{cases} . \tag{C.24}$$

Solving Eq. C.23 for A_0 and B_0 and replacing in Eq. C.22, the deformation $\xi(r)$ of the plate under spatially uniform harmonic pressure reads

$$\xi(r) = \frac{\Delta p}{k^4 D} \left\{ \frac{I_1(ka)}{J_0(ka) I_1(ka) + J_1(ka) I_0(ka)} J_0(kr) + \frac{J_1(ka)}{J_0(ka) I_1(ka) + J_1(ka) I_0(ka)} I_0(kr) - 1 \right\}. \tag{C.25}$$

As mentioned earlier Eq. C.25 determines the vibration of clamped plate under uniform pressure. Thus, only axisymmetric modes can be excited, that is, the modes with ϕ dependence vanish ($n \neq 0$). These axisymmetric modes extracted from Ref. [77] are depicted in the red box in Fig. C.1. Using Eq. C.25 and the definition of mechanical impedance Z_m, the impedance of the vibrating plate for ($n = 0$) is calculated as:

$$Z_m = \frac{F}{V} = \frac{\int \int_S \Delta p(r) ds}{\frac{j\omega}{S} \int \int_S \xi(r) ds} \tag{C.26}$$

$$F = \int \int_S \Delta p(r) ds = \Delta p \pi a^2 = \Delta p \tag{C.27}$$
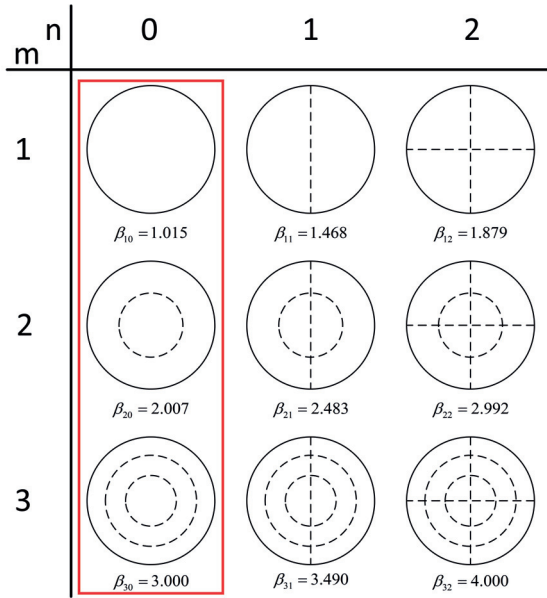
Figure C.1: Vibration modes of a circular plate clamped at its edge and corresponding solutions of Eq. C.21 where $k_{nm} = (\frac{\pi}{a})\beta_{nm}$. Modes in the red rectangle are the excited modes for a plate under forced vibration of spatially uniform harmonic pressure. Nodal lines are presented with dashed lines.

$$V = \frac{j\omega}{S}\int\int_S \xi(r)ds = \frac{j\omega}{S}\int\int_S \frac{\Delta p}{k^4 D}\left\{\frac{I_1(ka)}{J_0(ka)I_1(ka) + J_1(ka)I_0(ka)}J_0(kr)\right.$$
$$\left. + \frac{J_1(ka)}{J_0(ka)I_1(ka) + J_1(ka)I_0(ka)}I_0(kr) - 1\right\}ds \qquad \text{(C.28)}$$
$$= \frac{j\omega\Delta p}{k^4 D}\cdot\frac{J_2(ka)I_1(ka) - J_1(ka)I_2(ka)}{J_0(ka)I_1(ka) + J_1(ka)I_0(ka)}$$

$$Z_m = -j\omega\rho_m Sh.\frac{J_0(ka)I_1(ka) + J_1(ka)I_0(ka)}{J_2(ka)I_1(ka) - J_1(ka)I_2(ka)} \qquad \text{(C.29)}$$

and acoustic impedance (Z_a) is found as

$$Z_a = \frac{Z_a}{S^2} = \frac{-j\omega\rho_m h}{S}.\frac{J_0(ka)I_1(ka) + J_1(ka)I_0(ka)}{J_2(ka)I_1(ka) - J_1(ka)I_2(ka)}. \qquad \text{(C.30)}$$

C.3.2   Energy method

For the lossless vibration of clamped plate, the energy of the vibrating plate is transformed between kinetic and potential energies. These energies can be used to find the equivalent mass and compliance of a vibrating plate. The first mode deformation of the circular vibrating

plate with radius a can be approximated by [139]

$$\xi = A\left(1 - \frac{r^2}{a^2}\right)^2.$$ (C.31)

Using Eq. C.5 and C.31, the first mode kinetic energy of a circular plate is

$$
\begin{aligned}
K_t &= \frac{1}{2}h\rho_m \iint \dot{\xi}^2 r\,dr\,d\phi = \frac{1}{2}h\rho_m \iint \dot{A}^2\left(1 - \left(\frac{r}{a}\right)^2\right)^4 r\,dr\,d\phi \\
&= \frac{\pi h\rho_m a^2 \dot{A}^2}{10}\left(\frac{x^2}{a^2} - 1\right)^5 \Big|_0^a = \frac{\pi h\rho_m a^2 \dot{A}^2}{10}.
\end{aligned}
$$ (C.32)

Using Eq. C.7 and C.31 the equivalent deformation is

$$\xi_{eq} = \frac{1}{\pi a^2}\iint A\left(1 - \left(\frac{r}{a}\right)^2\right)^2 r\,dr\,d\phi = \frac{A}{3}.$$ (C.33)

Equating kinetic energies derived from Eq. C.5 and Eq. C.6 by plugging the exact and equivalent values of deformation (Eq. C.31 and Eq. C.33), the equivalent mass of the vibrating plate is found as,

$$m_{eq} = \frac{9}{5}\rho_m h\pi a^2.$$ (C.34)

Following the same procedure and using Eq. C.8 and C.31 the exact first mode potential energy of a circular plate reads

$$
\begin{aligned}
U &= \frac{DA^2}{2}\iint \left\{ \left(\frac{12}{a^2}\left(\frac{r}{a}\right)^2 - \frac{4}{a^2}\right)^2 + \frac{1}{r^2}\left(\frac{4}{a}\left(\frac{r}{a}\right)^3 - \frac{4}{a}\left(\frac{r}{a}\right)\right)^2 \right. \\
&\quad \left. + \frac{2\nu}{r}\left(\frac{4}{a}\left(\frac{r}{a}\right)^3 - \frac{4}{a}\left(\frac{r}{a}\right)\right)\left(\frac{12}{a^2}\left(\frac{r}{a}\right)^2 - \frac{4}{a^2}\right)\right\} r\,dr\,d\phi \\
&= \frac{2A^2 D\pi}{2}\left[\frac{8r^2(a^4 - 3a^2 r^2 + 3r^4)}{a^8} + \frac{8(3a^4 r^2 - 3a^2 r^4 + r^6)}{3a^8} \right. \\
&\quad \left. + \frac{16\nu(r^3 - a^2 r)^2}{a^8}\right]_0^a = \frac{32A^2 D\pi}{3a^2}
\end{aligned}
$$ (C.35)

Following the same procedure used for kinetic energy and equating potential energies derived from exact and equivalent values of Eq. C.8 and Eq. C.10 by plugging the exact and equivalent deformations of C.31 and C.33, the first mode equivalent compliance of the vibrating plate is calculated as,

$$C_{eq} = \frac{a^2(1 - \nu^2)}{16\pi E h^3}.$$ (C.36)

Using Eq. C.34 and Eq. C.36, the mechanical and acoustic impedances of the circular plate in the first vibrating mode can be calculated as

$$Z_m \simeq j\omega m_{eq} + \frac{1}{j\omega C_{eq}} = j\frac{\frac{9}{5}\omega^2(1-v^2)\rho_m\pi h a^4 - 16\pi E h^3}{\omega a^2(1-v^2)}, \tag{C.37}$$

$$Z_a \simeq \frac{Z_m}{S^2} = j\frac{\frac{9}{5}\omega^2(1-v^2)\rho_m\pi h a^4 - 16\pi E h^3}{S^2\omega a^2(1-v^2)}. \tag{C.38}$$

C.3.3   Resonance frequency

Considering the fact that for the lossless vibration of the plate, the energy is transformed between potential and kinetic energy and the maximum energy stored in the plate is fixed, the resonance frequency can be calculated from $U_{max} = K_{max}$ [137]. Indeed, using the frequency domain kinetic energy of Eq. C.5 and potential energy of Eq. C.8, and plugging the deformation shape of the circular plate Eq. C.31 the resonance frequency reads:

$$\omega_r^2 = \frac{U_{max}}{\frac{\rho_m h}{2}\int\int\xi^2 r\,dr\,d\phi} = \frac{\frac{32A^2 D\pi}{3a^2}}{\frac{1}{2}\frac{h\rho_m\pi a^2 A^2}{5}} = \frac{80}{9}\frac{Eh^2}{\rho_m a^4(1-v^2)}, \tag{C.39}$$

$$f_r = \sqrt{\frac{20}{9}}\frac{h}{\pi a^2}\sqrt{\frac{E}{\rho_m(1-v^2)}} \simeq 0.4745\frac{h}{a^2}\sqrt{\frac{E}{\rho_m(1-v^2)}}. \tag{C.40}$$

C.4   Impedance of a rectangular plate with clamped edges

C.4.1   Closed form method

For centuries, researchers are trying to find an exact solution for the problem of the vibration of the fully clamped rectangular plate and still they have not been successful. Indeed, it is currently considered that an exact solution does not exist for the rectangular plate clamped at its edges (that is Eq. C.4 with boundary conditions of Eq. C.3). All the solutions that are found in the articles are for free vibration and they are approximate and are derived in series format [140], so to find the first mode acoustic impedance of the clamped vibrating rectangular plate under uniform pressure the energy method is used here.

C.4.2 Energy method

Sinusoidal deformation

To use the energy method to find the mechanical impedance of the rectangular vibrating plate, a mathematical function is required which models the deformation of the plate [139, 141].

$$\xi = A\left(\cos\frac{2\pi x}{a} - 1\right)\left(\cos\frac{2\pi y}{b} - 1\right) \tag{C.41}$$

Using the Eq. C.41 and following the steps similar to the case of the circular plate leads to:

$$K_t = \frac{1}{2}h\rho_m \int\int \dot{\xi}^2 dxdy = \frac{1}{2}\frac{9}{4}\rho_m hab\dot{A}^2 = \frac{1}{2}m_{eq}\dot{\xi}_{eq}^2, \tag{C.42}$$

$$\dot{\xi}_{eq} = \frac{1}{ab}\int\int \dot{\xi}\,dxdy = \dot{A}, \tag{C.43}$$

$$m_e = \frac{9}{4}\rho_m hab, \tag{C.44}$$

$$
\begin{aligned}
U = \frac{DA^2}{2}\int\int &\left\{\left(\frac{2\pi}{a}\right)^4\cos^2\left(\frac{2\pi x}{a}\right)\left(\cos\left(\frac{2\pi y}{b}\right)-1\right)^2 + \left(\frac{2\pi}{b}\right)^4\cos^2\left(\frac{2\pi y}{b}\right)\left(\cos\left(\frac{2\pi x}{a}\right)-1\right)^2 \right.\\
&\left. +2v\left(\frac{2\pi}{a}\right)^2\left(\frac{2\pi}{b}\right)^2\cos\left(\frac{2\pi x}{a}\right)\cos\left(\frac{2\pi y}{b}\right) + 2(1-v)\left(\frac{2\pi}{a}\right)^2\left(\frac{2\pi}{b}\right)^2\sin^2\left(\frac{2\pi x}{a}\right)\sin^2\left(\frac{2\pi y}{b}\right)\right\}\\
= \frac{DA^2}{2}&\left\{\left(\frac{2\pi}{a}\right)^4\left(\frac{a\sin\left(\frac{4\pi x}{a}\right)}{8\pi} + \frac{x}{2}\right)\left(\frac{-8b\sin\left(\frac{2\pi y}{b}\right) + b\sin\left(\frac{4\pi y}{b}\right) + 12\pi y}{8\pi}\right)\right.\\
&+\left(\frac{2\pi}{b}\right)^4\left(\frac{b\sin\left(\frac{4\pi y}{b}\right)}{8\pi} + \frac{y}{2}\right)\left(\frac{-8a\sin\left(\frac{2\pi x}{a}\right) + a\sin\left(\frac{4\pi x}{a}\right) + 12\pi x}{8\pi}\right)\\
&+2v\left(\frac{2\pi}{a}\right)\left(\frac{2\pi}{b}\right)\sin\left(\frac{2\pi x}{a}\right)\sin\left(\frac{2\pi y}{b}\right)\\
&\left.+2(1-v)\left(\frac{2\pi}{a}\right)^2\left(\frac{2\pi}{b}\right)^2\left(\frac{x}{2} - \frac{a\sin\left(\frac{4\pi x}{a}\right)}{8\pi}\right)\left(\frac{y}{2} - \frac{b\sin\left(\frac{4\pi y}{b}\right)}{8\pi}\right)\right\}\Bigg|_0^a\Bigg|_0^b\\
= \frac{6\pi^4 A^2 Db[1 + \frac{2}{3}(1-v)(\frac{a}{b})^2 + (\frac{a}{b})^4]}{a^3}
\end{aligned}
\tag{C.45}
$$

$$C_{eq} = \frac{a^3 \left(1 - v^2\right)}{\pi^4 E h^3 b \left[1 + \frac{2}{3}(1-v)\left(\frac{a}{b}\right)^2 + \left(\frac{a}{b}\right)^4\right]}. \tag{C.46}$$

Using the equivalent mass Eq. C.44 and the equivalent compliance Eq. C.46 the mechanical and acoustic impedance of the rectangular plate reads

$$Z_m = j \frac{\frac{9}{4}\omega^2 \rho_m h a^4 b(1-v^2) - \pi^4 E h^3 b[1 + \frac{2}{3}(1-v)(\frac{a}{b})^2 + (\frac{a}{b})^4]}{\omega a^3 (1-v^2)} \tag{C.47}$$

$$Z_a = j \frac{\frac{9}{4}\omega^2 \rho_m h a^4 b(1-v^2) - \pi^4 E h^3 b[1 + \frac{2}{3}(1-v)(\frac{a}{b})^2 + (\frac{a}{b})^4]}{S^2 \omega a^3 (1-v^2)} \tag{C.48}$$

Polynomial Deformation

A polynomial function can also be used to model the deformation of the rectangular vibrating plate [137], as

$$\xi = A x^2 y^2 (a-x)^2 (b-y)^2. \tag{C.49}$$

and following the steps as in previous sections,

$$K_t = \frac{1}{2} h \rho_m \int \int \dot{\xi}^2 \, dx dy = \frac{1}{2} h \rho \int \int \dot{A}^2 \left(a^2 x^2 - 2ax^3 + x^4\right)^2 \left(b^2 y^2 - 2by^3 + y^4\right)^2 \, dx dy =$$
$$\frac{\dot{A}^2}{2} h \rho_m \left(\frac{a^4 x^5}{5} - \frac{2a^3 x^6}{3} + \frac{6a^2 x^7}{7} - \frac{ax^8}{2} + \frac{x^9}{9}\right)\left(\frac{b^4 y^5}{5} - \frac{2b^3 y^6}{3} + \frac{6b^2 y^7}{7} - \frac{by^8}{2} + \frac{y^9}{9}\right)\Big|_0^a\Big|_0^b$$
$$= \frac{\dot{A}^2}{793800} \rho_m h a^9 b^9 \tag{C.50}$$

$$\xi_{eq} = \frac{1}{ab} \int \int \xi \, dx dy = \frac{1}{ab} \int \int A \left(a^2 x^2 - 2ax^3 + x^4\right)\left(b^2 y^2 - 2by^3 + y^4\right) dx dy$$
$$= \frac{A}{ab}\left(\frac{1}{30} x^3 \left(10a^2 - 15ax + 6x^2\right)\right)\left(\frac{1}{30} y^3 \left(10b^2 - 15by + 6y^2\right)\right)\Big|_0^a\Big|_0^b = \frac{1}{30^2} A a^4 b^4 \tag{C.51}$$

$$m_{eq} = \frac{100}{49} \rho_m h a b \tag{C.52}$$

Following the same steps for potential energy, the compliance, mechanical and acoustic impedance is calculated as,

$$
U = \frac{DA^2}{2} \int \int \Bigg\{ \left(2a^2 - 12ax + 12x^2\right)^2 \left(b^2 y^2 - 2by^3 + y^4\right)^2 + \left(a^2 x^2 - 2ax^3 + x^4\right)^2 \left(2b^2 - 12by + 12y^2\right)^2
$$

$$
+ 2\nu \left(a^2 x^2 - 2ax^3 + x^4\right) \left(2a^2 - 12ax + 12x^2\right) \left(b^2 y^2 - 2by^3 + y^4\right) \left(2b^2 - 12by + 12y^2\right)
$$

$$
+ 2(1-\nu) \left(2a^2 x - 6ax^2 + 4x^3\right)^2 \left(2b^2 y - 6by^2 + 4y^3\right)^2 \Bigg\} dx\,dy
$$

$$
= \frac{4DA^2}{2} \Bigg\{ \left(a^4 x - 6a^3 x^2 + 16a^2 x^3 - 18ax^4 + \frac{36}{4} x^5 \right) \left(\frac{b^4 y^5}{5} - \frac{2b^3 y^6}{3} + \frac{6b^2 y^7}{7} - \frac{by^8}{2} + \frac{y^9}{9} \right)
$$

$$
+ \left(b^4 y - 6b^3 y^2 + 16b^2 y^3 - 18by^4 + \frac{36}{4} y^5 \right) \left(\frac{a^4 x^5}{5} - \frac{2a^3 x^6}{3} + \frac{6a^2 x^7}{7} - \frac{ax^8}{2} + \frac{x^9}{9} \right)
$$

$$
+ 2\nu \left(\frac{2a^4 x^3}{3} - 4a^3 x^4 + \frac{38a^2 x^5}{5} - 6ax^6 + \frac{12x^7}{7} \right) \left(\frac{2b^4 y^3}{3} - 4b^3 y^4 + \frac{38b^2 y^5}{5} - 6by^6 + \frac{12y^7}{7} \right)
$$

$$
+ 2(1-\nu) \left(\frac{4a^4 x^3}{3} - 6a^3 x^4 + \frac{52a^2 x^5}{5} - 8ax^6 + \frac{16x^7}{7} \right) \left(\frac{4b^4 y^3}{3} - 6b^3 y^4 + \frac{52b^2 y^5}{5} - 8by^6 + \frac{16y^7}{7} \right) \Bigg\} \Bigg|_0^a \Bigg|_0^b
$$

$$
= \frac{2}{3150} DA^2 a^5 b^9 \left(1 + \left(\frac{a}{b}\right)^4 + \frac{2}{3.5} \left(\frac{a}{b}\right)^2 \right) = \frac{2Eh^3 A^2 a^5 b^9 \left(1 + \left(\frac{a}{b}\right)^4 + \frac{2}{3.5} \left(\frac{a}{b}\right)^2 \right)}{37800 \left(1 - \nu^2\right)}
$$

$$\tag{C.53}$$

$$
C_{eq} = \frac{7a^3 (1 - \nu^2)}{600 Eh^3 b[1 + \frac{2}{3.5}(\frac{a}{b})^2 + (\frac{a}{b})^4]}
\tag{C.54}
$$

$$
Z_m = j \frac{\frac{100}{7}\omega^2 \rho_m h a^4 b(1 - \nu^2) - 600 Eh^3 b[1 + \frac{2}{3.5}(\frac{a}{b})^2 + (\frac{a}{b})^4]}{7\omega a^3 (1 - \nu^2)}
\tag{C.55}
$$

$$
Z_a = j \frac{\frac{100}{7}\omega^2 \rho_m h a^4 b(1 - \nu^2) - 600 Eh^3 b[1 + \frac{2}{3.5}(\frac{a}{b})^2 + (\frac{a}{b})^4]}{7S^2 \omega a^3 (1 - \nu^2)}
\tag{C.56}
$$

C.4.3 Resonance Frequency

To find the resonance frequency of the vibrating rectangular plate the same steps as in circular plate are followed, thus

$$
\omega_r^2 = \frac{U_{max}}{\frac{\rho h}{2} \int \int \xi^2 dx\,dy}.
\tag{C.57}
$$

Appendix C. Dynamics of plate vibrations

Using the sinusoidal deformation the resonant frequency is found as

$$\omega^2_{r-\sin} = \frac{\frac{6\pi^4 A^2 E h^3 b [1+\frac{2}{3}(1-\nu)(\frac{a}{b})^2+(\frac{a}{b})^4]}{12a^3(1-\nu^2)}}{\frac{1}{2}\frac{9}{4}\rho_m hab A^2} \tag{C.58}$$

$$f_{r-\sin} = \frac{\pi h}{3a^2}\sqrt{\frac{E}{\rho_m(1-\nu^2)}\left[1+\frac{2}{3}(1-\nu)\left(\frac{a}{b}\right)^2+\left(\frac{a}{b}\right)^4\right]}. \tag{C.59}$$

Using the polynomial deformation the resonant frequency is calculated as

$$\omega^2_{r-\text{poly}} = \frac{\frac{2Eh^3 A^2 a^5 b^9(1+(\frac{a}{b})^4+\frac{2}{3.5}(\frac{a}{b})^2)}{(1-\nu^2)}}{\frac{A^2}{21}\rho_m ha^9 b^9}, \tag{C.60}$$

$$f_{r-\text{poly}} \simeq 1.03144\frac{h}{a^2}\sqrt{\frac{E}{\rho_m(1-\nu^2)}\left[1+\frac{2}{3.5}\left(\frac{a}{b}\right)^2+\left(\frac{a}{b}\right)^4\right]}. \tag{C.61}$$

D Network analysis

Using the equivalent circuit model of the mechanical elements, one can easily deal with very complicated problems and the theory of network analysis adopted from electrical engineering is a method to deal with complex systems using circuit elements. Using the network analysis, all the constituent elements of a network is represented by a matrix where, this matrix relates the input and output of the network. There are several ways to represent the network using matrices including [Z], [Y], [T], [S] and each of these relates different combinations of input and output parameters. Any of these matrices can be transformed to the other one which is an advantage in the analysis of complex systems. In acoustics [T] and [S] matrices are the two important network representations, the first one is of much importance in theoretical works and the second one conveys practical information about the network performance [133].

D.1 Transfer matrix [T]

The transfer matrix relates the sound pressures (p) and normal acoustic volume velocities (q) on the two faces of a network. [T] or ABCD matrix representation is useful when a network consists of a cascade connection of two or more two-port networks. Indeed, a 2×2 [T] or ABCD matrix can be easily defined for an individual 2 port network. Then the ABCD matrix of the cascade connection of several two-port networks can be found by simple matrix multiplication of the ABCD matrices of each two-port networks. Figure D.1 depicts a single two-port network with [T] matrix as well as the cascade connection of the two two-port networks and Eq. D.1 and D.2 presents the corresponding mathematical descriptions.

$$\begin{pmatrix} p_1 \\ q_1 \end{pmatrix} = \begin{pmatrix} T_{11} & T_{12} \\ T_{21} & T_{22} \end{pmatrix} \begin{pmatrix} p_2 \\ q_2 \end{pmatrix} \tag{D.1}$$

$$\begin{pmatrix} p_1 \\ q_1 \end{pmatrix} = \begin{pmatrix} T_{11} & T_{12} \\ T_{21} & T_{22} \end{pmatrix} \begin{pmatrix} T'_{11} & T'_{12} \\ T'_{21} & T'_{22} \end{pmatrix} \begin{pmatrix} p_3 \\ q_3 \end{pmatrix}. \tag{D.2}$$
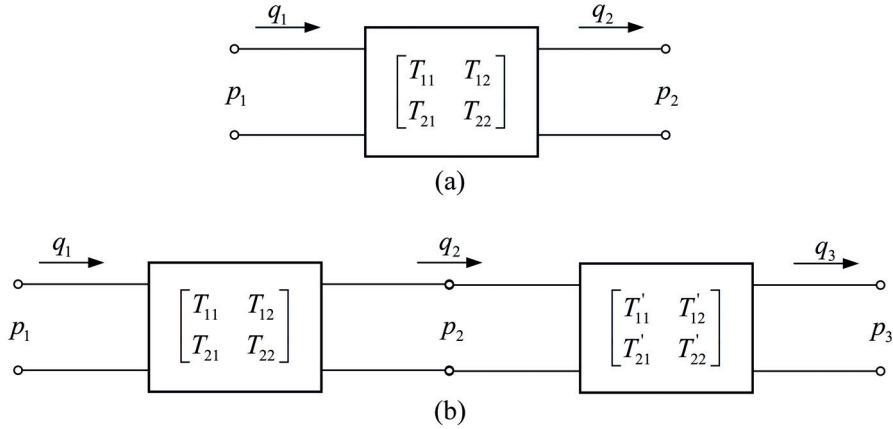
Figure D.1: (a) A two-port network with transfer matrix representation; (b) A cascade connection of two two-port networks.

For a symmetrical and reciprocal network it is proved that

$$T_{11} = T_{22} \tag{D.3a}$$
$$T_{11} T_{22} - T_{12} T_{21} = 1, \tag{D.3b}$$

respectively.

D.2 Scattering matrix [S]

The scattering matrix [S] which was developed for electromagnetic waves relates the incoming and outgoing waves in the two faces of a network. This is due to the difficulty in defining voltages and currents for non-TEM electromagnetic lines. In addition, 'a practical problem exists when trying to measure voltages and currents at microwave frequencies because direct measurements usually involve the magnitude (inferred from power) and phase of a wave travelling in a given direction, or of a standing wave. Thus, equivalent voltages and currents, and the related impedance and admittance matrices, become somewhat of an abstraction when dealing with high-frequency networks [133].' Moreover, [S] matrix conveys some practical information which are directly obtained from matrix elements such as reflection and transmission coefficients or symmetry and reciprocity of the network. Furthermore, due to the importance and functionality of [S] representation, it has been used in the design and characterization of electromagnetic components. In order to simplify the transfer of knowledge from electromagnetic to acoustic it is useful to define the [S] matrix for acoustic which relates the incoming and outgoing pressure waves for a two-ports network as in Fig. D.2 by

$$\begin{pmatrix} b \\ c \end{pmatrix}_{\text{Refflected}} = \begin{pmatrix} S_{11} & S_{12} \\ S_{21} & S_{22} \end{pmatrix} \begin{pmatrix} a \\ d \end{pmatrix}_{\text{Incident}} \tag{D.4}$$
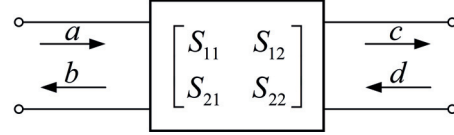
Figure D.2: A two-port network with [S] matrix representation

where a and b are the incident and reflected waves to/from the input face, respectively and d and c are the incident and reflected waves for the output face. For a symmetrical and reciprocal network following equations hold, respectively.

$$S_{11} = S_{22} \tag{D.5a}$$
$$S_{12} = S_{21} \tag{D.5b}$$

D.3 Periodic networks

The [T] matrix is one of the useful tools to analyse cascaded networks or to derive the [T] matrix for a complex network. This can be done by multiplication of [T] matrices of individual modules to get the total transfer matrix. The functionality of transfer matrix becomes more evident when dealing with periodic networks, since the same [T] matrix of the unit-cell is multiplied by itself for n times ($[T]^n$), where n is the number of the periodic networks. Figure D.3 depicts the three different circuit models which can be used for the periodic structures. The ABCD or [T] matrices for one unit-cell of these models are obtained using Eq. D.6 to D.8.

$$\begin{pmatrix} T_{11} & T_{12} \\ T_{21} & T_{22} \end{pmatrix}_L = \begin{pmatrix} 1 & Z \\ 0 & 1 \end{pmatrix} \begin{pmatrix} 1 & 0 \\ Y & 1 \end{pmatrix} = \begin{pmatrix} 1+YZ & Z \\ Y & 1 \end{pmatrix} \tag{D.6}$$

$$\begin{pmatrix} T_{11} & T_{12} \\ T_{21} & T_{22} \end{pmatrix}_T = \begin{pmatrix} 1 & \frac{Z}{2} \\ 0 & 1 \end{pmatrix} \begin{pmatrix} 1 & 0 \\ Y & 1 \end{pmatrix} \begin{pmatrix} 1 & \frac{Z}{2} \\ 0 & 1 \end{pmatrix} = \begin{pmatrix} 1+\frac{YZ}{2} & Z(1+\frac{YZ}{4}) \\ Y & 1+\frac{YZ}{2} \end{pmatrix} \tag{D.7}$$

$$\begin{pmatrix} T_{11} & T_{12} \\ T_{21} & T_{22} \end{pmatrix}_\Pi = \begin{pmatrix} 1 & 0 \\ \frac{Y}{2} & 1 \end{pmatrix} \begin{pmatrix} 1 & Z \\ 0 & 1 \end{pmatrix} \begin{pmatrix} 1 & 0 \\ \frac{Y}{2} & 1 \end{pmatrix} = \begin{pmatrix} 1+\frac{YZ}{2} & Z \\ \frac{Y}{4}(1+YZ) & 1+\frac{YZ}{2} \end{pmatrix} \tag{D.8}$$
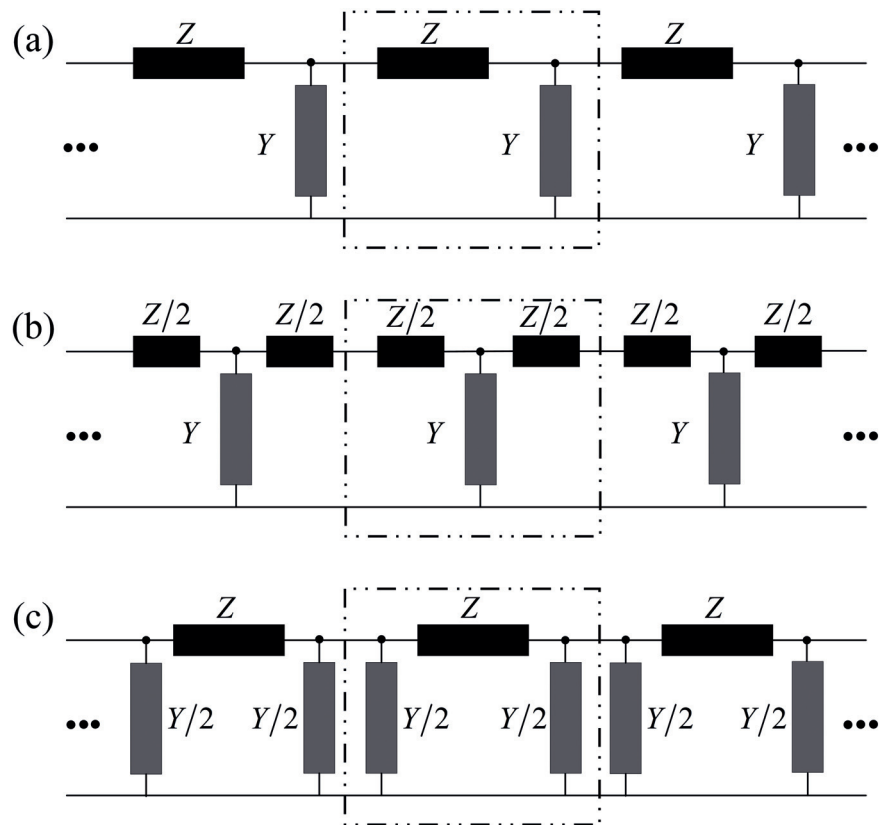
Figure D.3: Circuit models for periodic networks. (a) Ladder-Model; (b) T-Model ; (c) Π-Model. Here, $Z = z_1$ is the impedance and $Y = \frac{1}{z_2}$ is the admittance, where z_1 and z_2 may have any arbitrary complex value of impedance type.

E [S] and [T] matrix retrieval

E.1 Scattering parameters retrieval

In the approach considered here, a loudspeaker was used to generate a plane wave field in a standing wave tube and four microphones shown in Fig. E.1 are used to measure the pressure in four locations denoted by x_1 to x_4, where

$$p_1 = (ae^{-jkx_1} + be^{jkx_1})e^{j\omega t}, \qquad \text{(E.1a)}$$

$$p_2 = (ae^{-jkx_2} + be^{jkx_2})e^{j\omega t}, \qquad \text{(E.1b)}$$

$$p_3 = (ce^{-jkx_3} + de^{jkx_3})e^{j\omega t}, \qquad \text{(E.1c)}$$

$$p_4 = (ce^{-jkx_4} + de^{jkx_4})e^{j\omega t}, \qquad \text{(E.1d)}$$

and k represents the wave number in the ambient fluid and $e^{+j\omega t}$ sign convention has been adopted. The four complex pressures, p_1 to p_4, comprise various superposition of plane waves travelling in positive and negative directions. Using the measured pressure p of the four microphones in the test tube (a, b, c, d) can be found and summarized as,

$$a = \frac{j(p_1 e^{jkx_2} - p_2 e^{jkx_1})}{2\sin k(x_1 - x_2)}, \qquad \text{(E.2a)}$$

$$b = \frac{j(p_2 e^{-jkx_1} - p_1 e^{-jkx_2})}{2\sin k(x_1 - x_2)}, \qquad \text{(E.2b)}$$

$$c = \frac{j(p_3 e^{jkx_4} - p_4 e^{jkx_3})}{2\sin k(x_3 - x_4)}, \qquad \text{(E.2c)}$$

$$d = \frac{j(p_4 e^{-jkx_3} - p_3 e^{-jkx_4})}{2\sin k(x_3 - x_4)}. \qquad \text{(E.2d)}$$

The Scattering matrix [S] relates the incoming and outgoing waves in the two faces of a Network. For the measurement setup of Fig. E.1 this relation is defined with

$$\begin{pmatrix} b \\ ce^{-jks} \end{pmatrix}_{\text{Refflected}} = \begin{pmatrix} S_{11} & S_{12} \\ S_{21} & S_{22} \end{pmatrix} \begin{pmatrix} a \\ de^{jks} \end{pmatrix}_{\text{Incident}}. \qquad \text{(E.3)}$$

Equation E.3 is composed of four unknowns but two equations, therefore two additional
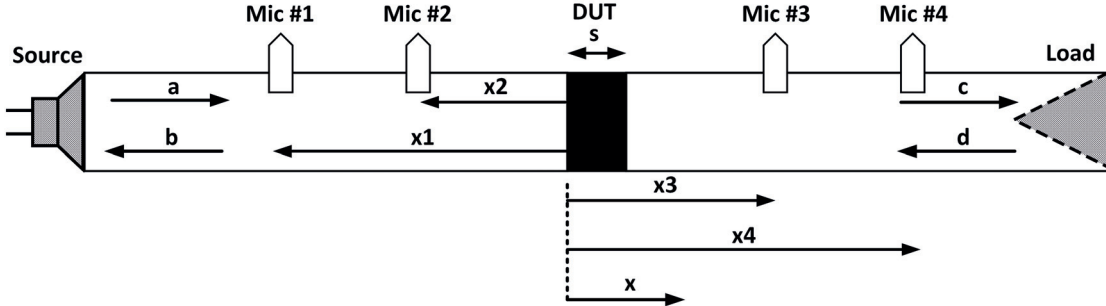
Figure E.1: Schematic representation of four microphone measurement setup.

equations are required to solve it. The additional equations can be defined by secondary measurement using different terminations or any other measurement configuration which leads to additional equations different from the first setup. If the results of two measurements with different loadings are represented by subscript 1 and 2 then, using (a_1, b_1, c_1, d_1) and (a_2, b_2, c_2, d_2) the elements of [S] matrix (S_{11}, S_{21}, S_{12}, S_{22}) are found as,

$$S_{11} = \frac{b_1 d_2 e^{jks} - b_2 d_1 e^{jks}}{a_1 d_2 e^{jks} - a_2 d_1 e^{jks}}, \tag{E.4a}$$

$$S_{12} = \frac{a_1 b_2 - a_2 b_1}{a_1 d_2 e^{jks} - a_2 d_1 e^{jks}}, \tag{E.4b}$$

$$S_{21} = \frac{c_1 e^{-jks} d_2 e^{jks} - c_2 e^{-jks} d_1 e^{jks}}{a_1 d_2 e^{jks} - a_2 d_1 e^{jkl}}, \tag{E.4c}$$

$$S_{22} = \frac{a_1 c_2 e^{-jks} - a_2 c_1 e^{-jks}}{a_1 d_2 e^{jks} - a_2 d_1 e^{jks}}. \tag{E.4d}$$

For symmetrical and reciprocal network single measurement is sufficient and this is due to the unique behaviour of such a network which provides two additional equations, $S_{11} = S_{22}$ and $S_{12} = S_{21}$, which decrease the numbers of unknowns to two. Using the additional conditions which is valid for the proposed unit-cell, [S] matrix is defined by

$$S_{11} = S_{22} = \frac{ab - cd}{a^2 - d^2 e^{2jks}}, \tag{E.5a}$$

$$S_{12} = S_{21} = \frac{ace^{-jks} - bde^{jks}}{a^2 - d^2 e^{2jks}}. \tag{E.5b}$$

If the anechoic termination is used as a load in the test tube then $d = 0$ and

$$R = S_{11} = S_{22} = \frac{b}{a}, \tag{E.6a}$$

$$T = S_{12} = S_{21} = \frac{c}{a} e^{-jks}. \tag{E.6b}$$

Note that these coefficients are calculated with respect to the two planes of the sample as input and output $x = 0$ and $x = s$.

E.2   Transfer matrix retrieval

In the approach considered here, a loudspeaker was used to generate a plane wave field in a standing wave tube, and four microphone shown in Fig. E.1 are used to measure the pressure in these four points at locations x_1 to x_4 [78]. The transfer matrix is used to relate the sound pressures and normal acoustic particle velocities on the two faces of a porous layer extending from $x = 0$ to $x = s$ as in Fig. E.1 having p and v as the exterior normal acoustic pressure and particle velocity respectively. Using Eq. E.1 the pressures and particle velocities on the two surfaces of the porous layer are expressed in terms of the positive- and negative-going amplitude components of the plane wave, as

$$p_{x=0} = a + b, \tag{E.7a}$$

$$v_{x=0} = \frac{a - b}{\rho_0 c}, \tag{E.7b}$$

$$p_{x=s} = c e^{-jkd} + d e^{jkd}, \tag{E.7c}$$

$$v_{x=s} = \frac{c e^{-jkd} - d e^{jkd}}{\rho_0 c}, \tag{E.7d}$$

where ρ_0 and c are the fluid density and sound speed respectively. Thus, the pressures and the normal particle velocities at the two faces of the porous layer can be determined, by the plane wave components the positive and negative going pressure waves. Where, these components are found based on measurements of the complex pressures at four locations. Plugging Eq. E.7 in [T] matrix Eq. D.1, two equations with four unknowns are found T_{11}, T_{12}, T_{21}, and T_{22}. Thus, two additional equations are required in order to determine the four unknowns of the transfer matrix. Those equations may be generated, by making a second measurement. For example, the new measurement at the four microphone positions can be performed after changing the terminating impedance in the downstream section of the standing wave tube. By applying two-load method and doing the second measurement (A, B, C, D) matrix elements are calculated as

$$T_{11} = \frac{p_{01} v_{s2} - p_{02} v_{s1}}{p_{s1} v_{s2} - p_{s2} v_{s1}}, \tag{E.8a}$$

$$T_{12} = \frac{p_{02} p_{s1} - p_{01} p_{s2}}{p_{s1} v_{s2} - p_{s2} v_{s1}}, \tag{E.8b}$$

$$T_{21} = \frac{v_{01} v_{s2} - v_{02} v_{s1}}{p_{s1} v_{s2} - p_{s2} v_{s1}}, \tag{E.8c}$$

$$T_{22} = \frac{p_{s1} v_{02} - p_{s2} v_{01}}{p_{s1} v_{s2} - p_{s2} v_{s1}}, \tag{E.8d}$$

where the the first and second symbol in the subscript represent the location and measurement number respectively.

F Periodic structures

F.1 Dispersion relation

For an arbitrary periodic structure, the propagating wave along the structure at point z differ from the fields one period d farther, at the point $z + d$ by $e^{\gamma d}$, where $\gamma(\omega) = \alpha(\omega) + j\beta(\omega)$ is the propagation constant, $\beta(\omega)$ is responsible for phase shift in the propagation process and $\alpha(\omega)$ is the attenuation coefficient [142]. As shown in Fig. F.1, for a wave propagating in a periodic structure, composed of sequential networks representing unit-cells, the pressure p and volume velocity q at the terminal n and $n+1$ can be related by

$$p_{n+1} = e^{-\gamma d} p_n \tag{F.1a}$$

$$q_{n+1} = e^{-\gamma d} q_n. \tag{F.1b}$$

Using the transmission matrix to relate pressure and velocity, it is concluded that

$$\begin{pmatrix} p_n \\ q_n \end{pmatrix} = \begin{pmatrix} T_{11} & T_{12} \\ T_{21} & T_{22} \end{pmatrix} \begin{pmatrix} p_{n+1} \\ q_{n+1} \end{pmatrix} = e^{\gamma d} \begin{pmatrix} p_{n+1} \\ q_{n+1} \end{pmatrix}, \tag{F.2}$$

which is simplified as a matrix eigenvalue problem of

$$\left[\begin{pmatrix} T_{11} & T_{12} \\ T_{21} & T_{22} \end{pmatrix} - \begin{pmatrix} e^{\gamma d} & 0 \\ 0 & e^{\gamma d} \end{pmatrix} \right] \begin{pmatrix} p_{n+1} \\ q_{n+1} \end{pmatrix} = 0. \tag{F.3}$$

To solve the matrix eigenvalue Eq. F.3 for γ, the determinant of the matrix should be calculated and this leads to the following equation

$$T_{11} T_{22} - T_{12} T_{21} + e^{2\gamma d} - e^{\gamma d} (T_{11} + T_{22}) = 0. \tag{F.4}$$

For a reciprocal network, it is dictated that $T_{11} T_{22} - T_{12} T_{21} = 1$ and the Eq. F.4 is simplified to

$$\cosh \gamma d = \frac{T_{11} + T_{22}}{2}. \tag{F.5}$$

The Eq. F.5 can also be written using S-parameters by,

$$\cosh \gamma d = \frac{1 - S_{11} S_{22} + S_{12} S_{21}}{2 S_{21}}. \tag{F.6}$$

Bearing in mind the Eq. F.6 is valid for a reciprocal network.
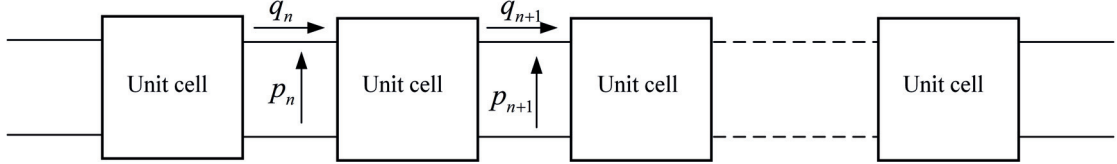
Figure F.1: Period structure composed of unit-cells connected in sequential series order and each unit-cell can be modelled by a two port network.

F.1.1 Bloch-Impedance

Considering the ratio of pressure to velocity in the network of Fig. F.1, since, the network is periodic, this ratio is constant at the terminals of the unit-cell and it is called the Bloch impedance Z_B. Bloch impedance is calculated using Eq. F.3 and mathematically described as

$$Z_B = \frac{P_{n+1}}{V_{n+1}} = -\frac{T_{12}}{T_{11} - e^{\gamma d}} = -\frac{T_{22} - e^{\gamma d}}{T_{21}}. \tag{F.7}$$

By solving Eq. F.7 for $e^{\gamma d}$, and assuming a reciprocal unit-cell $T_{11} T_{22} - T_{12} T_{21} = 1$, $e^{\gamma d} = \left[(T_{11} + T_{22}) \pm \sqrt{(T_{11} + T_{22})^2 - 4} \right] / 2$ is obtained which results in an explicit form for the Bloch impedance as a function of [T] parameters,

$$Z_{B_\pm} = \frac{-2 T_{12}}{(T_{11} - T_{22}) \mp \sqrt{(T_{11} + T_{22})^2 - 4}} = \frac{(T_{11} - T_{22}) \pm \sqrt{(T_{11} + T_{22})^2 - 4}}{2 T_{21}}. \tag{F.8}$$

In these expressions, the ($\pm$) solutions correspond to positively and negatively travelling waves, respectively. If $T_{11} = T_{22}$ then

$$Z_{B_\pm} = \frac{\pm T_{12}}{\sqrt{T_{11}^2 - 1}} = \frac{\pm \sqrt{T_{22}^2 - 1}}{T_{21}}. \tag{F.9}$$

Bibliography

[1] Nader Engheta and Richard W Ziolkowski. *Metamaterials: physics and engineering explorations*. John Wiley & Sons, 2006.

[2] Winston E Kock. Metallic delay lenses. *Bell System Technical Journal*, 27(1):58–82, 1948.

[3] Viktor G Veselago. The electrodynamics of substances with simultaneously negative values of ϵ and μ. *Soviet physics uspekhi*, 10(4):509, 1968.

[4] John B Pendry, AJ Holden, WJ Stewart, and I Youngs. Extremely low frequency plasmons in metallic mesostructures. *Physical review letters*, 76(25):4773, 1996.

[5] John B Pendry, AJ Holden, DJ Robbins, and WJ Stewart. Low frequency plasmons in thin-wire structures. *Journal of Physics: Condensed Matter*, 10(22):4785, 1998.

[6] John B Pendry, A J Holden, DJ Robbins, and WJ Stewart. Magnetism from conductors and enhanced nonlinear phenomena. *Microwave Theory and Techniques, IEEE Transactions on*, 47(11):2075–2084, 1999.

[7] David R Smith, Willie J Padilla, DC Vier, Syrus C Nemat-Nasser, and Seldon Schultz. Composite medium with simultaneously negative permeability and permittivity. *Physical review letters*, 84(18):4184, 2000.

[8] David R Smith and Norman Kroll. Negative refractive index in left-handed materials. *Physical Review Letters*, 85(14):2933, 2000.

[9] Richard A Shelby, David R Smith, and Seldon Schultz. Experimental verification of a negative index of refraction. *science*, 292(5514):77–79, 2001.

[10] John Brian Pendry. Negative refraction makes a perfect lens. *Physical review letters*, 85(18):3966, 2000.

[11] Steven A Cummer, Johan Christensen, and Andrea Alù. Controlling sound with acoustic metamaterials. *Nature Reviews Materials*, 1:16001, 2016.

[12] Guancong Ma and Ping Sheng. Acoustic metamaterials: From local resonances to broad horizons. *Science advances*, 2(2):e1501595, 2016.

Bibliography

[13] Nadège Kaina, Fabrice Lemoult, Mathias Fink, and Geoffroy Lerosey. Negative refractive index and acoustic superlens from multiple scattering in single negative metamaterials. *Nature*, 525(7567):77–81, 2015.

[14] Winston E Kock and FK Harvey. Refracting sound waves. *The Journal of the Acoustical Society of America*, 21(5):471–481, 1949.

[15] Zhengyou Liu, Xixiang Zhang, Yiwei Mao, YY Zhu, Zhiyu Yang, CT Chan, and Ping Sheng. Locally resonant sonic materials. *Science*, 289(5485):1734–1736, 2000.

[16] Jensen Li and CT Chan. Double-negative acoustic metamaterial. *Physical Review E*, 70(5):055602, 2004.

[17] AB Movchan and S Guenneau. Split-ring resonators and localized modes. *Physical Review B*, 70(12):125116, 2004.

[18] Nicholas Fang, Dongjuan Xi, Jianyi Xu, Muralidhar Ambati, Werayut Srituravanich, Cheng Sun, and Xiang Zhang. Ultrasonic metamaterials with negative modulus. *Nature materials*, 5(6):452–456, 2006.

[19] Vladimir Fokin, Muralidhar Ambati, Cheng Sun, and Xiang Zhang. Method for retrieving effective properties of locally resonant acoustic metamaterials. *Physical review B*, 76(14):144302, 2007.

[20] Sam Hyeon Lee, Choon Mahn Park, Yong Mun Seo, Zhi Guo Wang, and Chul Koo Kim. Acoustic metamaterial with negative density. *Physics letters A*, 373(48):4464–4469, 2009.

[21] Sam Hyeon Lee, Choon Mahn Park, Yong Mun Seo, Zhi Guo Wang, and Chul Koo Kim. Acoustic metamaterial with negative modulus. *Journal of Physics: Condensed Matter*, 21(17):175704, 2009.

[22] Sam Hyeon Lee, Choon Mahn Park, Yong Mun Seo, Zhi Guo Wang, and Chul Koo Kim. Composite acoustic medium with simultaneously negative density and modulus. *Physical review letters*, 104(5):054301, 2010.

[23] Julien de Rosny and Mathias Fink. Overcoming the diffraction limit in wave physics using a time-reversal mirror and a novel acoustic sink. *Physical review letters*, 89(12):124301, 2002.

[24] Graeme W Milton, Marc Briane, and John R Willis. On cloaking for elasticity and physical equations with a transformation invariant form. *New Journal of Physics*, 8(10):248, 2006.

[25] Huanyang Chen and CT Chan. Acoustic cloaking in three dimensions using acoustic metamaterials. *Applied physics letters*, 91(18):183518, 2007.

[26] Steven A Cummer, Bogdan-Ioan Popa, David Schurig, David R Smith, John Pendry, Marco Rahm, and Anthony Starr. Scattering theory derivation of a 3d acoustic cloaking shell. *Physical review letters*, 100(2):024301, 2008.

[27] Mohamed Farhat, Sébastien Guenneau, Stefan Enoch, Alexander Movchan, Frédéric Zolla, and André Nicolet. A homogenization route towards square cylindrical acoustic cloaks. *New Journal of Physics*, 10(11):115030, 2008.

[28] Daniel Torrent and José Sánchez-Dehesa. Acoustic cloaking in two dimensions: a feasible approach. *New Journal of Physics*, 10(6):063015, 2008.

[29] Andrew N Norris. Acoustic metafluids. *The Journal of the Acoustical Society of America*, 125(2):839–849, 2009.

[30] Johan Christensen, AI Fernandez-Dominguez, F de Leon-Perez, L Martin-Moreno, and FJ Garcia-Vidal. Collimation of sound assisted by acoustic surface waves. *Nature Physics*, 3(12):851–852, 2007.

[31] Johan Christensen, PA Huidobro, L Martín-Moreno, and FJ Garcia-Vidal. Confining and slowing airborne sound with a corrugated metawire. *Applied Physics Letters*, 93(8):083502, 2008.

[32] Sébastien Guenneau, Alexander Movchan, Gunnar Pétursson, and S Anantha Ramakrishna. Acoustic metamaterials for sound focusing and confinement. *New Journal of physics*, 9(11):399, 2007.

[33] Muralidhar Ambati, Nicholas Fang, Cheng Sun, and Xiang Zhang. Surface resonant states and superlensing in acoustic metamaterials. *Physical Review B*, 75(19):195447, 2007.

[34] Shu Zhang, Leilei Yin, and Nicholas Fang. Focusing ultrasound with an acoustic metamaterial network. *Physical review letters*, 102(19):194301, 2009.

[35] Xianyu Ao and CT Chan. Far-field image magnification for acoustic waves using anisotropic acoustic metamaterials. *Physical Review E*, 77(2):025601, 2008.

[36] Jensen Li, Lee Fok, Xiaobo Yin, Guy Bartal, and Xiang Zhang. Experimental demonstration of an acoustic magnifying hyperlens. *Nature materials*, 8(12):931–934, 2009.

[37] Ming-Hui Lu, Xiao-Kang Liu, Liang Feng, Jian Li, Cheng-Ping Huang, Yan-Feng Chen, Yong-Yuan Zhu, Shi-Ning Zhu, and Nai-Ben Ming. Extraordinary acoustic transmission through a 1d grating with very narrow apertures. *Physical review letters*, 99(17):174301, 2007.

[38] Héctor Estrada, Pilar Candelas, Antonio Uris, Francisco Belmar, FJ García De Abajo, and Francisco Meseguer. Extraordinary sound screening in perforated plates. *Physical review letters*, 101(8):084302, 2008.

[39] Choon Mahn Park, Jong Jin Park, Seung Hwan Lee, Yong Mun Seo, Chul Koo Kim, and Sam H Lee. Amplification of acoustic evanescent waves using metamaterial slabs. *Physical review letters*, 107(19):194301, 2011.

[40] Jie Zhu, Johan Christensen, Jesper Jung, Luis Martin-Moreno, X Yin, Lee Fok, Xiang Zhang, and FJ Garcia-Vidal. A holey-structured metamaterial for acoustic deep-subwavelength imaging. *Nature physics*, 7(1):52–55, 2011.

[41] Shu Zhang, Chunguang Xia, and Nicholas Fang. Broadband acoustic cloak for ultrasound waves. *Physical Review Letters*, 106(2):024301, 2011.

[42] Jun Mei, Guancong Ma, Min Yang, Zhiyu Yang, Weijia Wen, and Ping Sheng. Dark acoustic metamaterials as super absorbers for low-frequency sound. *Nature communications*, 3:756, 2012.

[43] Min Yang, Guancong Ma, Zhiyu Yang, and Ping Sheng. Coupled membranes with doubly negative mass density and bulk modulus. *Physical review letters*, 110(13):134301, 2013.

[44] Bogdan-Ioan Popa and Steven A Cummer. Non-reciprocal and highly nonlinear active acoustic metamaterials. *Nature communications*, 5, 2014.

[45] Romain Fleury, Dimitrios L Sounas, Caleb F Sieck, Michael R Haberman, and Andrea Alù. Sound isolation and giant linear nonreciprocity in a compact acoustic circulator. *Science*, 343(6170):516–519, 2014.

[46] Lucian Zigoneanu, Bogdan-Ioan Popa, and Steven A Cummer. Three-dimensional broadband omnidirectional acoustic ground cloak. *Nature materials*, 13(4):352–355, 2014.

[47] Yangbo Xie, Wenqi Wang, Huanyang Chen, Adam Konneker, Bogdan-Ioan Popa, and Steven A Cummer. Wavefront modulation and subwavelength diffractive acoustics with an acoustic metasurface. *Nature communications*, 5, 2014.

[48] Romain Fleury, Dimitrios Sounas, and Andrea Alù. An invisible acoustic sensor based on parity-time symmetry. *Nature communications*, 6, 2015.

[49] Yangbo Xie, Tsung-Han Tsai, Adam Konneker, Bogdan-Ioan Popa, David J Brady, and Steven A Cummer. Single-sensor multispeaker listening with acoustic metamaterials. *Proceedings of the National Academy of Sciences*, 112(34):10595–10598, 2015.

[50] Hussein Esfahlani, Sami Karkar, Hervé Lissek, and Juan R Mosig. Exploiting the leaky-wave properties of transmission-line metamaterials for single-microphone direction finding. *The Journal of the Acoustical Society of America*, 139(6):3259–3266, 2016.

[51] Hussein Esfahlani, Sami Karkar, Herve Lissek, and Juan R Mosig. Acoustic dispersive prism. *Scientific reports*, 6, 2016.

[52] Hussein Esfahlani, Sami Karkar, Herve Lissek, and Juan R Mosig. Acoustic carpet cloak based on an ultrathin metasurface. *Physical Review B*, 94(1):014302, 2016.

[53] Cédric Faure, Olivier Richoux, Simon Félix, and Vincent Pagneux. Experiments on metasurface carpet cloaking for audible acoustics. *Applied Physics Letters*, 108(6):064103, 2016.

[54] Hussein Esfahlani, Herve Lissek, and Juan R Mosig. Generation of acoustic helical wavefronts using metasurfaces. *Physical Review B*, 95(2):024312, 2017.

[55] Gianluca Memoli, Mihai Caleap, Michihiro Asakawa, Deepak R Sahoo, Bruce W Drinkwater, and Sriram Subramanian. Metamaterial bricks and quantization of meta-surfaces. *Nature Communications*, 8:14608, 2017.

[56] Richard Phillips Feynman, Robert B Leighton, and Matthew Sands. *Feynman lectures on physics. vol. 1: Mainly mechanics, radiation and heat.* Addison-Wesley, 1963.

[57] Frédéric Bongard, Hervé Lissek, and Juan R Mosig. Acoustic transmission line metamaterial with negative/zero/positive refractive index. *physical Review B*, 82(9):094306, 2010.

[58] Anne-Sophie Moreau, Hervé Lissek, and Frédéric Bongard. Design of acoustic metamaterials based on the concept of dual transmission line. In *Proceedings of the COMSOL Conference*, 2010.

[59] George V Eleftheriades and Keith G Balmain. *Negative-refraction metamaterials: fundamental principles and applications.* John Wiley & Sons, 2005.

[60] George V Eleftheriades, Ashwin K Iyer, and Peter C Kremer. Planar negative refractive index media using periodically lc loaded transmission lines. *IEEE transactions on Microwave Theory and Techniques*, 50(12):2702–2712, 2002.

[61] Christophe Caloz and Tatsuo Itoh. *Electromagnetic metamaterials: transmission line theory and microwave applications.* John Wiley & Sons, 2005.

[62] Xinhua Hu, Kai-Ming Ho, Che Ting Chan, and Jian Zi. Homogenization of acoustic metamaterials of helmholtz resonators in fluid. *Physical Review B*, 77(17):172301, 2008.

[63] Nathan Marcuvitz. *Waveguide handbook.* Number 21. Iet, 1951.

[64] Leon Brillouin. *Wave propagation in periodic structures: electric filters and crystal lattices.* Courier Corporation, 2003.

[65] Hussein Esfahlani, Sami Karkar, and Hervé Lissek. Optimization of an acoustic leaky-wave antenna based on acoustic metamaterial. In *Acoustics 2013*, number EPFL-CONF-197906, 2013.

[66] Hervé Lissek, Hussein Esfahlani, Sami Karkar, and Juan Ramon Mosig. Développement et validation d'une d'antenne acoustique à ondes de fuite. In *Actes du 13e Congrès Français d' Acoustique*, number EPFL-CONF-215183, 2016.

Bibliography

[67] Hussein Esfahlani, Sami Karkar, Herve Lissek, and Juan R Mosig. Electromagnetic inspired acoustic leaky-wave antenna. In *Antennas and Propagation (EuCAP), 2016 10th European Conference on*, pages 1–4. IEEE, 2016.

[68] William W Hansen. Radiating electromagnetic wave guide, June 25 1946. US Patent 2,402,622.

[69] S Abielmona, HV Nguyen, and C Caloz. Analog direction of arrival estimation using an electronically-scanned crlh leaky-wave antenna. *IEEE Transactions on Antennas and Propagation*, 59(4):1408–1412, 2011.

[70] Shulabh Gupta, Samer Abielmona, and Christophe Caloz. Microwave analog real-time spectrum analyzer (rtsa) based on the spectral–spatial decomposition property of leaky-wave structures. *IEEE Transactions on Microwave Theory and Techniques*, 57(12):2989–2999, 2009.

[71] Mário G Silveirinha. Anomalous refraction of light colors by a metamaterial prism. *Physical review letters*, 102(19):193903, 2009.

[72] Hideo Kosaka, Takayuki Kawashima, Akihisa Tomita, Masaya Notomi, Toshiaki Tamamura, Takashi Sato, and Shojiro Kawakami. Superprism phenomena in photonic crystals. *Physical review B*, 58(16):R10096, 1998.

[73] Lijun Wu, Michael Mazilu, Tim Karle, and Thomas F Krauss. Superprism phenomena in planar photonic crystals. *IEEE Journal of Quantum Electronics*, 38(7):915–918, 2002.

[74] Jie Zhu, Yongyao Chen, Xuefeng Zhu, Francisco J Garcia-Vidal, Xiaobo Yin, Weili Zhang, and Xiang Zhang. Acoustic rainbow trapping. *Scientific reports*, 3, 2013.

[75] Xu Ni, Ying Wu, Ze-Guo Chen, Li-Yang Zheng, Ye-Long Xu, Priyanka Nayar, Xiao-Ping Liu, Ming-Hui Lu, and Yan-Feng Chen. Acoustic rainbow trapping by coiling up space. *Scientific reports*, 4:7038, 2014.

[76] AA Oliner, DR Jackson, and JL Volakis. Antenna engineering handbook. *New York, McGraw-Hill Book Company*, 1, 2007.

[77] Philip McCord Morse and K Uno Ingard. *Theoretical acoustics*. Princeton university press, 1968.

[78] Bryan H Song and J Stuart Bolton. A transfer-matrix approach for estimating the characteristic impedance and wave numbers of limp and rigid porous materials. *The Journal of the Acoustical Society of America*, 107(3):1131–1152, 2000.

[79] Hussein Esfahlani, Sami Karkar, and Hervé Lissek. Acoustic metasurface. In *META'15, the 6th International Conference on Metamaterials, Photonic Crystals and Plasmonics*, number EPFL-CONF-210445, 2015.

154

[80] Nanfang Yu, Patrice Genevet, Mikhail A Kats, Francesco Aieta, Jean-Philippe Tetienne, Federico Capasso, and Zeno Gaburro. Light propagation with phase discontinuities: generalized laws of reflection and refraction. *science*, 334(6054):333–337, 2011.

[81] Nanfang Yu and Federico Capasso. Flat optics with designer metasurfaces. *Nature materials*, 13(2):139–150, 2014.

[82] Christos Argyropoulos, Khai Q Le, Nadia Mattiucci, Giuseppe D'Aguanno, and Andrea Alu. Broadband absorbers and selective emitters based on plasmonic brewster metasurfaces. *Physical Review B*, 87(20):205112, 2013.

[83] Yang Zhao and Andrea Alù. Manipulating light polarization with ultrathin plasmonic metasurfaces. *Physical Review B*, 84(20):205428, 2011.

[84] Hou-Tong Chen, John F O'hara, Abul K Azad, Antoinette J Taylor, Richard D Averitt, David B Shrekenhamer, and Willie J Padilla. Experimental demonstration of frequency-agile terahertz metamaterials. *Nature Photonics*, 2(5):295–298, 2008.

[85] Jing Zhang, Zhong Lei Mei, Wan Ru Zhang, Fan Yang, and Tie Jun Cui. An ultra-thin directional carpet cloak based on generalized snell's law. *Applied Physics Letters*, 103(15):151115, 2013.

[86] Xingjie Ni, Zi Jing Wong, Michael Mrejen, Yuan Wang, and Xiang Zhang. An ultrathin invisibility skin cloak for visible light. *Science*, 349(6254):1310–1314, 2015.

[87] Jiajun Zhao, Baowen Li, Zhi Ning Chen, and Cheng-Wei Qiu. Redirection of sound waves using acoustic metasurface. *Applied Physics Letters*, 103(15):151604, 2013.

[88] G D'Aguanno, KQ Le, R Trimm, A Alu, N Mattiucci, AD Mathias, N Aközbek, and MJ Bloemer. Broadband metamaterial for nonresonant matching of acoustic waves. *Scientific reports*, 2, 2012.

[89] Yi-Fan Zhu, Xin-Ye Zou, Bin Liang, and Jian-Chun Cheng. Broadband unidirectional transmission of sound in unblocked channel. *Applied Physics Letters*, 106(17):173508, 2015.

[90] Yi-Fan Zhu, Xin-Ye Zou, Bin Liang, and Jian-Chun Cheng. Acoustic one-way open tunnel by using metasurface. *Applied Physics Letters*, 107(11):113501, 2015.

[91] Wenqi Wang, Yangbo Xie, Adam Konneker, Bogdan-Ioan Popa, and Steven A Cummer. Design and demonstration of broadband thin planar diffractive acoustic lenses. *Applied Physics Letters*, 105(10):101904, 2014.

[92] Guancong Ma, Min Yang, Songwen Xiao, Zhiyu Yang, and Ping Sheng. Acoustic meta-surface with hybrid resonances. *Nature materials*, 13(9):873–878, 2014.

[93] Pai-Yen Chen, Mohamed Farhat, Sébastien Guenneau, Stefan Enoch, and Andrea Alù. Acoustic scattering cancellation via ultrathin pseudo-surface. *Applied Physics Letters*, 99(19):191913, 2011.

[94] Mohamed Farhat, Pai-Yen Chen, Sébastien Guenneau, Stefan Enoch, and Andrea Alu. Frequency-selective surface acoustic invisibility for three-dimensional immersed objects. *Physical Review B*, 86(17):174303, 2012.

[95] Yong Li, Bin Liang, Zhong-ming Gu, Xin-ye Zou, and Jian-chun Cheng. Reflected wavefront manipulation based on ultrathin planar acoustic metasurfaces. *Scientific reports*, 3:2546, 2013.

[96] Baoguo Yuan, Ying Cheng, and Xiaojun Liu. Conversion of sound radiation pattern via gradient acoustic metasurface with space-coiling structure. *Applied Physics Express*, 8(2):027301, 2015.

[97] Zixian Liang and Jensen Li. Extreme acoustic metamaterial by coiling up space. *Physical review letters*, 108(11):114301, 2012.

[98] Yi-Fan Zhu, Xin-Ye Zou, Rui-Qi Li, Xue Jiang, Juan Tu, Bin Liang, and Jian-Chun Cheng. Dispersionless manipulation of reflected acoustic wavefront by subwavelength corrugated surface. *Scientific reports*, 5, 2015.

[99] Rasha Al Jahdali and Ying Wu. High transmission acoustic focusing by impedance-matched acoustic meta-surfaces. *Applied Physics Letters*, 108(3):031902, 2016.

[100] Jun Mei and Ying Wu. Controllable transmission and total reflection through an impedance-matched acoustic metasurface. *New Journal of Physics*, 16(12):123007, 2014.

[101] Changlin Ding, Huaijun Chen, Shilong Zhai, Song Liu, and Xiaopeng Zhao. The anomalous manipulation of acoustic waves based on planar metasurface with split hollow sphere. *Journal of Physics D: Applied Physics*, 48(4):045303, 2015.

[102] Shilong Zhai, Huaijun Chen, Changlin Ding, Fangliang Shen, Chunrong Luo, and Xiaopeng Zhao. Manipulation of transmitted wave front using ultrathin planar acoustic metasurfaces. *Applied Physics A*, 120(4):1283–1289, 2015.

[103] Ye Tian, Qi Wei, Ying Cheng, Zheng Xu, and Xiaojun Liu. Broadband manipulation of acoustic wavefronts by pentamode metasurface. *Applied Physics Letters*, 107(22):221906, 2015.

[104] Jiajun Zhao, Baowen Li, Zhining Chen, and Cheng-Wei Qiu. Manipulating acoustic wavefront by inhomogeneous impedance and steerable extraordinary reflection. *Scientific reports*, 3:2537, 2013.

[105] Monica Carfagni, Edoardo Lenzi, and Marco Pierini. The loss factor as a measure of mechanical damping. In *Proceedings-spie the international society for optical engineering*, volume 1, pages 580–284. SPIE INTERNATIONAL SOCIETY FOR OPTICAL, 1998.

[106] Nasim Mohammadi Estakhri and Andrea Alù. Ultra-thin unidirectional carpet cloak and wavefront reconstruction with graded metasurfaces. *IEEE Antennas and Wireless Propagation Letters*, 13:1775–1778, 2014.

[107] B Orazbayev, N Mohammadi Estakhri, M Beruete, and A Alù. Terahertz carpet cloak based on a ring resonator metasurface. *Physical Review B*, 91(19):195444, 2015.

[108] Hussein Esfahlani, Sami Karkar, and Hervé Lissek. On the design of unit-cells for acoustic metasurfaces. In *Advanced Electromagnetic Materials in Microwaves and Optics (METAMATERIALS), 2015 9th International Congress on*, pages 397–399. IEEE, 2015.

[109] JH Poynting. The wave motion of a revolving shaft, and a suggestion as to the angular momentum in a beam of circularly polarised light. *Proceedings of the Royal Society of London. Series A, Containing Papers of a Mathematical and Physical Character*, 82(557):560–567, 1909.

[110] Richard A Beth. Mechanical detection and measurement of the angular momentum of light. *Physical Review*, 50(2):115, 1936.

[111] John David Jackson and Ronald F Fox. Classical electrodynamics. *American Journal of Physics*, 67(9):841–842, 1999.

[112] Les Allen, Marco W Beijersbergen, RJC Spreeuw, and JP Woerdman. Orbital angular momentum of light and the transformation of laguerre-gaussian laser modes. *Physical Review A*, 45(11):8185, 1992.

[113] Miles Padgett and Richard Bowman. Tweezers with a twist. *Nature Photonics*, 5(6):343–348, 2011.

[114] Michael V Berry, JF Nye, and FJ Wright. The elliptic umbilic diffraction catastrophe. *Philosophical Transactions of the Royal Society of London A: Mathematical, Physical and Engineering Sciences*, 291(1382):453–484, 1979.

[115] Brian T Hefner and Philip L Marston. Acoustical helicoidal waves and laguerre-gaussian beams: Applications to scattering and to angular momentum transport. *J. Acoust. Soc. Am*, 103(5):2971–2971, 1998.

[116] Jean-Louis Thomas and Régis Marchiano. Pseudo angular momentum and topological charge conservation for nonlinear acoustical vortices. *Physical review letters*, 91(24):244302, 2003.

[117] Régis Marchiano and Jean-Louis Thomas. Synthesis and analysis of linear and nonlinear acoustical vortices. *Physical Review E*, 71(6):066616, 2005.

Bibliography

[118] Likun Zhang and Philip L Marston. Angular momentum flux of nonparaxial acoustic vortex beams and torques on axisymmetric objects. *Physical Review E*, 84(6):065601, 2011.

[119] Arturo O Santillán and Karen Volke-Sepúlveda. A demonstration of rotating sound waves in free space and the transfer of their angular momentum to matter. *American Journal of Physics*, 77(3):209–215, 2009.

[120] Andreas Anhäuser, Régis Wunenburger, and Etienne Brasselet. Acoustic rotational manipulation using orbital angular momentum transfer. *Physical review letters*, 109(3):034301, 2012.

[121] Joao L Ealo, Jose Carlos Prieto, and Fernando Seco. Airborne ultrasonic vortex generation using flexible ferroelectrets. *IEEE transactions on ultrasonics, ferroelectrics, and frequency control*, 58(8):1651–1657, 2011.

[122] Brian T Hefner and Philip L Marston. An acoustical helicoidal wave transducer with applications for the alignment of ultrasonic and underwater systems. *The Journal of the Acoustical Society of America*, 106(6):3313–3316, 1999.

[123] Ling Yang, Qingyu Ma, Juan Tu, and Dong Zhang. Phase-coded approach for controllable generation of acoustical vortices. *Journal of Applied Physics*, 113(15):154904, 2013.

[124] Stefan Gspan, Alex Meyer, Stefan Bernet, and Monika Ritsch-Marte. Optoacoustic generation of a helicoidal ultrasonic beam. *The Journal of the Acoustical Society of America*, 115(3):1142–1146, 2004.

[125] Tian Wang, Manzhu Ke, Weiping Li, Qian Yang, Chunyin Qiu, and Zhengyou Liu. Particle manipulation with acoustic vortex beam induced by a brass plate with spiral shape structure. *Applied Physics Letters*, 109(12):123506, 2016.

[126] Christina J Naify, Charles A Rohde, Theodore P Martin, Michael Nicholas, Matthew D Guild, and Gregory J Orris. Generation of topologically diverse acoustic vortex beams using a compact metamaterial aperture. *Applied Physics Letters*, 108(22):223503, 2016.

[127] Xue Jiang, Yong Li, Bin Liang, Jian-chun Cheng, and Likun Zhang. Convert acoustic resonances to orbital angular momentum. *Physical Review Letters*, 117(3):034301, 2016.

[128] Liping Ye, Chunyin Qiu, Jiuyang Lu, Kun Tang, Han Jia, Manzhu Ke, Shasha Peng, and Zhengyou Liu. Making sound vortices by metasurfaces. *AIP Advances*, 6(8):085007, 2016.

[129] Yong Li, Xue Jiang, Rui-qi Li, Bin Liang, Xin-ye Zou, Lei-lei Yin, and Jian-chun Cheng. Experimental realization of full control of reflected waves with subwavelength acoustic metasurfaces. *Physical Review Applied*, 2(6):064002, 2014.

[130] Bahaa EA Saleh, Malvin Carl Teich, and Bahaa E Saleh. *Fundamentals of photonics*, volume 22. Wiley New York, 1991.

[131] Lawrence E Kinsler, Austin R Frey, Alan B Coppens, and James V Sanders. *Fundamentals of acoustics*. 1999.

[132] Allan D Pierce et al. *Acoustics: an introduction to its physical principles and applications*, volume 20. McGraw-Hill New York, 1981.

[133] David M Pozar. *Microwave engineering*. John Wiley & Sons, 2009.

[134] Mahmoud I Hussein, Michael J Leamy, and Massimo Ruzzene. Dynamics of phononic materials and structures: Historical origins, recent progress, and future outlook. *Applied Mechanics Reviews*, 66(4):040802, 2014.

[135] Leo L Beranek. *Acoustics*. McGraw-Hill New York, 1954.

[136] Zdenek Skvor. Vibrating systems and their equivalent circuits. *Studies in electrical and electronic engineering*, 40:11–241, 1991.

[137] GB Warburton. The vibration of rectangular plates. *Proceedings of the Institution of Mechanical Engineers*, 168(1):371–384, 1954.

[138] Snehashish Chakraverty. *Vibration of plates*. CRC press, 2008.

[139] Mario Rossi. *Acoustics and electroacoustics*. Artech House Publishers, 1988.

[140] Jiu Hui Wu, AQ Liu, and HL Chen. Exact solutions for free-vibration analysis of rectangular plates using bessel functions. *Journal of Applied Mechanics*, 74(6):1247–1251, 2007.

[141] Arthur W Leissa. Vibration of plates. Technical report, DTIC Document, 1969.

[142] Robert E Collin. *Foundations for microwave engineering*. John Wiley & Sons, 2007.

Hussein Esfahlani

EPFL-Ecole Polytechnique Federale de Lausanne
Electrical Engineering Department
Address: EPFL STI IEL LEMA
ELB 032 (Batiment ELB)
CH-1015 Lausanne, Switzerland
Date of Birth: February 16, 1987
Marital Status: Single

Mobile: (+41)787655413
Office: (+41)216932717
Email: hussein.esfahlani@epfl.ch
hsesfahlan@gmail.com
Homepage: http://people.epfl.ch
/hussein.esfahlani

Education

P.hD. Electrical Engineering, Ecole Polytechnique Federale de Lausanne, December 2012-May 2017.
Supervisor: Juan R. Mosig, Herve Lissek

Visiting P.hD. Electrical and Computer Engineering, University of Texas at Austin, August 2016-January 2017. (SNSF Doctoral Mobility Fellowship)
Supervisor: Andrea Alu

M.sc. Electrical Engineering, Amirkabir University of Technology, 2009-2011.
Supervisor: Ahad Tavakoli

B.sc. Electrical Engineering, Amirkabir University of Technology, 2005-2009.
Supervisor: Ahad Tavakoli

Research Interests

Electromagnetics, Acoustics, Antenna, Metamaterial

Academic Experience

Research Assistant

Amirkabir University of Technology, Department of Electrical Engineering

Research Assistant, Electromagnetic Research Lab, September 2009–April 2011.

K. N. T University of Technology, Department of Electrical Engineering

Research Assistant, Electromagnetic Research Lab, May 2011–June 2011.

University of Texas at Austin, Department of Electrical and Computer Engineering

Visiting Research Scholar, Metamaterials & Plasmonics Research Laboratory, August 2016–January 2017.

Ecole Polytechnique Federale de Lausanne, Department of Electrical Engineering

Research Assistant, Laboratory of Electromagnetics and Acoustics LEMA, December 2012–2015.

Research Assistant, Signal Processing Laboratory 2 (LTS2), January 2016–Present.

Teaching Assistant

Amirkabir University of Technology, Department of Biomedical Engineering

Teaching Assistant, Electromagnetic, Prof A. Tavakoli, Autumn 2010.

Ecole Polytechnique Federale de Lausanne, Department of Electrical Engineering

Teaching Assistant, Electroacoustics, Dr. Herve Lissek, Autumn 2014, Autumn 2015.

Work Experience

Antenna Design Engineer, Qandi Research Center, K. N. T University of Technology

Designing Shaped reflector antenna and low cross-polarization corrugated horn antenna for broad casting GEO stationary satellite, June 2011–September 2012.

Projects

High gain array antenna synthesis for sapce application as final project to get Bachelor's degree in 2009.

Design and fabrication of compact single-layer dual-band microstrip antenna for LEO satellite applications as final project to get master's degree in 2011.

Shaped reflector antenna design for broadcasting GEO satellite as design engineer at Qandi research center in 2012.

Low cross polarized corrugated horn antenna as a feed for shape reflector antenna as design engineer at Qandi research center in 2012.

Acoustic Leaky wave antenna and acoustic prism as doctoral research assistant at EPFL in 2013.

Acoustic reflect array antenna and acoustic carpet cloak design as doctoral research assistant at EPFL in 2014.

Acoustic orbital angular momentum metasurface design as doctoral research assistant at EPFL in 2016.

Publications

Journals

S. H. S. Esfahlani, A. Tavakoli and P. Dehkhoda, A compact Single-Layer Dual-Band Microstrip Antenna for Satellite Applications, in IEEE Antennas Wireless Propag. Lett.vol 10, pp.931 - 934, 2011.

H. Esfahlani, S. Karkar, H. Lissek and J. R. Mosig, Acoustic dispersive prism, in Sci. Rep. 6, 18911, 2016.

H. Esfahlani, S. Karkar, H. Lissek and J. R. Mosig, Exploiting the leaky-wave properties of transmission-line metamaterials for single-microphone direction finding, in The Journal of the Acoustical Society of America, vol. 139, num. 6, p. 3259-3266, 2016.

H. Esfahlani, S. Karkar, H. Lissek and J. R. Mosig, Acoustic carpet cloak based on ultra-thin metasurface, in Physical Review B, vol. 94, num. 1, p. 014302, 2016.

H. Esfahlani, H. Lissek, and J. R. Mosig, Generation of acoustic helical wavefronts using metasurfaces, in Physical Review B, vol. 95, num. 2, p. 024312, 2017.

Conferences

H. Esfahlani, S. Karkar, H. Lissek and J. R. Mosig. Electromagnetic Inspired Acoustic Leaky-wave Antenna, 10th European Conference on Antennas and Propagation (EuCAP), Davos, Switzerland, April, 10-15, 2016.

H. Lissek, H. Esfahlani, S. Karkar and J. R. Mosig. Dveloppement et validation dune dantenne acoustique ondes de fuite. 13e Congrs Franais d'Acoustique, Le Mans, 2016.

H. Esfahlani, S. Karkar and H. Lissek. On the design of unit-cells for acoustic metasurfaces. 9th International Congress on Advanced Electromagnetic Materials in Microwaves and Optics - Metamaterials 2015, Oxford, United Kingdom, 2015.

H. Esfahlani, S. Karkar and H. Lissek. Acoustic Metasurface. META15, the 6th International Conference on Metamaterials, Photonic Crystals and Plasmonics, City College of New York, New York City, NY, USA, 2015. [**Best Poster Award**]

H. Esfahlani, S. Karkar and H. Lissek. Acoustic Leaky-Wave Antenna. 8th International Congress on Advanced Electromagnetic Materials in Microwaves and Optics - Metamaterials 2014, Copenhagen, Denmark, 2014.

H. Esfahlani, S. Karkar and H. Lissek. Optimization of an acoustic leaky-wave antenna based on acoustic metamaterial. Acoustics 2013, New Delhi, India, 2013

Honors & Awards

Doc.Mobility fellowship, Swiss National Science Foundation (SNSF), August 2016 - January 2017.

Best Poster Award Winner, META'15, the 6th International Conference on Metamaterials, Photonic Crystals and Plasmonics

Honours student, Master of Science, 2011.

Honours student, Bachlor of Sience, 2009.

Member of the Exceptional Talented Student Centre of the Amirkabir University of Technology, 2005-2011.

Top 20, Physics Lab Student Competition, Iran, 2005.

Miscellaneous

Software Skills

COMSOL, HFSS, CST, FEKO, MATLAB, SolidWorks

Language Skills

Azerbaijani, Turkish, Persian, English, French (B_1)

Hussein Esfahlani

References

Juan Ramon Mosig
Professor of Electrical Engineering
Ecole Polytechnique Federale de Lausanne
(+41 21 69) 32669
`juan.mosig@epfl.ch`

Andrea Alu
Professor of Electrical Engineering
University of Texas at Austin
(+1512) 4715922
`alu@mail.utexas.edu`

Ahad Tavakoli
Professor of Electrical Engineering
Amirkabir University of Technology
(+9821) 64543317
`tavakoli@aut.ac.ir`

Herve Lissek
Head of the Acoustic Group
Ecole Polytechnique Federale de Lausanne
(+41 21 69) 34630
`herve.lissek@epfl.ch`

Press

SCIENTIFIC AMERICAN: Engineers Debut the Acoustic Prism
Scientific American (November 2016), 315, 19.
(`https://www.scientificamerican.com/...`)
(`www.nature.com/scientificamerican/journal/v315/n5/...`)

NEWS MEDIACOM: Acoustic Prism Invented at EPFL
(`http://actu.epfl.ch/news/acoustic-prism-invented-at-epfl/`)

PHYS.ORG: Researchers invent acoustic prism
(`https://phys.org/news/2016-08-acoustic-prism.html`)

EXTREME TECH: An acoustic prism can split sound the way a regular prism splits light
(`https://www.extremetech.com/extreme/....`)

IN COMPLIANCE MAGAZINE: Introducing The Acoustic Prism
(`http://incompliancemag.com/introducing-the-acoustic-prism/`)

UPI.com: Scientists invent new type of 'acoustic prism'
(`http://www.upi.com/...`)

ALL ABOUT CIRCUIT: New Acoustic Prism Splits Sound Like Optical Prisms Split Light
(`https://www.allaboutcircuits.com/news/...`)

<div align="center">Last updated: May 18, 2017</div>